Technische Universität München
Institut für Energietechnik

Lehrstuhl für Thermodynamik

Flame Flashback in Wall Boundary Layers of Premixed Combustion Systems

Christian Thomas Eichler

Vollständiger Abdruck der von der Fakultät für Maschinenwesen der Technischen Universität München zur Erlangung des akademischen Grades eines

DOKTOR – INGENIEURS

genehmigten Dissertation.

Vorsitzender:

Univ.-Prof. Dr.-Ing. habil. Nikolaus A. Adams

Prüfer der Dissertation:

1. Univ.-Prof. Dr.-Ing. Thomas Sattelmayer
2. Prof. Vince McDonell, Ph.D.,
   University of California, Irvine/USA

Die Dissertation wurde am 07.07.2011 bei der Technischen Universität München eingereicht und durch die Fakultät für Maschinenwesen am 17.11.2011 angenommen.

Abstract

The utilization of hydrogen-rich fuels in premixed and undiluted combustion systems faces a particular type of operational instability, which is flame propagation against the mean flow direction inside the wall boundary layer. This process, also known as wall flashback, has been investigated in a generic combustion experiment for laminar and turbulent flow conditions and different fuels using optical measurement techniques. The results have revealed that the existing physical model of wall flashback is inadequate. A static pressure rise upstream of the flame causes the boundary layer to separate and the flame to propagate upstream inside the associated backflow region. Based on these experimental findings and numerical simulation with a reduced kinetic mechanism, a new physical model for wall flashback and an according correlation method is presented.

Zusammenfassung

Die Verwendung wasserstoffreicher Brennstoffe ruft in vorgemischten und unverdünnten Verbrennungssystemen eine Instabilität hervor, bei der sich die Flamme entgegen der Hauptströmung in der Wandgrenzschicht ausbreitet. Dieser Prozess, der als Grenzschichtrückschlag bezeichnet wird, wurde in einem generischen Verbrennungsexperiment für laminare und turbulente Strömungen sowie unterschiedliche Brennstoffe mittels optischer Messtechniken untersucht. Die bisherige physikalische Modellvorstellung wurde durch die experimentellen Ergebnisse widerlegt. Ein statischer Druckanstieg stromauf der Flamme führt zu einem Ablösen der Grenzschicht. Die Flamme propagiert innerhalb der resultierenden Rückströmzone stromauf. Basierend auf den experimentellen Daten und numerischen Simulationen mit einem reduzierten kinetischen Mechanismus wird ein neues physikalisches Modell für Grenzschichtrückschläge und eine entsprechende Korrelationsmethode vorgestellt.

Preface

This work has been conducted at the *Lehrstuhl für Thermodynamik* at TUM from December 2007 to June 2011. It forms a part of the BIGCO2 project, performed under the strategic Norwegian research program Climit. The partners: Statoil, GE Global Research, Statkraft, Aker Clean Carbon, Shell, TOTAL, ConocoPhillips, ALSTOM, the Research Council of Norway (178004/I30, 176059/I30) and Gassnova (182070) are acknowledged for their support.

I'd like to express my sincere gratitude to my supervisor Professor Dr.-Ing. Thomas Sattelmayer for his guidance and support in all aspects. Without the atmosphere of trust and scientific freedom he provided, this work would not have evolved as it eventually did. Furthermore, the opportunities to lead the Reactive Flows group at the chair and to assist international project acquisition were a valuable experience for me.

Special thanks go to Professor Ph.D. Vince McDonell from the University of California, Irvine, for the review of this thesis and for being the second examiner. Professor Dr.-Ing. habil. Nikolaus Adams kindly organized the doctoral examination and was chairman during the exam.

The collaboration with my project partners in Trondheim was always pleasant, fruitful and inspiring. Especially my project team leader Dr. Mario Ditaranto and Dr. Andrea Gruber shall be mentioned here.

I'd like to thank everybody at the chair who helped in solving all sorts of small and big challenges which come up during an experimental research project. Foremost, our chief engineer Dr.-Ing. Christoph Hirsch shared some of his deep insights into flow and combustion physics with me during many discussions. The guidelines from my colleague Dr.-Ing. Martin Lauer played an

essential role in successfully applying laser diagnostics. Thanks also go to my laboratory neighbor Christoph Mayer for the steady flux of tools, material and good ideas. Last but not least, my office mate Igor Pribicevic greatly helped to get things started at the beginning and to keep a positive spirit at any time.

Many students have worked with great enthusiasm to assist in building up the experimental rig, conducting ambitious measurement campaigns and post-processing the data. I'd like to thank all of them for their commitment at this point, which often went beyond what I would have expected.

This piece of work could not have been realized without the support of my family, especially from my wife Juliane. Her love and empathy are the foundation of all my efforts.

Munich, November 2011 Christian Eichler

Contents

Nomenclature

Latin Symbols

A	m^2	Area
a	m^2/s	Thermal diffusivity
c	m/s	Velocity of light
c	mol/m^3	Concentration
c_p	J/kgK	Heat capacity at constant pressure
D	m^2/s	Mass diffusivity
d	m	Diameter
E_a	kJ/mol	Activation energy
$\mathbf{e}$	–	Unit vector
F, f	–	Function
f	$1/s$	Frequency
g	$1/s$	Gradient of axial velocity at the wall
g_c	$1/s$	Gradient of axial velocity at the wall at flashback limit
h	m	Channel half-height
h	m	Step height
h	J/kg	Static enthalpy
$\mathbf{I}$	–	Two-dimensional intensity map
I	A	Current
i, j	–	Counter
K	–	Constant
K_p^0	variable	Equilibrium constant for formation at constant pressure
K_p	variable	Equilibrium constant at constant pressure
k	W/mK	Thermal conductivity
k	variable	Reaction rate factor

$\mathscr{L}$	m	Markstein length
L	m	Length
L_+	m	Wall length scale
l_t	m	Integral turbulent length scale
$\mathbf{n}$	–	Normal vector
N, n	–	Counter
p	Pa	Static pressure
p_f	Pa	Flame backpressure
q_f	J/kg	Heat of combustion
$\mathbf{R}$	–	Two-dimensional correlation function
R	m	Radius
R	m	Radius of curvature
r	m	Radial coordinate
$\mathbf{S_f}$	m/s	Flame speed vector
S_f	m/s	Flame speed
S_L	m/s	Laminar, one-dimensional and adiabatic flame speed
T	K	Temperature
t	s	Time
t^*	–	Relative time
t_+	s	Wall time scale
$\mathbf{u}$	m/s	Velocity vector
u	m/s	Axial velocity component
$\overline{u}$	m/s	Bulk flow velocity
$u_t^{'}$	m/s	Turnover velocity of integral length scale eddy
u_τ	m/s	Shear stress velocity
V	V	Voltage
$\mathbf{v_p}$	m/s	Particle velocity vector
v	m/s	Wall-normal velocity component
w	m/s	Lateral velocity component
w	m	Width
X	–	Mole fraction
$\mathbf{x}$	m	Cartesian coordinate vector
x	m	Axial coordinate
Y	–	Mass fraction

y	m	Wall-normal coordinate
z	m	Lateral coordinate

Greek Symbols

α	$^\circ$	Angle
Γ	m^2/s	Circulation
γ	$-$	Ratio of specific heats
δ	m	Boundary layer thickness
δ^*	m	Displacement thickness
δ_b	m	Balance height, also called penetration distance
δ_F	m	Depth-of-field
δ_f	m	Flame thickness
δ_L	m	Lightsheet thickness at focus
δ_q	m	Quenching distance
δ_r	m	Maximum height of backflow region
δ_{ij}	$-$	Kronecker symbol
ϵ	m^2/s^3	Dissipation rate of turbulent kinetic energy
η	m	Kolmogorov length scale
κ	$1/s$	Stretch rate
λ	m	Wavelength of light
μ	Pa s	Dynamic viscosity
ν	m^2/s	Kinematic viscosity
ν	$-$	Stoichiometric factor
ξ	$-$	Pressure gradient parameter
Π	$-$	Nondimensional correlation variable
ρ	kg/m^3	Density
τ	Pa	Shear stress
Φ	$-$	Equivalence ratio
ϕ	$^\circ$	Angle
ω	rad/s	Angular frequency
ω	$mol/m^3\,s$	Reaction rate

Superscripts

$+$	Non-dimensionalized by inner coordinates
$'$	Fluctuating quantities
$'$	Educt
$''$	Product
$\tilde{}$	Ramp coordinate system

Subscripts

0	Reference
1	Unburnt mixture
2	Adiabatic burnt mixture
∞	Freestream
air	Air
b	Backward
c	Value at flashback limit
$corr$	Correlation
D	Doppler
d	Diameter
def	Deficient
$dual$	Dual-beam LDA
ex	Excess
f	Flame
f	Forward
$flow$	Flow
$fuel$	Fuel
i, j	Counter
il	Inner layer
L	Laminar, one-dimensional and adiabatic
l	Laminar
l	Laser
mix	Mixture

PIV	PIV system
p	Particle
$pulse$	Laser pulse of PIV system
q	Quenching
r	Reaction zone
r	Reflected light
s	Shift
t	Turbulent
tan	Tangential
th	Thermal
w	Wall
x	Axial coordinate

Nondimensional Numbers

Da	Damköhler number
Ka	Karlovitz number
Le	Lewis number
M	Mach number
Ma	Markstein number
Pe	Peclet number
Re	Reynolds number

Abbreviations

BBO	**B**asset-**B**oussinesq-**O**seen
BSA	**B**urst **S**pectrum **A**nalyzer
CCS	**C**arbon **C**apture and **S**torage
CDF	**C**umulative **D**istribution **F**unction
CFD	**C**omputational **F**luid **D**ynamics
$CIVB$	**C**ombustion **I**nduced **V**ortex **B**reakdown
CNG	**C**ompressed **N**atural **G**as

CTA	**C**onstant **T**emperature **A**nemometry
DDT	**D**eflagration-**D**etonation **T**ransition
DFT	**D**iscrete **F**ourier **T**ransform
DNS	**D**irect **N**umerical **S**imulation
$FIFO$	**F**irst-**I**n **F**irst-**O**ut
LDA	**L**aser **D**oppler **A**nemometry
$NSCBC$	**N**avier-**S**tokes **C**haracteristic **B**oundary **C**onditions
PDF	**P**robability **D**ensity **F**unction
PIV	**P**article **I**mage **V**elocimetry
$RANS$	**R**eynolds-**A**veraged **N**avier-**S**tokes
rms	**r**oot **m**ean **s**quare
RSM	**R**eynolds **S**tress **M**odel
SST	**S**hear **S**tress **T**ransport
$URANS$	**U**nsteady **R**eynolds-**A**veraged **N**avier-**S**tokes

Mathematical Operators

$\langle ... \rangle$	Time average of ...
D/Dt	Substantial derivative
$\cdot$	Scalar product
$\times$	Vector product
∇	Nabla operator

Constants

κ	–	von Kármán constant
B	–	Constant in logarithmic law-of-the-wall
$\mathscr{R}$	J/kmol K	Universal gas constant

1 Introduction

In recent years, Carbon Capture and Storage (CCS) processes have become a realistic option as an interim solution towards sustainable power generation with a minimized carbon footprint [REC08]. Before CO_2 can be stored safely under the ground at the end of the CCS chain, it must be efficiently separated at some stage of the power generation process. In each of the two principal routes, either pre-combustion separation of CO_2 by fuel reforming or post-combustion separation from CO_2-rich exhaust gases, the resulting combustion processes have to be carefully designed to guarantee safe and reliable operation. Pre-combustion reforming of hydrocarbons mainly into H_2 and CO_2 allows a separation of CO_2 with well-established gas scrubbing technologies, leaving H_2-rich fuel for the combustion process. In the light of regulations on power plant emissions, undiluted and stable combustion of such H_2-rich fuels with low NO_x production, which implies premixed burning technology, can be regarded as an enabling technology for the realization of pre-combustion CCS. Looking at post-combustion separation, the CO_2 fraction in the exhaust gases of gas turbines has to be raised as high as possible to increase capture efficiency. This can be achieved by the Oxyfuel process, where fuel is burned in O_2-rich atmosphere, or by exhaust gas recirculation. While both processes are applicable to combustion of hydrocarbon fuels in their original form, such as natural gas or coal powder, there is a tendency in the energy sector to utilize Syngas as fuel, which emerges from coal gasification and mainly comprises H_2 and CO. This trend implicates that proper burner designs to cope with the peculiarities of H_2-rich combustion are important for any CCS system that should be prepared for future market demands.

The major difficulty in designing safe and reliable premixed H_2-rich fuel burners is to achieve a stable mean flame position. While lean blow-out limits are shifted to leaner operation points by H_2 chemistry, the danger of flame flash-

back into the premixing zone becomes a dominant failure type. Per definition, flame flashback designates the propagation of a flame against the mean flow as seen by an external observer. In practice, flame flashback in gas turbine combustors is usually assigned to four mechanisms:

1. **Flashback in the core flow**: The flow velocity falls below the burning velocity in the core area of the flow [KKW85, KL88, WK92, WOK93]. This mechanism plays a negligible role during regular gas turbine operation as the freestream velocity in the fuel-air supply commonly exceeds turbulent burning velocities.

2. **Flashback due to combustion instabilities**: The interaction of acoustic modes, flow structure and the energy release of the flame can lead to acoustic velocities in the order of the flow velocity. In such a situation, the flow effectively stagnates during each acoustic cycle, allowing for an upstream propagation of the flame into the fresh gases [MS68, Coa80, KVK$^+$81, BBZ$^+$93, TC98, GPW$^+$05]. The use of H_2-rich fuels instead of hydrocarbons does not necessarily worsen thermoacoustic pulsations, though.

3. **Combustion Induced Vortex Breakdown (CIVB)**: This mechanism specifically relates to swirl-stabilized burners. A typical configuration comprises a swirl generator, followed by a straight or conical duct which opens into the combustion chamber with a sudden area change. During normal operation, the flame stabilizes due to a breakdown of the duct vortex on exiting the duct, sometimes supported by a center body, which leads to a recirculation zone just downstream of the duct outlet. An increase in the fuel rate eventually leads to an upstream propagation of the recirculation zone, induced by a pressure rise on the symmetry line of the burner. This upstream propagation causes the vortex inside the duct to break down, and the flame propagates further upstream in four distinctive phases. Experiments at atmospheric and pressurized conditions, using H_2 as fuel amongst others, as well as numerical simulations have led to a detailed understanding of the involved physics along with guidelines for a safe design [FKS01, KKS07, Bur08, KS09]. Generally, CIVB propensity increases with increasing H_2 content of the fuel.

4. **Flashback in the wall boundary layer**: The no-slip condition leads to continuously reducing flow velocities close to the wall, even for high freestream velocities. Accordingly, there is a potential for the burning velocity to outbalance the flow velocity at a particular height from the wall. While this mechanism, termed *wall flashback* in the following, is usually negligible for turbulent combustion of natural gas, it becomes important for H_2-containing fuels.

A review [PM78] of reported combustor flashbacks revealed that apart from the flashback mechanisms described above, there may be other reasons for upstream flame stabilization. These emerge from flow separations or retardations upstream of the main flame in the premixing section or supply duct. If the stable combustor flame comes into contact with these regions of flow disturbance, or if the flow residence time exceeds the mixture ignition delay time in high temperature regions, combustion will be displaced upstream as well. Such processes rather represent accidental flame holding than flame flashback in its proper sense. As a conclusion, there are two flashback mechanisms of increasing concern for the design of gas turbine burners which utilize H_2 as fuel. While CIVB has been investigated thoroughly using state-of-the-art measurement techniques and advanced numerical models, this has not been the case for wall flashback, as will be shown further below.

The flow and flame configuration which is associated with the term wall flashback in this work shall be defined clearly at this point. For this purpose, four typical wall flashback situations in gas turbine burners are shown in Fig. 1.1. Configuration (a) represents flashback inside a mixing duct with unswirled flow. The flow profile close to the wall corresponds to a 'classical' boundary layer or internal flow situation as usually observed in straight ducts, tubes or on a flat plate. Only this configuration will be considered in this work since it is the most general one. Configuration (b), where the flame flashes back in the wall-near wake of transverse fuel jets, as well as (c) and (d), which represent wall flashback in swirl burners, feature boundary layers which are influenced by distinct flow properties such as wake vortices or large-scale vortex dynamics. For such cases, wall flashback behavior is probably different from situation (a), such that they require separate investigation (e.g., [HGT+10, MSS+11]). In

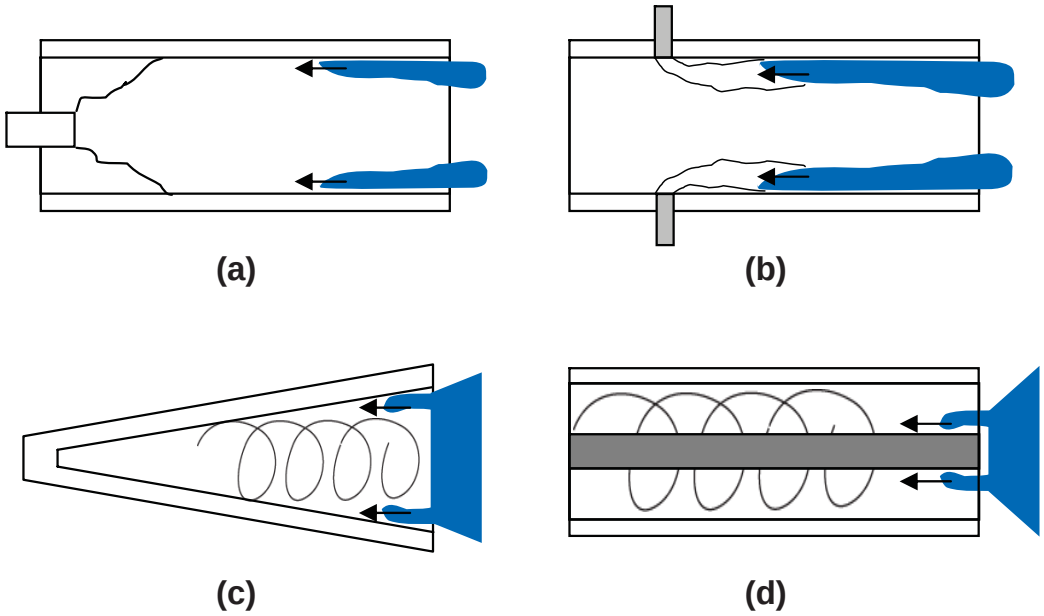

Figure 1.1: Wall flashback scenarios in gas turbine burners.

the following, the state of knowledge concerning wall flashback is summarized based on a literature survey, which will reveal still unresolved issues to be investigated in this project.

1.1 State of Knowledge

Due to its fundamental role in the design of premixed combustion devices, wall flashback has been investigated since the early days of combustion research. For the literature review presented here, only publications which explicitly cover wall flashback are considered. Please note that there exists a large body of literature on combustion in boundary layers without flame motion against the main flow direction (e.g., [Gro55, Tur58, CS83, CN85, TnSP90, VT04, Law06]) which will not be included in the following discussion.

1.1.1 Wall Flashback in Laminar Flows

The first detailed discussion of laminar wall flashback was given by Lewis and von Elbe [LE43]. Their experimental setup is representative for most of the

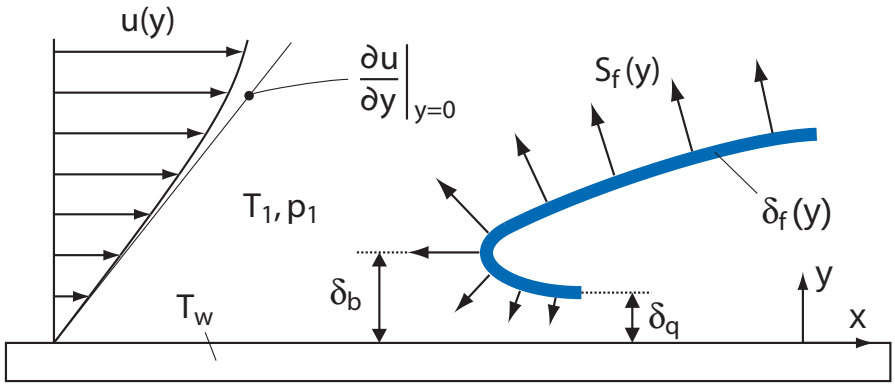

Figure 1.2: Critical velocity gradient model for the correlation of laminar wall flashback.

subsequent experimental studies. A tube burner with a free atmosphere outlet was used. The flame stabilized on top of the tube similar to a Bunsen burner arrangement. The tubes were made of Pyrex glass and had rather small diameters, ranging from 3 mm to 16 mm, a wall thickness of 1 mm and a length of 1 m to ensure fully developed laminar tube flow. In order to obtain reproducible flashback limits, it was important to control the temperature of the burner rim. While in [LE43] the tube was just left to cool down after each flashback, water cooling was applied to the rim in successive experiments [EM45]. For the initial studies [LE43], natural gas and air were mainly used as mixture components. Flashback was provoked by either reducing the flow rate, thus decreasing the flow velocities in the boundary layer, or by approaching more stoichiometric conditions. Lewis and von Elbe observed that the luminous combustion zone did not touch the wall during wall flashback. Moreover, the part of the flame next to the wall trailed behind the leading part of the flame. Based on these observations, they developed the idea of a *critical velocity gradient* at the wall, which has become a widely adopted model for the quantification of wall flashback and appears in many textbooks on combustion today. Figure 1.2 illustrates the critical velocity gradient model of Lewis and von Elbe. On the left hand side, the axial velocity profile $u(y)$ of a laminar boundary layer is sketched. The streamwise velocity gradient at the wall,

$$g = \left.\frac{\partial u}{\partial y}\right|_{y=0} = \frac{|\tau_w|}{\mu_1}, \tag{1.1}$$

is marked as a straight line tangential to the linear part of the velocity profile. In Eq. (1.1), τ_w is the wall shear stress of the two-dimensional boundary layer and μ_1 is the dynamic viscosity of the unburnt mixture at pressure p_1 and preheat temperature T_1. The wall is assumed isothermal at T_w. On the right hand side of the figure, a flame with thickness $\delta_f(y)$ is sketched which burns inside the premixed boundary layer flow. From the wall up to a distance δ_q, the reaction is completely quenched. This region has been called *dead space above the wall* [Woh53, Dug55]. Further above, the absolute value of the flame speed $S_f(y)$ develops towards its freestream value under the influence of quenching by the wall and stretch effects by the gradient flow. At the limit of wall flashback, the flame velocity at a certain balancing distance δ_b above the wall equals the flow velocity of the boundary layer velocity at the same height:

$$S_f(\delta_b) = g_c \delta_b \,, \tag{1.2}$$

where g_c is the critical velocity gradient at the flashback limit. According to Eq. (1.2), the g_c-concept is limited to linear regions of the boundary layer profile. The distance δ_b is also called the *penetration distance* in the literature [Woh53, Dug55]. For the evaluation of g_c in Eq. (1.2), Lewis and von Elbe assumed an *isothermal* flow profile, hence the hydrodynamic interaction between flame and flow is not taken into account by the model. From Eq. (1.2), the wall distance δ_b at the onset of flashback can be approximated by

$$\delta_b = \frac{S_L}{g_c} \tag{1.3}$$

if $S_f(\delta_b)$ is approximated by the laminar, adiabatic and one-dimensional flame speed S_L.

The velocity gradient g is sometimes interpreted as a stretch rate (see Sec. 2.3) which tends to decrease the flame velocity of angled parts of the flame due to convective heat losses to the unburnt gases. Then at the flashback limit, g_c is small enough to allow for sufficiently fast flame propagation at the height δ_b. However, this interpretation does not correspond to the model concept of Fig. 1.2 since the flame surface is perpendicular to the streamlines at wall distance δ_b, such that stretch losses only occur above and below that height.

After all, the critical gradient concept can be considered as an explanation of the validity of g as a sensible choice of correlation parameter. It is not pre-

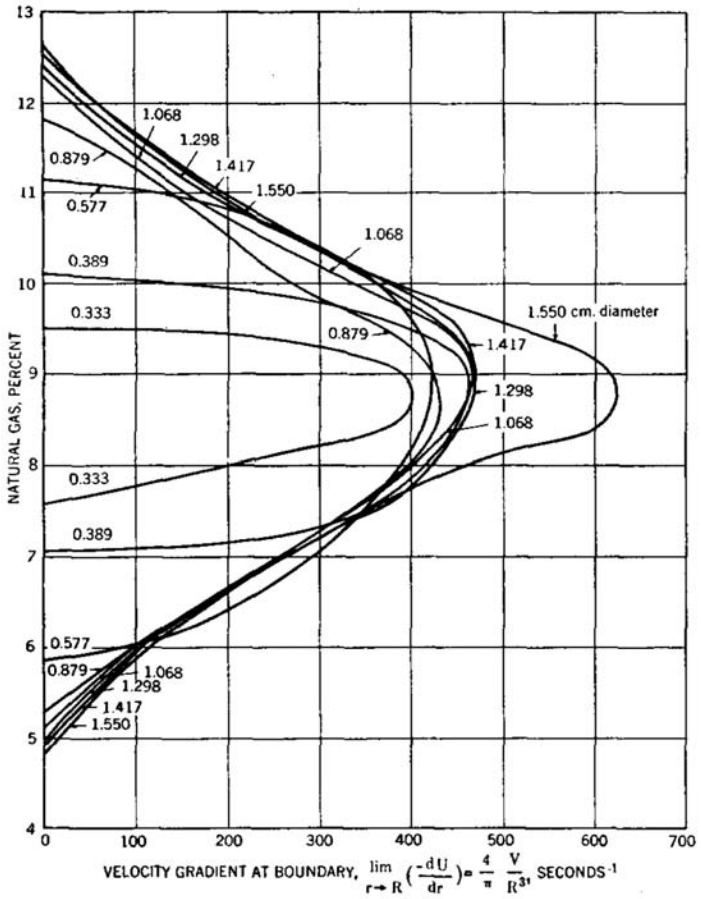

Figure 1.3: Critical velocity gradients for laminar natural gas-air flames in cylindrical, unconfined tubes at room temperature and pressure ([LE87], with permission).

dictive for g_c, though, since the flame speed $S_f(y)$ close to the wall, which is influenced by quenching and stretch effects, cannot be evaluated without considerable effort. Figure 1.3 shows wall flashback limits obtained by Lewis and von Elbe [LE43, LE87] for natural gas-air mixtures at atmospheric conditions in Pyrex tubes without active cooling. For their laminar experiments, the gradient at the wall was calculated from the Poiseuille paraboloid according to

$$\left.\frac{\partial u}{\partial r}\right|_{r=R} = \frac{4\overline{u}}{R}\,. \tag{1.4}$$

In Eq. (1.4), r is the radial coordinate, R is the radius of the tube and $\overline{u}$ designates the bulk flow velocity. The authors state that for an increase in wall temperature of up to 100 °C, the results were little affected. Between stable

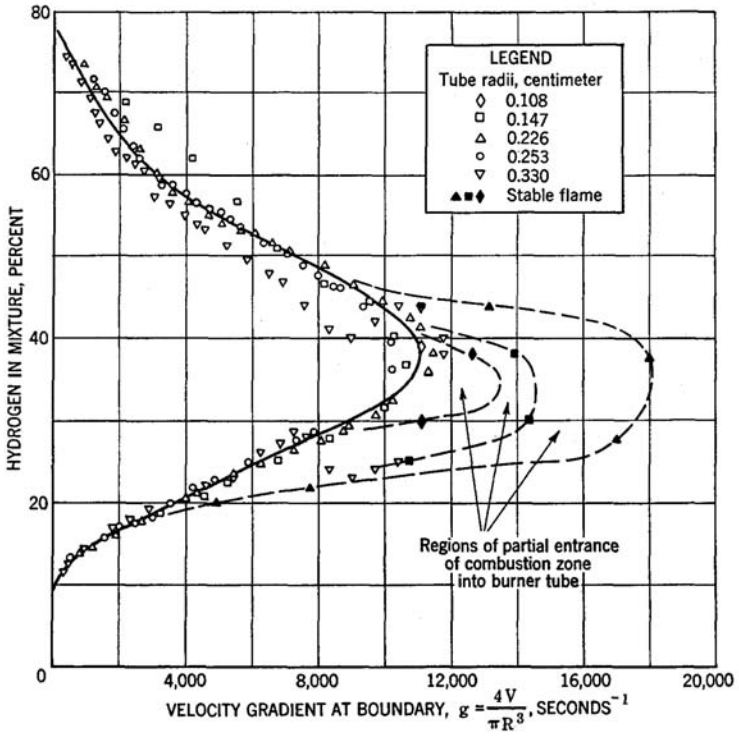

Figure 1.4: Critical velocity gradients for laminar H_2-air flames in cylindrical, water-cooled, unconfined tubes at room temperature and pressure ([LE87], with permission).

flames and full flashback, heating of the burner rim by an irregular flame motion sometimes caused the flame to penetrate partly into the tube, while the expanding gases compressed the unburnt gases. The resulting distortion of the flow profile can lead to reduced values of g in front of the flame tip which promotes flashback. This phenomenon was termed a *tilted flame* in a follow-up investigation [EM45]. The curves for different tube diameters and varying mixture composition in Fig. 1.3 coincide well except for very small tube diameters, which was explained by the fact that the flow profile is not linear at δ_b anymore for small diameters. The offset of the largest diameter (1.550 cm) around stoichiometry was caused by the occurrence of tilted flames which developed into flashback.

In a later study of the same research group, von Elbe and Mentser [EM45] used a water-cooled burner and investigated H_2-air mixtures, amongst others. Figure 1.4 shows critical velocity gradients obtained for H_2-air mixtures at atmospheric conditions. The solid curve designates the limit for flashback

along the full length of the tube, while the dashed curves border the regions where flashback was preceded by tilted flames. By comparing Figs. 1.3 and 1.4, it becomes clear that critical velocity gradients strongly increase when hydrogen is used instead of natural gas. Further elaborating on the tilted flame phenomenon, the authors stated [EM45, LE87] that tilted flames can be stable for configurations with cooled walls, small diameters and mixtures with low burning velocity. However, for the H_2-air mixtures shown in Fig. 1.4, a tilted flame was always followed by flashback except for very lean or very rich mixtures. The authors explained these observations by comparing the pressure loss along the tube due to wall friction with the pressure difference across a one-dimensional flame.

The fundamental studies of Lewis, von Elbe and Mentser were extended by several researchers. Wohl [Woh53] derived expressions for quenching distances, based upon which he deduced the pressure dependence of g_c for laminar flow to be between square-root and directly proportional for atmospheric or higher pressures.

Dugger [Dug55] conducted experiments using preheated propane-air mixtures and heated tube walls at the same temperature as the fresh gases. He argued that critical velocity gradients are expected to raise with increasing temperature for two reasons:

- The laminar burning velocity increases.
- For a given increase in the preheat temperature, the flame temperature changes by a smaller degree. Thus, the heat loss to the wall effectively decreases, which causes decreasing penetration distances δ_b with increasing temperature of the unburnt mixture and the wall.

Dugger compared experimental penetration distances δ_b for laminar flashback, as approximated by Eq. (1.3), with half the value for experimental quenching distances in tubes. The resulting ratio is

$$\frac{2\,\delta_b}{d_q} < 0.5\,. \tag{1.5}$$

Other studies revealed similar ratios between 0.4 to 0.8 for a wide range of fuels [BP57], which were shown to depend on the actual value of g_c. The question arises why the approximated penetration distances δ_b are only less than half of the according distance at full quenching. Dugger considered the back pressure of the flame to be a possible explanation, which is likely to decrease the local velocity gradient in front of the flame during flashback such that the true value for δ_b is increased.

Fine [Fin59] presented a similar study in which he experimentally evaluated the temperature dependence of the critical velocity gradient for H_2-air mixtures at sub-atmospheric pressures to

$$g_{c,\mathrm{H_2-air}} \sim T^{1.5} \,. \tag{1.6}$$

Equation (1.6) was nearly independent of pressure within the measured range. Furthermore, the proportionality is the same for laminar and turbulent tube flows. The presentation of results in [Fin59] suggests that Eq. (1.6) is based on results at a single equivalence ratio of $\Phi = 1.5$. However, since studies of the same author on pressure dependencies [Fin58] explicitly considered several equivalence ratios while presenting results in the same way, this interpretation may not be correct.

Another study [KMSS65] on the dependence of laminar wall flashback on preheat temperature at atmospheric pressure interpreted the data in terms of the dependence of g_c on S_L for methane-oxygen mixtures. Their result,

$$g_c \sim S_L^2 \qquad \text{for varying composition at T=const.} \tag{1.7a}$$

$$g_c \sim S_L \qquad \text{for varying temperature at } \Phi\text{=const.} \tag{1.7b}$$

was explained by reasoning that the thermal diffusivity of the methane-oxygen mixture stays essentially constant for changes in stoichiometry at constant preheat temperature, but increases simultaneously with S_L if the preheat temperature raises.

A study on the dependence of wall flashback on the wall temperature of the burner rim for constant preheat temperatures and H_2-O_2 mixtures was carried out by Bollinger and Edse [BE56]. Most of their results are specific for their tube burner arrangement and shall not repeated here. On the whole,

they showed that flashback propensity increases at higher wall temperatures, which have to be controlled properly in order to obtain reproducible critical velocity gradients. The influence of preheated walls is also covered in [SY05], who confirm the trend of rising g_c with increasing T_w.

Fine [Fin58] conducted experiments on the pressure dependence of critical velocity gradients for various fuel types. He considered sub-atmospheric to atmospheric pressures at room temperature. The experimental setup comprised a water-cooled burner tube. Flow velocities and diameters were chosen to provide laminar as well as turbulent flow conditions. The measurements revealed a pressure dependence of the critical velocity gradient of about

$$g_{c,\mathrm{H_2-air}} \sim p^{1.35} \tag{1.8}$$

for laminar H_2-air mixtures between $\Phi = 0.95$ to 2.25 within the measured pressure range. However, the equation becomes inaccurate for equivalence ratios Φ considerable less than unity (no specific value is given by the author). Moreover, Eq. (1.8) was shown to be approximately valid for both, laminar and turbulent flow conditions. The results for g_c were independent of the tube diameter except for $\Phi > 2$.

Up to this point, all studies presented were limited to fully developed, laminar tube flow. However, mixture supply ducts in practical geometries usually do not have a sufficiently large length/diameter ratio L/d in order to allow a fully developed internal flow assumption. In order to investigate the influence of L/d on flashback, France [Fra77] looked at water-cooled tube and mono-port burners with ratios $L/d = 0.1$ to 100 and various fuel-air mixtures. He observed that the flow velocities at wall flashback decreased if the flow was not fully developed. This observation can be explained by the fact that wall friction is maximum at the inlet section and subsequently drops towards the fully developed value in downstream direction.

Fuel flexibility and variability have become important issues for gas turbine operators [PMSJ07, LMSS08]. Therefore, studies which determine the flashback characteristics of typical alternative fuels are of increasing interest. Fox and Bhargava [FB84] measured adiabatic flame speeds and critical velocity gradients for gas-air mixtures representing biomass gasification products on

water-cooled tube burners with a diameter of 7 mm. The resulting values for g_c lay roughly in the same range as those for natural gas. Davu et al. [DFC05] generated maps of g_c for various hydrocarbon and hydrogen fuel blends (Syngas) using uncooled tube burners with three different diameters (6 mm, 7 mm and 10.6 mm). They conclude that S_L as well as the Lewis number Le of the different mixtures determine g_c. The influence of external acoustic excitation on flashback was also investigated, but this topic is beyond the scope of this work. Another recent publication [Mis07] reported atmospheric flashback measurements for Compressed Natural Gas (CNG)-air flames, using an uncooled tube burner arrangement with diameters of 12 mm and 15 mm.

Experiments on laminar wall flashback using optical measurement techniques are rare in literature. Sogo and Yuasa [SY05] used Particle Image Velocimetry (PIV) to study the velocity field of a stationary flame just before flashback at the exit of a burner with rectangular cross section for lean CH_4-air mixtures at atmospheric conditions. They tried to estimate the influence of the heat flux from the flame to the burner rim, the dilution with ambient air and flame stretch at the flame base at conditions close to flashback. The authors calculated a stretch rate based on the observed flame curvature and the velocity distribution just above the burner rim in two dimensions. The resulting maximum increase of the burning velocity of lean CH_4-air mixtures due to flame stretch effects was quite low, only within a few percentage points from the undisturbed value for S_L. However, it was argued that the influence probably increases if mixtures with Lewis numbers considerably different than one are used.

Although chances to observe laminar flow in gas turbine combustors are actually very low, the examination of laminar wall flashback experiments above has provided an insight in the basic mechanisms, influential factors and experimental procedures, which provides the basics for a review of wall flashback in turbulent flow to be presented now.

1.1.2 Wall Flashback in Turbulent Flows

An early experiment on wall flashback in turbulent flows was conducted by Bollinger [Bol52]. He investigated H_2-oxygen mixtures in tube burners of different materials and cooling configurations at atmospheric pressures and temperatures as well as at elevated pressures of 14.6 bar. Bollinger transferred the concept of a critical velocity gradient for laminar wall flashback to the turbulent case. In that case, the wall shear stress has to be calculated from a suitable expression for turbulent flow instead of Eq. (1.4). For tube flow, the resistance concept of Blasius leads to the following equation [Sch82]:

$$\tau_w = 0.03955\,\rho\,\overline{u}^{7/4}\,\nu^{1/4}\,d^{-1/4}\,, \tag{1.9}$$

where ρ is the density and ν is the kinematic viscosity of the flow. In combination with Eq. (1.1), the critical velocity gradient for fully developed turbulent tube flow can be calculated. It is evident from Eq. (1.9) that the tube diameter d only plays a minor role, while $\overline{u}$ has a high influence on the value of g. Thus on the one hand, the exact determination of the flow rate is a critical issue for turbulent wall flashback experiments. On the other hand, higher flow velocities also cause substantially higher velocity gradients as opposed to the laminar situation described by Eq. (1.4), where $g \sim \overline{u}$. Bollinger showed that critical gradients for turbulent flames are larger than for laminar flames and that higher pressures strongly increase flashback propensity. Furthermore, the tip temperature of the burner was again found to have a large effect on flashback tendency. However, the author did not derive a scaling law for the pressure influence on flashback limits.

Wohl [Woh53] cited two publications which report flashback measurements in tube burners which used H_2-iso-octane-air and propane-air mixtures as fuels. Inner diameters lay between 0.46 cm to 2.0 cm and Reynolds numbers were between $\mathrm{Re}_d = 2790$ to 5550. In both studies, wall flashback took place at significantly higher flow velocities than for laminar conditions. Ratios of $g_{c,t}/g_{c,l} \approx 3$ at $\Phi \approx 1.1$ were reported for atmospheric propane-air mixtures. Wohl interpreted the higher velocity gradients to be an indication that turbulent wall flashback takes place outside the laminar region of the velocity profile, where turbulence increases the flame speed. As will be shown below,

however, most successive researchers adopted the interpretation that flashback takes place in the laminar sublayer, where S_L is a measure for the flame velocity, at the compromise of doubtfully small penetration distances δ_b (see Eq. (1.3)).

Bollinger and Edse [BE56] investigated the influence of several experimental factors on turbulent wall flashback in partly cooled tube burners using H_2-O_2 mixtures. Burner diameters were between 0.2 cm to 1.4 cm. Critical velocity gradients for atmospheric conditions lay roughly between 20000 1/s to 70000 1/s. The authors approximated the depth of penetration δ_b by using Eq. (1.3). A comparison with the approximate laminar sublayer thickness showed that δ_b is much smaller than this thickness. This fact has been further explained in a follow-up paper of Bollinger [Bol58].

Some of the results of Fine [Fin58, Fin59] regarding temperature and pressure influence on turbulent flashback limits have already been discussed in the laminar section. His turbulent data for H_2-air mixtures ranged up to Reynolds numbers of about 5500. Fine suggested that turbulent flames are stabilized in the laminar sublayer during wall flashback, using the same calculation procedure as in [BE56]. The ratio $g_{c,t}/g_{c,l} \approx 3$ was shown to hold for H_2-air mixtures at atmospheric conditions and $\Phi \approx 1.5$.

Grumer [Gru58] used tube burners of considerably larger diameters than his predecessors, 5.08 cm and 7.62 cm, in combination with natural gas-air mixtures. From the observation of the turbulent flame shape above the tube, which was short and wide-angled, he deduced that flashback could also take place outside of the laminar sublayer. However, Grumer did not include a detailed analysis of this hypothesis.

Khitrin et al. [KMSS65] provided a comprehensive data base for turbulent wall flashback of H_2-air flames. Their tube burners with temperature-controlled rims had diameters between 18 mm to 38 mm. Wall flashback was observed at Reynolds numbers up to $Re_d = 20000$. Since only flow velocities at flashback were given in the paper, the critical velocity gradients have been derived from their data for the present work using Eq. (1.9). Dynamic viscosities of the pure components were taken at 300 K and 1 bar. The dynamic viscosi-

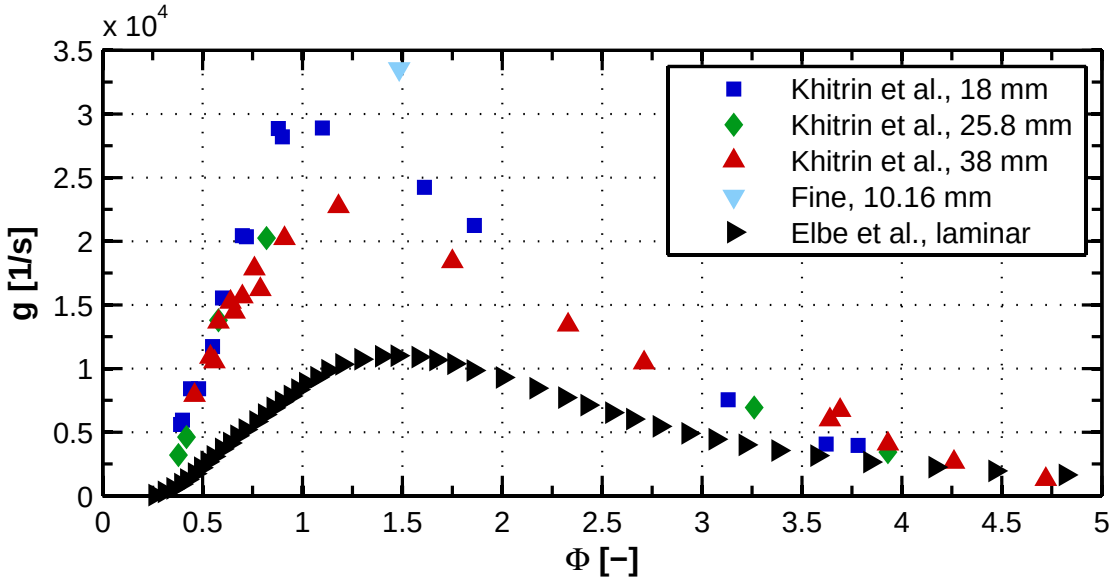

Figure 1.5: Critical velocity gradients at wall flashback for laminar and turbulent hydrogen-air flames in unconfined tube burners at atmospheric conditions [KMSS65, Fin58, EM45].

ties of the H_2-air mixture were calculated according to the method of Wilke [Whi05]. The results are illustrated in Fig. 1.5 together with a comparable data point of Fine [Fin58] and laminar H_2-air flashback limits [EM45]. Again, a ratio of $g_{c,t}/g_{c,l} \approx 3$ can be determined from the graphs at maximum flashback propensity around $\Phi = 1.5$. However, this ratio varies at other equivalence ratios, especially towards rich mixtures. While the turbulent data shows good consistency at lean and rich conditions, relatively large scatter exists around stoichiometric conditions. The authors made no statement on the observation of tilted flames for turbulent experiments.

A more recent investigation partly concerned with wall flashback was published by Schäfer et al. [SKW01]. The propagation of turbulent, premixed kerosene-air flames was investigated at atmospheric conditions in a test rig providing optical access. Flashback was observed in the premixing duct of a combustion chamber which comprised a center body for flame stabilization. The annular premixing duct had a diameter of 4.1 cm and a length of 55 cm. The axial velocity distribution at the entrance to the combustor was measured by Laser Doppler Anemometry (LDA). The authors reported critical Reynolds

numbers between 3000 to 6500. Their data for critical velocity gradients suggests that again, the penetration distance according to Eq. (1.3) is smaller than the respective thickness of the laminar sublayer.

On the whole, there are considerably less publications on turbulent wall flashback than for the laminar case. The next subsection gives an overview on numerical investigations of wall flashback.

1.1.3 Numerical Work

Lee and T'ien [LT82] were probably the first to present numerical simulations of laminar wall flashback. They considered premixed methane-air flames at $\Phi = 1$ confined in a circular duct. Their simulation was two-dimensional using cylindrical coordinates, assuming constant heat capacity of the mixture, ideal gas behavior and a Lewis number of unity. The transport coefficients of the mixture were functions of temperature. The chemical reaction was assumed to be a single-step global reaction with an Arrhenius-type rule for the production rate. The velocity profile at the inlet was prescribed as parabolic and the wall temperature was constant at the inlet temperature of the mixture. The simulation assumed steady final conditions since the solver used a false transient method. Thus, the simulation converged to the flow condition at which the flame was barely stable just before flashback. The simulation predicted the deviation of critical velocity gradients of tubes with small diameters from flashback limits of larger tubes for which critical gradients become approximately independent of the diameter (see Fig. 1.3). The flame had a two-dimensional structure and its curvature was in the order of the flame thickness, which marks the general importance of non-equidiffusion effects on such flames. At the bottom of the flame close to the wall, unburnt mixture diffused into the reaction zone. The expansion of gases behind the flame caused a high-pressure field in front of the flame such that streamlines were divergent. Tests with another prescribed inlet velocity profile showed that the shape of the stabilized flame differs clearly from the parabolic case, and it was concluded that not only the velocity gradient at the wall, but also the curvature of the velocity profile is an important factor for wall flashback. The authors

generally questioned the critical gradient concept due to obvious influence of the flame backpressure on the velocity field.

Mallens and de Goey [MDG98] combined experimental and numerical efforts for the determination of critical velocity gradients for laminar CH_4-air mixtures. Water-cooled rectangular burners and uncooled tube burners were used in the experiments. They checked the assumption of a fully developed velocity profile at burner exit by LDA. Their numerical simulations comprised a two-dimensional domain with a parabolic velocity profile at the inlet and isothermal walls at the temperature of the entering mixture. The domain included the outlet of the burner, a part of the burner rim and extended a certain distance into the environment. A one-step Arrhenius-type reaction was used as chemical model. The calculation procedure differed from [LT82] in that the critical velocity of the mixture at wall flashback was taken at the point when the steady-state solver did not converge any more. The comparison between experiment and numerics revealed deviations of about 10 %. The authors concluded from this reasonable accuracy that the quenching phenomenon is governed by heat loss to the wall and not by radical recombination or surface chemistry, both of which were not modeled in the simulations.

Kurdyumov et al. [KFTT$^+$07] compared experimental and numerical investigations, too. For their experiments, they used propane and methane as fuels in an uncooled tube burner setup. The simulated domain was similar to the one described in [LT82]. The specific heat of the mixture was taken as constant, while the viscosity, thermal conductivity and mass diffusivity changed with temperature. Thermal expansion is included as opposed to an earlier publication of the same group [KFL00]. The Prandtl number was taken constant as 0.72 and the Lewis number was also assumed to be constant, but not necessarily unity. The chemistry was assumed as irreversible one-step using an Arrhenius law. The boundary condition at the wall could be switched smoothly between adiabatic and isothermal by a heat loss parameter. The main non-dimensional parameter describing wall flashback was given by the authors in the form of a critical Damköhler number,

$$\mathrm{Da}_c = \frac{S_L^2}{D\, g_c}\,, \tag{1.10}$$

where D is the fuel diffusivity at a reference temperature. It turned out that the critical velocity at wall flashback was extremely sensitive to Da_c. Therefore, a precise calculation of Da_c in an unsteady simulation was very hard to achieve. The steady simulations revealed that the most influential factors on Da_c were the Lewis number and the heat loss to the wall. The numerical model gave the right order of magnitude for Da_c when compared to the experiments.

Turbulent wall flashback has not been studied numerically in the open literature until the start of the work presented here. However, a recent Direct Numerical Simulation (DNS) of Andrea Gruber [Gru10] shall be mentioned here, who is the first to simulate this very complex flame phenomenon with detailed H_2-O_2 chemistry.

1.1.4 Nondimensional Form of the Critical Gradient Model

It has been shown that the velocity gradient g at the wall represents the influence of the bulk flow velocity $\overline{u}$ and a characteristic length of internal flow for a given mixture (Eqs. (1.4) and (1.9)). However, according to Eq. (1.2) and the experimental results for laminar and turbulent flows, correlations of wall flashback by critical velocity gradients depend *at least* on the following parameters:

$$g_c = f(T_1, p_1, T_w, \Phi, \text{fuel, oxidizer, turbulence}) \,. \tag{1.11}$$

It was already shown that the burner diameter has an influence on critical gradients within a certain range (see Fig. 1.3). Furthermore, a strong influence of the flame holder geometry prior to flashback will be demonstrated in a later chapter, such that the variables in Eq. (1.11) only constitute a minimum parameter set for similar geometrical conditions.

In order to reduce the number of parameters in Eq. (1.11), a dimensionless form of Eq. (1.2) was introduced by Putnam and Jensen [PJ49]. They made the fundamental assumption that the penetration distance is a *fixed* multiple of the laminar flame thickness:

$$\delta_b = K \frac{a}{S_L} \,, \tag{1.12}$$

where K is a constant and a is the thermal diffusivity of the mixture. Using this definition, the following set of equations was derived specifically for laminar, fully developed tube flow:

$$\mathrm{Pe}_{\mathrm{flow}} = \frac{1}{8K}\,\mathrm{Pe}_{\mathrm{f}}{}^{2}\,, \tag{1.13a}$$

$$\mathrm{Pe}_{\mathrm{flow}} = \frac{\overline{u}\,d}{a} \qquad \mathrm{Pe}_{\mathrm{f}} = \frac{S_L\,d}{a} \qquad K = \text{const.}\,. \tag{1.13b}$$

where $\mathrm{Pe}_{\mathrm{flow}}$ and Pe_{f} are Peclet numbers of the tube flow and the flame, respectively. Equation (1.13a) compares the ratio of advection of fluid to thermal diffusion with the ratio of advection of the flame surface to thermal diffusion. For both diffusive terms, the burner diameter appears as a characteristic length in Eqs. (1.13b), which is a somewhat questionable assumption in the limit of diameter independence and for the microscopic scales involved in the critical gradient concept.

As will be shown now, Eqs. (1.13) can be reduced to a universal criterion independent of burner geometry and flow regime. The derivation results in a critical Damköhler number Da_{c} similar to Eq. (1.10), which compares the timescale of the linear velocity profile with the flame transit time and a quenching Peclet number Pe_{q}, which is a measure of the ratio between penetration distance δ_b and flame thickness. From the definitions

$$\mathrm{Da}_{\mathrm{c}} = \frac{S_L^2}{a\,g_c}\,, \tag{1.14}$$

$$\mathrm{Pe}_{\mathrm{q}} = \frac{S_L\,\delta_b}{a}\,, \tag{1.15}$$

By simply multiplying with S_L/a on both sides, Eq. (1.3) can be expressed as

$$\mathrm{Da}_{\mathrm{c}} = \mathrm{Pe}_{\mathrm{q}}\,. \tag{1.16}$$

By using Eq. (1.4) to replace g_c in Eq. (1.16) and rearranging, Eq. (1.16) can be converted to Eq. (1.13a) and the constant K is shown to be identical to Pe_{q}. The interpretation of Eq. (1.16), i.e. why the critical Damköhler number should be equal to the quenching Peclet number at the flashback limit, is not obvious. Therefore this equation should be regarded as a formal reduction of the

original Peclet number criterion of Eq. (1.13a) without adding further physical insight. The aim of correlating data by Eq. (1.16) should be a universal curve which is independent of Φ, pressure, temperature and fuel of the unburnt mixture. This has been partly confirmed by various plots of experimental data [PJ49, KMSS65] for laminar flashback data using Eq. (1.13a) and K as a free parameter to fit the data set.

For turbulent tube flow, a conversion of Eq. (1.16) towards dependence on $\overline{u}$ instead of g can be made by using Eq. (1.9) and (1.1), which leads to an expression of the form

$$\mathrm{Pe}_{flow}\,\mathrm{Re}_d^{3/4} = \frac{1}{0.03955\,\mathrm{Pe}_q}\mathrm{Pe}_f^2\,. \tag{1.17}$$

Again, Eq. (1.17) is only an algebraic conversion of the Damköhler-Peclet model in Eq. (1.16) to the variables $\mathrm{Pe}_{\mathrm{flow}}$ and Pe_{f} which were used by Putnam and Jensen. Compared to their original correlation for laminar conditions (Eq. (1.13a)), the Reynolds number with respect to the tube diameter, Re_d, appears as a further nondimensional variable at turbulent conditions.

1.2 Scope of the Project

The literature review has revealed several interesting facts. First, wall flashback has almost been neglected in combustion research since the 1970's. This can probably be explained by the fact that this type of flashback is not relevant for most turbulent burners running on hydrocarbon fuels, such that research and development was focused on other types of flashback once that the basics were believed to be understood. Furthermore, the process is rather difficult to assess experimentally or numerically due to the presence of the wall and the small scales involved. Second, the critical gradient concept of Lewis and von Elbe was the first and still is the only model for laminar wall flashback which has been proposed in the literature. It has become the accepted standard and has been used for numerical and experimental studies until today. Third, the critical gradient concept has been adopted for turbulent flows in spite of the fact that arguably small penetration distances are the consequence. Fourth, the experimental data basis is limited to burners which held the flame in free

atmosphere or in a chamber with considerable jump in cross section prior to flashback. These configurations can be characterized as *unconfined* flame holding. In contrast, if the flame is stabilized already inside the duct prior to flashback, such as in the laminar flashback simulations of [LT82, KFTT+07], a *confined* flame holding takes place.

Conclusively, several questions remain unresolved from the available literature, which can be categorized by the degree of complexity needed to answer them. For the first set of open issues, a simple determination of flashback limits is sufficient:

- **Is there a difference between unconfined and confined flame holding regarding wall flashback limits?** This question has not been addressed by an experiment so far.
- **Is the shape of the duct cross-section an influential parameter?** Only tube burners have been used to obtain turbulent wall flashback limits up to now.
- **What is the influence of adverse global pressure gradients on wall flashback limits for a given velocity gradient?** This issue is important for the layout of diverging fuel ducts and has not been treated so far.

For the second set of open questions, detailed observation of the flame during wall flashback is necessary:

- **What is the true wall distance of flame propagation during turbulent wall flashback?** All results in the literature are based on indirect estimations.
- **How does the propagation path of a flame in a turbulent boundary layer look like in detail?** This question is important for modeling turbulent wall flashback.
- **How strong is the coupling between boundary layer flow and flame backpressure?** Again this question is important for model development.

The aim of the work presented here is to address these open issues by a suitable generic experiment, using state-of-the-art measurement techniques with high spatial and temporal resolution. At the end, the critical gradient concept will be critically compared with the findings and a new model for wall flashback will be proposed.

2 Premixed Flame Propagation in Proximity to Walls

The process of wall flashback in fully premixed fuel-oxidizer mixtures combines premixed flame propagation influenced by spatial (laminar and turbulent) and temporal (turbulent) velocity gradients and heat losses with the dynamics of boundary layer flow. The first two sections in this chapter introduce basic principles separately for each subject area which are important for the understanding of the observed phenomena during wall flashback. The third and fourth section discuss specific aspects of reacting boundary layer flow.

2.1 Laminar and Turbulent Boundary Layers

The *boundary layer* concept was introduced by Prandtl [Pra04] to conceptually separate the thin layer close to the wall, which is affected by viscous retardation due to the no-slip condition at the wall, from the surrounding fluid, called the *freestream*, which can effectively be described by inviscid flow equations for high Reynolds numbers. Historically, this separation was favorable since it enabled efficient calculation of many flow situations by treating the viscous layer with a simplified set of partial differential equations, called the *boundary layer equations*, and the outer flow by inviscid Euler or potential flow equations. A comprehensive treatment of laminar and turbulent boundary layer theory has been provided by Schlichting [Sch82], while White [Whi05] gives a very useful overview on the subject. Both texts form the basis of the following review, for which only non-swirling main flow with constant time-averaged massflow will be considered.

It is important at the beginning to clarify the concept of boundary layers for internal flows. The definition of a boundary layer only makes sense if a well-

defined freestream exists which is not appreciably affected by viscous forces. For internal flows, this situation is typically found at the entrance of a device, where boundary layers are thin with respect to the duct cross-section. As the boundary layer thickness grows in downstream direction, the core flow is accelerated, which in turn causes a slower growth of the boundary layer as compared to a flat plate geometry. At some point, however, the 'boundary layer' fills the whole duct, and a *developed* duct velocity profile is formed. The definition of a boundary layer is not sensible anymore in this situation. However, the term *boundary layer* will also be used in the following for the near-wall region of turbulent flow in closed geometries, since a strong similarity exists between external and internal wall-bounded flow close to the wall for turbulent conditions.

2.1.1 Boundary Layer Approximations

The derivation of boundary layer equations for the momentum equation will be conducted in the following to illustrate the inherent assumptions (similar approximations can be introduced in the energy equation, which will not be shown here for brevity). The basis is formed by applying momentum conservation according to Newton's second law to a compressible, isotropic, Newtonian fluid element and using Stoke's equations for the shear stress tensor and volume viscosity, which results in the Navier-Stokes equations. Neglecting body forces and using tensor notation, the resulting expression is

$$\frac{\partial}{\partial t}(\rho u_i) + \frac{\partial}{\partial x_j}(\rho u_i u_j) = -\nabla p + \frac{\partial}{\partial x_j}\left[\mu\left(\frac{\partial u_i}{\partial x_j} + \frac{\partial u_j}{\partial x_i} - \frac{2}{3}\delta_{ij}\frac{\partial u_k}{\partial x_k}\right)\right] . \tag{2.1}$$

The essential assumption for boundary layer approximations is that the boundary layer thickness δ is thin with respect to a characteristic length scale L of the geometry, which is true if the Reynolds number Re_L with respect to the freestream velocity u_∞ and L is very large.

The derivation of the boundary layer equations is achieved by nondimensionalizing Eq. (2.1) by L, u_∞ and a reference pressure p_0. Subsequently, all terms in the resulting equations which are multiplied by $1/\mathrm{Re}_L$ or $1/\mathrm{Re}_L^2$ are ne-

glected. For steady, two-dimensional flow with variable density and dynamic viscosity, the boundary layer equation for momentum is

$$\rho u \frac{\partial u}{\partial x} + \rho v \frac{\partial u}{\partial y} = -\frac{dp}{dx} + \frac{\partial}{\partial y}\left(\mu \frac{\partial u}{\partial y}\right). \tag{2.2}$$

Neglecting small-order terms has led to a significant simplification of the equation structure and further allows physical insight into boundary layer flows:

- Boundary layer equations are of parabolic type instead of elliptic, which simplifies solution by numerical treatment.
- For $\delta \ll L$ and $\mathrm{Re_L} \gg 1$:

$$v \ll u\,, \qquad \frac{\partial u}{\partial x} \ll \frac{\partial u}{\partial y}\,, \qquad \frac{\partial v}{\partial x} \ll \frac{\partial v}{\partial y}\,. \tag{2.3}$$

- Transverse pressure gradients are negligible:

$$\frac{\partial p}{\partial y} \approx 0\,, \qquad p = p(x)\,. \tag{2.4}$$

  The pressure $p(x)$ is impressed on the boundary layer by the freestream.

- Axial pressure gradients $\partial p/\partial x$ may exist as long as the boundary layer is sufficiently far away from the separation point.

Equation (2.2) can be directly used to solve laminar boundary layer problems. For large $\mathrm{Re_L}$, however, the solution becomes unstable due to transition to turbulent conditions. Nevertheless, turbulent boundary layer equations can be derived from Reynolds-Averaged Navier-Stokes (RANS) equations from the same assumptions as used for Eq. (2.2), which then include additional turbulent shear terms.

2.1.2 Time-mean Structure of Laminar Boundary Layers

Equation (2.2) was transformed to an ordinary differential equation by Blasius [Bla08] by the introduction of a similarity variable and the definition of a

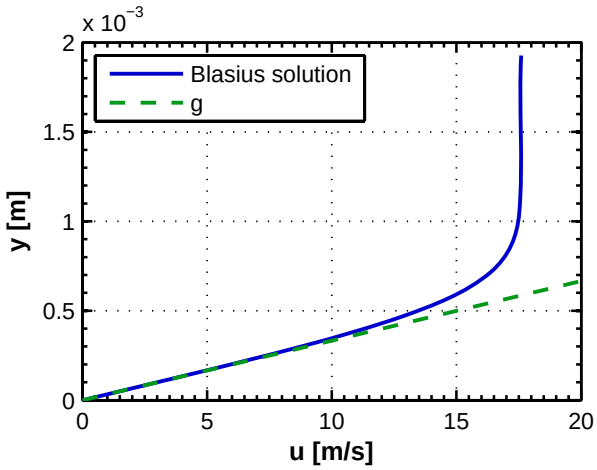

Figure 2.1: Blasius solution of a flat plate boundary layer at $\mathrm{Re_x} = 50000$ and $g = 30000$.

stream function for an incompressible laminar boundary layer with constant properties on a flat plate. The freestream velocity u_∞ is assumed to be constant for this transformation. The resulting equation,

$$f''' + f f'' = 0, \qquad f'(0) = f(0) = 0, \qquad f'(\infty) = 1\,, \tag{2.5}$$

where $f' = u/u_\infty$, has not been solved exactly by analytical methods so far. A numerical solution of Eq. (2.5) using a Runge-Kutta scheme is tabulated in [Whi05]. A realization of the self-similar velocity profile for $\mathrm{Re_x} = 50000$ and $g = 30000$ is shown in Fig. 2.1. The velocity gradient at the wall is plotted as a straight line in the diagram. It can be determined that the laminar profile has a pronounced linear section, starting from the wall and going up to about $y/\delta = 0.3$.

Similarity solutions for compressible laminar boundary layers, such as the Illingworth-Stewartson transformation, do exist, but incorporate significantly more assumptions on physical variables than the incompressible Blasius equation (2.5), for which only $u_\infty = \text{const.}$ has been assumed in addition to the boundary layer approximations. For more details and a summary of literature resources on compressible boundary layers, the reader is referred to [Whi05].

2.1.3 Time-mean Structure of Turbulent Boundary Layers

Analytical solutions do not exist for turbulent boundary layers, such that similarity considerations are based on dimensional analysis and experimental as well as DNS results. In order to investigate similarity of these profiles, the turbulent boundary layer is divided into three distinct regions:

1. **Inner region**. Viscous (molecular) shear is dominating.
   - *Laminar (viscous) sublayer* ($y^+ \leq 5$, $u^+ = y^+$). Much smaller than linear region in laminar boundary layers with respect to δ (see Fig 2.1).
   - *Buffer layer* ($5 < y^+ \lesssim 30$), merge between linear and logarithmic profile.
2. **Overlap layer**. Viscous and turbulent shear are important. Extent in y^+ is Reynolds-number dependent. Also called *logarithmic region* due to Eq. (2.12).
3. **Outer region**. Turbulent (eddy) shear is dominating, profile depends on pressure gradient.

For the inner and outer regions, nondimensional variables and their functional dependence can be deduced from dimensional analysis. The shape of the overlap layer follows from the postulation of a smooth connection between inner and outer layer. The nondimensional function for wall-parallel velocity u and wall distance y in the inner region are

$$u^+ = \frac{\langle u \rangle}{u_\tau} = f(y^+)\,, \qquad y^+ = \frac{y}{\nu} u_\tau \qquad \text{with} \quad u_\tau = \sqrt{\frac{\tau_w}{\rho}}\,, \tag{2.6}$$

In Eqs. (2.6), the operator $\langle ... \rangle$ represents the time average. The variable u_τ is called *friction velocity* or *shear stress velocity*. It can be concluded from Eq. (2.6) that the inner region of a turbulent boundary layer scales only with three variables: ρ, μ and τ_w. From Eqs. (2.6), characteristic length and time scales for the inner region of a turbulent boundary layer can be defined as

$$L_+ = \frac{\nu}{u_\tau}\,, \qquad t_+ = \frac{\nu}{u_\tau^2} = \frac{1}{g}\,. \tag{2.7}$$

For Eq. (2.7), the wall shear stress has been related to the velocity gradient. For laminar two-dimensional flow,

$$\tau = \mu\left(\frac{\partial u}{\partial y} + \frac{\partial v}{\partial x}\right). \tag{2.8}$$

However, the boundary layer approximations show that $\partial u/\partial y$ is two orders of magnitude larger than $\partial v/\partial x$, such that the wall shear stress can be well approximated by

$$\tau_w \approx \mu \left.\frac{\partial u}{\partial y}\right|_{y=0} = \mu g \tag{2.9}$$

in a laminar boundary layer. For turbulent boundary layers, the introduction of boundary layer approximations in the RANS equations results in the following expression for shear stress inside the boundary layer:

$$\tau = \mu\frac{\partial\langle u\rangle}{\partial y} - \rho\langle u' v'\rangle . \tag{2.10}$$

In Eq. (2.10), u' and v' are fluctuating velocities according to the concept of Reynolds decomposition. The shear influence of turbulent fluctuations, however, tends to zero in the laminar sublayer, such that Eq. 2.9 also holds for turbulent boundary layer flow.

The nondimensional variables for wall-parallel velocity $\langle u\rangle$ and wall distance y in the outer region are

$$\frac{u_\infty - \langle u\rangle}{u_\tau} = f\left(\frac{y}{\delta}, \xi\right), \qquad \xi = \frac{\delta}{\tau_w}\frac{\partial p}{\partial x}. \tag{2.11}$$

Equation (2.11) is called the *velocity defect law*, as the difference between the freestream velocity u_∞ and the local mean velocity $\langle u\rangle$ appears in the nondimensional velocity. It can be seen from the definition of ξ that the mean velocity profile shape depends on the pressure gradient $\partial p/\partial x$ impressed by the freestream.

Inside the overlap layer, the nondimensional function $u^+ = f(y^+)$ is determined by the equality between inner and outer profiles solely based on mathematical reasoning as

$$u^+ = \frac{1}{\kappa}\ln y^+ + B , \tag{2.12}$$

where κ and B are empirical constants. The constant κ is also known as the von Kármán constant. Equation (2.12) is called the *logarithmic law* or *law-of-the-wall*, which is used by several methods, e.g. the Clauser plot [Cla54] or wall functions in Computational Fluid Dynamics (CFD) codes, to determine the wall shear from the turbulent velocity profile for lack of explicit velocity data in the inner region or vice versa. For the rest of this work, the following values for the constants in Eq. (2.12) are used [Whi05]:

$$\kappa = 0.41 \qquad B = 5.0\,. \tag{2.13}$$

However, it is important to mention that the values of Eq. 2.13 are subject to discussion in the literature, as is the logarithmic form of Eq. 2.12 and its universality for different turbulent flow situations (e.g., [ZS98,ZDN03,Wil07], also see comment in [Sch82], S. 602).

If mean streamwise velocity profiles of turbulent boundary layers are plotted in inner variables as defined in Eq. (2.6), they assume a canonical form which is kept inside the inner region and the overlap layer for zero pressure gradient flows. The canonical form has been fitted by empirical functions in the inner region and the overlap layer [Spa61,Mus79]. In this text, the function proposed by Spalding [Spa61],

$$y^+ = u^+ + \mathrm{e}^{-\kappa B}\left[\mathrm{e}^{\kappa u^+} - 1 - \kappa u^+ - \frac{(\kappa u^+)^2}{2} - \frac{(\kappa u^+)^3}{6}\right] \tag{2.14}$$

will be adopted. Figure 2.2 shows the resulting profile together with a sample of LDA boundary layer data in a commonly used semi-logarithmic diagram. The inner region and the logarithmic overlap layer (a straight line in semi-logarithmic coordinates) can be determined from the Spalding function. The LDA data sample follows the canonical form in the inner region and shows an overlap layer up to about $y^+ = 100$, after which the profile departs from the logarithmic law in the outer region of the boundary layer.

An interesting property of turbulent flows is a strong similarity of near-wall velocity and turbulence profiles for the different geometries of a flat plate (boundary layer flow), a plane channel and a pipe (both fully-developed flow). Please note that this is not the case for laminar flow. The agreement observed for turbulent flows probably originates from the fact that all reasoning for

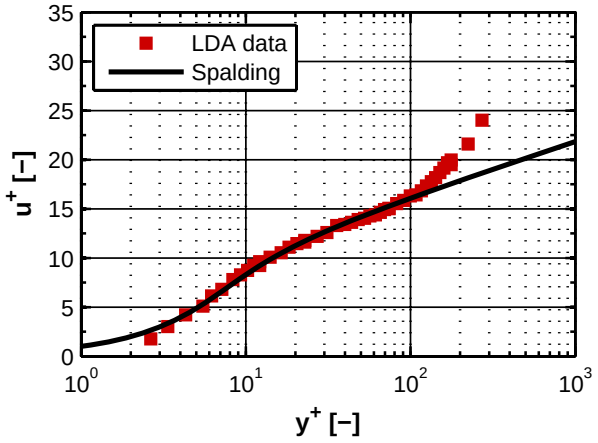

Figure 2.2: Wall function of Spalding according to Eq. (2.14) and LDA boundary layer data.

the derivation of Eqs. (2.6) and (2.12) was based only on physical considerations and dimensional analysis. Schlichting [Sch82] summarizes measurements on time-averaged velocity profiles, which showed that deviations between flat plate and tube exist in the outer region of the boundary layer, which is caused by different turbulence intensities in that region. A recent investigation of Monty et al. [MHN$^+$09] compares time-averaged velocities and turbulence statistics and energy spectra of turbulent pipe, channel and boundary layer flow. The length scale δ was defined as either the channel half height, pipe radius or boundary layer thickness in their study. They conclude that the mean velocity profiles are identical for $y < 0.25\delta$, thereby confirming the results reported by Schlichting, while higher order statistics for streamwise fluctuations (RMS values, skewness and curtosis) show even further agreement within $y < 0.5\delta$. The energy spectra of turbulent pipe and channel flows agree well throughout the flow. Comparison of internal and boundary layer flow, however, revealed that large-scale turbulent structures hold a higher fraction of turbulence energy in internal flows. For the present work, the strong similarity between tube and channel flows forms the basis for a later comparison of turbulent wall flashback limits in these geometries.

The distributions of turbulent normal and Reynolds shear stresses in turbulent boundary layers are generally Reynolds number dependent. DeGraaf and Eaton [DE00] gave a summary of the literature discussion on this topic. Figure 2.3 shows DNS results of Moser et al. [MKM99] who simulated turbulent

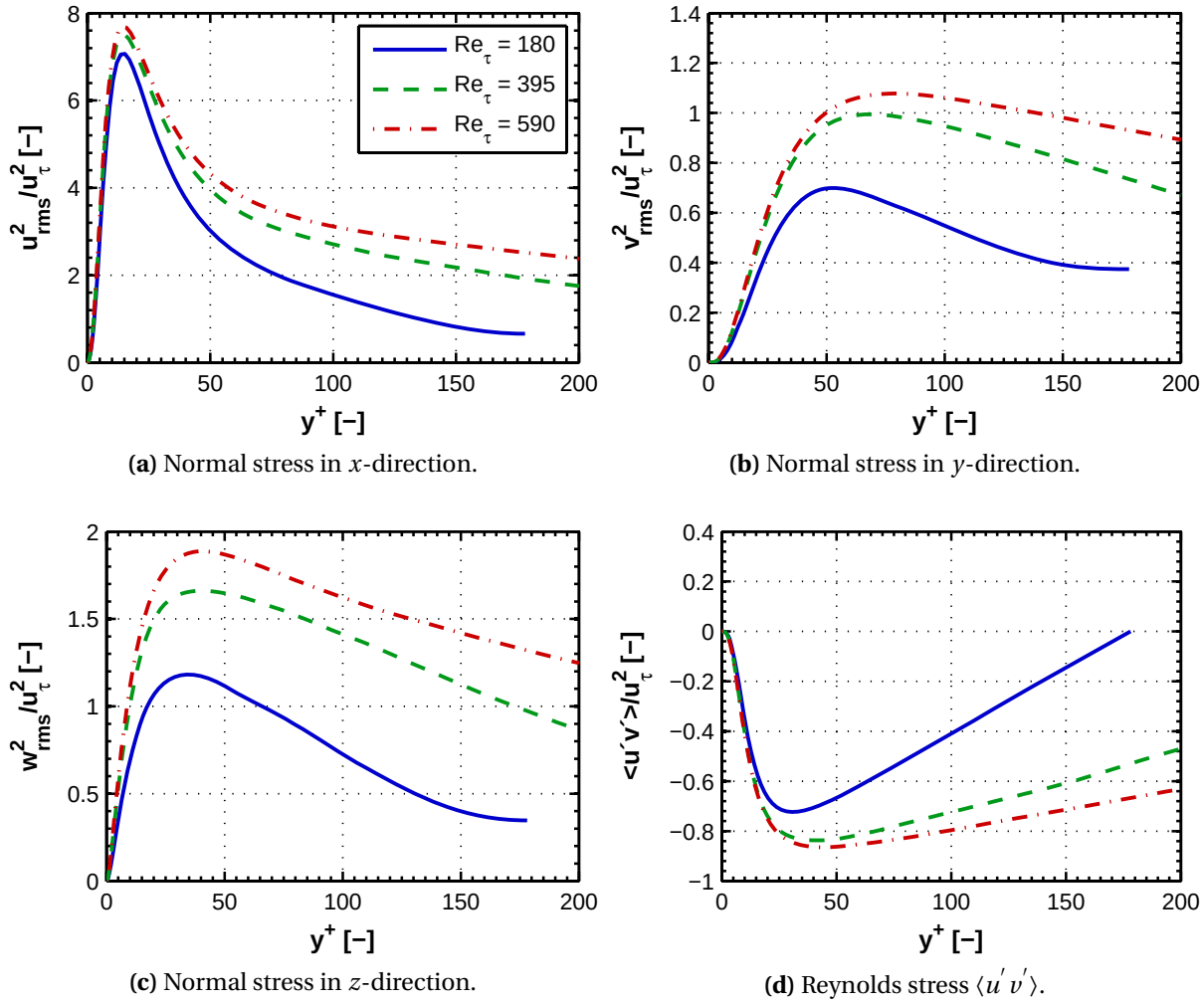

(a) Normal stress in x-direction.

(b) Normal stress in y-direction.

(c) Normal stress in z-direction.

(d) Reynolds stress $\langle u' v' \rangle$.

Figure 2.3: DNS results of near-wall turbulent fluctuations in plane channel flow at three different Re_τ [MKM99].

boundary layers in plane channel flow at three different channel Reynolds numbers, which are defined as

$$\mathrm{Re}_\tau = \frac{u_\tau h}{\nu} . \tag{2.15}$$

In Eq. (2.15), h is half of the channel height. Their simulations covered the range $\mathrm{Re}_\tau = 180...590$, which is representative for the flow conditions in the present experimental rig (see Sec. 3.3). Figures 2.3a-c show squared root mean square (rms) values of turbulent fluctuations u_i', defined as

$$u_{i,rms} = \sqrt{\langle u_i' u_i' \rangle} , \tag{2.16}$$

nondimensionalized by u_τ. By comparing Figs. 2.3a-c, it becomes obvious that streamwise fluctuations u' contain most of the turbulent kinetic energy. They show a characteristic peak at about $y^+ = 15$ and a subsequent decay towards the outer region. Both the peak value and location are a weak function of Reynolds number. Wall normal fluctuations v' shown in Fig. 2.3b peak at higher nondimensional wall distances and have a slower decline afterwards. Similar statements can be made about w' fluctuations shown in Fig. 2.3c. Figure 2.3d shows the time average of $u'v'$, which is by far the most significant Reynolds stress contributor in boundary layers. The negative values are consistent with the fact that a term with a negative sign, $-\rho\langle u'v'\rangle$, appears in the RANS shear stress tensor (see Eq. (2.10)).

2.1.4 Time-resolved Structure of Turbulent Boundary Layers

The time-resolved fluid motion inside turbulent boundary layers is the key for the understanding and modeling of many time-averaged physical processes of such flows, such as turbulence production, momentum, heat and mass transfer between flow and wall as well as boundary layer separation. A comprehensive overview and literature review on coherent fluid motion close to the wall is given in the work of Robinson [Rob91b, Rob91a], which will be used here as a guideline to present the widely accepted fundamental concepts. However, as numerical simulations at high Reynolds numbers and especially two- and three-dimensional velocity measurements close to the wall have become feasible in recent years, physical insight and modeling of near-wall turbulence is constantly evolving (e.g., [JHSK97, TA03, KÖ4a, KÖ4b, HM07, SMK09]), such that a closed presentation of the subject cannot be given at this stage.

The inner region and part of the logarithmic region of turbulent boundary layers is characterized by quasi-periodic patterns of small-scale coherent flow structures which apparently are responsible for the production and dissipation of turbulence in a boundary layer. In the outer region, large-scale coherent motion is dominant. In this context, Robinson [Rob91a] defines the term *coherent motion* as a "*...three-dimensional region of the flow over which at least one fundamental flow variable (velocity component, density, temperature, etc.)*

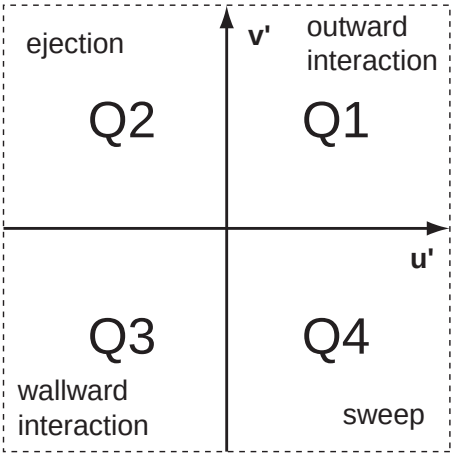

Figure 2.4: Quadrant sectioning of the instantaneous $u'v'$ plane.

exhibits significant correlation with itself or with another variable over a range of space and/or time that is significantly larger than the smallest local scales of the flow.". For the discussion of motion in the x-y plane, the quadrant analysis scheme shown in Fig. 2.4 was introduced by Wallace et al. [WEB72]. The instantaneous product $u'v'$ is used as a marker for characteristic flow events. Low-speed fluid moving away from the wall (Q2) is called an *ejection*, while high-speed fluid rushing towards the wall (Q4) is a *sweep*. The interaction quadrants mark events were neighboring ejection and sweep events interact with each other, such that low-speed fluid is pushed back towards the wall (Q3) or high-speed fluid pushed back in outward direction (Q1).

Robinson [Rob91a] presented a list of facts about the fundamental turbulence structure in turbulent boundary layers at comparably low Reynolds numbers which are of consensus within the research community. The relevant points for the context of the work presented here are as follows:

1. The sublayer cannot be considered as laminar. It consists of x-wise elongated and unsteady regions above (high-speed streaks) and below (low-speed streaks) the average streamwise velocity. The mean z-wise spacing between low-speed streaks in the sublayer is approximately 100 L_+.

2. The buffer layer is characterized by a Q2 bursting process during which low-speed fluid, existing near the wall in the form of streaks, is ejected outward from the wall. This process accounts for most of the turbulence

production in the boundary layer. The view that laminar-to-turbulent transition occurs in the buffer region is not justified.

3. Outward Q2 ejections of low-speed fluid and wallward Q4 sweeps of high-speed fluid occur intermittently throughout the boundary layer. Ejection motions are more frequent above $y^+ = 12$, while sweep motions are predominant very close to the wall.

4. Thin, sloping shear layers with respect to streamwise fluctuations ($\partial u'/\partial x$, $\partial u'/\partial y$, $\partial u'/\partial z$) are observed throughout the boundary layer at interfaces between upstream high-speed fluid and downstream low-speed fluid. The shear layers are frequently observed below $y^+ = 100$ and often form on the upstream side of lifted or curved low-speed streaks. A region of high wall pressure is located beneath the shear layers since the deceleration and redirection of high-speed fluid by the downstream low-speed region creates a convecting stagnation point (see also [Rob91b], S. 267).

5. Relatively strong quasi-streamwise vortices are frequently observed in the near-wall region. The vortices are tilt upward at an angle that increases with distance from the wall and have an average diameter of approximately 30 L_+ [KMM87, Rob91b]. These quasi-streamwise vortices are closely associated with ejections of low-speed fluid and sweeps of high-speed fluid and thus are major contributors to the Reynolds shear stress close to the wall. Quasi-streamwise vortices in the buffer layer apparently play a role in the formation of low-speed streaks but are an order of magnitude shorter than the low-speed streaks observed in the laminar sublayer. A wide-spread conclusion is that vortices "drag" through the wall region, leaving behind prolonged trails of low-speed fluid from the upward-rotating sides of the vortices.

6. Loop-shaped vortices (e.g. horseshoe-, hairpin-, λ-eddies) exist and influence the dynamics of turbulence production, but structural details as well as statistical relevance are controversial.

A large range of models exist for the variety of vortical structures, their interaction and their role on the formation of ejection and sweep events, low- and

high-speed streaks and other phenomena. Since a consensus about the involved physical processes still has to be found, no particular model shall be presented at this point.

2.1.5 Influence of Adverse Pressure Gradients

Experimental results for turbulent boundary layers show that dimensional mean velocity profiles can have very different shapes in the outer region, depending on size and sign of the global pressure gradient in the geometry. This finding has already been indicated by the similarity variables in Eq. (2.11). However, canonical profiles should be observed for flows with constant values of ξ. Clauser [Cla54] redefined ξ by using the well-defined displacement thickness

$$\delta^* = \int_0^\infty \left(1 - \frac{\langle u \rangle}{u_\infty}\right) dy \tag{2.17}$$

instead of boundary layer thickness δ to form his well-known *equilibrium parameter*

$$\beta = \frac{\delta^*}{\tau_w} \frac{dp}{dx} . \tag{2.18}$$

Boundary layers for which β = const. are called *equilibrium boundary layers*, and their outer mean velocity profiles collapse on a single curve if plotted in the coordinates y/δ and $(u_\infty - \langle u \rangle)/u_\tau$. This holds for positive (adverse) as well as negative axial pressure gradients.

For the inner region and the overlap layer, the dependence of mean streamwise velocity profiles on adverse pressure gradients is still in discussion in the literature. While White [Whi05], for example, proclaims validity of the canonical form according to Eq. (2.14) in the inner and logarithmic region even for very strong adverse or favorable pressure gradients, recent experiments ([NTH98]: $\beta = 0.77$ to 5.32, [Ind05]: $\beta = 0.96$ to 25.81) showed that mean velocity profiles lay below the canonical distribution in the buffer layer and the logarithmic region for moderate to strong adverse pressure gradients. For mild to moderate adverse pressure gradients, a reasonable match has been observed experimentally ([AE05]: $\beta \approx 2.5$ to 3.5) , while DNS results ([LS09]: $\beta = 0.73$ to 1.68) revealed a slight downward shift with respect to the log-profile. As a

nondimensional measure of strength of the adverse pressure gradient in inner variables, Nagano et al. [NTT93] used the expression

$$p^+ = \frac{\nu}{\rho u_\tau^3} \frac{dp}{dx} \tag{2.19}$$

Equation (2.19) will be used later to set pressure gradients in the experimental rig into relation with literature values.

The structural changes of time-averaged and instantaneous turbulent quantities under adverse pressure gradients will be discussed here mainly for the inner region and overlap layer, as these regions are relevant for the later interpretation of turbulent wall flashbacks in diffuser geometries. In inner scaling (Eq. (2.6)), Nagano et al. [NTT93] measured an increase of rms fluctuations close to the wall for moderate to strong adverse pressure gradients. At the beginning of the outer region, a second peak is formed for each component, the height of which increases with β. Reynolds shear stresses $\langle u' v' \rangle$ also increase strongly in the outer region. These findings have been confirmed by other studies [AE05, Ind05, LS09] for mild, moderate and strong adverse pressure gradients. The peak values of nondimensional streamwise fluctuations u_{rms}^2 / u_τ^2 lay between 6 and 9 [NTT93, Ind05, LS09].

An early flow visualization experiment on the influence of adverse pressure gradients on instantaneous boundary layer turbulence was published by Kline et al. [KRSR67], who discovered the existence of low-speed streaks close to the wall. For increasing adverse pressure gradients, the low-speed streaks tend to shorten and to waver more violently, whereas streaks tend to be elongated and more quiescent in favorable pressure gradients. In strong adverse pressure gradients some of the low-speed streaks move temporarily upstream and are washed downstream again after a certain time. The authors related this phenomenon to transitory stall (see Sec. 2.1.6) in wide-angle diffusers. Nagano et al. [NTH98] investigated the contributions of the different sectors shown in Fig. 2.4 to the overall Reynolds shear stress $\langle u' v' \rangle$. While in zero pressure gradient flows the contribution of Q2 events dominates Q4 events in the inner region and the overlap layer, the events become equally important and are responsible for an increasing fraction of $\langle u' v' \rangle$ towards the wall for adverse pressure gradients, both of which indicate a change in coherent turbu-

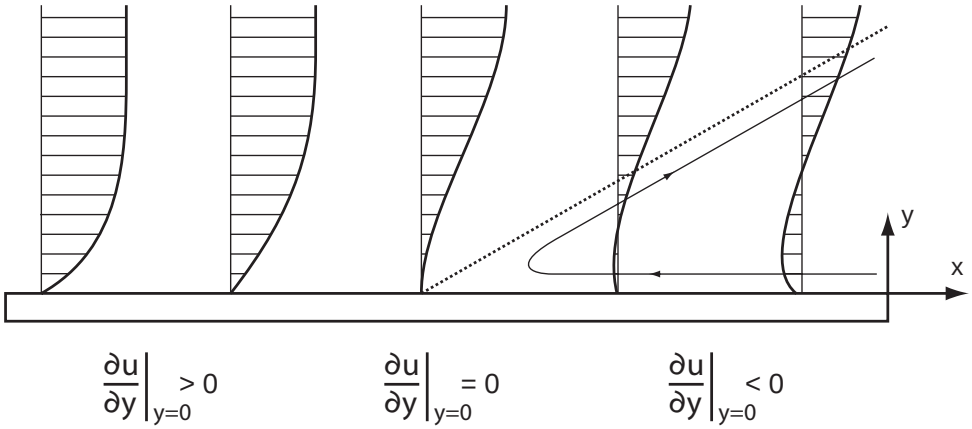

Figure 2.5: Laminar boundary layer separation due to an adverse pressure gradient.

lence structures. The detailed DNS study of Lee and Sung [LS09] worked out the influences of adverse pressure gradients on low-speed streaks and quasi-streamwise vortices in the buffer layer. The width of low-speed streaks was not affected by the pressure gradient, but their mean lateral distance became larger, up to a factor of approximately 4, and the distance distribution more irregular. The length of low-speed streaks decreased from more than 1000 L^+ to about 700 L^+, which is in accordance with the observations in [KRSR67]. In the logarithmic layer, the authors observed regions of low-momentum fluid which were longer in the streamwise direction and of higher lateral width than observed in zero pressure gradient flow (see [TA03] for a detailed description of such low-momentum regions).

2.1.6 Boundary Layer Separation

An important aspect of boundary layer flow with adverse pressure gradients is flow separation, also called flow detachment. In the following, only two-dimensional flow configurations will be considered. Generally speaking, the flow structure in the separating region is quite different for laminar and turbulent flows. Figure 2.5 illustrates a two-dimensional laminar separation process. As the pressure rises in positive x-direction, the fluid close to the wall is continuously decelerated. However, the velocity gradient $\partial u/\partial y$ at the wall is still positive. At some point, the fluid close to the wall cannot advance towards

higher pressures in x-direction anymore as its x-wise kinetic energy vanishes. As a consequence, the fluid particles are deflected away from the wall and a backflow region with a characteristic wedge shape is formed. The separation point is defined by

$$\left.\frac{\partial u}{\partial y}\right|_{y=0} = 0 \tag{2.20}$$

which is a single point for an ideal steady laminar two-dimensional separation process. In the case of moving walls, unsteady boundary layers and three-dimensional separation, Eq. (2.20) is not sufficient to determine the separation point, though [Wil77]. Close to the separation point and beyond, the boundary layer approximations are not valid anymore since the boundary layer thickness rapidly increases due to fluid motion away from the wall and the inequalities in Eqs. (2.3) are not fulfilled anymore in proximity to the backflow region.

For turbulent flows, separation due to adverse pressure gradients is a process rather than a sudden event and starts intermittently close to the wall at a certain location. Going downstream, the fraction of time for which fluid is moving upstream progressively increases. This qualitative picture has been observed for a flat plate as well as for cylindrical geometries. A detailed summary of the turbulent separation process has been provided by Simpson [Sim96], according to which the separation process can be phenomenologically divided into three regions:

1. **Incipient detachment**: Instantaneous backflows for ≥1% of the time ('occasionally').
2. **Intermittent transitory detachment**: Instantaneous backflows for ≥20% of the time ('noticeably more frequent than occasionally').
3. **Detached flow**: Instantaneous backflows for ≥50% of the time. The detachment point with time-averaged wall shear stress equal to zero lies at ≈50% backflow time.

During incipient detachment, small three-dimensional flow elements move upstream for a certain distance, are disintegrated by Reynolds stresses and

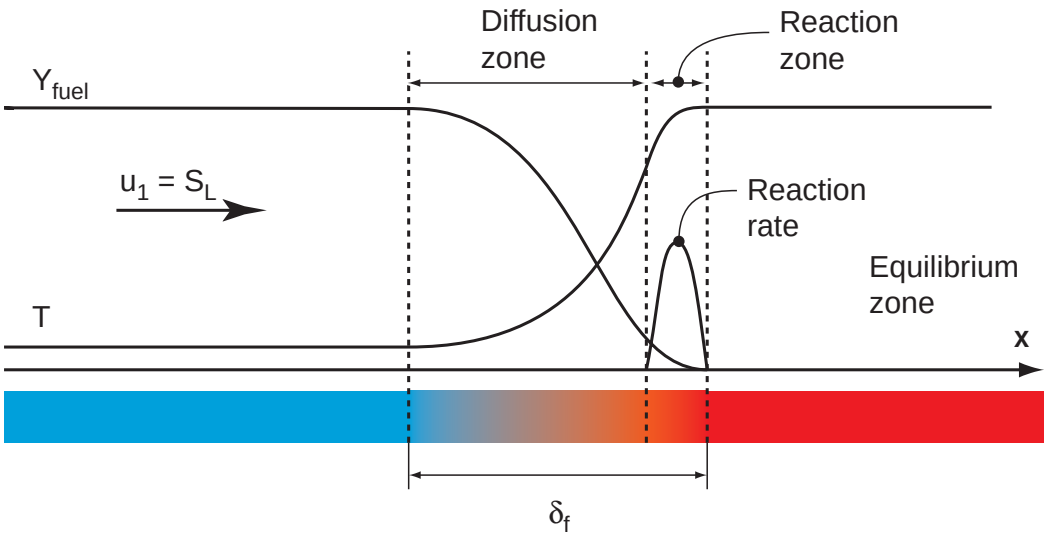

Figure 2.6: Structural model of a one-dimensional premixed laminar flame (after [Law06]).

carried downstream again. The backflow regions probably involve reverse flows of low-speed streaks with low kinetic energy due to the adverse pressure gradient [KBS83]. Intermittent transitory detachment is associated with strong shear layer growth. Intermittent backflow regions are observed up to $y/\delta \approx 0.5$ and have high turbulence levels.

2.2 Basics of Premixed Flame Propagation

Combustion takes place in the form of a *premixed flame* if fuel and oxidizer are perfectly mixed prior to consumption by the flame. The following overview of premixed flame physics is based on the work of Law [Law06] and Peters [Pet00] if not specified otherwise. For modeling and scaling of premixed flames, a one-step reaction with large activation energy is usually assumed. The resulting flame structure for a laminar, one-dimensional flame is shown in Fig. 2.6. Far upstream of the flame, the gas mixture has a constant temperature T_1 and a fuel mass fraction $Y_{1,fuel}$. The fresh mixture flows at the one-dimensional, adiabatic laminar flame speed S_L such that the flame is stationary. In the following, S_L and also flame speed in general, S_f, are assumed as the relative speed between the *unburnt* gases and the flame. In the chemically inert diffusion zone, heat and mass diffusion cause continuous changes in temperature

and species concentrations, which is overlaid by convective transport. Due to the large activation energy of the one-step chemistry model, the reaction and thus heat release only takes place after considerable heating of the mixture. After all fuel has been consumed, the products tend to their equilibrium composition in the equilibrium zone. The thickness of the diffusion zone is assumed to be much larger than the reaction zone, such that the overall flame thickness δ_f is usually approximated by the thickness of the preheat zone.

To illustrate the degree of approximation of the model shown in Fig. 2.6, the detailed structure of a lean H_2-air flame is shown in Fig. 2.7. The flame has been simulated using the chemical kinetics software Cantera [Goo07] and the detailed H_2-O_2 mechanism by Li et al. [LZKD04], which will be used for the rest of this text to obtain various chemical quantities of H_2-air combustion. Dry air only consisting of N_2 and O_2 with $X_{N2}/X_{O2} = 79/21$ is always assumed. Figure 2.7a shows the mole fractions of global reaction species and the mixture temperature as a function of the one-dimensional flame coordinate. It can be seen that the thickness of the diffusion zone of H_2 upstream of the flame is thicker than the thermal diffusion zone, which is caused by the non-unity Lewis number of the mixture, defined as

$$\mathrm{Le} = \frac{a_{mix}}{D_{fuel,mix}} \tag{2.21}$$

for a fuel-lean mixture. In Eq. (2.21), a_{mix} is the thermal diffusivity of the mixture and $D_{fuel,mix}$ is the diffusivity of the fuel into the mixture of the remaining species of the fresh gases. For the H_2-air flame shown in Figs. 2.7, the Lewis number is Le = 0.36 in the unburnt gases. Due to the strong diffusion of H_2 towards its consumption zone, X_{O_2} has a distinct overshoot at the beginning of the temperature rise. Figure 2.7b shows mole fractions of the radical species. At the low-temperature side of the flame, HO_2 and subsequently H_2O_2 are produced by back-diffusion of H radicals from the high-temperature region. Plots of fractional heat release and mixture temperature in [Law06] for a stoichiometric flame reveal that a substantial fraction of overall heat release (30% at $\Phi = 1$) already occurs in the HO_2-H_2O_2 region, where also the peak heat release rate can be found. By comparing Figs. 2.7 with the model in Fig. 2.6, it can be concluded that the detailed structure of the H_2-air flame is actually quite different from the model assumption of a one-step reaction with large

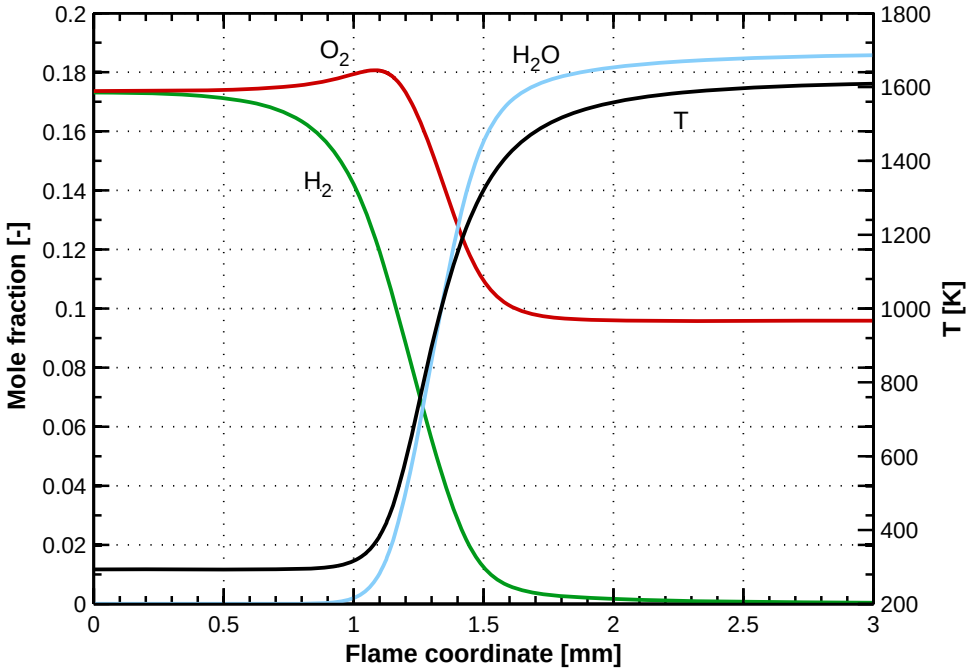

(a) Global reaction species.

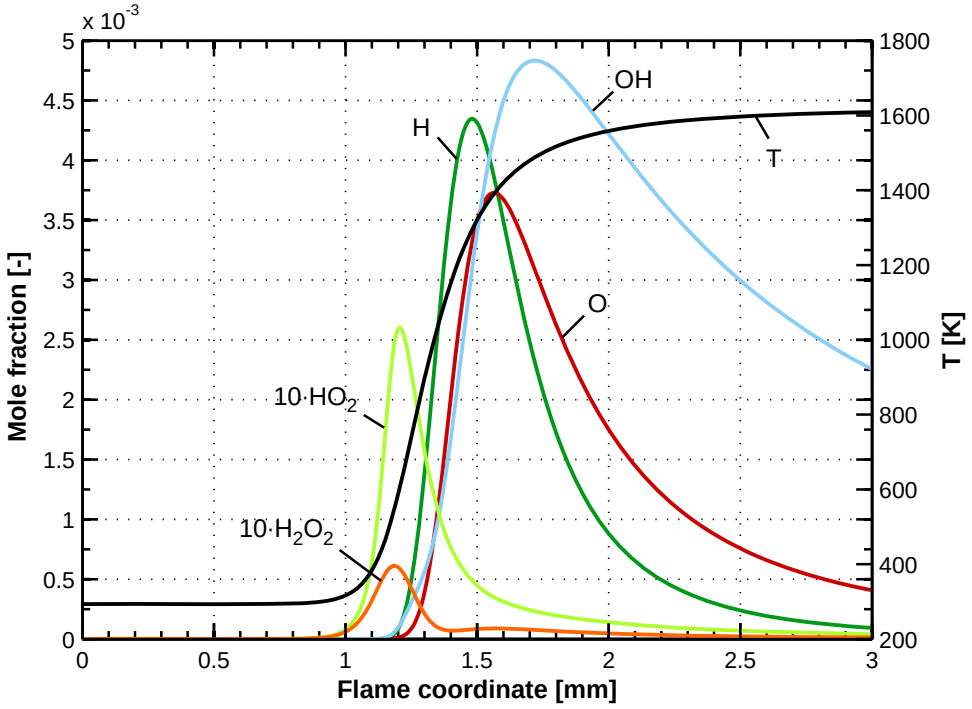

(b) Radical species.

Figure 2.7: Detailed structure of a lean H_2-air flame in dry air at $\Phi = 0.5$, 293.15 K and 1 atm.

activation energy, as appreciable radical production and heat release occurs over the whole extent of the flame. For scaling purposes, however, the structural model of Fig. 2.6 is generally accepted as valid [Tur00, Pet00, Law06].

The identification of a preheat zone, where heat and mass diffusion are in balance with convection, and a reaction zone, where temperature-sensitive reaction rates and species diffusion are in balance, underlines that a premixed flame principally is a two-parameter system. Flame thickness δ_f and flame speed S_L shall be chosen here as the two independent variables since two important aspects of flashback, flame propagation velocity and quenching by heat loss (see Sec. 2.4), are described by them. While laminar flame speeds can be readily obtained experimentally, the flame thickness is hard to measure. Therefore, δ_f and S_L are related to each other by the thermal diffusivity of the mixture, which then acts as independent parameter instead of δ_f [Law06]. In the literature, several definitions for this relation exist, three of which shall be discussed here. The first is according to Turns [Tur00],

$$\delta_f = \frac{2a_1}{S_L}\,, \tag{2.22}$$

where a_1 is the thermal diffusivity of the unburnt mixture. Equation (2.22) is derived by assuming, amongst others, equal thicknesses of preheat and reaction zone, unity Lewis number as well as constant and equal specific heats for all species. The second relation is used by Peters [Pet00]:

$$\delta_f = \frac{(k/c_p)_{il}}{\rho_1 S_L}\,. \tag{2.23}$$

In Eq. (2.23), k is the thermal conductivity and c_p is the heat capacity at constant pressure. The index 'il' specifies properties at the temperature of the *inner layer*, which is defined as the part of the premixed flame where the fuel is consumed. As a third definition of flame thickness, the *temperature gradient thickness* is described in Fig. 2.8. The flame thickness is represented by the distance during which the gases are heated from their initial temperature T_1 to

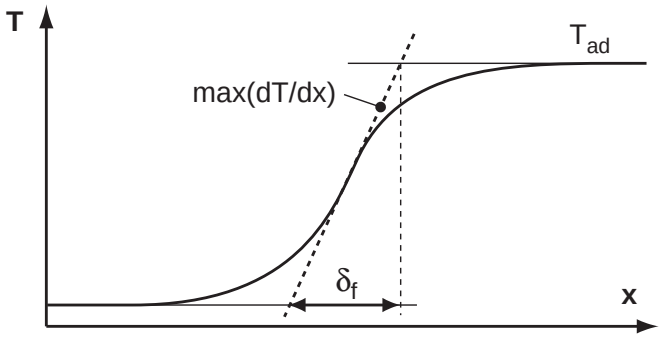

Figure 2.8: Flame thickness defined by maximum temperature gradient.

the adiabatic flame temperature T_2, which is approximated by a linear slope with the maximum gradient of the temperature with respect to x:

$$\delta_f = \frac{T_2 - T_1}{\max\left(\frac{dT}{dx}\right)}. \tag{2.24}$$

This definition of flame thickness has been used by Turns [Tur00] to derive Eq. (2.22).

Figures 2.9 show results for S_L and the three different definitions of δ_f for H_2-air flames at different preheat temperatures and pressures. For the evaluation of Eq. (2.23), averages of unburnt and burnt gas properties were used as an approximation for inner layer properties.

Figure 2.9a illustrates S_L as a function of $1/\Phi$ at atmospheric conditions. The wide flammability limits and high laminar flame speeds are obvious. The strong shift of the maximum of S_L towards rich mixtures (much more than observed for a methane flame, for example) is a Lewis number effect, as pointed out by Law [Law06]. For a given fuel-oxidizer mixture,

$$S_L \sim \sqrt{\mathrm{Le}}\,. \tag{2.25}$$

As for lean mixtures, Le ≈ 0.3 and for rich mixtures, Le ≈ 2.3, S_L is decreased for lean and increased for rich conditions. Figure 2.9b shows the laminar flame thicknesses for equal conditions. The definitions of flame thickness according to Eqs. (2.22) and (2.23) compare well to each other, while the temperature gradient thickness is off these curves and furthermore does not follow stoichiometric reasoning. A higher grid resolution does not change these trends,

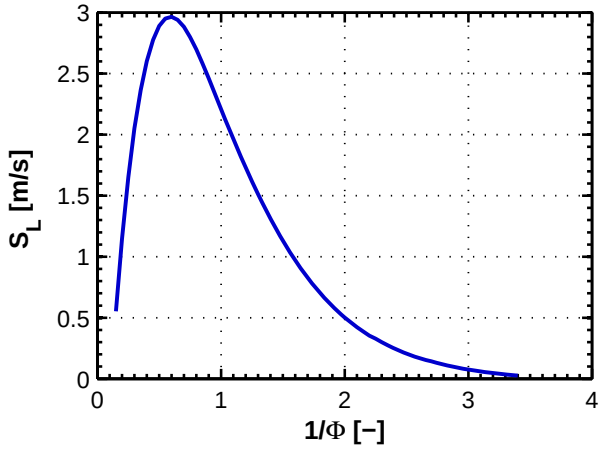

(a) Flame speed at 293.15 K, 1 atm.

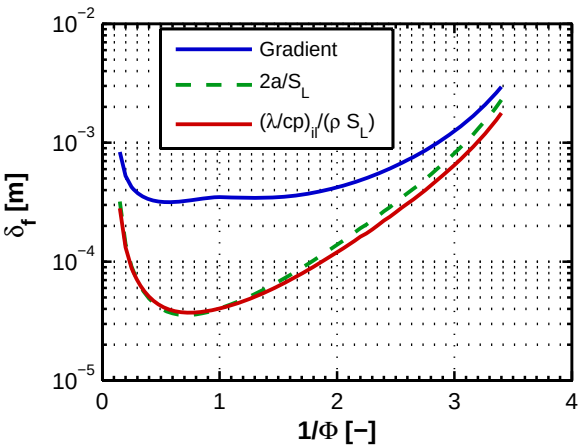

(b) Flame thickness at 293.15 K, 1 atm.

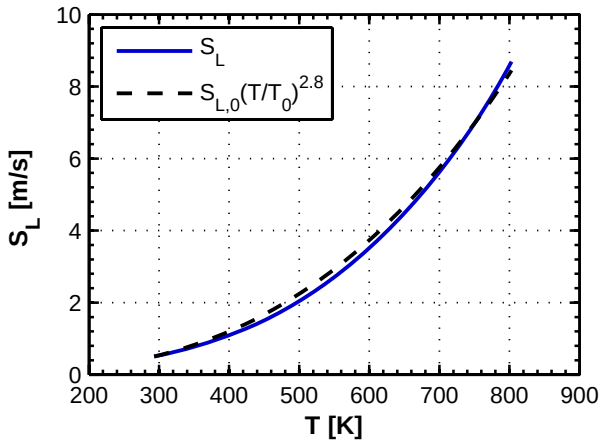

(c) Flame speed at $\Phi = 0.5$, 1 atm.

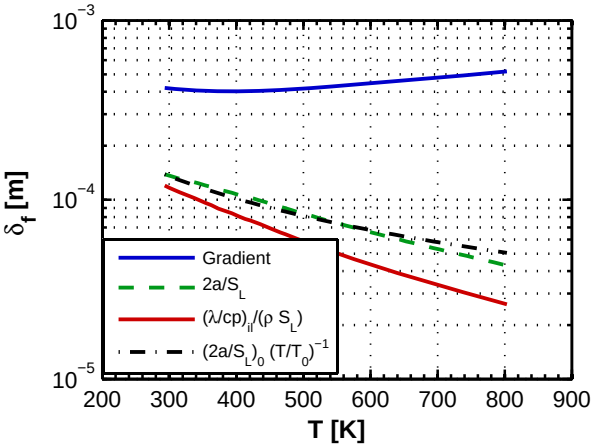

(d) Flame thickness at $\Phi = 0.5$, 1 atm.

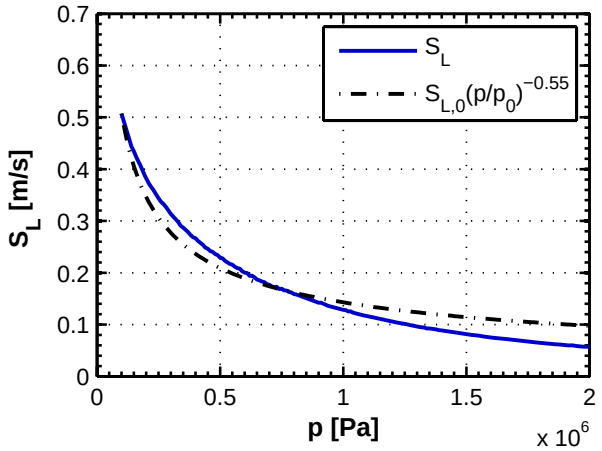

(e) Flame flame speed at $\Phi = 0.5$, 293.15 K.

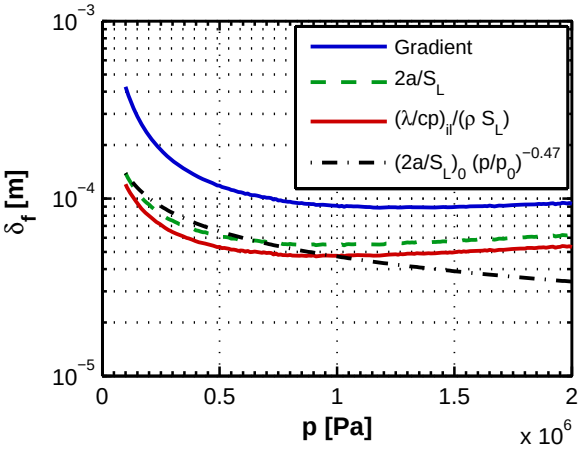

(f) Flame thickness at $\Phi = 0.5$, 293.15 K.

Figure 2.9: Laminar flame speed and thickness of H_2-air flames at different T and p from chemical kinetics simulations.

such that a definition of δ_f according to Eq. (2.24) is not sensible with the numerical setup used here. The influence of preheat temperature on S_L and δ_f at $\Phi = 0.5$ is shown in Figs. 2.9c and 2.9d. The laminar flame speed rises monotonously. A power law approximation according to

$$S_L(T) = S_{L,0}\left(\frac{T}{T_0}\right)^{2.8} \tag{2.26}$$

is included in Fig. 2.9c, which fits the temperature slope quite well. In Eq. (2.26), indices '0' indicate conditions at $T_0 = 293.15\,\mathrm{K}$ and $p_0 = 1\,\mathrm{atm}$. Often, a square dependence of $S_L(T)$ is assumed across fuels, which apparently is not correct for lean H_2-air mixtures. As shown by Fig. 2.9d, flame thickness is decreasing by almost one order of magnitude from room temperature to typical combustor entry temperatures. The power law fit

$$\delta_f(T) = \delta_{f,0}\left(\frac{T}{T_0}\right)^{-1} \tag{2.27}$$

is a good approximation for the slope of the flame thickness according to Eq. (2.22). The pressure influence on S_L and δ_f is shown in Figs. 2.9e and 2.9f. The flame speed is monotonously decreasing with p, and the expression

$$S_L(p) = S_{L,0}\left(\frac{p}{p_0}\right)^{-0.55} \tag{2.28}$$

is a good approximation for this trend. The flame thickness is decreasing to a minimum at about 10 bar, from where it starts to increase slightly again. This slope cannot be fitted well by a simple power law, however, the curve

$$\delta_f(p) = \delta_{f,0}\left(\frac{p}{p_0}\right)^{-0.47} \tag{2.29}$$

is a good approximation to the calculated values up to 10 bar. Finally, it can be stated that the flame thicknesses according to Eqs. (2.22) and (2.23) are close to each other for Figs. 2.9d and 2.9f, while the gradient thickness is not well-defined again.

After the analysis of the structure of a premixed flame, the pressure field of a one-dimensional flame propagating in an infinite domain shall be discussed

now, which is also known as the *backpressure* of a premixed flame. Since a premixed flame propagates into the fresh gases in the form of a thin sheet, it can be treated as a planar wave for this purpose. Using a coordinate system that moves with the wave, and assuming steady, adiabatic conditions and neglecting potential energy, the conservation equations can be formulated as follows:

$$\text{Mass:} \qquad \rho_1 u_1 = \rho_2 u_2 \,, \tag{2.30a}$$

$$\text{Momentum:} \qquad \rho_1 u_1^2 + p_1 = \rho_2 u_2^2 + p_2 \,, \tag{2.30b}$$

$$\text{Energy:} \qquad h_1 + \frac{1}{2} u_1^2 = h_2 + \frac{1}{2} u_2^2 \,. \tag{2.30c}$$

Indices '1' refer to fresh, unburnt gases and indices '2' to products in equilibrium, and h is the static enthalpy of the mixture. Equations (2.30a) and (2.30b) can be combined to

$$\mathrm{M}_1^2 = -\frac{\dfrac{p_2}{p_1} - 1}{\gamma\left(\dfrac{u_2}{u_1} - 1\right)} \,, \tag{2.31}$$

where M_1 is the Mach number of the unburnt gases and γ is the ratio of specific heats. Lines in a u_2/u_1-p_2/p_1 diagram which satisfy Eq. (2.31) are termed *Rayleigh lines*. To include the internal heat addition due to combustion, the enthalpy difference across the flame is expressed by

$$h_2 - h_1 = -q_f + c_p(T_2 - T_1) \,. \tag{2.32}$$

In Eq. (2.32), q_f is the heat of combustion in J per kg mixture. Using Eqs. (2.30c) and (2.32), the expression

$$\left(\frac{p_2}{p_1} + \frac{\gamma-1}{\gamma+1}\right)\left(\frac{u_2}{u_1} - \frac{\gamma-1}{\gamma+1}\right) = \frac{4\gamma}{(\gamma+1)^2} + 2\frac{\rho_1 q_f}{p_1}\left(\frac{\gamma-1}{\gamma+1}\right) \tag{2.33}$$

can be derived. Curves in the u_2/u_1-p_2/p_1 diagram that satisfy Eq. (2.33) are called *Hugoniot curves*. The pressure and velocity field upstream and downstream of the flame is given by states that fulfill Eqs. (2.31) and (2.33) simul-

taneously. A constituting equation for the pressure ratio p_2/p_1 can be derived from this requirement to [Law06]

$$\frac{p_2}{p_1} = 1 - \frac{(1-\mathrm{M}_1^2)\gamma}{\gamma+1}\left\{1 \pm \left[1 - \frac{2(\gamma^2-1)}{\gamma}\frac{\mathrm{M}_1^2}{(1-\mathrm{M}_1^2)^2}\frac{\rho_1 q_f}{p_1}\right]^{1/2}\right\}. \tag{2.34}$$

An according expression for u_2/u_1 can also be derived. Premixed flames with $\mathrm{M}_1 > 1$ are called *detonation waves*, while $\mathrm{M}_1 < 1$ implies *deflagration waves*. Only deflagrations are observed in the combustion experiments to be presented, thus the rest of the discussion will be limited to this case. Generally, the pressure and velocity fields must fulfill $p_2 < p_1$ and $v_2 > v_1$, respectively, for deflagrations, such that Eq. (2.34) is bounded by $0 \leq p_2/p_1 \leq 1$. Furthermore, the $\pm$ sign in Eq. (2.34) designates *strong deflagrations* (+) and *weak deflagrations* (-). For the low velocity deflagrations observed in the present work, strong deflagrations cannot exist due to $p_2/p_1 < 0$ for low M_1 in that case, thus only weak deflagrations have to be considered (the existence of strong deflagrations is doubtful anyway due to a decrease in entropy across such waves, see [Law06]). For the determination of the flame backpressure for laminar premixed flames, a simplified version of Eq. (2.34) is commonly used (e.g., [LE87], S. 221), which is derived from combining Eqs. (2.30a) and (2.30b) and assuming that the density has changed from ρ_1 to ρ_2 across the flame:

$$p_f = p_1 - p_2 = \rho_1 S_L^2\left(\frac{\rho_1}{\rho_2} - 1\right) \approx \rho_1 S_L^2\left(\frac{T_2}{T_1} - 1\right). \tag{2.35}$$

For the term on the right-hand side in Eq. (2.35), $p_2 \approx p_1$ has been assumed in the ideal gas law to replace the density, which is a feasible assumption since $(p_1 - p_2)/p_1 \ll 1$. By looking at the energy conservation equation (2.30c), it is clear that the kinetic energy has been neglected for the derivation of Eq. (2.35), which will be referred to as *isokinetic* in the following. However, Eq. (2.35) is a very good approximation for weak deflagrations of laminar premixed flames as illustrated by Fig. 2.10. The graph shows the pressure difference $p_1 - p_2$ across the flame for the Rayleigh-Hugionot relation (2.34), for the isokinetic derivation of the most right of Eq. (2.35), using $T_2 \approx T_1 + q_f/c_p$ in analogy to Eq. (2.34), and finally for the isokinetic derivation with T_2 being the true adiabatic flame temperature. It can be seen that the exact solution and the first

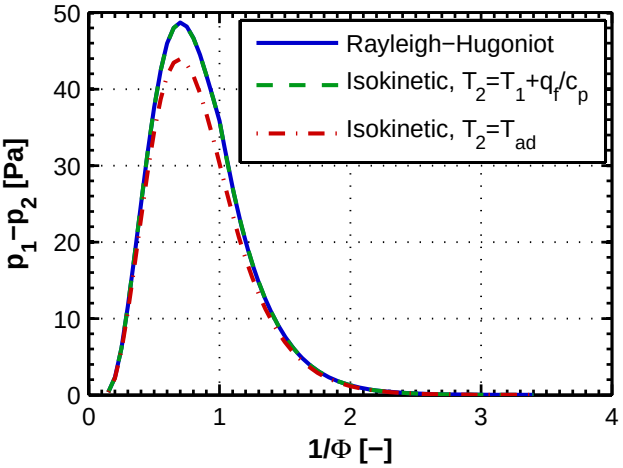

Figure 2.10: Flame backpressure according to Rayleigh-Hugionot relation and isokinetic derivations.

isokinetic approximation fit perfectly together as expected. The flame backpressure is slightly overpredicted around stoichiometry due to the assumption of a constant specific heat capacity, compared to a realistic value for T_2 in Eq. (2.35).

2.3 Interaction between Flame and Boundary Layer Flow

Up to this point, only adiabatic, one-dimensional and steady premixed flame propagation was considered. Premixed flames that burn in two- or three-dimensional, unsteady flow fields show a much more complex propagation behavior in terms of their local flame speed $\mathbf{S_f}(\mathbf{x}, t)$, where bold letters designate vector quantities. Law and Sung [LS00] provided a review on the aerodynamics of such flames which forms the basis for the following discussion if not indicated otherwise.

2.3.1 Laminar Boundary Layer

In general, the effect of spatial non-uniform and unsteady flow on a premixed flame is called *stretch*. Based on the length scale of observation, stretch effects are separated into two groups:

- **Hydrodynamic stretch**: The flame is treated as an infinitely thin surface that separates unburnt and burnt gases. The combination of normal and tangential velocity components upstream of the flame lead to flame displacement, wrinkling and change of the burning rate through increase or decrease of the flame surface.
- **Flame stretch**: The flame is represented by a heat and mass diffusion zone and a thin reaction zone according to Fig. 2.6. Tangential velocity components affect heat and mass diffusion upstream of the reaction zone, while normal components can change the residence time in the diffusion zone. This influences the flame velocity and can lead to local extinction of the reaction.

The two effects are strongly coupled as the hydrodynamic stretch defines the local flow conditions relevant for flame stretch analysis, which in turn provides the relative velocity between flame and flow.

The influence of hydrodynamic stretch on the evolution of the flame surface can be summarized in a single parameter known as the stretch rate:

$$\kappa = \frac{1}{A}\frac{DA}{Dt}\,. \tag{2.36}$$

In Eq. (2.36), A is the area of an infinitesimal element of the flame surface and D/Dt is the substantial derivative. For a general flame surface in a *fixed* Cartesian coordinate system, Eq. (2.36) corresponds to [LS00]

$$\kappa = \underbrace{\nabla_{\tan}\cdot[\mathbf{n}\times(\mathbf{u}\times\mathbf{n})]}_{\substack{\text{curvature, aerodynamic strain}}} + \underbrace{(\mathbf{S_f}\cdot\mathbf{n})(\nabla\cdot\mathbf{n})}_{\substack{\text{unsteady flame motion}}}\,, \tag{2.37}$$

where $\nabla_{\tan}$ is a tangential gradient operator, i.e. the spatial derivatives along a curvilinear coordinate system on the flame surface, and $\mathbf{n}$ is the normal vector on the flame surface. It becomes clear from Eq. (2.37) that on the one hand, hydrodynamic stretch is induced by flame curvature (variation in $\mathbf{n}$) and strain by the flow field $\mathbf{u}$. As an important point, both contributions are zero if $\mathbf{u}\times\mathbf{n} = 0$, i.e. if the streamlines are perpendicular to the flame surface. On the other hand, hydrodynamic stretch is produced if the flame surface is not steady in

the fixed Cartesian coordinate system ($\mathbf{S_f} \neq 0$) and the flame is curved ($\nabla \cdot \mathbf{n} \neq 0$) at the same time.

The effect of flame stretch on the burning velocity is particularly strong for mixtures where the involved species have different diffusivities. As Law and Sung [LS00] point out, there are three diffusivities of main interest for an inert-abundant mixture of two reactants, which are the thermal diffusivity a, the mass diffusivity of the excess reactant D_{ex} and that of the deficient reactant D_{def}. Two effects are considered in the literature, which are described by the diffusivity ratio of the decisive processes depending on stoichiometry:

- **Nonunity Lewis-number effects**: $a/D_{def} = \mathrm{Le}$ for off-stoichiometric mixtures (see Eq. (2.21)).
- **Preferential diffusion effects**: D_{def}/D_{ex} for near-stoichiometric mixtures

Both are commonly summarized in the term *nonequidiffusion effects*. However, nonunity Lewis-number effects are predominant in lean premixed combustion. For a given unstretched flame, its change in propagation speed in response to the flame stretch rate κ is depending on the following parameters of the unstretched flame [Law06]:

$$\frac{S_f}{S_L} = f(\kappa, \rho S_L, \delta_{th}, E_a, \mathrm{Le}) \,. \tag{2.38}$$

In Eq. (2.38), S_f is the stretched flame speed, δ_{th} is the length of the thermal diffusion zone and E_a is the activation energy of a representative one-step global reaction described by an Arrhenius term. For convenience, this rather complicated function can be expressed by nondimensional quantities as

$$\frac{S_f}{S_L} = 1 + \mathrm{Ma_1}\mathrm{Ka_1} \,, \tag{2.39}$$

where $\mathrm{Ma_1}$ is the Markstein number and $\mathrm{Ka_1}$ is the Karlovitz number representing the nondimensionalized stretch rate κ. Both are evaluated in the unburnt mixture. While $\mathrm{Ka_1}$ can be calculated from unstretched flame properties if κ is known, the definition of the Markstein number is more complicated

such that it is conveniently determined from experiments or numerical simulations. A simplified version of Eq. (2.39) is often used:

$$S_f = S_L + \mathscr{L}_1 \kappa \,. \tag{2.40}$$

The dimensional variable $\mathscr{L}_1$ [m] is called the *Markstein length* of the unburnt mixture, which again is determined from experiments or numerical simulations (see e.g. [STK06] for H_2-air results).

The complex nature of laminar premixed flame propagation is underlined by two flame front instabilities which are observed for these flames:

- **Hydrodynamic instability**: The backpressure of the flame promotes the propagation of convex flame segments into the mixture while concave segments are retarded. This instability is observed for thin flames, i.e. at high pressures and temperatures, since a finite flame thickness tends to stabilize the flame.
- **Diffusional-thermal instability**: For mixtures with Le $<$ 1, non-equidiffusion effects lead to an increase in flame speed at convex flame segments and a decrease for concave zones. The opposite occurs for Le $>$ 1 which tends to smooth a wrinkled flame.

Both instabilities lead to the formation of a cellular substructure on the flame surface and can interact with each other.

2.3.2 Turbulent Boundary Layer

The preceding explanations on stretched laminar flames are essential to understand the influence of turbulent fluctuations in the unburnt gases on the combustion process. The monograph of Peters [Pet00] provides the basis for the following summary if not indicated otherwise.

Turbulent flows consist of eddies of different length scales. According to the eddy cascade hypothesis, kinetic energy is transferred from large towards

small scales until the energy is dissipated by viscous effects in the smallest eddies at the *Kolmogorov scale* η. For isotropic, homogeneous turbulence,

$$\eta = \left(\frac{\nu^3}{\epsilon}\right)^{1/4}, \tag{2.41}$$

where ϵ is the rate of turbulent energy dissipation. The size of the eddies which contain most of the turbulent kinetic energy is called the *integral length scale* l_t, which is formally defined by the area under a two-point correlation of the turbulent fluctuations in a flow.

In the same way as previously described for hydrodynamic stretch and flame stretch situations, the turbulent eddies can interact with the flame in different ways, depending on their turnover time scale and diameter, causing changes in flame propagation speed by flame wrinkling and non-equidiffusion effects and potentially leading to local or global distinction for very high turbulence levels. The physical model behind this view is called the *laminar flamelet concept*, which assumes that a turbulent flame consists of an ensemble of stretched laminar flamelets with a thin reactive layer. Based on the definition of a turbulent Reynolds number,

$$\mathrm{Re_t} = \frac{u_t^{'} l_t}{S_L \delta_f}, \tag{2.42}$$

where δ_f is calculated according to Eq. (2.23) and $u_t^{'}$ is the turnover velocity of the integral scale eddies, and two Karlovitz numbers based on the flame thickness δ_f and the thickness of the reaction zone δ_r,

$$\mathrm{Ka_f} = \frac{\delta_f^2}{\eta^2}, \qquad \mathrm{Ka_r} = \frac{\delta_r^2}{\eta^2}, \tag{2.43}$$

Peters [Pet99] introduced a diagram of turbulent combustion regimes as shown in Fig. 2.11. Along the x-axis, the ratio of integral length scale and flame thickness is shown. Given this information, the ratio of eddy turnover time to the laminar burning velocity on the y-axis is a time scale comparison between flame motion and turbulent fluctuations. The different regimes are characterized as follows:

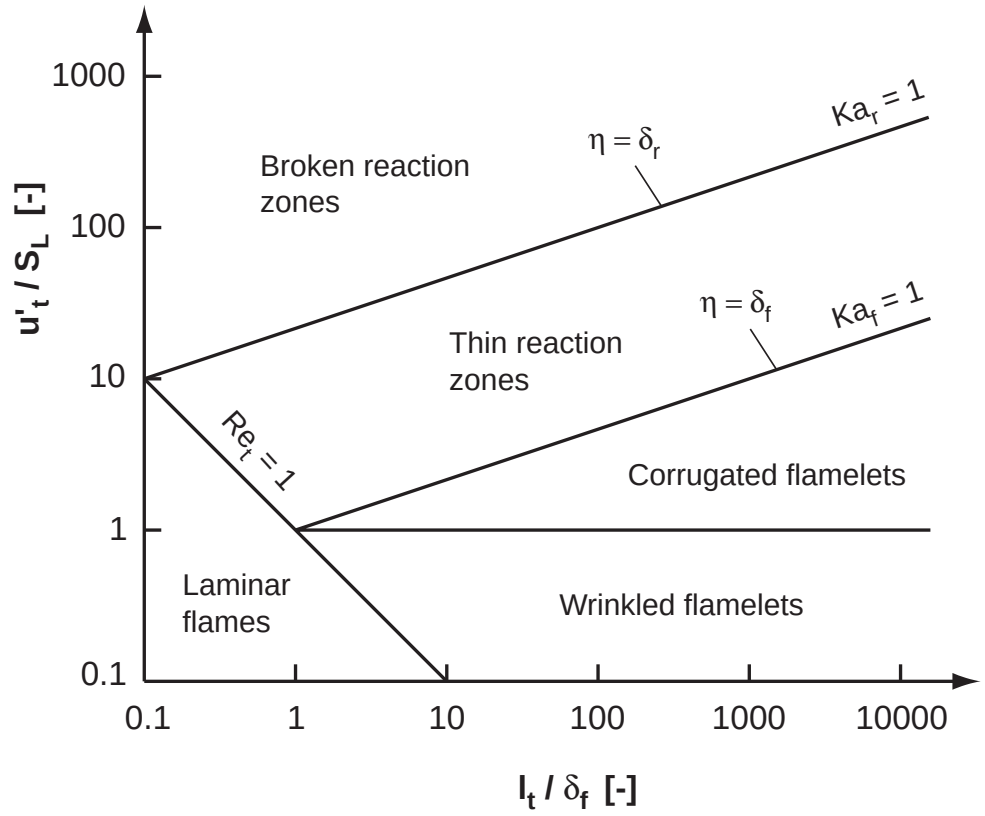

Figure 2.11: Turbulent combustion regimes according to Peters [Pet99].

- **Laminar flames**: $\mathrm{Re_t} < 1$. Laminar combustion.

- **Wrinkled flamelets**: $u_t^{'} < S_L$. Laminar flame propagation is only weakly influenced by flame front corrugation due to turbulence.

- **Corrugated flamelets**: $\mathrm{Ka_f} < 1$. The flame thickness δ_f, which comprises the preheat zone as well as the reaction zone, is smaller than the Kolmogorov eddies. Although the flame is wrinkled by turbulence, its internal structure is not perturbed.

- **Thin reaction zones**: $\mathrm{Ka_r} < 1$,$\mathrm{Ka_f} > 1$. The smallest turbulent eddies can penetrate into the preheat zone since $\eta < \delta_f$, which results in an increase in scalar mixing and hence in a thicker preheat zone. However, as $\delta_r \ll \delta_f$ is assumed ($\delta_r/\delta_f = 0.1$ for Fig. 2.11), the reaction zone is still not directly affected by turbulence.

- **Broken reaction zones**: $\mathrm{Ka_r} > 1$. Kolmogorov eddies can penetrate into the reaction zone since $\eta < \delta_r$, causing increased heat loss to the preheat zone and local distinction of the reaction as a consequence. The flamelet concept is no longer valid in this regime.

As mentioned before, laminar flamelets are subject to stretch and non-equidiffusion effects, which influence their propagation velocity and thus the effective turbulent flame speed [MP91, WZS08].

2.4 Interaction between Flame and Cold Wall

The presence of a cold wall influences a premixed flame by three mechanisms:

- **Heat loss**: The temperature gradient between the flame zone and the wall causes conductive heat loss which lowers the flame temperature and reaction rates.
- **Third body reaction partner**: The wall acts as an inert third body for recombination reactions due to collision losses of impinging molecules.
- **Surface reaction**: Chemically non-inert walls catalyze or inhibit reactions.

In general, the rapid deceleration of chemical reactions is called *quenching*. In conjunction with combustion close to cold walls, this term is used to describe the influence of the three mechanisms mentioned above on the decaying reaction rate of the flame with decreasing wall distance. For systematic studies of wall quenching, three generic situations shown in Fig. 2.12 are commonly referred to. Flame quenching by parallel plates or tubes is characterized by the minimal distance δ_q for which a premixed flame is able to propagate through the passage. Head-on quenching is a dynamic process during which the flame propagates towards a cold wall in normal direction. Due to wall quenching, the reaction of the flame is stopped at a finite distance δ_q above the wall. Finally, side-wall quenching is a continuous process as the

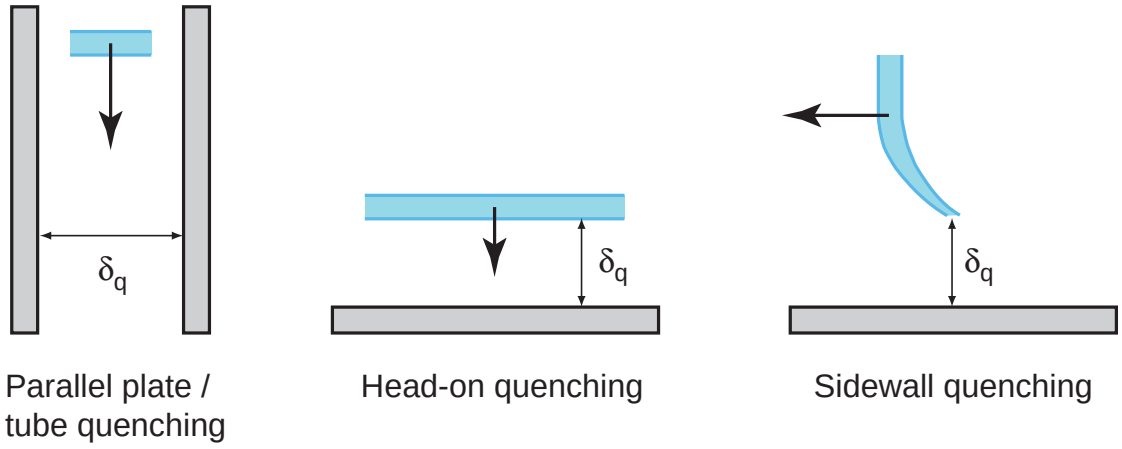

Figure 2.12: Definitions of flame quenching situations next to cold walls.

flame propagates parallel to a cold wall. Towards the wall, the reaction rate is reduced such that the flame speed falls behind the values at higher distance from the wall. Again, at a finite distance δ_q above the wall the reaction is completely stopped. It is clear that for head-on and sidewall quenching, the distance δ_q is not clearly defined for complex chemistry. In the literature, the flame luminescence has been used as a marker of the flame border in experimental studies [Eno02, BKLS03, BSLB07], while the position of maximum heat release or maximum fuel consumption rate is commonly used for numerical studies [DCVP03].

The quenching distance generally is a complicated function:

$$\delta_q = f(\text{fuel}, \text{oxidizer}, \text{wall material}, \Phi, T_1, p_1, T_w, \mathbf{u_w}) \,, \tag{2.44}$$

where $\mathbf{u_w}$ is the velocity field in vicinity to the wall. A broad consensus exists in the literature that quenching distances of laminar flames are proportional to the laminar flame thickness δ_f. The proportionality constant is called the *quenching Peclet number*:

$$\mathrm{Pe_q} = \frac{\delta_q}{\delta_f} \,. \tag{2.45}$$

However, $\mathrm{Pe_q}$ is not independent of the influential variables listed in Eq. (2.44), either. Experimental and numerical studies have revealed influences of wall material and quenching configuration (head-on and sidewall in [BKLS03]), fuel-oxidizer mixture (sidewall, parallel plates and head-on in [AH81, Eno02,

DM02, GSHC10]) and the presence of flow velocity in a duct (parallel plates in [DM02]). Contradictory results exist for the influence of equivalence ratio. While several authors observed noticeable influence of Φ on Pe_q (parallel plates for propane-air in [AH81]; parallel plates for several fuels in [DM02]; head-on for CH_4-air in [Eno01]), others (general analysis in [BL77]; sidewall quenching for CH_4-air in [Eno02]) conclude that $Pe_q \neq f(\Phi)$ within the range of their data scatter. The influence of pressure was analyzed by Aly and Hernance [AH81] who calculated vanishing variation of Pe_q for subatmospheric pressures, whereas Enomoto [Eno01] observed a slight increase of Pe_q with increasing pressure in the subatmospheric regime. Regarding the influence of preheat temperature on Pe_q, no statements could be found in the analyzed literature.

The situation of sidewall quenching is similar to the flame position during wall flashback. Thus for later reference, the results of Enomoto [Eno02] shall be given here, who investigated sidewall quenching of CH_4-air flames between $\Phi = 0.8$ to 1.0 as well as H_2-air flames for $\Phi = 0.6$. For comparison, the absolute quenching distances between parallel plates given by Turns [Tur00] have been converted to Pe_q numbers. For both sources, Eq. (2.22) was used for the flame thickness. The results are summarized in Table 2.1 together with literature values for head-on quenching. The Peclet numbers of parallel plate quenching

Table 2.1: Quenching Peclet numbers in sidewall and parallel plate configurations for atmospheric mixtures.

Fuel-oxidizer	*Configuration*	Φ [-]	Pe_q [-]	Source
CH_4-air	Sidewall	0.8...1	3.4	[Eno02]
H_2-air	Sidewall	0.6	3.8	[Eno02]
CH_4-air	Parallel plates	1	20.7	[Tur00]
H_2-air	Parallel plates	1	15.9	[Tur00]
CH_4-air	Head-on	1	≈ 3	[BSLB07]
H_2-air	Head-on	1.5	1.4	[GSHC10]
H_2-O_2	Head-on	1	1.7	[DCVP03]

are much larger compared to sidewall and head-on quenching. The head-on quenching cases suggest a dependence on fuel-oxidizer mixture. However, the H_2-air and H_2-O_2 simulations [GSHC10, DCVP03] had a preheated mixture and wall at 750 K which could contribute to the deviations.

The understanding of quenching processes at a cold wall in turbulent flames has gained a lot in the past years from DNS of such flows. Bruneaux et al. [BAPF96] simulated three-dimensional channel flow at $Re_\tau = 180$ with one-step chemistry. The flame propagated normal to the main flow direction towards the wall, starting from the center region of the channel. In such a configuration, coherent turbulent structures locally push the flame surface towards the wall, such that the maximum wall heat flux rises compared to a laminar head-on quenching case. The minimum wall distance observed for turbulent flamelets was about 60% of the laminar value for the head-on quenching situation. Alshaalan and Rutland [AR02] computed a V-shape flame in a Couette flow. The flame was anchored at about 1/3 channel height by fixing a small portion of grid cells to the adiabatic flame temperature, such that the lower branch of the flame steadily hit the lower wall during simulation. They compared the maximum wall heat flux of the turbulent flame with a flame at laminar conditions in the same geometry. While the mean ratio was about 1.1 to 1.2, the maximum was slightly below 1.4. The timewise distribution of the observed peaks in heat flux was explained by different coherent motions in the approaching boundary layer. Assuming that the maximum heat flux is inversely proportional to the quenching distance of the flame, typical turbulent values are within 80% to 90% of the laminar values. Interestingly, the time-mean heat flux was lower in the turbulent case. Recently, Gruber et al. [GSHC10] published results from a three-dimensional DNS of a V-flame in H_2-air channel flow at $Re_\tau = 180$ with detailed H_2-O_2 chemistry [Gru06]. Downstream of the flame holder, which was located on the centerline of the domain, the flame touched the upper and lower channel wall. These regions were analyzed in terms of flame-wall interaction. The maximum of the time-averaged heat flux to the wall was 1.14 times the maximum value during laminar head-on quenching, which compares well to the mean value approximated from [AR02] (1.1 to 1.2, see above). It was pointed out by the authors that as the flame loses heat to the wall, its thickness increases due to an in-

crease in chemical timescale, while the turbulent timescale of the fresh gases becomes smaller with decreasing wall distance, both of which can cause a change of the turbulent combustion regime close to the wall (see Fig. 2.11).

Since a detailed chemistry model was used by Gruber et al., they were able to analyze the detailed evolution of radical concentration and heat release during flame-wall interaction. In the event that a flame was pushed towards the wall by turbulent coherent structures, a process which is similar to head-on quenching, they observed a strong increase in heat release right at the wall by about one order of magnitude. Indeed, a similar pattern was observed during head-on quenching of a laminar H_2-air flame reported in the same publication [GSHC10]. The physical origin of this local maximum in heat release rate was shown to be an exothermic radical recombination process. The time Δt_q during which this exothermic recombination takes place shall be calculated here to compare it to the timescale of turbulent wall flashback later on. The time evolution of the quenching process shown in [GSHC10] allows an estimation of $\Delta t_q \approx 40\,\mu$s. The timescale of the investigated laminar flame ($\Phi = 1.5$, $T_1 = 750\,$K, $p_1 = 1\,$atm) equals

$$\Delta t_f = \frac{\delta_f}{S_L} = 2.9\,\mu\text{s} \tag{2.46}$$

as obtained from a Cantera simulation and Eq. (2.22), such that

$$\frac{\Delta t_q}{\Delta t_f} \approx 14\,. \tag{2.47}$$

Finally, the influence of non-inert walls on the quenching process shall be discussed. Popp and Baum [PB97] simulated laminar head-on quenching of stoichiometric CH_4-air flames with detailed chemistry and an inert wall. Up to a wall temperature of 400 K, inert simulations match experiments well because of the very low radical concentration right at the wall. Between 400 K-600 K, the radical concentration strongly increases, such that not only radical destruction by the wall, but also surface reactions in the form of adsorption of radicals and desorption of recombined stable molecules may become important. The authors reasoned that this fact could be responsible for large discrepancies between their inert simulations and experiments at high wall temperatures, however, this estimation was not further elaborated. Andrae and

Björnbom [AB00] simulated lean H_2-air flames ($\Phi = 0.1$ and $\Phi = 0.5$) with detailed chemistry burning inside an axisymmetric boundary layer. They considered completely inert walls, walls that act as recombination partner as well as catalytic platinum walls at temperatures 400 K and 600 K. The gas mixture had a temperature of 975 K. Change from an inert wall to radical-recombining wall at 600 K and $\Phi = 0.5$ caused a decrease in H-radicals right at the wall, however, the overall structure of the reaction zone regarding H and H_2 distribution did not change appreciably. A direct study of the effect of wall reactions on flashback limits at atmospheric conditions was conducted by Lewis and von Elbe [LE43]. They covered Pyrex tubes with salts like sodium tungstate and potassium chloride or with silver, which are known to strongly influence reactions in heated vessels. However, the same flashback limits were observed in experiments. It can be concluded that at the maximum preheat temperature of $T_w \approx 673$ K considered in the present work, variations in the wall material and the associated surface reactions probably play a negligible role for the quenching process during wall flashback.

2.5 Transfer to Wall Flashback Process

The basic theory of premixed flame propagation in proximity to walls that has been provided above allows further perspective relative to the questions about the wall flashback process raised at the end of Sec. 1.2:

- The existence of coherent flow structures in a turbulent boundary layer may influence or control the detailed propagation path of the flame.
- In connection with the first item, the influence of global adverse pressure gradients on turbulent wall flashback may be manifested in the different time-resolved turbulence structure close to the wall as compared to straight channel flow.
- The difficulty of determining the true wall distance of the flame during wall flashback has been underlined by a large number of influential factors, which include the flame backpressure, stretch and implicated Lewis number effects, flame-turbulence interaction and the dependence

of quenching Peclet numbers on flame-wall configuration, temperature boundary conditions and mixture properties.

- Since the turbulence structure close to the wall in channel and tube flow is very similar, flashback limits should not depend appreciably on the duct cross-section.
- If the flame backpressure has a decisive influence on the onset of flashback, then a difference should exist between unconfined and confined flame holding prior to flashback because the pressure boundary condition at the flame base is different.

On the one hand, these considerations imply that the flow structure close to the wall must be known in high spatial and temporal detail for a given experiment in order to draw useful conclusions from the measurements. On the other hand, the simultaneous observation of flame position and flow field close to the wall is essential. Both aspects are accounted for in the design of the experimental rig and the choice of measurement techniques which will be presented in the following chapter.

3 Experimental Setup

The experimental rig has been designed to address the open questions regarding the wall flashback process as outlined in Sec. 1.2 and 2.5. Table 3.1 gives an overview of the requirements for the setup needed to address these questions and the resulting features that have been implemented. The detailed design of the combustion chamber and the experimental infrastructure will be described in the following section. The measurement systems used for the qualitative and quantitative description of flow and reaction are introduced subsequently in terms of basic principles and actual implementation in the rig. Finally, the aerodynamic design of the combustion chamber is validated based on experimental and numerical results in order to provide a solid base for the analysis of observed flashback modes.

3.1 Experimental Rig and Infrastructure

An overview of the experimental rig is shown in Fig. 3.1. Its main components can be divided into a mixture and flow conditioning section, the measurement section and the exhaust system.

3.1.1 Mixture and Flow Conditioning

The rig has been designed for fully premixed operation with arbitrary mixtures of two fuels, CH_4[1] and H_2, at lean to stoichiometric mixture fractions. The layout of the mixture and flow preparation section serves three objectives, namely large- and fine-scale mixing of fuel and oxidizer, the establishment of a uniform and steady flow at combustion chamber inlet and safety in the case of

[1] Natural gas with a mean CH_4 content of 97.63 % vol. was used as substitute.

Table 3.1: Performance specifications for the experimental rig.

Criterion	*Target*	*Reason / Comment*
Mixture preparation		
Components	CH_4, H_2, air	Influence of fuel properties, possibility to observe laminar and turbulent flashback.
Equivalence ratio	$0 \leq \Phi \leq 1$	Lean premixed gas turbine combustion as technology standard.
Mixing process	Fully premixed	Comparability with premixed flame theory.
Inlet conditions		
Reynolds number	$\mathcal{O}(10^3)$ up to $\mathcal{O}(10^5)$	Laminar and turbulent flow.
Mixture temperature	up to 400° C	Conditions in gas turbine combustors.
Static pressure	atmospheric	Compromise to reduce rig complexity and cost.
Measurement section		
Cross section	rectangular	Optical measurements in the near-wall region. Distinction from literature.
Flame holding	confined	Distinction from literature.
Optical access	three sides	Simultaneous optical measurements in two planes.
Channel aspect ratio	high	Exclusion of sidewall influence, 2D time-mean boundary layer.
Global pressure gradient	zero or adverse	Channel and diffuser geometries.
Wall temperature	controllable	High impact on flashback propensity.

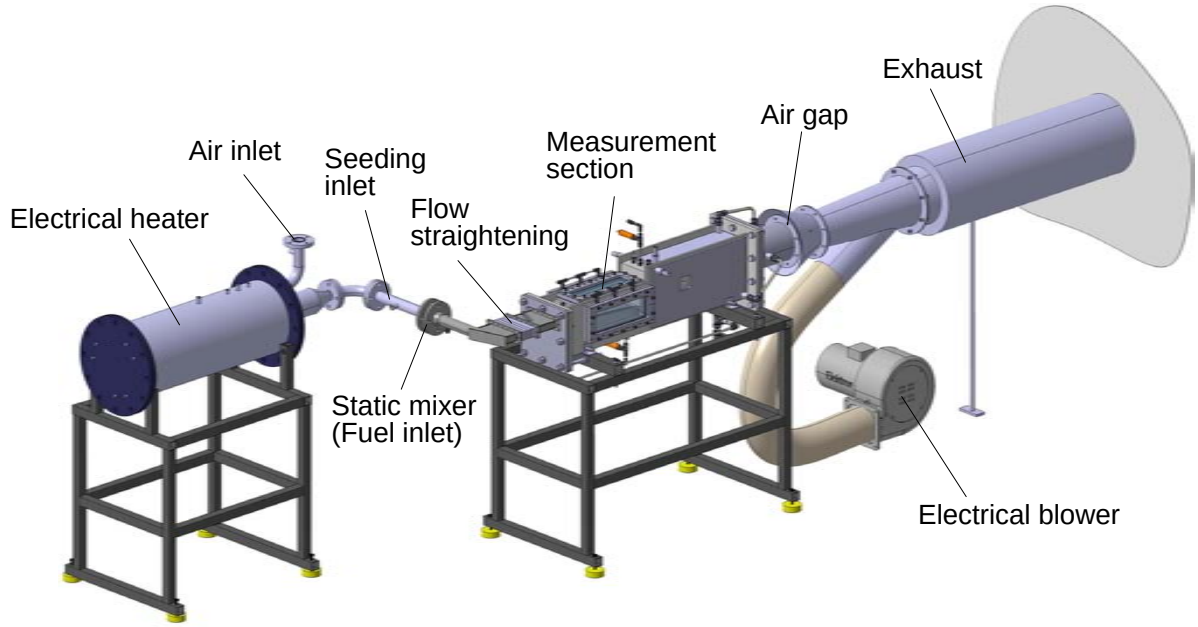

Figure 3.1: Overview of the experimental rig.

flashback. The latter becomes especially important for H_2-air mixtures, where duct lengths of approximately one meter can be sufficient for Deflagration-Detonation Transition (DDT) to occur at atmospheric conditions [CD08].

Pressurized air delivered at a total pressure of 12 bar and room temperature is used as oxidant. The fuel supply delivers CH_4 and H_2 at room temperature and a pressure of 9 bar. Upstream of the rig, the air flow is filtered to separate residual oil droplets from the compressor facility. The air enters the rig through an electrical heater with adjustable power input up to 65 kW, which has a DN40 flange at the outlet. After a 90° bend, a straight tube is attached which has a radial inlet for seeding injection at its center. Downstream of the tube, a static flow mixer (Sulzer Chemtech CompaX DN40) is located between two flanges. The fuel mixture is injected radially through a single dosing point. Owing to the avoidance of DDT in the premixed duct portion, the transition from the DN40 tubing to the rectangular, high aspect-ratio inlet port of the measurement section has to be as short as possible. Furthermore, recirculation zones have to be strictly avoided to prevent accidental flame holding. Two design ideas have been assessed, a classical diffuser with several grids or guiding plates in order to anticipate separation and an elbow configura-

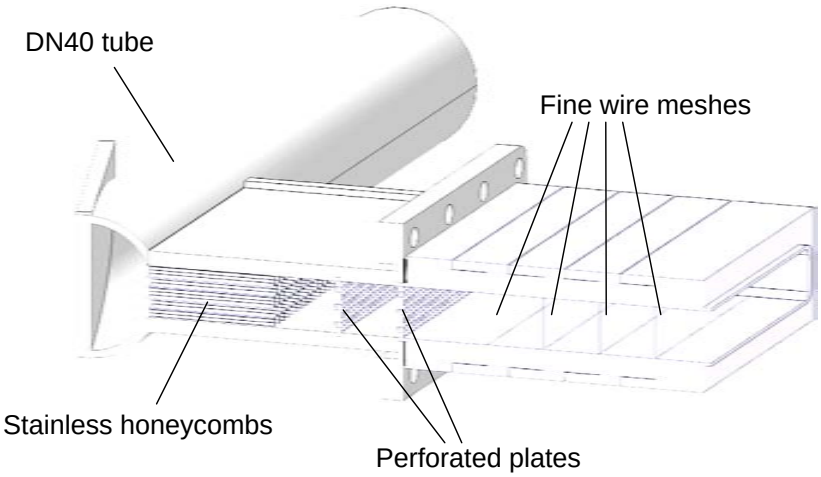

Figure 3.2: Elbow duct and flow straightening section.

tion, where the rectangular duct is tangentially flanged on the tube wall. In terms of overall length and manufacturing complexity, the elbow duct design is preferable at the cost of higher pressure losses necessary for flow straightening downstream of the device. Since the combustion chamber is working at atmospheric conditions, total pressure as provided from the mixture supply is not a limiting factor and consequently the elbow duct design was chosen. Details of the elbow configuration and the subsequent flow straightening section are shown in Fig. 3.2. In order to prevent the flow from stagnating in the elbow corner and to adjust the pressure distribution at the channel inlet, the tube is cut at an angle of 75° with respect to the vertical axis and a flat plate is welded onto the angled plane. Stainless steel honeycombs are placed as vortex suppressors just after the bend. Two perforated plates with different solidities follow the honeycomb section in order to even the velocity distribution. After a short settling distance, four fine wire meshes are clamped between brass supports. The mesh solidities and wire diameters have been chosen according to [MB79].

Downstream of the last wire mesh, a rectangular duct of 150 mm length is attached to allow for initial boundary layer development upstream of the inlet of the measurement section.

3.1.2 Measurement Section an Combustion Chamber

A rectangular duct with a vertical sudden cross section increase and a constant width of 157 mm forms the basic geometry of measurement section and combustion chamber, which has been welded from stainless steel plates of 10 mm thickness. Figures 3.3 show an overview of the setup. Figure 3.3a provides details about relevant physical dimensions of the duct. Areas with coarse contours denote ceramic or metallic components mounted into the duct as described below. The measurement section is the location where wall flashback is observed during the experiment. The purpose of the internally cooled combustion chamber is a safe burnout of the premixed gases. Figure 3.3b shows a picture of the laboratory setup.

A cross-section of the measurement section is depicted in Fig. 3.4, with all dimensions given in mm. It has a modular structure such that zero pressure gradient as well as adverse pressure gradient flows can be realized by inserting different stainless steel ramps with inclination angles of $\phi = 0°$, $2°$ or $4°$ and a constant width of 143 mm. The ramps have been welded from plates of 5 mm thickness and subsequently machined to end dimensions. The premixed gases enter the rectangular flow section from the right-hand side of the figure through an inlet height of $2h = 17.5$ mm and width of $w = 157$ mm. Due to this large aspect ratio, a quasi two-dimensional flow section exists in the center region of the ramp which allows the observation of wall flashback under well-defined conditions. The roughness height of the machined ramp surfaces is less than 50 μm, which results in a hydraulically smooth wall for all flow situations considered in this work. The ramps are fixed on a support block of 157 mm width, which is mounted on the lower wall of the chamber. The gaps of 7 mm between the side walls of the ramp and the duct walls are filled with ceramic inserts (see Fig. 3.6). The material used for these inserts and all other ceramic parts is a compound of Al_2O_3, SiO_2 and ZrO_2. The upper wall of the ramp is cooled by three air jets impinging on the wall from below inside the cavity between ramp and support block at its downstream end, which is located next to the flame anchoring position. The coolant convects in the upstream direction inside the ramp and leaves the cavity through a bore hole at the upstream end of the ramp. A flush mounted ceramic tile follows the ramp.

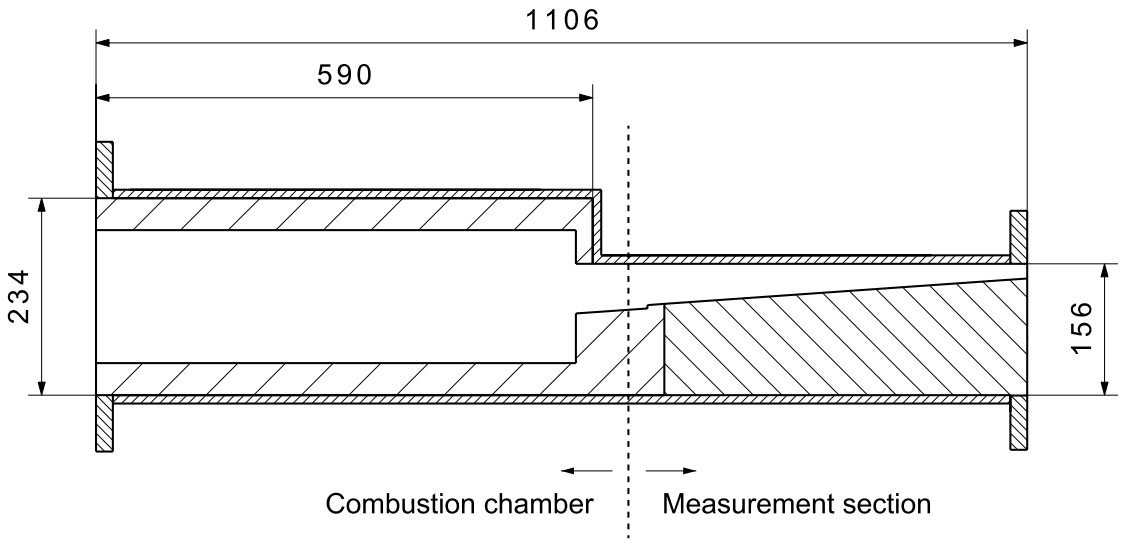

(a) Basic geometry of measurement section and combustion chamber.

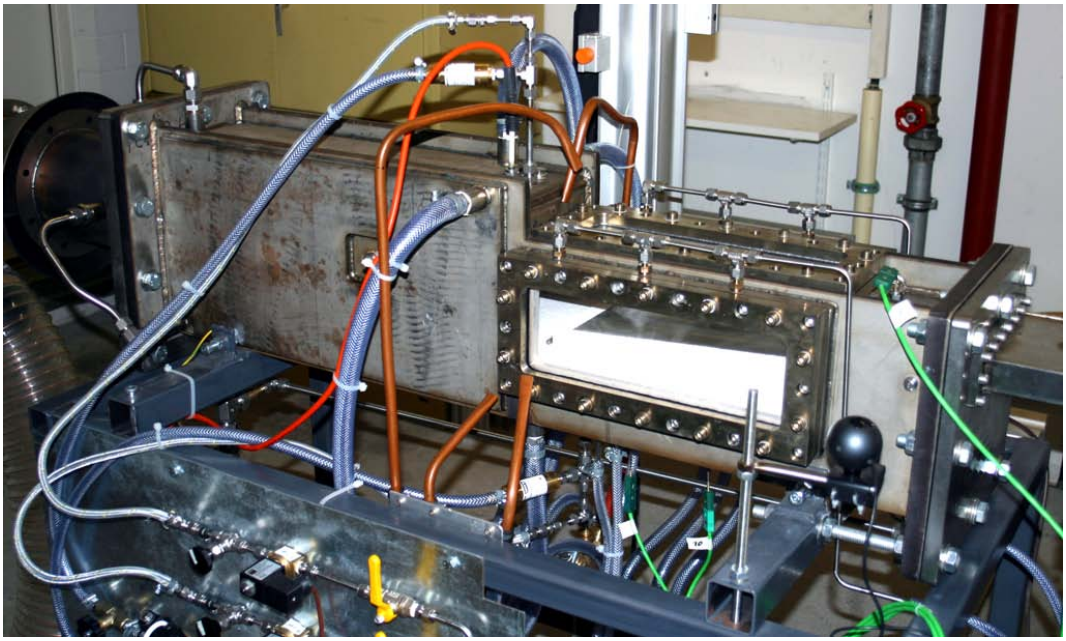

(b) Picture of the laboratory setup.

Figure 3.3: Overview of measurement section and combustion chamber.

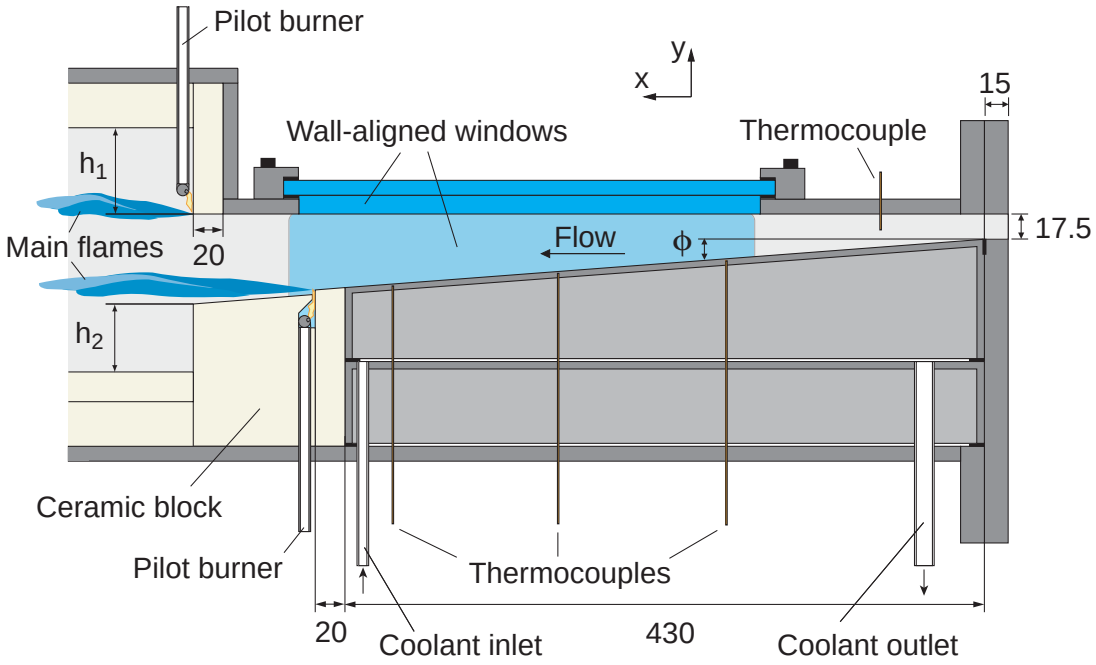

Figure 3.4: Sketch of the measurement section.

The tile ensures thermal insulation during stable operation and also serves as a thermal flame holder for some operating points.

Optical access to the diffuser section is provided by three silica windows along the y- and z-direction. The window surfaces in contact with the flow are aligned with the inner duct walls. As a result, there are no lateral or vertical steps at any point of the measurement section prone to accidental flame stabilization which could lead to misinterpretation of such upstream flame motion as wall flashback. Window alignment is achieved by bonding two windows together as illustrated in Fig. 3.5. The outer face of the window assembly is formed by a silica window of 10 mm thickness, which is clamped between two stiff metal frames with interjacent graphite seals. On the inner side of this window, a heat-resistant adhesive is deposited in a narrow seam of about 5 mm width inside the circumference of the clamp frame. A second silica window of 31 mm thickness is positioned on the adhesive seam.

During start-up of a flashback experiment, the combustible mixture is continuously ignited by two pilot burners at the end of the ramp section such that two main flames are formed which extend into the combustion chamber, as

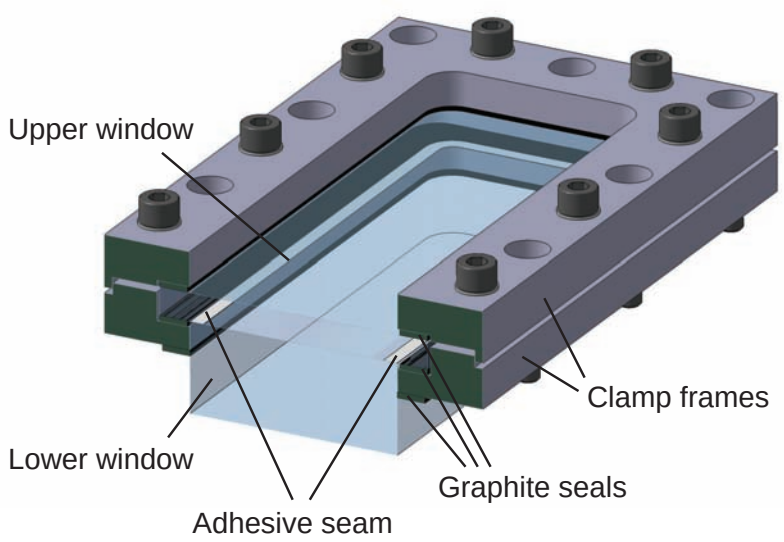

Figure 3.5: Bonding configuration of wall-aligned windows.

indicated on the left-hand side in Fig. 3.4. The step heights h_1 and h_2 depend on the ramp angle and are listed in Table 3.2. The lower pilot burner is em-

Table 3.2: Step heights at combustion chamber inlet.

Ramp angle [°]	h_1 *[mm]*	h_2 *[mm]*
0	58	75
2	58	56
4	58	67

bedded by the trapezoidal part of a ceramic block, which forms a gap together with the opposite ceramic tile. The surface of the ceramic block is also inclined toward the horizontal by ϕ, but is offset below the ramp plane by about 4 mm.

The lower pilot burner has its position still inside the section expanding by ϕ for two reasons: On the one hand, the influence of the shear layer and the recirculation zone behind the trailing edge of the ceramic block on the anchor of the lower main flame is minimized. On the other hand, the flow displacement by the lower main flame causes a contraction of streamlines above it such that the upper wall boundary layer is accelerated. When flashback conditions are

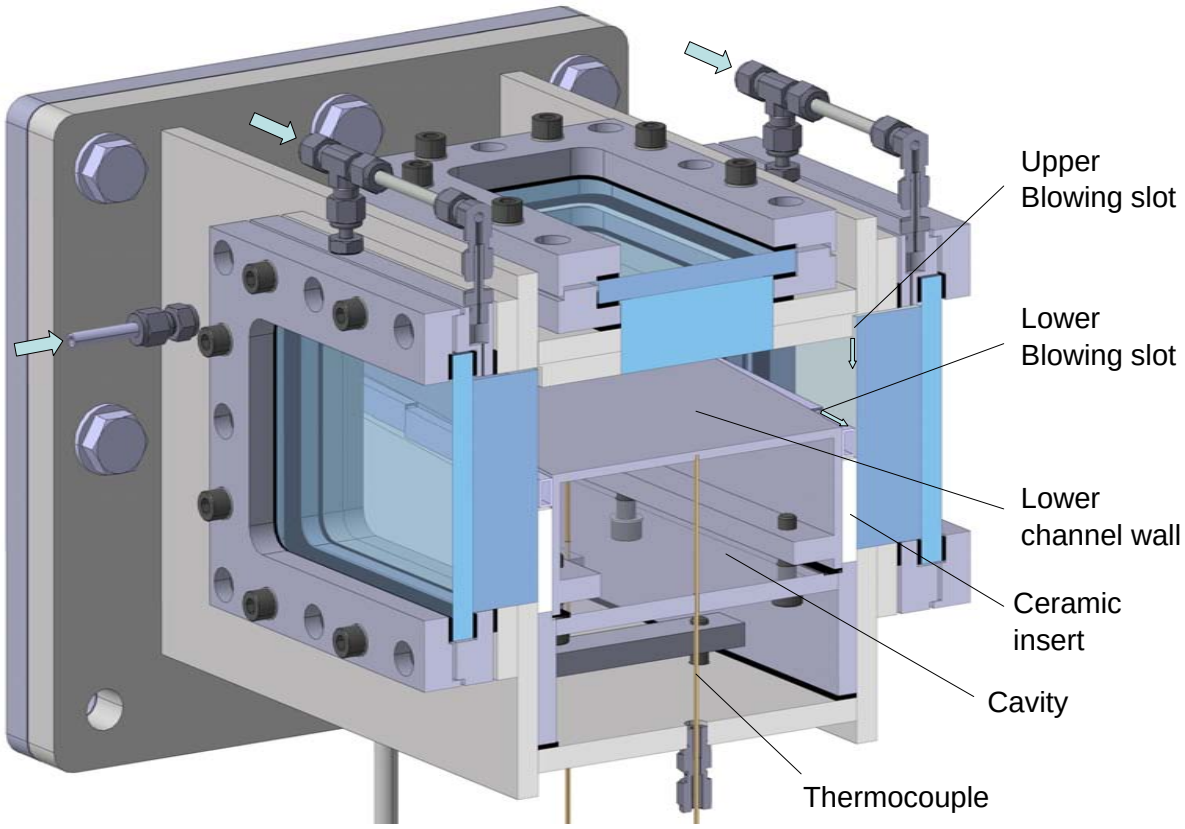

Figure 3.6: Cross-section of the measurement section.

approached, this configuration results in a self-stabilizing system where the flame flashes back only on the lower wall of the ramp, which is the target location for flashback.

It is well known that boundary layer development in rectangular channels induces a region of reduced velocity gradients at the edges of the duct due to the simultaneous influence of two walls. Therefore, flashback is likely to occur only along the corners in this type of geometry and indeed, the present experiment shows this behavior as expected. However, flashback should only take place in the center region of the ramp as otherwise the assumption of a quasi two-dimensional flow would not be feasible anymore. In order to avoid corner flashback, pure air is locally injected into the corner boundary layers in two different ways. Figure 3.6 shows a cross-section through the measurement section in full detail. In each of the upper corners of the flow channel, the air enters through a slot of 2 mm width perpendicular to the main flow direction.

The duct is formed between the inner face of the side window and the upper wall plate of the duct, thus it only extends along the window region, which does not cover the beginning of the measurement section (see Fig. 3.4). In each of the lower corners, air is injected aligned with the main flow by means of five slots (4 mm x 1 mm) in a stepped arrangement. The axial distance between two slots is 80 mm and the last slot is aligned with the downstream end of the ramp. During experiments, the amount of blowing air was adjusted by volume flow meters such that the sum fed to all slots did not exceed 2% to 3% of the main air massflow.

3.1.3 Exhaust System

Downstream of the outlet of the combustion chamber, a tube of 160 mm diameter and 264 mm length is attached such that the center axis of the tube is approximately tangential to the lower wall of the inlet at the beginning of the measurement section. Downstream of the tube, an open air gap is formed by a flange attached to the tube and a conical nozzle overlapping with the tube (see Figs. 3.1 and 3.3b). This gap decouples the exhaust duct acoustics from the combustion chamber, which otherwise exhibited a strong thermoacoustic instability in the low-frequency range for medium to high mixture velocities. Downstream of the air gap, the flue gases are mixed with ambient air provided by an electrical blower located inside the laboratory and are subsequently blown into the atmosphere.

3.1.4 Instrumentation

The experimental rig is operated via a Labview control interface, using a NI PCI-6229 data acquisition card in conjunction with NI SCB-68 connector blocks for I/O purposes.

Massflow Controllers for Main Combustion Gases

Prior to entering the experimental rig, the massflows of the main mixture components are controlled by three separate Bronkhorst digital thermal massflow

controllers (F-206BI-RAD-99-V for pressurized air, F-206AI-RAD-44-V for H_2 and F-203AV-1M0-RAD-44-V for CH_4) which are preceded by in-line filters with 1 μm separation size. Measurement accuracies are given by the manufacturer as ±0.8% of the actual massflow rate plus ±0.2% of the maximum massflow rate of the respective controller for both, air and H_2 devices and ±0.5% of the actual massflow rate plus ±0.1% of the maximum massflow rate for the CH_4 controller. The massflow controller setup and the control interface have been validated experimentally by exhaust gas composition measurements.

Temperature Measurement

Thermocouples of type K are used as temperature sensors at various positions inside the rig. The mixture temperature at the inlet of the measurement section is monitored by a single thermocouple at the center of the duct cross-section as shown in Fig. 3.4. The same thermocouple acts as a flame detector during flashback, and the fuel supply is shut down on reaching a preset temperature increase. The surface temperature of the upper wall of the ramp is monitored at three axial locations at the lateral center. The positions are at distances of 35 mm, 135 mm and 235 mm measured from the downstream end of the ramp in upstream direction. The thermocouples are inserted into blind holes inside of the block filled with heat-conductive paste (see Fig. 3.4 and 3.6). The remaining wall thickness above the thermocouple tip is approximately 0.5 mm, which results in a rather quick thermal response and low temperature drop between wall and sensor. Cold junction compensation of the thermocouple measurements is provided by the NI SCB-68 connector block by an internal thermistor element which has a nominal accuracy of ±0.3 K.

3.2 Measurement Techniques

The basic principles of the measurement systems utilized to investigate the wall flashback process as well as their actual implementation into the experimental rig will be described in this section.

3.2.1 Chemiluminescence

The observation of the flame position is an essential part for any flashback experiment. A convenient way to detect the flame surface experimentally is the observation of light emitted from the flame. In general, two intrinsic sources of light can be distinguished:

- **Thermal radiation**: The gas mixture emits light in spectral bands due to thermal excitation of the constituent species and subsequent transition to a state of lower internal energy, the difference being the energy of the emitted photons. Generally every species is generating thermal radiation, and the spectral content of the emitted light as well as the integral radiation intensity is depending on species and temperature.
- **Chemiluminescence**: Light is emitted by molecules which are directly formed in an excited state by a chemical reaction, for example a combination of two atoms, and subsequently undergo transition to a state of lower internal energy. The basic question whether a chemically excited molecule produces chemiluminescence as well as the spectral band depend on its electron configuration. The integral radiation intensity is dependent on the rate of formation of the excited molecule.

For combustion of hydrogen or hydrocarbons in air, thermal radiation is usually confined to the infrared part of the spectrum, where other sources of thermal radiation, for example hot casing parts, are also contributing. In contrast, chemiluminescence of such flames is observed in the visible and near-UV range. In H_2-air flames, the OH radical produces chemiluminescence bands with an intensity peak at 306.4 nm and slightly weaker bands starting from 281.1 nm, 287.5 nm and 294.5 nm during the transition of its excited state OH^* to its ground state. A summary of the underlying elementary reactions can be found in [KFB+10]. In CH_4-air flames, chemiluminescence is mainly produced by OH^*, CH^* (431.5 nm), C_2^* (473.7 nm, 516.5 nm and 563.6 nm) and CO_2^* (complex structure from 300 nm to beyond 500 nm superimposed on a continuum) [Gay74]. A summary of the underlying elementary reactions can be found in [NPMW98].

For the experiments conducted in this work, the chemiluminescence is used as a binary marker to determine the position of the leading part of the flame. In order to obtain a high signal-to-noise ratio, optical filters are used to confine the recorded signal mainly to the OH^* radiation since other appreciable UV sources are not present in the experimental environment. Table 3.3 lists the filters used during the experiments.

Table 3.3: Optical filters for OH^* chemiluminescence measurements.

Name	Center wavelength [nm]	Full width at half maximum [nm]
BrightLine HC 320/40	320	40
L.O.T-Oriel 302FS10	313	12
Schott DUG 11	340	70

Two cameras are used for chemiluminescence recording. For flame monitoring and recordings at low repetition rate, a Hamamatsu C4336-02 intensified camera with a resolution of 720x576 pixel and a fixed frame rate of 30 Hz is used. For high-speed measurements, a Photron Ultima Fastcam APX I^2 intensified camera with a resolution of 1024x1024 pixel up to 2 kHz repetition rate is applied.

3.2.2 Constant Temperature Anemometry

Constant Temperature Anemometry (CTA) will be used in this work to measure axial velocities at the inlet of the measurement section. The measurement principle is based on the relation of the forced convective heat transfer from a hot wire immersed in a cold crossflow with the local flow velocity. The wire is heated by an electrical current such that the electrical resistance of the wire, which is a function of its temperature, stays constant. The current through the wire is adjusted by a control circuit, which usually includes a Wheatstone bridge that incorporates the hot wire in one leg and an amplifier to adjust the bridge current such that the bridge is always balanced. The

flow velocity perpendicular to the wire can be determined from an empirical correlation between bridge voltage and flow velocity, which involve constants that have to be calibrated individually for each probe for a given fluid state. By using suitable amplifiers, cut-off frequencies of the CTA probe response to velocity fluctuations in the order of 100 kHz can be achieved [Bru95]. Since heat loss from the wire is dependent on the temperature difference between wire and fluid, the fluid temperature must be kept constant and the wire should be overheated as high as the material allows in order to obtain precise measurements. Wire materials with high temperature coefficients of resistivity as well as good high-temperature strength, such as platinum or tungsten, are chosen to optimize the signal-to-noise ratio and sensitivity of the sensor. Wire diameters are commonly in the order of 1 μm for several reasons:

- High length/diameter ratio, which reduces heat loss to the wire mounts.
- High spatial resolution of flow structures moving perpendicular to the wire.
- Low Reynolds numbers with respect to the wire diameter to avoid eddy shedding from the wire, which can distort time-resolved measurements.

Compared to other high-frequency velocity measurement techniques, one-component CTA probes are of rather low complexity in terms of costs and implementation, have a high spatial resolution and do not require optical access. As drawbacks, CTA probes need individual calibration, are prone to flow misalignment, can cause considerable flow disturbance depending on the support geometry and are easily damaged or deteriorated during experiments. In the present work, CTA probes have been used to measure mean flow velocities only. For this reason, details about the frequency response of CTA probes will not be discussed at this point and can be found in [Bru95], for example.

Rig Implementation

A Teltron ASM-1 anemometer was used for all measurements. The CTA probes were custom-made using platinum-plated tungsten wire. Two pointed stainless steel rods of 0.6 mm diameter form the prongs for the wire. Details of the

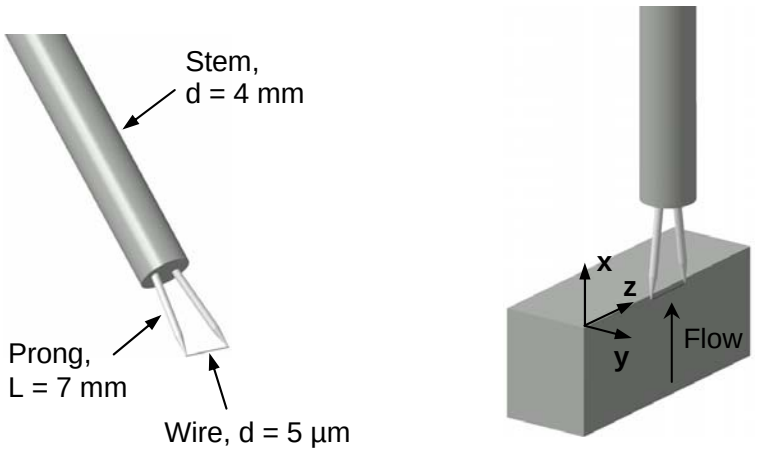

(a) CTA probe dimensions.

(b) Probe alignment at duct exit.

Figure 3.7: CTA probe arrangement.

CTA probe arrangement are illustrated in Figs. 3.7. In Fig. 3.7a, the CTA probe along with its main dimensions is shown. The orientation of the probe during measurements is shown in Fig. 3.7b. The probe is located at the outlet of the rectangular duct attached to the flow straightening section, which was detached from the inlet flange of the measurement section and thus blowing into free air during the measurements. The wire is always aligned with the z-axis.

Boundary Layer Measurements

The accurate measurement of flow velocities in the laminar sublayer and the buffer region with CTA probes requires additional efforts. As Bruun [Bru95] points out, the wire has to be straight and always parallel to the smooth wall surface. The influence of aerodynamic interferences between probe support and the wall on the flow around the wire has to be minimized by using comparably long wires. The probe stem has to be separated from the near-wall region, either by inclining the wire prongs or the stem itself. Of high importance is the precise determination of the distance between wall and wire. Several elaborate methods exist in the literature, which include setups using a reference point at a known distance from the wall, the observation of the reflection of the wire on a polished wall, consideration of the heat loss of the wire to the wall for zero flow velocity or a fit to a point-of-origin line in the linear near-wall

region. In the context of the present work, the CTA technique has been used primarily to characterize the flow distribution across the inlet of the measurement section. In the boundary layer region, a simplified procedure has been adopted to determine the wall distance of the wire with reasonable accuracy. Starting from the duct exit plane, the wire of the CTA probe is inserted in negative x-direction into the channel by defined small distance adjusted by a micrometer gauge. Afterwards, the probe is moved towards the wall by a second micrometer gauge until the prong tips make electrical contact with the wall. From this point, the probe is moved back into positive y-direction until the resistance of the probe increases to its original value. This procedure allowed a positioning of the wire at a wall distance of approximately 0.2 mm with satisfying repeatability.

Calibration

The calibration of the CTA probe has been conducted at the center of the duct exit using the full range of the massflow controller. The simplifying assumption was made that the ratio of the center velocity to the massflow-averaged velocity is constant for each massflow. Since the duct velocity profile is not fully developed yet and thus boundary layers are thin, this approximation is feasible. The procedure has the advantage of in-situ calibration such that any blockage effects by the probe support are included.

3.2.3 Laser Doppler Anemometry

Laser Doppler Anemometry (LDA) is an optical technique to measure the velocity of particles convected by a fluid flow. It is commonly used to determine the velocity of the fluid flow indirectly by choosing particles with negligible slip velocity. In the present work, LDA will be used to characterize the mean and time-resolved aerodynamic conditions in the measurement section for non-reacting flow with high accuracy. The particles are illuminated by monochromatic laser light at a fixed position in space. To a receiver at rest, the frequency of the light scattered by the moving particles is shifted due to the Doppler effect as illustrated in Fig. 3.8. Since the particles are receiver and transmitter at the same time, a Doppler shift is taking place twice [ABDT03].

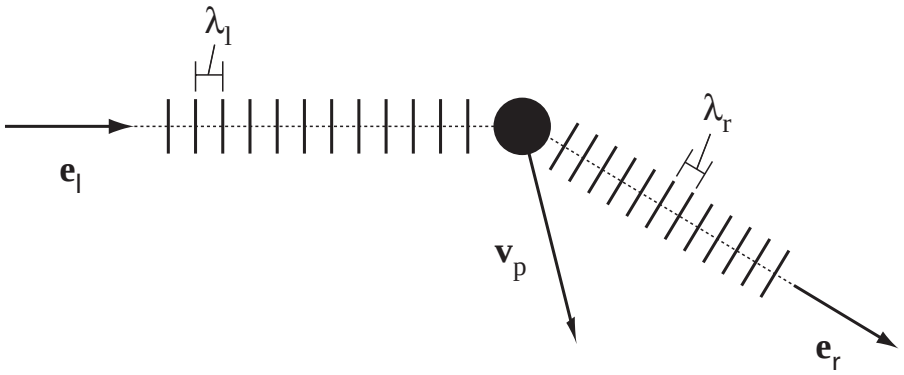

Figure 3.8: Doppler phase shift of light scattered by a moving particle.

The monochromatic, coherent laser light at wavelength λ_l emitted in direction $\boldsymbol{e_l}$ as seen from an observer moving with the particle at velocity $\boldsymbol{v}_p$ is shifted to

$$\lambda_p = \frac{\lambda_l}{1 - \dfrac{\boldsymbol{v}_p\,\boldsymbol{e}_l}{c}}\,. \tag{3.1}$$

In Eq. (3.1), c is the velocity of light. The receiver at rest, on the other and, receives light of wavelength

$$\lambda_r = \lambda_p\left(1 - \frac{\boldsymbol{v}_p\,\boldsymbol{e}_r}{c}\right). \tag{3.2}$$

Using $f = c/\lambda$, Eqs. (3.1) and (3.2) can be combined to

$$f_r = f_l\,\frac{1 - \dfrac{\boldsymbol{e}_l\,\boldsymbol{v}_p}{c}}{1 - \dfrac{\boldsymbol{e}_r\,\boldsymbol{v}_p}{c}} \approx f_l\left(1 - \frac{\boldsymbol{v}_p\,(\boldsymbol{e}_l - \boldsymbol{e}_r)}{c}\right). \tag{3.3}$$

The approximated term in Eq. (3.3) simply results from expanding the full term and assuming $|\boldsymbol{v}_p| \ll c$. It can be seen from the approximate term on the right that the resulting frequency difference between laser and receiver is extremely small compared to the frequency f_l of the laser light, and a direct derivation of the velocity would be very difficult. For this reason, a dual-beam configuration is used in many LDA systems, which involves two coplanar laser beams with different directions $\boldsymbol{e}_{l,1}$ and $\boldsymbol{e}_{l,2}$ crossing at one point in space. Then, according to Eq. 3.3, the scattered light seen by the receiver is a

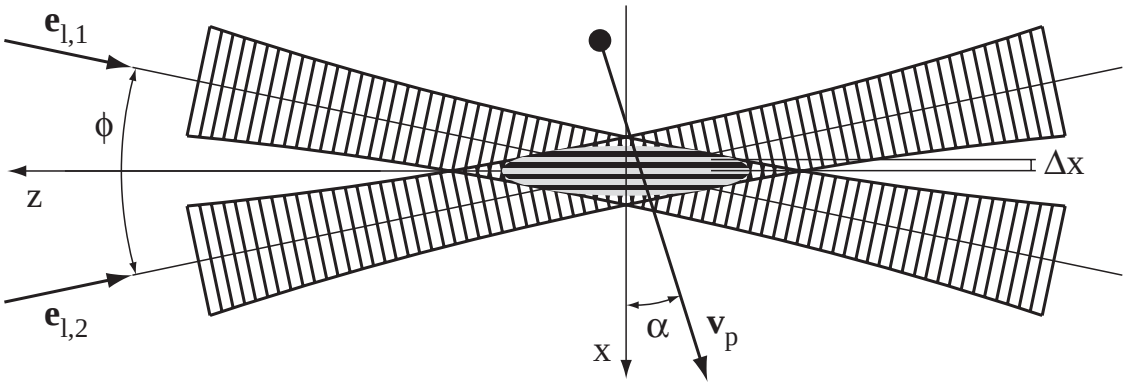

Figure 3.9: Interference fringes of a dual-beam LDA measurement volume.

superposition of two waves at different frequencies $f_{r,1}$ and $f_{r,2}$. Such a superposition results in a high-frequency wave modulated by a low beat frequency

$$f_{dual} = f_{r,2} - f_{r,1} = \frac{\boldsymbol{v}_p\,(\boldsymbol{e}_{l,1} - \boldsymbol{e}_{l,2})}{\lambda_l}\,. \tag{3.4}$$

It is interesting to note that the beat frequency f_{dual} is not depending on the receiver orientation $\boldsymbol{e}_r$ any more. Furthermore, Eq. (3.4) does not contain any unknown constants, meaning that LDA systems do not require calibration.

Besides the description based on wave theory, a second model based on the interference pattern of two planar waves provides a very accessible description of dual-beam LDA systems. Figure 3.9 shows the structure of the interference pattern in the measurement volume which is formed by the intersection of two focused laser beams and thus has a shape similar to a rotational ellipsoid. The laser beams are located in the x-z-plane and are intersecting at an angle ϕ. The resulting interference pattern has a periodic intensity distribution in x-direction with a wavelength of

$$\Delta x = \frac{\lambda_l}{2\sin(\phi/2)} \tag{3.5}$$

If a particle passes the measurement volume inclined by an angle α with respect to the x-direction, the scattered light intensity is modulated with the frequency

$$f_D = \frac{2\sin(\phi/2)}{\lambda_l}\,v_{p,x} \tag{3.6}$$

The frequency f_D in Eq. (3.6) is called the *Doppler frequency* since it is the result of the superposition of two Doppler shifted laser waves. The modulation depth of the scattered light intensity is maximized if the laser beams have equal intensity and polarization. It can be shown by evaluating Eq. (3.4) in the coordinate system of Fig. 3.9 that $f_{dual} = f_D$, hence both descriptions lead to the same equation for the determination of the particle velocity component $v_{p,x}$ perpendicular to the fringe pattern.

Generation of Tracer Particles

A cyclone seeding generator was used to disperse TiO_2 particles (ρ_p = 3800 kg/m^3, d_p = 0.20 μm based on number distribution [Wäs07]). Konle [Kon05] conducted Malvern measurements of the particle size distribution of a generator similar to the device used here, using identical seeding materials. A very good breakup of agglomerated particles is reported, with a number peak at about 0.35 μm and a cumulative number fraction of about 80% between $0-1\,\mu$m. The seeding generator is operated with pressurized air taken from a reservoir with adjustable pressure downstream of the massflow controller for main combustion air. The main air flow is seeded globally upstream of the static flow mixer and flow straightening section, as described in Sec. 3.1.1. By doing so, neither the overall equivalence ratio nor the fuel-air mixing process is influenced by the relative amount of air passing through the seeding generator.

Tracking Characteristics of Particles

The assumption of negligible slip velocity of particles used as flow velocity tracers has to be verified for flows involving strong velocity gradients. For steady boundary layer experiments, acceleration imposed by mean pressure gradients are low compared to turbulent fluctuations, such that the central question is whether particles follow the turbulent fluctuations to a satisfying degree.

Since turbulent flows involve a cascade of length and time scales, the particles are likely to follow only a certain low-frequency part of the involved eddies, whereas acceleration forces are too small to displace the particle sufficiently

for high-frequency fluctuations. Therefore, only a certain part of the turbulent spectrum will be represented by the particle motion. For the present work, the determination of turbulent spectra is not intended. Only one-point correlations along one coordinate, $\langle u_i' u_i' \rangle$, will be measured, which effectively are integral means over the whole spectrum. Since the spectrum will only be represented in part by the fluctuating particles, the measured mean turbulent fluctuations will not correspond exactly to the fluid motion. In order to obtain meaningful mean turbulent statistics, the mean turbulent kinetic energy of the particles should approximate the respective value of the flow to a high degree.

In order to estimate the mean turbulent kinetic energy of particles, Melling [Mel97] provided a solution for the general Basset-Boussinesq-Oseen (BBO) equation of particle acceleration [Mel97, ABDT03] for the assumption $\rho_p/\rho_{mix} \gg 1$. The solution involves a Fourier transform of the BBO equation and the derivation of an energy transfer function from the flow to the particles. Considering the energy spectrum of fully developed turbulent pipe flow, the ratio of mean kinetic energies of particle velocity fluctuations and fluid velocity fluctuations is calculated as

$$\frac{u_{p,rms}^2}{u_{rms}^2} = \left(1 + \frac{\omega_c \rho_p d_p^2}{18\mu}\right)^{-1} . \tag{3.7}$$

Besides material constants, Eq. (3.7) involves the particle diameter d_p and a characteristic frequency ω_c. For a consideration of the complete turbulent spectrum, ω_c has to be set equal to the smallest turbulent fluctuations contained in the flow. Since near-wall fluctuations in the x-y plane are strongly connected to longitudinal vortical microstructures, as described in Sec. 2.1.4, the timescale of these structures will be used here for an estimation of ω_c. Following Orlandi and Jiminez [OJ94], who cited a DNS [Spa88] of turbulent boundary layers up to $\mathrm{Re}_\tau = 650$, the mean circulation of streamwise vortices is around

$$\Gamma^+ = \frac{\Gamma}{\nu} \approx 200 . \tag{3.8}$$

For an infinite, straight, forced vortex tube of radius r located in an otherwise irrotational flow, $\Gamma = 2\pi r^2 \omega$ [GTG04], where ω designates the angular

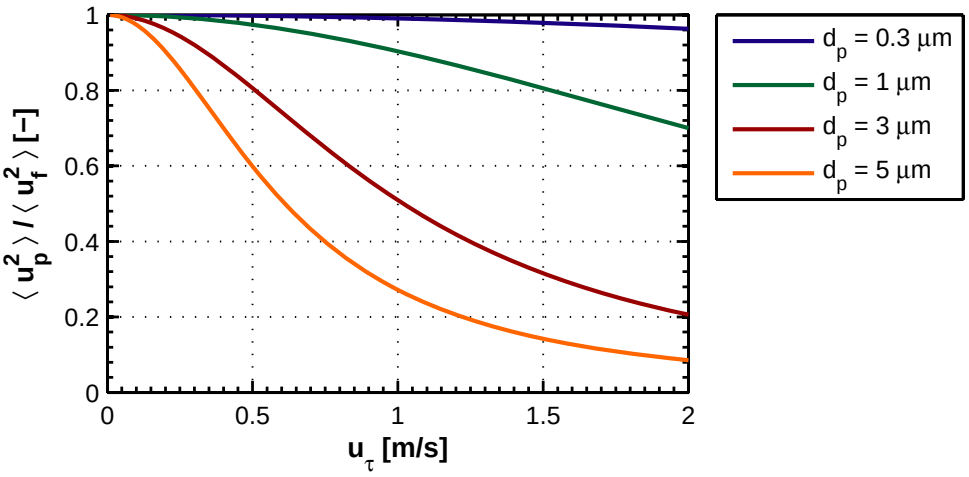

Figure 3.10: Energy transfer between flow and tracer particles inside the boundary layer.

frequency of rotation of streamwise vortices. Finally, by assuming $r^+ \approx 15$ for streamwise vortices, ω can be calculated for given shear stress velocity and kinematic viscosity of the flow.

The result of Eqs. (3.7) and (3.8) is shown in Fig. 3.10, which plots the energy transfer ratio between tracer particles and flow as a function of u_τ with the particle diameter as parameter. The tracer density has been set to 3800 kg/m^3, which corresponds to the TiO_2 particles used in the experiments, and fluid properties correspond to air at 20 °C. This graph will be referred to later in order to estimate the validity of experimental mean turbulent fluctuations.

System Components and Measurement Positions

An overview of the forward-scattering LDA setup in the experimental rig is illustrated in Fig. 3.11. A commercial Dantec LDA system is used which receives light from a Spectra-Physics 2020 Argon-Ion-laser operated at a power output between 1 – 3 W in TEM_{00} mode. The laser beam is separated into its main components at 476.5 nm, 488 nm and 514.5 nm inside the transmitter box (Dantec 60X41), only the last of which is used for the present experiments. Each component is again split into two beams, one of which is frequency-shifted by 40 MHz for negative velocity detection using a Bragg cell inside the transmitter box. Both beams are coupled into optical fibers used to transmit the light to the sending probe (Dantec 60X83), which focuses the two beams to

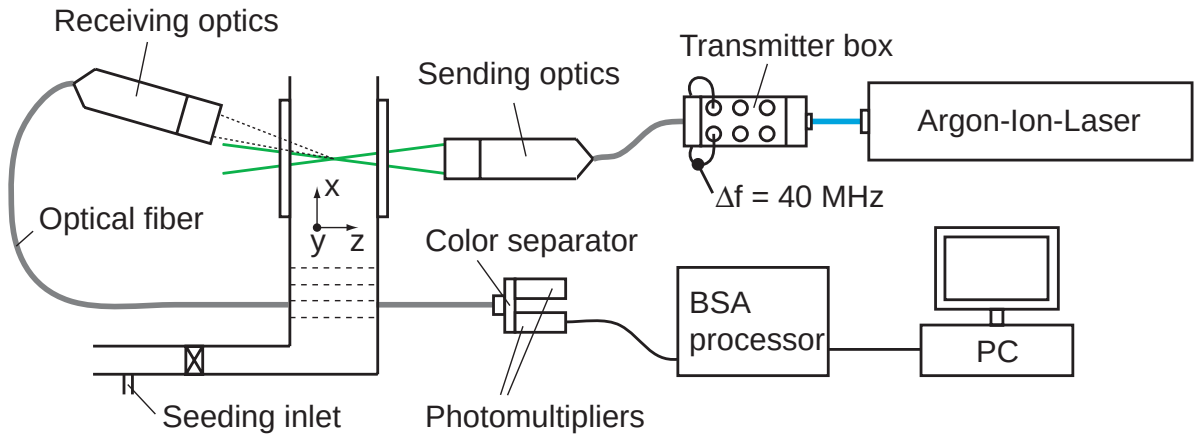

Figure 3.11: Overview of the LDA setup in the experimental rig.

form the measurement volume inside the measurement section. Geometrical details of the LDA beam configuration and the measurement volume are listed in Appendix A. The receiving optics (Dantec LDA-PR) are focused on the measurement volume at an inclination angle of 15° with respect to the z-axis. Due to this off-axis orientation, the effective z-size of the measurement volume is reduced. The two LDA probes are mounted on a common support and are traversed by a three-axis traverse system described in Appendix A. Sending and receiving optics have a focal length of 310 mm and are equipped with beam expanders (Dantec 55X12) in order to reduce the length of the measurement volume and to increase the aperture of the receiving optics. The received scattered light is guided to a color separator (Dantec 55X35) and attached photomultipliers (Dantec 57X08) through an optical fiber. The voltage signal of the photomultiplier tube is the final output of the LDA system, which is further processed by a Burst Spectrum Analyzer (BSA, Dantec 57N21 Master) which is controlled by a computer.

LDA measurements were conducted for a ramp angle of 4° only. Figure 3.12 depicts the definition of measurement planes and coordinate systems inside the measurement section. Three y-z measurement planes E1, E2 and E3 are defined by their x-wise distance from the downstream corner of the stainless steel ramp. During LDA-measurements, the plane which contains the beams forming the measurement volume is aligned with the ramp surface, which is described by a local coordinate system $\tilde{x}$, $\tilde{y}$ and z, and hence velocity compo-

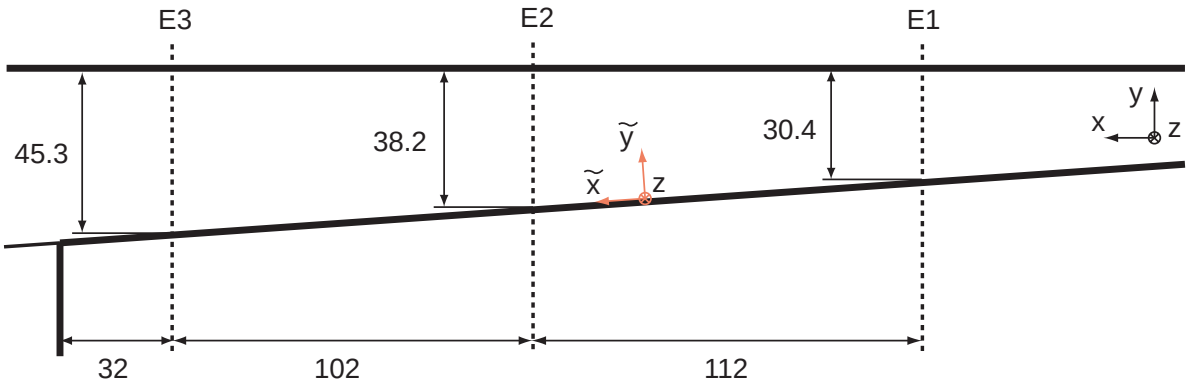

Figure 3.12: Definition of measurement planes inside the measurement section.

nents in $\tilde{x}$-direction are measured. Due to the small ramp angle of 4°, however, deviations between x- and $\tilde{x}$-wise velocity components in the x-y plane do not exceed 0.24% and thus are neglected. The origin of the z-coordinate is the left channel wall as seen in downstream direction and is identical for all three planes. The origin of the $\tilde{y}$-coordinate is located on the ramp surface position of the respective measurement plane. For simplicity, the $\tilde{y}$ coordinate is referred to as y in the following since each measurement plane will be treated separately.

Data Capture and Analysis

The BSA unit performs a spectral analysis of the photomultiplier signal in order to determine the Doppler frequencies of the scattered light. The signal is digitized and a Discrete Fourier Transform (DFT) is separately applied to characteristic signal portions known as *bursts*, which are generated by tracer particles passing the measurement volume. The Doppler frequency of a burst is taken as a valid velocity measurement if the global maxima of the DFT spectrum is at least four times higher than any local maxima. Hardware specifications of the present BSA are documented in [Fri03] and shall not be repeated. Important details of the DFT settings will rather be discussed, which are indispensable for successful boundary layer measurements. Since Doppler frequencies usually lie between $f_D = 1-100\,\mathrm{MHz}$, very high sampling frequencies during A/D conversion of the detected signal would be needed to fulfill the Nyquist criterion for a DFT of the digital signal in the whole frequency range

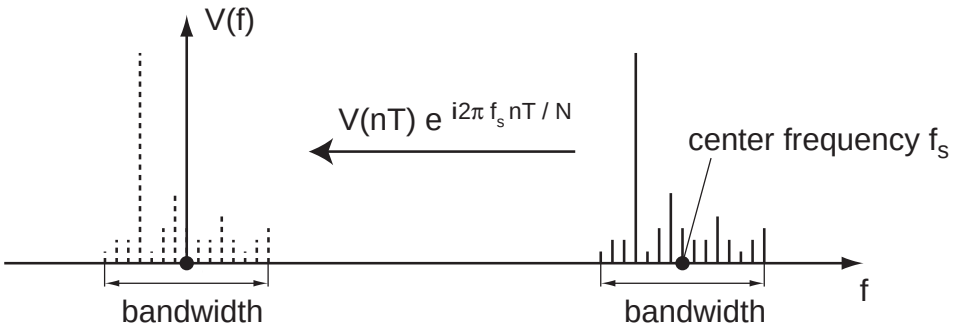

Figure 3.13: Zoom DFT process for frequency range extension.

of 0 Hz to f_D. This problem is avoided by only analyzing a small segment of the frequency spectrum, a procedure also known as *Zoom-DFT*. As illustrated in Fig. 3.13, the signal is downshifted by f_s in the frequency domain, which corresponds to a multiplication in the time domain in the DFT algorithm [Bri74]:

$$F(f - f_s) \Longleftrightarrow f(nT)\, \mathrm{e}^{\mathrm{i}2\pi f_s nT/N} \tag{3.9}$$

In Eq. (3.9), $0 \leq n \leq N-1$ is a counter and T is the sampling interval within the sample $f(nT)$. By only considering a limited bandwidth of the shifted signal symmetrical to $f = 0$ for the DFT evaluation, the sampling frequency can be largely reduced now. Using equation (3.6), the frequency shift f_s and the bandwidth can be interpreted as a center velocity u_s and velocity span. These two values are input parameters for the BSA processing which have to be specified by the user.

For the measurement of boundary layer velocity profiles, it is important to specify the center velocity and span carefully in the near wall region, since otherwise inconsistent data sets will be recorded. For the boundary layer measurements presented here, intersecting measurement intervals based on nondimensional coordinates y^+ and u^+ have been defined, which are illustrated in Fig. 3.14. Each interval has a distinguished center and span value. Estimates for u_τ at each measurement position were provided by numerical simulations of the diffuser flow (see Sec. 4.1.2) beforehand. The intervals overlap each other, such that data consistency between two intervals can be checked.

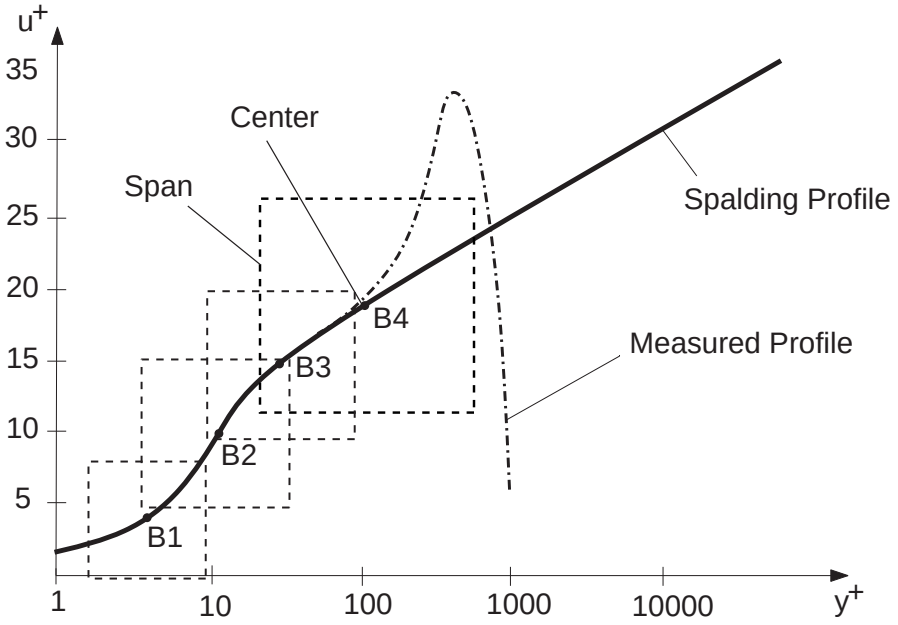

Figure 3.14: Nondimensional definition of LDA measurement intervals in the near-wall region.

Data capturing was controlled such that at every measurement point either 5000 validated bursts or a maximum measurement time of 40 s was reached. However, the number of recorded busts never lay below 1000. For the calculation of mean and variance of the velocity time series at a given measurement point, a transit-time weightening [Geo75] of each individual velocity record was applied in order to avoid statistical bias towards higher values.

Determination of the Position of the Measurement Volume

The windows of the measurement section reduce the effective focal length of the sending and receiving probes due to refraction. In order to exclude a distortion of the measurement volume by refraction effects, the optical axis of the sending probe is adjusted perpendicular to the planar window face such that both beams are refracted only within the $\tilde{x}$-z plane in the same way. However, the focus of the receiving probe is displaced from its optical axis due to the probe inclination by 15°. In order to include both refraction effects during the system setup, all adjustments are done already inside the flow duct with both side windows mounted. The position of the center of the measurement

volume in the three coordinates $\tilde{x}$, $\tilde{y}$, z has been measured separately for each coordinate. The z coordinate was determined by a pinhole mounted in the center of the duct. The $\tilde{x}$ coordinate was determined by traversing the measurement volume to hit the tip of a needle of known $\tilde{x}$ position. Finally, the $\tilde{y}$ coordinate was determined by traversing towards the wall observing the voltage signal from the photomultiplier caused by reflections of the measurement volume at the wall.

3.2.4 Particle Image Velocimetry

Particle Image Velocimetry (PIV) is comparable to LDA as to both techniques use the light scattered by small tracer particles to determine the local fluid velocity. As a consequence, all aspects regarding seeding particles discussed in Sec. 3.2.3 are applicable to PIV measurements as well. However, the key difference is that PIV provides velocity information in a two-dimensional field whereas LDA is a point measurement. In the present work, the PIV technique will be used to characterize cold flow conditions in the measurement section, partly overlapping with the LDA campaign for cross-validation, and to capture the velocity field upstream of the flame during wall flashback with high temporal and spatial resolution. Particle illumination and evaluation of the scattered light in a PIV setup are illustrated in Fig. 3.15. The tracer particles convected by the flow are illuminated by a laser sheet of local thickness δ_L. The sheet commonly has a Gaussian intensity distribution in y- and z-direction since it is formed from a TEM_{00} laser beam using cylindrical lenses. The light scattered by the particles is projected onto the image sensor of a digital camera through a lens with depth-of-field δ_F. The optical axis of the camera is positioned perpendicular to the laser sheet. The laser generates high-energy pulses of very short duration at a well-defined temporal separation, such that quasi-instantaneous images of the particle distribution are recorded by the image sensor. Figure 3.15 shows an overlay of two particle distributions recorded at t_1 and t_2. The PIV concept assumes that the velocity components u and v of the particles can simply be calculated by

$$u = \frac{\Delta x}{t_2 - t_1} \qquad \text{and} \qquad v = \frac{\Delta y}{t_2 - t_1}\,. \tag{3.10}$$

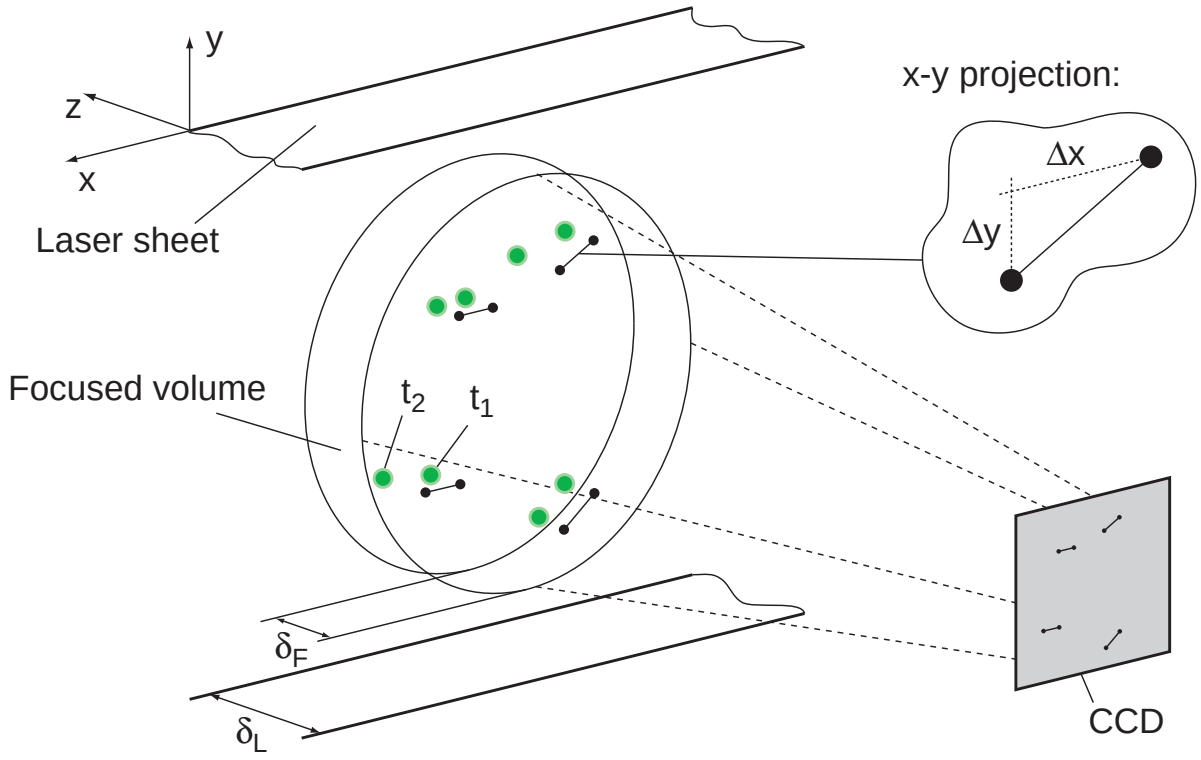

Figure 3.15: Principle of Particle Image Velocimetry.

It is advantageous to store the image of each laser pulse on a separate frame of the camera. However, the temporal separation between two laser pulses often has to be chosen smaller than the frame rate of the camera. To solve this problem, PIV laser systems produce pairs of pulses of individual length Δt_{pulse} at a separation of Δt_{PIV} at a repetition frequency f_{PIV}, while the camera is operated at a frame rate of $2 f_{PIV}$. The synchronization pattern is illustrated in Fig. 3.16. Laser and camera are synchronized such that each pulse pair lies symmetrically between to camera frames. By avoiding background illumination during experiments, only a single quasi-instantaneous particle image is effectively seen in one frame. Modern laser and digital camera systems allow high f_{PIV} in the kHz regime combined with an image sensor resolution in the megapixel range.

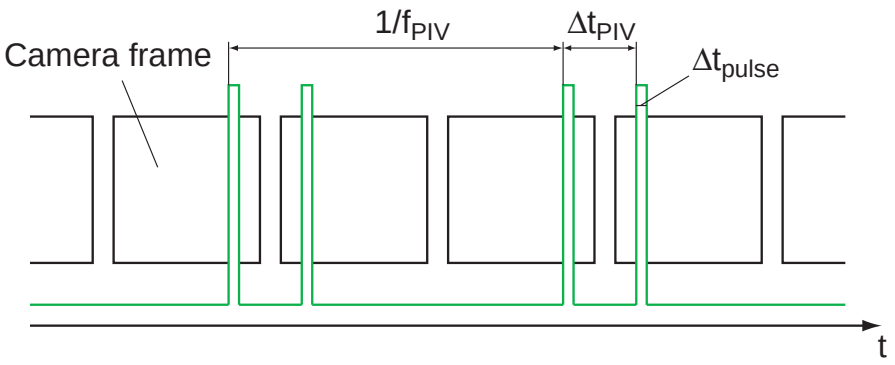

Figure 3.16: PIV synchronization between laser and camera.

Cross-Correlation of Digital PIV Images

The evaluation of Eq. (3.10) is efficiently computated by spatial cross-correlations of subsets of image pairs. These subsets, usually called *interrogation areas*, are used as samples for a statistical estimation of the displacement of the particles contained in the sample based on a discrete cross-correlation function [RWWK07]:

$$\mathbf{R}(\Delta x, \Delta y) = \sum_{i=1}^{N} \sum_{j=1}^{N} \mathbf{I_1}(i, j)\, \mathbf{I_2}(i + \Delta x, j + \Delta y)\,. \tag{3.11}$$

In Eq. (3.11), the paired images are represented by their pixel intensity maps $\mathbf{I_1}$ and $\mathbf{I_2}$, N^2 is the size of each interrogation area and $\Delta x, \Delta y$ represent the offset of the interrogation area in the second image $\mathbf{I_2}$ with respect to the interrogation area in $\mathbf{I_1}$. If Δx and Δy resemble the true displacement of the particles from their original position in $\mathbf{I_1}$, the value of R is maximized compared to all other shifts with high probability. Thus, the highest value of $\mathbf{R}$ and its associated displacement is used in practice to define the mean particle motion inside the interrogation area. Higher order derivatives of the particle trajectory between $\mathbf{I_1}$ and $\mathbf{I_2}$, such as curvature or acceleration, are not taken into account by the cross-correlation technique, which thus delivers an estimate of the mean particle displacement inside the interrogation area. For increased computational efficiency, the cross-correlation is usually implemented by a complex conjugate multiplication of the two-dimensional Fourier transforms of the data contained in the interrogation areas of $\mathbf{I_1}$ and $\mathbf{I_2}$. Furthermore, it is common practice to estimate the position of the correlation peak with

subpixel-resolution by fitting a statistical model function, for example a Gaussian peak, to the discrete values of **R** that form the correlation peak.

In more advanced codes, such as the commercial software VidPIV 4.6 used in this work, the position of the interrogation window in $\mathbf{I_2}$ is shifted and deformed based on the mean particle displacement Δx, Δy from an initial guess in an iterative process, which increases the number of correlating particles in the interrogation areas. The initial guess is provided by cross-correlations based on larger interrogation areas, such that the size of the interrogation area is reduced step by step until the desired value.

PIV with Micron-Resolution

The observation of the velocity field around the flame at flashback close to the wall puts high demands on the spatial resolution of the PIV system. The involved length scales, which are the viscous length unit L_+ and the flame thickness δ_f, are in the order of 10^{-4} to 10^{-5} m for the present experiments. Assuming interrogation areas of 16x16 pixels producing one velocity vector, the pixel size should be of order 10^{-6} m in order to resolve the flow field properly. The relatively new PIV derivative providing such spatial resolution is called micron-resolution PIV (μ-PIV), which was introduced by Santiago et al. [SWM+98] and has been recently reviewed by Williams et al. [WPW10]. Spatial resolution of the velocity field between 10^{-4} to 10^{-7} m is associated with μ-PIV, which is achieved by using microscope optics instead of standard lenses. Microscopes feature high numerical apertures and magnification factors, which imply a narrow depth-of-field δ_F. As a consequence, the thickness of common laser lightsheets $\delta_L \gg \delta_F$ (see Fig. 3.15). In highly three-dimensional flows, out-of-plane motion thus can have a much larger impact on particle image blur and the signal-to-noise ratio of the cross-correlation. A particular type of magnification optics are *long-distance microscopes*, which combine a moderate magnification factor of order 10 with typical working distances between some centimeters up to several meters. An overview on μ-PIV studies using long-distance microscopes can be found in [KSO06].

Table 3.4: Parameters of the μ-PIV lens in the current setup.

Variable	Value	Unit
Magnification	4.0	-
Field-of-view	5^2	mm^2
Numerical aperture	0.152	-
Spatial Resolution	2.2	μm
Depth-of-field d_F	0.02	mm

System Components and Measurement Positions

The μ-PIV technique will be used in this work to capture mean velocity and turbulence fields close to the wall as well as the velocity field in vicinity of the flame during flashback. An Infinity K2/S long-distance refractive microscope with a CF-3 objective is used as lens. The optical parameters of the microscope at its maximum working distance of 125 mm, which is close to the experimental distance, are listed in Table 3.4. Laser illumination is provided by a New Wave Research Pegasus-PIV laser, which uses two cavities with diode-pumped neodymium-doped yttrium lithium fluoride (Nd:YLF) crystals operated in Q-Switch mode to produce laser pulses of 527 nm wavelength and $\Delta t_{pulse} < 120$ ns. At a cavity pulse frequency of 1 kHz each pulse has a nominal energy of 10 mJ. Image recording is conducted by a Photron SA5 high speed camera. It comprises a sensor with 1024x1024 pixels, a physical pixel size of 20 μm and a 12-bit A/D-converter. The Photron SA5 acts as master clock for isothermal PIV measurements. The trigger signals for each laser cavity are provided by a Quantum Composer 9300 Series Pulse Generator synchronized with the camera. Pulse separations lie between $\Delta t_{PIV} = 1.6\,\mu$s to 18 μs for the μ-PIV experiments presented here.

The working distance of the microscope is large enough such that it can be placed in front of a side window of the measurement section and the mid-plane of the channel can be focused. The integration of the laser sheet to illuminate the particles close to the wall, however, is not straightforward. Kähler et al. [KMS05, KSO06] performed a μ-PIV study of a turbulent boundary layer

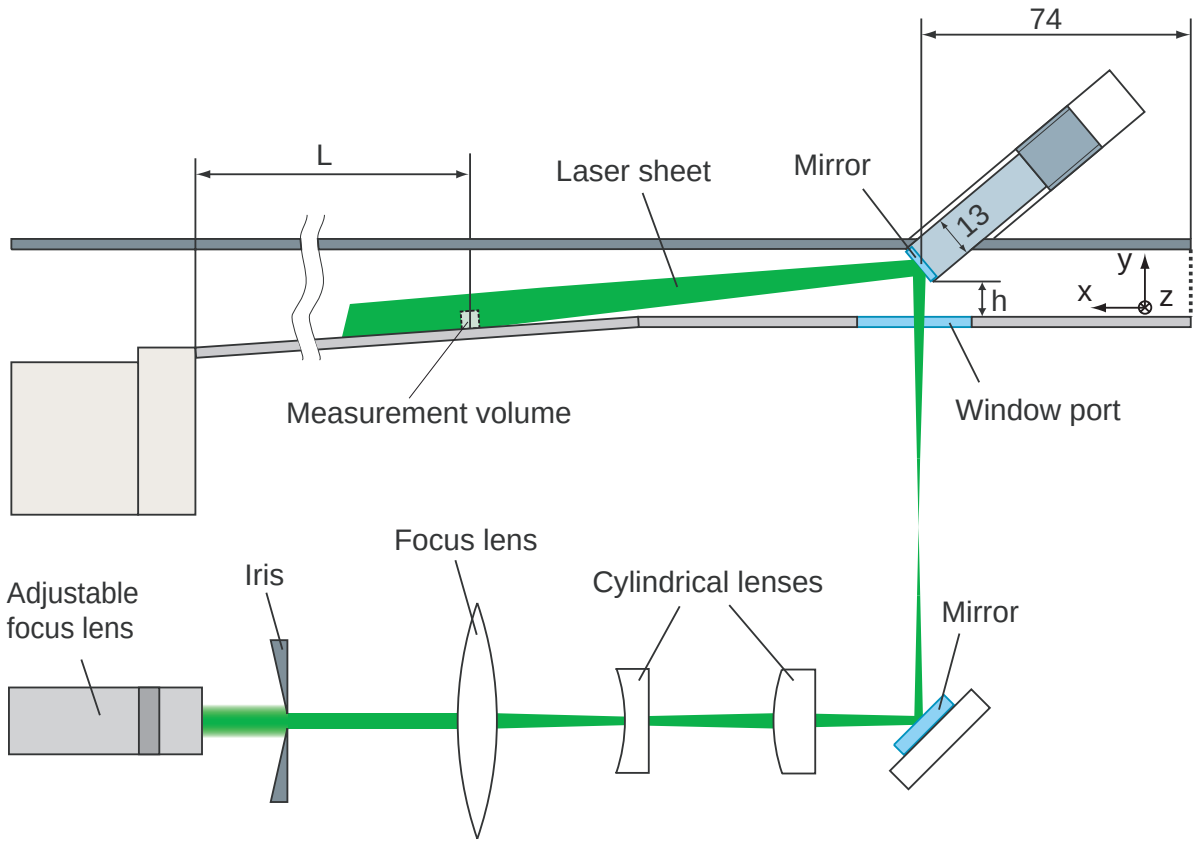

Figure 3.17: Side view of μ-PIV laser sheet insertion.

with a μ-PIV configuration comprising the same long-distance microscope model as applied here. They mention that diffusive reflections from the wall severely disturb measurements in the near-wall region if the laser sheet is not aligned approximately parallel to the wall surface. A further problem is local heating of the wall if the axis of the focused lightsheet is adjusted perpendicular to the wall. The only way to achieve a tiltable, wall-parallel lightsheet in the present setup is an internal reflector that deflects the lightsheet inside the flow path. The optical system for focusing and insertion of the lightsheet is shown in Fig. 3.17. After passing an adjustable focus lens, the approximately Gaussian laser beam is narrowed by an iris. The effect of the iris is a reduction of diffusive reflections from the ramp surface and a more homogeneous illumination of the measurement volume. A focus lens follows the iris which supports the adjustable focus at the beginning. A combination of a plano-concave and a plano-convex cylindrical lens is used to adjust the y-height of the lightsheet

in the measurement volume. After the cylindrical lenses, the laser beam is deflected by a 45° mirror towards a window port which is located at the center of the lower wall of the rectangular duct that follows the flow straightening section. From the top of the very same duct, a cylinder of 13 mm diameter extends into the flow. The distance between the last fine wire mesh and the cylinder position is 74 mm. The cylinder has a fine thread on its upper end for linear adjustment and is positioned such that the minimum distance between the cylinder and the lower wall of the duct is approximately 8.6 mm. On its lower end, a mirror is mounted which deflects the laser sheet with respect to the x-direction such that the measurement volume is completely illuminated. Finally, the adjustable focus lens is used to focus the laser sheet in z-direction at the measurement volume. In accordance with the definition of measurement positions for LDA measurements (see Fig. 3.12), the position of the center of the lower edge of the measurement volume is defined by its x-wise distance L from the downstream edge of the ramp. Spatial calibration of the PIV field was done using a machined aluminum target.

The cylindrical mirror mount clearly leads to mean flow displacement and to stochastic or periodic fluctuations in the wake of the cylinder. Looking at the first point, the global flow displacement is small since the blockage of the cylinder only amounts to 3.7% comparing the projected cylinder area and the duct cross-section. However, a local deficiency of the axial core velocity is expected, which will decay downstream depending on momentum diffusivity and the global pressure gradient. Fluctuating disturbances are concentrated in the upper half and the core region of the channel. Hence, the boundary layer on the lower wall of the channel, which is the region of interest for flame flashback, should not be disturbed severely in its development towards a canonical turbulent boundary layer at the measurement position. This assumption will be validated by comparing isothermal μ-PIV results with LDA measurements and results from boundary layer studies in the literature.

PIV Data Processing

The PIV images are stored in 8-bit uncompressed format and imported into VidPIV. No filter is applied to the images at any stage of the process. Each PIV

pair is cross-correlated using an adaptive algorithm with subpixel displacement and deformation of the interrogation window. A 50% overlap of the interrogation windows is used in both dimensions. The correlation analysis starts with interrogation windows of size 32x32 pixel, which subsequently are reduced to 16x16 pixel. In exceptional cases which will be mentioned separately in the text, the size is once again reduced to 8x8 pixel. After each correlation, outliers are identified using a median filter of size 3x3 vectors with a tolerance of twice the local standard deviation as well as a window filter with a border of $0\,\mathrm{m/s} \leq u$ for isothermal measurements. Filtered vectors are interpolated from their neighbors using a kernel size of 3x3 vectors. The resulting fractions of valid, non-filtered vectors after the last cross-correlation were between 95% and 100% for velocity fields without the presence of a flame, with the exception of a small fraction of 8x8 pixel interrogation area PIV pairs for which the valid fraction decreased down to 92%.

The influence of errors in the μ-PIV measurements is discussed in detail in Appendix B.

3.2.5 Flame Front Detection by PIV and Simultaneous Chemiluminescence

The μ-PIV system can also be used to localize a flame inside the boundary layer. For a weakly wrinkled flame, the boundary between unburnt and burnt gases is marked by a strong intensity gradient of the laser light scattered by the particles, which allows a flame front detection from PIV images. The intensity decreases for two reasons. First, the flow expansion downstream of the reaction zone causes a reduction in particle density. Second, the lightsheet is refracted by the strong density gradient across the reaction zone. An example of a μ-PIV image containing a flame inside the boundary layer is shown in Fig. 3.18a. Due to the two effects described before, there is a strong contrast between fresh gases and product side. Thus the position of the flame can be determined with reasonable accuracy in the x-y plane.

To be able to interpret the μ-PIV results, the shape of the reaction zone in the x-z plane, i.e. a top view on the measurement section, must be recorded si-

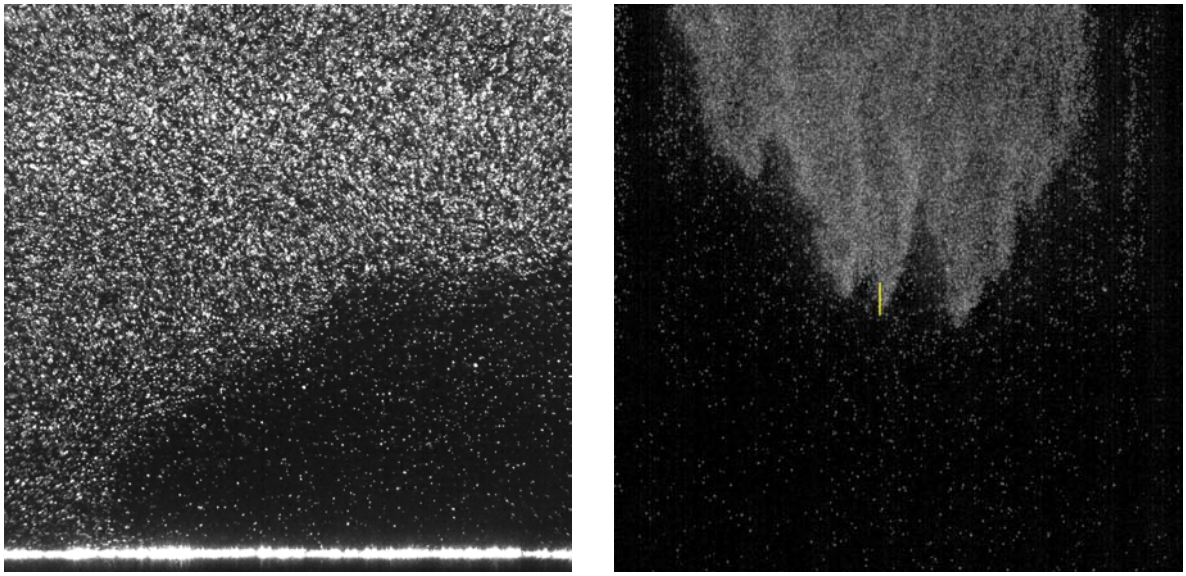

(a) PIV image with flame (side view).

(b) OH* chemiluminescence (top view).

Figure 3.18: Simultaneous μ-PIV and chemiluminescence of a flame inside the boundary layer.

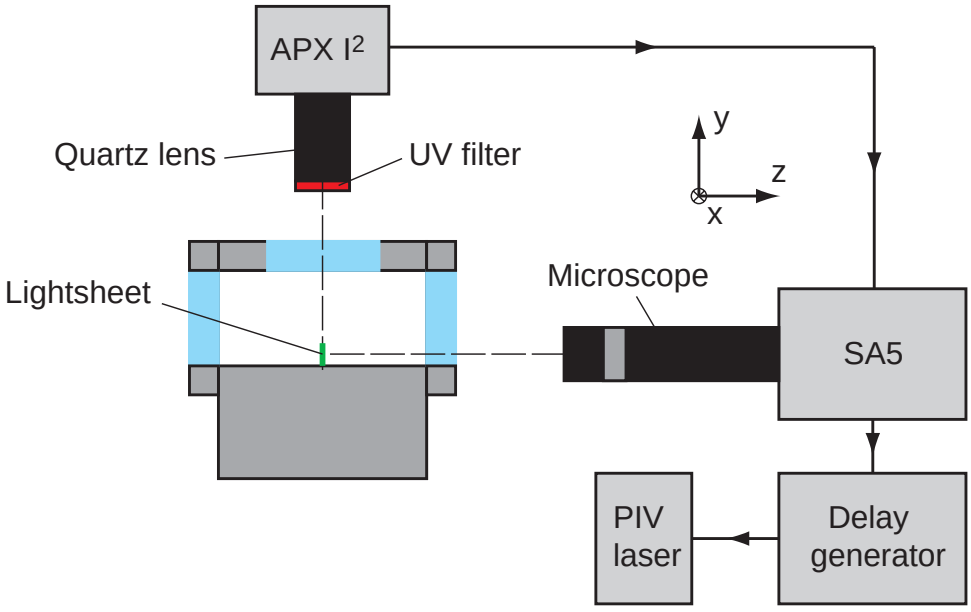

Figure 3.19: Setup for simultaneous μ-PIV and chemiluminescence.

multaneously. The according experimental setup is depicted in Fig. 3.19. The APX I^2 camera is mounted above the measurement section equipped with a UV filter for OH* chemiluminescence recordings. The filter additionally pro-

tects the image intensifier of the camera against the intense PIV laser light. The APX I^2 is operated at 1024x1024 resolution, a repetition frequency of 2 kHz and variable shutter time, depending on the OH^* intensity of the flame. The APX I^2 is now the master clock for the μ-PIV setup, which apart from that is assembled as described before. The simultaneous OH^* image corresponding to Fig. 3.18a is shown in Fig. 3.18b. The yellow line marks the μ-PIV measurement volume to scale in both dimensions.

3.3 Isothermal Flow Structure in the Measurement Section

Compared to isothermal or diffusion flame boundary layer channels reported in the literature, the present design for premixed, highly reactive mixtures has some distinct features which cause additional flow disturbances inside the measurement section:

- The sidewalls and the upper wall of the duct are formed by welded stainless steel plates which undergo thermal deformation during manufacturing. The resulting variations in duct height lie within approximately ±5% for the 0° channel.
- From the upper wall, a thermocouple for flashback detection with a diameter of 1 mm extends to the duct center at the beginning of the measurement section.
- Blowing air is inserted in each edge of the duct to avoid corner flashback.

The uniformity of the flow inside the measurement section is reduced by the factors described above. The aim of the following discussion is to verify that these non-uniformities do not impede the development of a reasonably uniform and reproducible boundary layer at the target location of flashback measurements, which is the lower wall of the duct. At the beginning, the inlet conditions will be presented. Afterwards, the flow structure inside the measurement section will be discussed for ramp angles of 0°, 2° and 4° in descending order. The results form the basis for the calculation of flashback limits based on local boundary layer variables and the interpretation of flame propagation

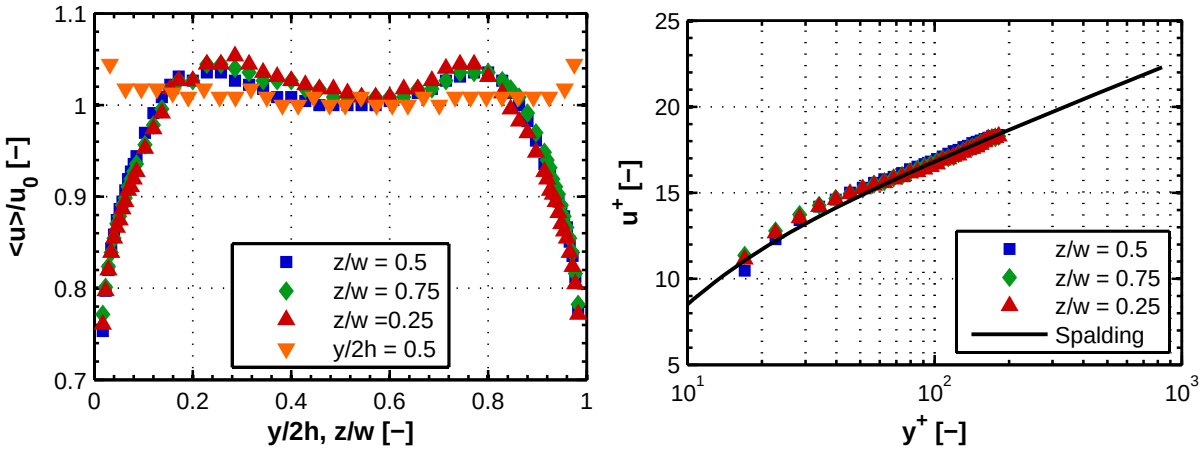

(a) Velocity profiles across channel height and width. **(b)** Near-wall velocities at the center of the lower wall.

Figure 3.20: Mean velocities at the inlet of the measurement section.

inside the boundary layer in later chapters. All measurements were carried out at room temperature (20 °C) and pressure using pure air as fluid. The amount of blowing air was adjusted to 2% of the main massflow if not stated otherwise.

3.3.1 Inlet Conditions

The flow at the inlet of the measurement section has been measured with a CTA probe as described in Sec. 3.2.2. Emphasis is put on the uniformity of the flow profile and mean velocities inside the boundary layer. Turbulence quantities have not been measured at the inlet position. Figures 3.20 show the mean flow distribution at the inlet of the measurement section for an air massflow rate of $\dot{m}_{air} = 50\,\mathrm{g/s}$. The velocity distributions along the channel height ($0 \leq y \leq 2h$) and width ($0 \leq z \leq w$) are shown in Fig. 3.20a. The nondimensional channel height $y/2h$ and width z/w are plotted on the x-axis. On the y-axis, nondimensionalized mean flow velocities $\langle u \rangle / u_0$ are shown. The mean velocity at the center of the duct was chosen as u_0, which thus is the same for all profiles. The velocity distribution along the channel width at half channel height $y/2h = 0.5$ shows good uniformity. Only close to the channel walls, the velocities rise above the center value. This fact is explained by the flow distribution properties of fine wire meshes, which produce a distinct velocity overshoot at the edge of the boundary layer due to a minimum of the

pressure loss coefficient in this region [Meh85]. A similar shape is observed for the mean velocity profiles along the channel height at three lateral positions $z/w = 0.25$, 0.5 and 0.75. While the profiles again show a good uniformity within ±1.5%, there exists a symmetric peak of velocities above the center value at $y/2h = 0.25$ and $y/2h = 0.75$. The boundary layer thickness amounts to approximately 3 mm at the top and bottom of the channel.

According to [Meh85], the wall friction produced by such mesh wake profiles tends to lie above the value for an undisturbed turbulent boundary layer at the same position. In order to estimate the wall friction, the experimental results were fitted to the correlation of Spalding (Eq. (2.14)). This fit has two independent variables, the absolute wall distance y and the wall friction τ_w. This means that the wall distance has to be known precisely in order to derive a unique value for τ_w from the fit. As described in Sec. 3.2.2, the wall distance of the CTA wire was not directly measured for each profile location. However, due to the logarithmic scaling of the x-axis in the Spalding plot, small variations in y do not appreciably shift the line location in the logarithmic part of the boundary layer. That is not the case for the second variable τ_w, which also changes the scaling of the linear y-axis. As a result, a fit to the Spalding profile based on the logarithmic part of the boundary layer can be achieved without exact knowledge of the absolute wall distance. It is clear though that the quality of the fit decreases with fewer data points, such that the result for τ_w is only approximate in the present case. Figure 3.20b shows the Spalding fit of the boundary layer on the lower wall of the channel. All three curves are scaled with the same absolute wall distance and a wall friction of $\tau_w = 0.9\,\mathrm{Pa}$.

3.3.2 Global Pressure Gradients in the 2° and 4° Diffusers

Before the presentation of velocity fields in the measurement section, the global pressure gradient in streamwise direction is derived in order to compare the strength of the adverse pressure gradients to literature setups mentioned in Sec. 2.1.5. The bulk velocity of the fluid is given by

$$\overline{u}(x) = u_0 \frac{A_0}{A_0 + w \tan(\phi)\, x}\,, \tag{3.12}$$

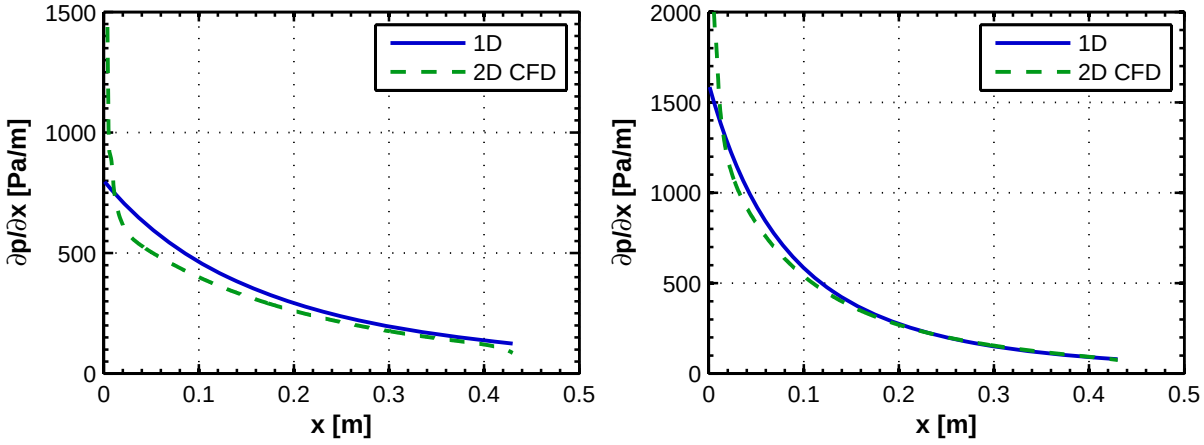

(a) 2° diffuser.

(b) 4° diffuser.

Figure 3.21: Axial pressure gradient in the 2° and 4° diffusers at $\dot{m} = 60\,\mathrm{g/s}$.

where A_0 is the inlet cross-section, w is the width of the measurement section and ϕ is the ramp angle. Starting at the inviscid Euler equation for momentum conservation in the absence of field forces,

$$\rho \frac{\partial \mathbf{u}}{\partial t} + \rho \mathbf{u} \cdot \nabla \mathbf{u} = -\nabla p \tag{3.13}$$

and assuming steady, incompressible, one-dimensional flow and $\mathrm{rot}\,\mathbf{u} = 0$, Eq. (3.13) reduces to

$$\frac{\rho}{2} \frac{d\,u^2}{dx} = \rho u \frac{du}{dx} = -\frac{dp}{dx}\,. \tag{3.14}$$

Inserting Eq. (3.12) in Eq. (3.14) and differentiation leads to an explicit expression for the pressure gradient inside the diffuser as a function of x. This function is plotted in Figs. 3.21 for both diffuser angles at an air massflow of $\dot{m} = 60\,\mathrm{g/s}$. The entry of the diffuser is at $x = 0$. In addition to the one-dimensional pressure gradient, the result of a two-dimensional numerical CFD simulations of the same geometries (see Sec. 4.1.2) are shown for comparison. At the beginning of the diffuser, the CFD result substantially lies above the one-dimensional curve due to the sudden expansion of the geometry and non-negligible gradients in y-direction. With increasing x, the results approach each other. The first measurement plane E1 lies at $x = 0.184\,\mathrm{m}$ in Figs. 3.21, which indicates that for all three measurement planes the one-dimensional approach is a good approximation for both diffuser angles.

3.3.3 Flow Structure in the 4° Diffuser

The influence of aerodynamic disturbances on the development of the boundary layer on the lower wall is likely to intensify with increasing ramp angle. While mean and fluctuating velocity variations with respect to the mean are reduced by a contraction of the duct cross-section [MB79], a diffuser has the opposite effect, as already noted by Buice [Bui97]. Thus an existing non-uniformity in the flow field is amplified relative to the mean velocity by a global deceleration due to an adverse pressure gradient. Consequently, a validation of the flow structure inside the measurement section should be concentrated on the maximum ramp angle of 4°, since the two other setups at 2° and 0° certainly produce a more uniform flow field. Hence, the LDA system was used for a detailed characterization of the flow structure inside the 4° diffuser since the LDA system does not introduce any additional disturbances and allows lateral traversing. In a second series of isothermal experiments, the μ-PIV system is used at the same inflow conditions to exhibit the influence of the mirror mount upstream of the measurement section and to specify the boundary layer state for later observations of the flame.

LDA Measurements

Contours of axial velocities at the three axial measurement planes E1, E2 and E3 (see Fig. 3.12) are shown in Fig. 3.22 for a massflow of $\dot{m} = 60\,\mathrm{g/s}$. Flow direction is opposite to the line of sight. The position increments during contour measurements were $\Delta y = 2\,\mathrm{mm}$ and $\Delta z = 5\,\mathrm{mm}$, such that a good resolution of the local flow structure was achieved. The axis frame of each contour plot approximately represents the full channel width at the respective measurement position. Measurements towards the sidewalls are restricted by reflections on the windows, which resulted in a distance of 11 mm of the first measurement point on each side.

A high degree of flow non-uniformity can be observed in the upper region of the diffuser. The wake of the thermocouple is visible at each measurement plane. At E2 and E3, the influence of the vertical blowing at the upper edges of the channel can clearly be seen from low velocity regions. In the middle

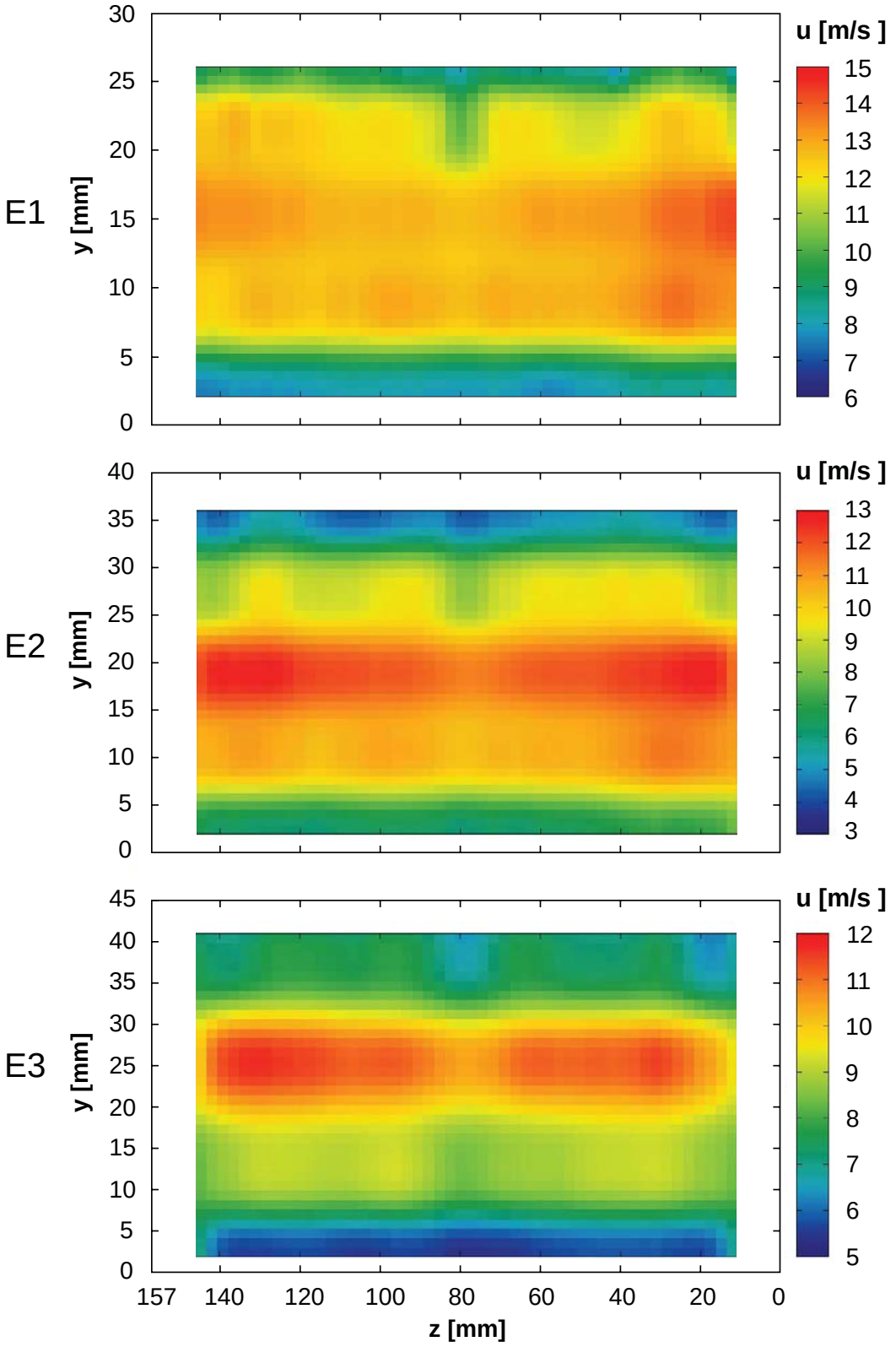

Figure 3.22: Contours of axial velocity in the 4° diffuser at $\dot{m} = 60\,\mathrm{g/s}$.

region of the diffuser, a tendency for elevated velocities exists in E1 for small values of z, i.e. at the left-hand side of the channel as seen in flow direction. This tendency is reduced downstream and vanishes in E3. The influence of the thermocouple extends well into the coreflow region, as can be observed from the dip of the channel velocity at E2 and E3. Boundary layer growth on the sidewalls of the channel is rather weak compared to the development in y-direction, which is probably caused by the streamwise blowing in the lower edges. The outer region of the boundary layer on the lower wall shows reasonable uniformity at all measurement planes. Within a width of ±60 mm from the center, lateral variations are within ±10%. Towards the sidewalls, the velocity is increased by the axial blowing in the lower edges.

To shed light on the homogeneity of the inner boundary layer region and especially the wall shear stress distribution on the lower wall, profiles of axial velocity as a function of y are presented in Figs. 3.23 and 3.24. At each measurement plane E1, E2 and E3, measurements were taken at the lateral center ($z = 71.5$ mm) and at a distance of 40 mm towards both directions. Mean velocity profiles have been fitted to the Spalding correlation in order to determine the wall shear stress, but in contrast to the CTA measurements described in Sec. 3.3.1, the wall distance could be determined more precisely such that only a variation of ±0.05 mm from the measured value was allowed during the least-squares fit. The second parameter of the fit, the wall shear stress, is listed in the first three columns of Table 3.5.

Figures 3.23a-c show profiles of the mean axial velocity for flows including edge blowing, which are nondimensionalized by the respective wall shear stress from Table 3.5. The plots reveal a very good match to a canonical turbulent boundary layer up to about $y^+ = 100$. Deviations are only visible in the laminar sublayer for some of the positions, which is probably caused by measurement uncertainties in that region. The profiles also include the freestream region and parts of the upper boundary layer, which show stronger deviations consistent with the contours in Fig. 3.22. The influence of these deviations on the actual wall shear can be deduced from Table 3.5 by analyzing the variations in each row. Deviations from the mean are within +6% and -3% in each measurement plane for experiments with edge blowing. It can be concluded

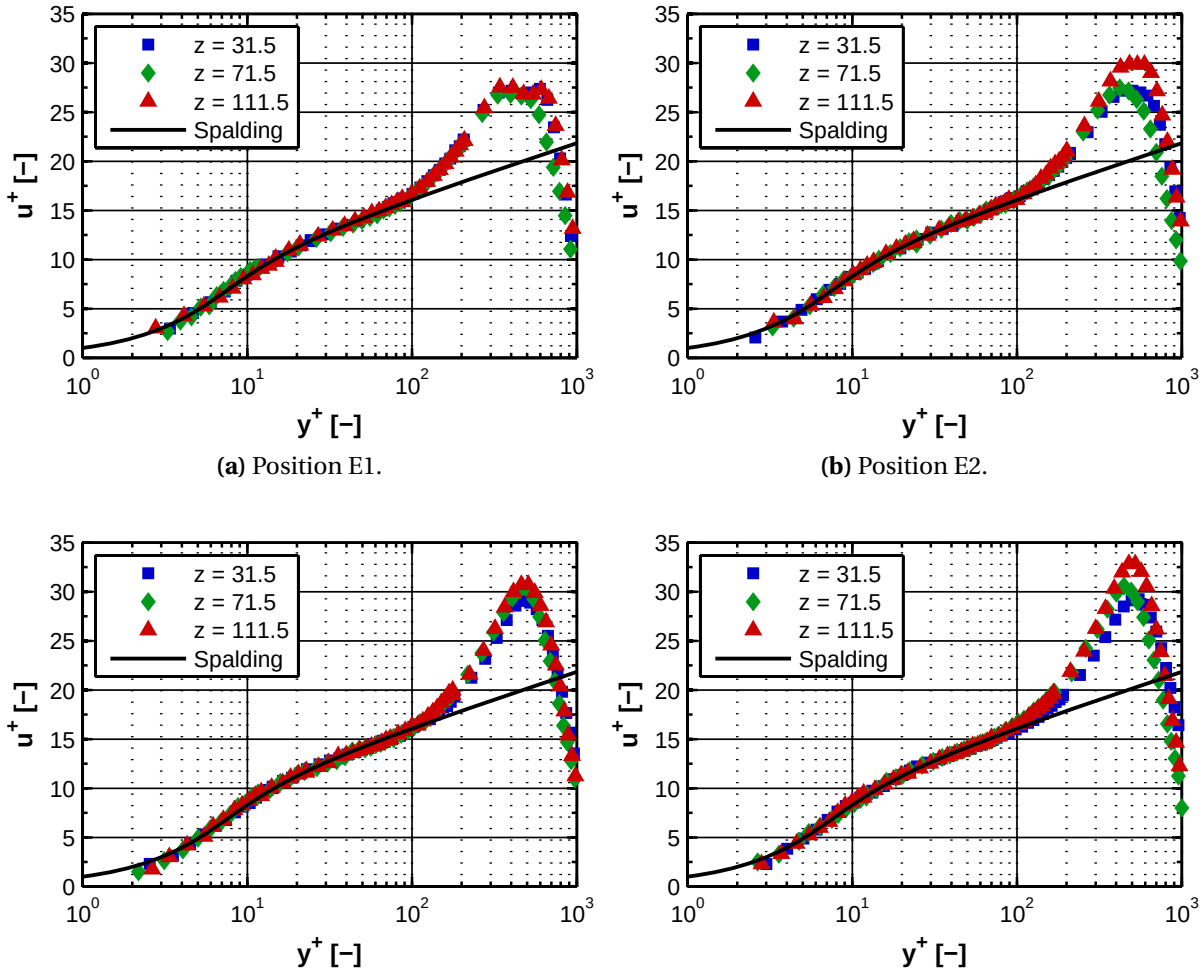

(a) Position E1.

(b) Position E2.

(c) Position E3.

(d) Position E3 without blowing.

Figure 3.23: Boundary layer velocity profiles in the 4° diffuser at $\dot{m} = 60\,\mathrm{g/s}$: LDA measurements.

that in spite of rather strong non-uniformities in the core flow and the upper boundary layer, the lateral wall shear stress distribution and mean flow profiles in the inner and logarithmic region of the boundary layer have a satisfying homogenity in light of the compromise between safety and optimum flow settling upstream of the test section.

The last column of Table 3.5 shows the nondimensional pressure gradient according to Eq. (2.19). These values can now be compared to the statement of Nagano et al. [NTT93], who categorized a range of $p^+ = 0.009$ to 0.025 as *mod-*

Table 3.5: Wall friction distribution in the 4° diffuser from LDA at $\dot{m} = 60\,\mathrm{g/s}$.

Position	*z = 31.5 mm* τ_w *[Pa]*	*z = 71.5 mm* τ_w *[Pa]*	*z = 111.5 mm* τ_w *[Pa]*	*Mean* p^+ [-]
E1	0.2961	0.2934	0.3130	0.031
E2	0.2394	0.2193	0.2202	0.024
E3	0.1652	0.1547	0.1567	0.024
E3	0.1817	0.1497	0.1386	
w/o blowing				

erate to strong adverse pressure gradients. According to their scaling, the pressure gradients at the measurement planes of the 4° diffuser are strong. As a consequence, the mean axial velocity profiles may fall below the Spalding plot in the logarithmic region, as already discussed in Sec. 2.1.5. Consequently, a fit of the measurement data to the Spalding profile including the logarithmic region, such as used here to determine wall friction from LDA results, may not be feasible. This issue will be further discussed after the presentation of PIV results from the 4° diffuser further below in this section.

Figures 3.24 show squared rms values of streamwise turbulent fluctuations nondimensionalized by the square of the *mean* friction velocity at each measurement plane. The choice of a common friction velocity at each plane allows a better comparison of absolute fluctuations between the three lateral locations. Close to the wall, the profiles show the characteristic increase in streamwise boundary layer turbulence towards a maximum located at about $y^+ = 15$ and $u^2_{rms}/u^2_\tau = 9...11$ at all measurement positions. An increase of this first maximum between E1 and E2 by about 10% is observable, which then stays approximately constant between E2 and E3. After the first maximum, the fluctuations reduce towards a local minimum at $y^+ = 50...60$, after which they increase again to a second maximum at the edge of their logarithmic region. The qualitative development follows the literature results for boundary layers under adverse pressure gradients described in Sec. 2.1.5. The lateral ho-

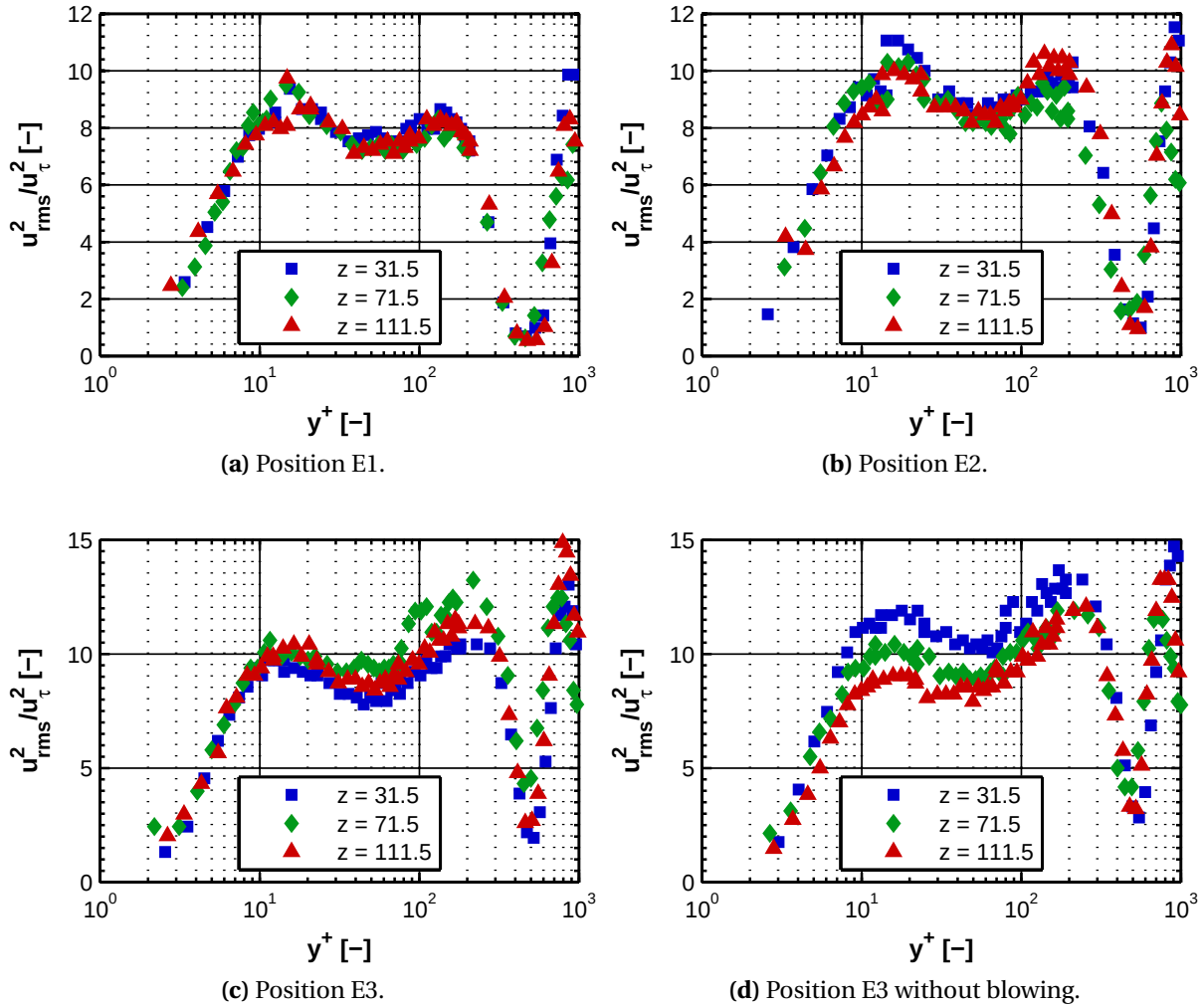

(a) Position E1.

(b) Position E2.

(c) Position E3.

(d) Position E3 without blowing.

Figure 3.24: Boundary layer and freestream turbulence in the 4° diffuser at $\dot{m} = 60\,\mathrm{g/s}$: LDA measurements.

mogenity of the turbulence profiles is satisfying within the bounds of measurement noise.

Towards the freestream, the axial turbulent fluctuations decline substantially. Table 3.6 lists the turbulence intensity $u_{rms}/\langle u \rangle$ at the centerline of the channel at each measurement plane. The core flow turbulence is at moderate levels throughout the diffuser. A continuous increase in downstream direction is obvious, which probably is the result of boundary layer growth and vertical turbulent momentum transfer towards the core.

Table 3.6: Freestream turbulence in the 4° diffuser at $\dot{m}$ = 60 g/s: LDA measurements.

	E1	*E2*	*E3*	*E3 w/o blowing*
Turb. intensity [%]	3.1	4.6	7.0	6.8

Influence of Blowing Air

The influence of edge blowing on the flow structure in the diffuser can be analyzed by comparing LDA results for diffuser flow with and without blowing. Only the most downstream measurement plane, E3, is considered since the integral amount of blowing air present in the flow and thus the expected deviations are largest there. Figures 3.23d and 3.24d show the axial mean and fluctuating velocities at E3 without blowing, which can be directly compared to Figs. 3.23c and 3.24c. Furthermore, the wall shear stresses without blowing are shown in the last row of Table 3.5. A comparison between flow with and without blowing reveals that the edge blowing effects a lateral homogenization of the wall shear stresses on the lower wall, the mean velocity profiles (also in dimensional form, which cannot be inferred from Figs. 3.23c and 3.23d directly since they are normalized by the *local* friction velocity) and the streamwise turbulent fluctuations. The homogenization approximates the respective lateral mean of the results without blowing. Conclusively, the edge blowing does not distort the flow structure inside the diffuser, but reduces flow deceleration and associated deviations by its momentum input in the lower edges of the diffuser, which probably is the cause for the observed homogenization of mean and fluctuating axial velocities. The mixing of blowing air into the main mixture was not investigated experimentally. However, three-dimensional numerical RANS mixing studies using a Reynolds Stress Model (RSM) in order to resolve the edge vortices have shown a negligible influence on the equivalence ratio in the region of interest.

The results of the LDA measurements in the 4° diffuser presented so far show that meaningful and justifiable measurements of flashback limits inside the measurement section can be made. In the next subsection, the same flow is measured with the μ-PIV system, which will be used to study the detailed

propagation of the flame during flashback, in order to determine any changes introduced by the mirror support.

PIV Measurements

While the LDA results were fit to the Spalding profile in order to determine the wall friction, the shear derivation from the PIV data follows a more general concept. Extrapolating from the strong influence of the thermocouple, the mirror mount is expected to have a rather large impact on the flow distribution in the center of the diffuser. Therefore, it is not known a priori whether the boundary layer profiles follow the universal curve properly in the logarithmic region. Thus a Spalding fit could lead to wrong conclusions. In such cases, a direct measurement of the velocity gradient in the laminar sublayer ($y^+ \leq 5$) is the only sensible method to determine wall friction, which is possible here due to the high spatial resolution of the μ-PIV system. This procedure is adopted for all isothermal μ-PIV measurements presented in this text. The true point of origin of the y-coordinate is then simply determined by seeking a zero-crossing of the linear interpolation line. Please note that the y-origin cannot be determined directly from the calibration target with high precision since the optical axis of the camera is not tangential to the lower wall, which results in a perspective shift if the laser sheet is not perfectly coincident with the calibration target, which is hardly achieved in practice. Each of the following isothermal PIV sets represents an average over 1092 image pairs which cover a physical flow time of 5 s.

Figures 3.25 show a comparison of PIV and LDA results for mean and fluctuating streamwise velocities at the centerline of the diffuser in non-dimensional coordinates. The corresponding wall shear stresses are listed in Table 3.7. The values indicate that the wake of the mirror mount is retarding the main flow, which effects the boundary layer development in E2 and E3 such that PIV wall frictions fall below the LDA results by 15% and 27%, respectively. An examination of Figs. 3.25a, 3.25c and 3.25e shows that the nondimensional PIV profiles of mean velocity follow the Spalding curve qualitatively, but are shifted below the curve in the logarithmic region by 5% to 10%. On the one hand, this could be caused by a velocity lag in the wake of the mirror mount which distorts the

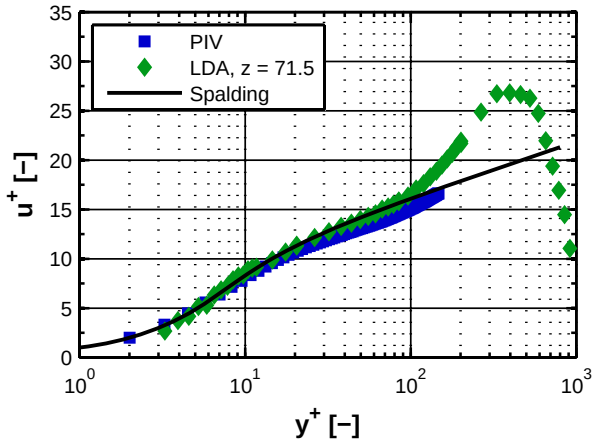

(a) Position E1: Mean velocities.

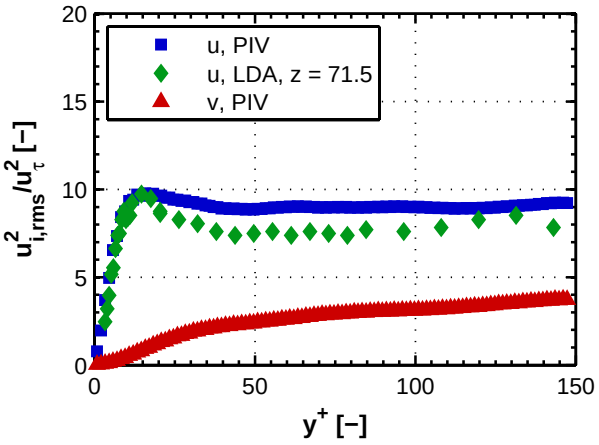

(b) Position E1: RMS velocities.

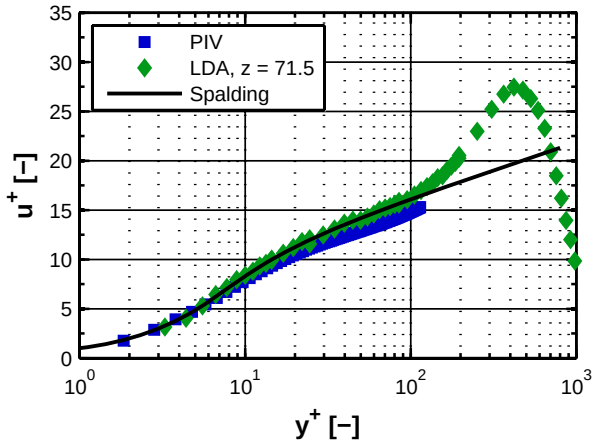

(c) Position E2: Mean velocities.

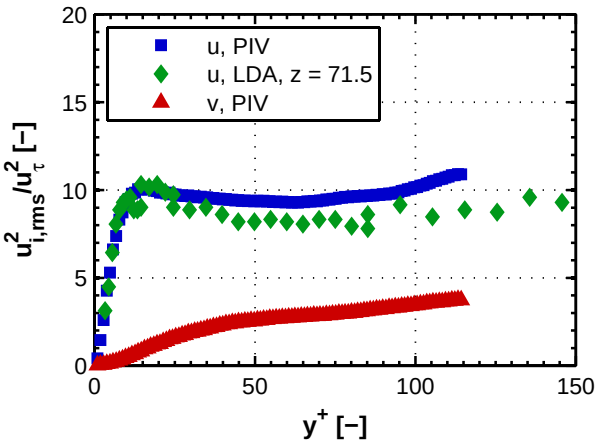

(d) Position E2: RMS velocities.

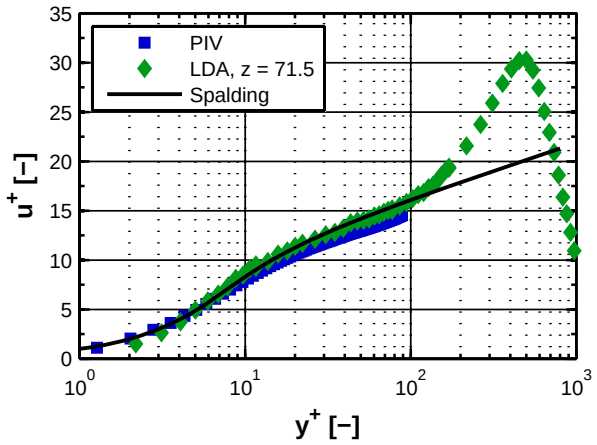

(e) Position E3: Mean velocities.

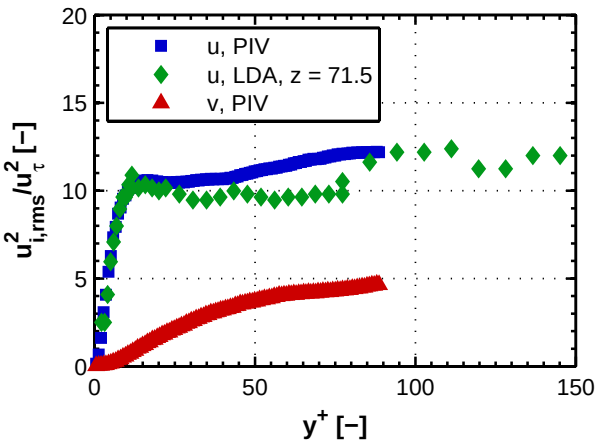

(f) Position E3: RMS velocities.

Figure 3.25: Turbulent boundary layer in the 4° diffuser at $\dot{m} = 60\,\mathrm{g/s}$: PIV measurements.

Table 3.7: Centerline wall friction in the 4° diffuser from PIV and LDA at $\dot{m} = 60\,\mathrm{g/s}$.

System	*E1*, τ_w *[Pa]*	*E2*, τ_w *[Pa]*	*E3*, τ_w *[Pa]*
LDA	0.2934	0.2193	0.1547
PIV	0.3044	0.1861	0.1131

velocity profile for a given wall friction. On the other hand, the deviation below the Spalding profile could be caused by the strong adverse pressure gradient, as discussed before, and the influence of the mirror mount on the shape of the profile may not be crucial. Thus at this point, it cannot be decided with confidence if the mirror causes the slight change in shape of the nondimensional mean velocity profile in the logarithmic region.

Turning to Figs. 3.25b, 3.25d and 3.25f, the streamwise fluctuations from the PIV measurements are in very good agreement with the LDA results up to $y^+ = 20$. Further away from the wall, the turbulence level in the PIV boundary layers is always above the LDA values, which is probably caused by fluctuations produced by the wake of the mirror mount. Nevertheless, an increase of turbulent fluctuations in the logarithmic part of the layer towards a second peak is also observed in the PIV data in accordance with prior results. Turbulent fluctuations in the wall-normal direction derived from the PIV measurements are also shown in Figs. 3.25b, 3.25d and 3.25f.

In summary, the comparison between LDA and PIV results above validate the concept of the μ-PIV setup using an internal mirror mount. The boundary layer essentially keeps a canonical mean structure and a turbulence development typical for adverse pressure gradient flows. While the measurement of flashback limits is not feasible in the PIV configuration due to its strong influence on the wall shear on the centerline, it is confirmed that the observation of the flame close to the wall with the μ-PIV system is taking place in a representative turbulent boundary layer even in the very sensitive 4° diffuser.

3.3.4 Flow Structure in the 2° Diffuser

Figures 3.26 summarize the mean and fluctuating velocities at the centerline of the 2° diffuser in non-dimensional coordinates at an air massflow of $\dot{m} = 60\,\mathrm{g/s}$. From Figs. 3.26a, 3.26c and 3.26e it can be seen that the structure of the flow at E1 is different from the planes further downstream in that the mean velocities fall below the Spalding curve right from the end of the laminar sublayer and the maximum of the turbulent fluctuations is substantially lower than at E2 and E3, between which the mean and fluctuation changes are less evident. Apparently, the turbulent boundary layer at E1 is not at a canonical equilibrium. A canonical structure has nevertheless been obtained at E2 and then prevails until the end of the diffuser. Interestingly, the deficiency at E1 is not observed to the same degree in the PIV results of the 4° diffuser. Figures 3.26b, 3.26d and 3.26f show that the gradient of the streamwise fluctuations in the 2° diffuser is always negative but still small after the maximum, while the wall-normal fluctuations nearly reach a constant level in the second half of the measurement area. These observations underline the decreasing influence of the adverse pressure gradient, as will obvious from the 0° channel results to be presented next.

Table 3.8 lists wall friction and nondimensional pressure gradients in the 2° diffuser. According to [NTT93], the values of p^+ correspond to a moderate adverse pressure gradient.

Table 3.8: Wall friction in the 2° diffuser from PIV at $\dot{m} = 60\,\mathrm{g/s}$.

Position	τ_w [Pa]	p^+ [-]
E1	0.6492	0.010
E2	0.4130	0.013
E3	0.2927	0.015

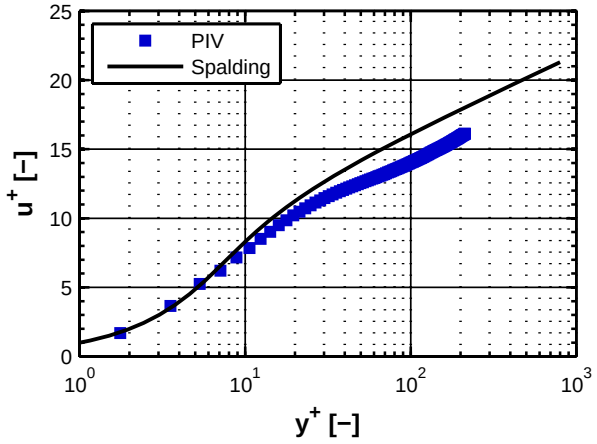

(a) Position E1: Mean velocities.

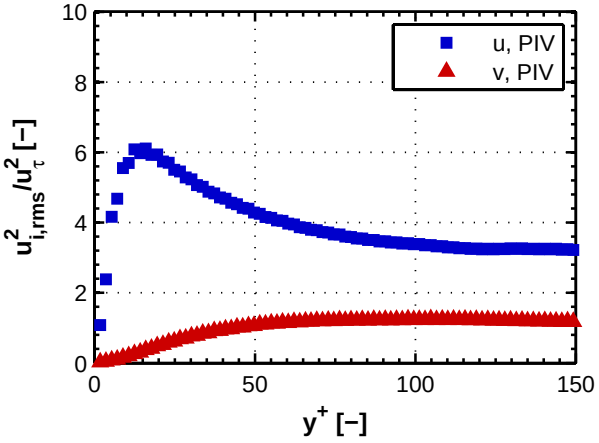

(b) Position E1: RMS velocities.

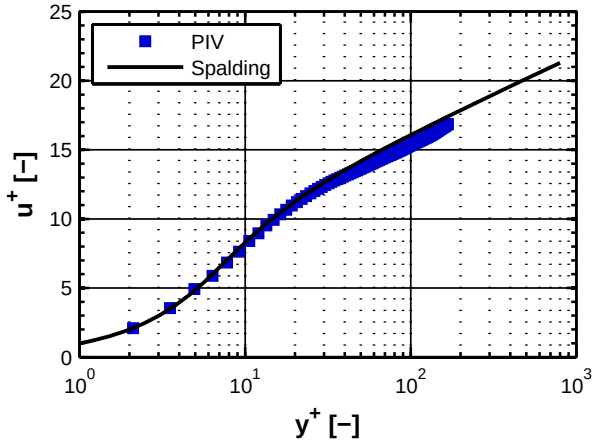

(c) Position E2: Mean velocities.

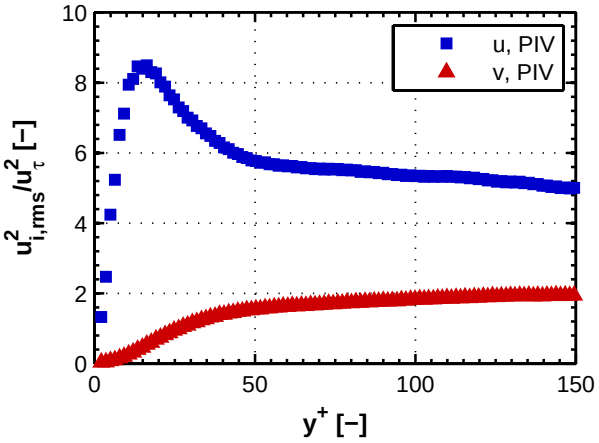

(d) Position E2: RMS velocities.

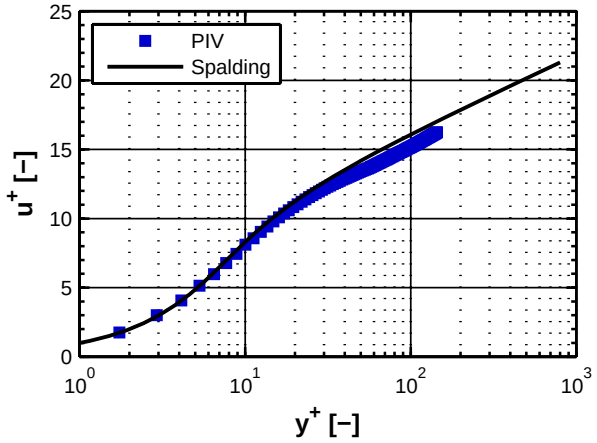

(e) Position E3: Mean velocities.

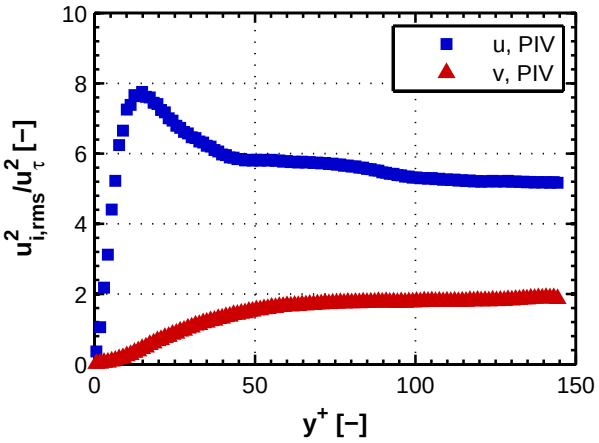

(f) Position E3: RMS velocities.

Figure 3.26: Turbulent boundary layer in the 2° diffuser at $\dot{m} = 60\,\mathrm{g/s}$: PIV measurements.

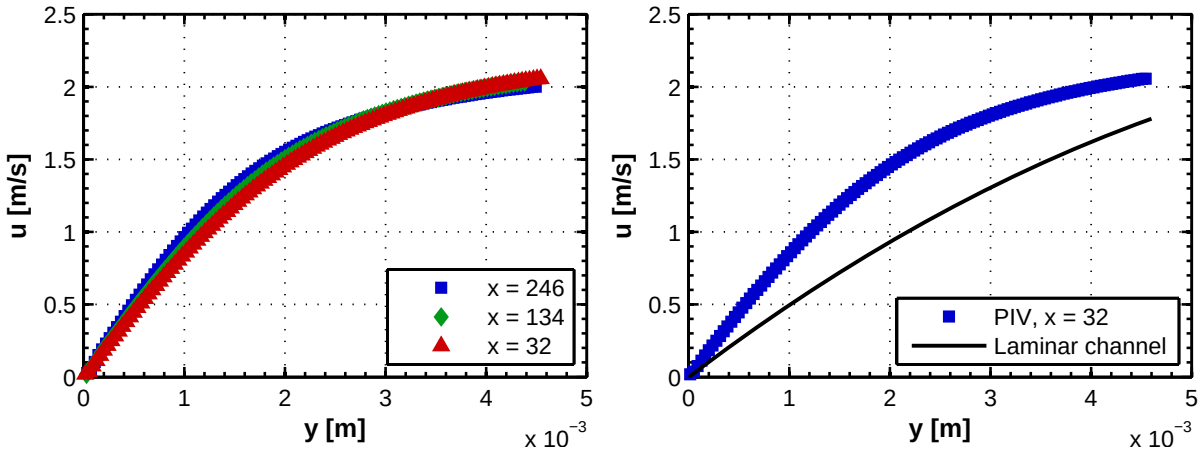

(a) Mean velocities.

(b) Comparison to laminar channel flow.

Figure 3.27: Laminar boundary layer in the 0° channel at $\dot{m} = 5\,\mathrm{g/s}$: PIV measurements.

3.3.5 Flow Structure in the 0° Channel

The channel geometry is apt for both, laminar and turbulent flashback experiments. For this reason, the flow in both regimes will be described at this point.

Laminar Boundary Layer

Figures 3.27 show mean axial flow velocities measured in the 0° channel at an air massflow of $\dot{m} = 5\,\mathrm{g/s}$. The Reynolds number based on the channel height is $\mathrm{Re}_{2h} = 1750$ at this operation point, which indicates laminar channel flow. Figure 3.27a shows the flow profiles at each measurement plane. The development of the laminar boundary layer towards a parabolic profile in downstream direction is clearly visible. The measured velocity gradients at the wall are summarized in Table 3.9. Figure 3.27b compares the experimental profile

Table 3.9: Wall velocity gradients of laminar channel flow at $\dot{m} = 5\,\mathrm{g/s}$.

E1, g [1/s]	*E2, g [1/s]*	*E3, g [1/s]*
1025.2	941.0	893.4

at E3 with fully developed laminar channel flow according to [Whi05],

$$u(y) = \frac{3}{2}\overline{u}\left(1 - \frac{y^2}{h^2}\right). \tag{3.15}$$

For Eq. (3.15), the origin of the y-coordinate is at the center of the channel. The laminar flow at E3 is far from being fully developed since the length between the last grid and E3 is only 32 duct heights. According to Schlichting [Sch82], a fully developed profile is expected after 70 duct heights at the given Reynolds number.

Turbulent Boundary Layer

Figures 3.28 show the mean and fluctuating streamwise velocities at the centerline of the 0° channel at air massflows of $\dot{m} = 30\,\mathrm{g/s}$ and 60 g/s. All results for 60 g/s were derived by cross-correlation with 8x8 pixel interrogation areas in order to raise spatial resolution in the laminar sublayer (see Appendix B, Fig. B.2 for a discussion). In Figs. 3.28a and 3.28c, the non-dimensional streamwise velocities at E1, E2 and E3 are plotted in a separate chart for each massflow. For 30 g/s, Fig. 3.28a reveals a good canonical structure with a slight overshoot in the buffer layer at all three measurement planes. For 60 g/s, however, mean velocities at E1 fall below the Spalding curve, whereas there is a good match in E2 and E3. This behavior follows the trend already observed in the 2° diffuser. Further illustration of the flow development is provided by Figs. 3.28e and 3.28f, which plot dimensional velocities in m/s for both massflows. For a massflow of 30 g/s, it can be clearly seen from Fig. 3.28e that the boundary layer is still evolving in the logarithmic region between E1 and E2. However, it is always in a self-similar state, as Fig. 3.28a has shown. For a massflow of 60 g/s, things are just the other way round. The dimensional velocities of Fig. 3.28f are very similar in general. However, the wall friction at E1 is slightly above its canonical value, such that the respective dimensionless profile in Fig. 3.28c falls below the Spalding curve.

The dimensionless turbulent fluctuations in Figs. 3.28b and 3.28d continue the development between the 4° and 2° diffusers. After the maximum is reached at $y^+ \approx 15$, the streamwise turbulent fluctuations are decaying strongly. The wall-normal fluctuations now reach a local maximum and are

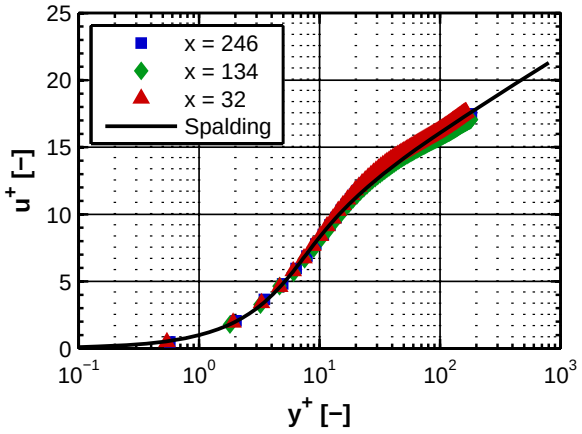

(a) $\dot{m} = 30\,g/s$: Mean velocities.

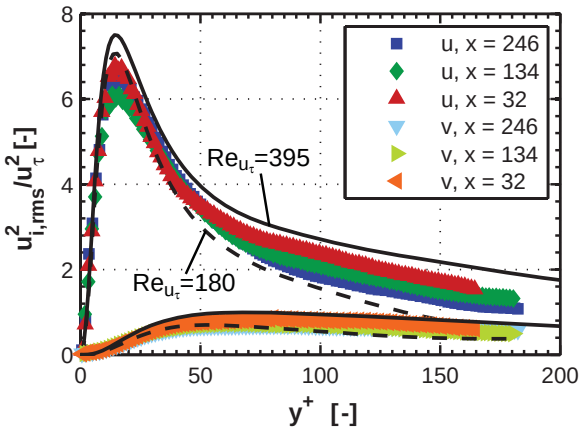

(b) $\dot{m} = 30\,g/s$: RMS velocities with DNS results [MKM99].

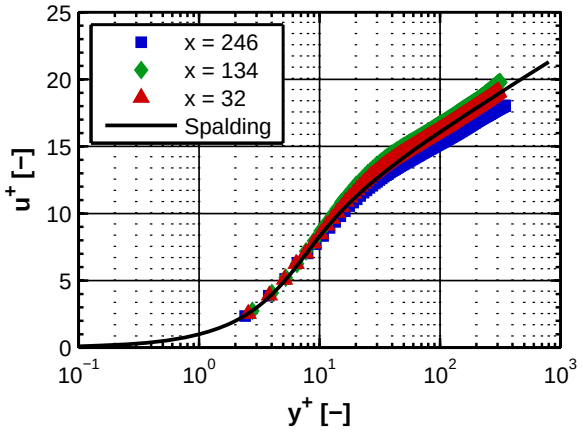

(c) $\dot{m} = 60\,g/s$: Mean velocities.

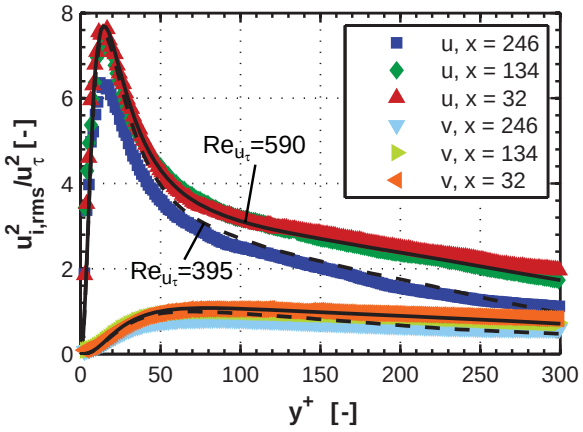

(d) $\dot{m} = 60\,g/s$: RMS velocities with DNS results [MKM99].

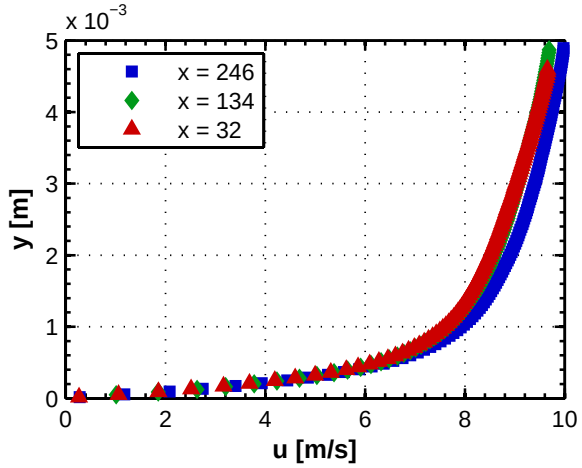

(e) $\dot{m} = 30\,g/s$: Dimensional mean velocities.

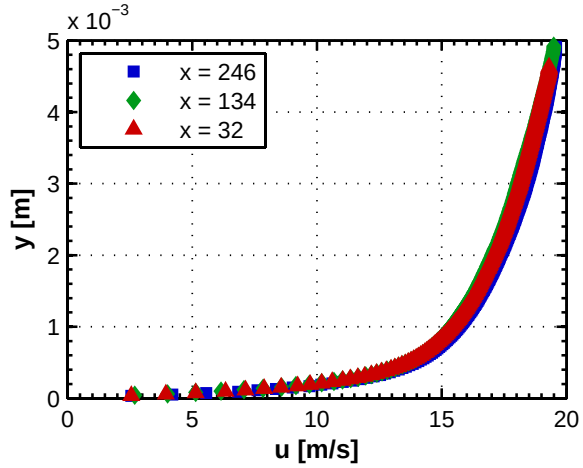

(f) $\dot{m} = 60\,g/s$: Dimensional mean velocities.

Figure 3.28: Turbulent boundary layer in the 0° channel: PIV measurements.

Table 3.10: Centerline wall friction in the 0° diffuser from PIV at $\dot{m} = 30\,\mathrm{g/s}$ and $60\,\mathrm{g/s}$.

Air massflow [g/s]	*E1,* τ_w *[Pa]*	*E2,* τ_w *[Pa]*	*E3,* τ_w *[Pa]*
30	0.388	0.383	0.356
60	1.399	1.153	1.218

decaying slowly in the second half of the measurement area. The uniformity of the dimensionless fluctuations for 30 g/s in Fig. 3.28b is good. It must be kept in mind that the fluctuations are normalized by the wall shear stress squared, meaning that measurement uncertainties in the linear sublayer fit have a strong impact on the position of the curves. For 60 g/s in Fig. 3.28d, the elevated wall shear at E1 causes the streamwise and wall-normal fluctuations to fall below the values at E2 and E3 as expected. For a quantitative comparison of the fluctuations, DNS results of Moser et al. [MKM99] are included as dashed and solid black lines. In Fig. 3.28b, the dashed line represents results for $\mathrm{Re}_{u_\tau} = 180$ and the solid line for $\mathrm{Re}_{u_\tau} = 395$, while the PIV measurements were made between $\mathrm{Re}_{u_\tau} = 310$ to 330. In Fig. 3.28d, the dashed line represents results for $\mathrm{Re}_{u_\tau} = 395$ and the solid line for $\mathrm{Re}_{u_\tau} = 590$, while the PIV measurements were taken between $\mathrm{Re}_{u_\tau} = 560$ to 620. The experimental fluctuations for 30 g/s agree well with the DNS at all measurement planes, only the maximum of the streamwise rms velocities is slightly shifted downwards. For 60 g/s, the agreement at E2 and E3 is very good. Table 3.8 lists wall friction values in the 0° channel. The wall friction at E1 and 60 g/s is the highest value in the present μ-PIV measurements. The corresponding friction velocity of $u_\tau = 1.1\,\mathrm{m/s}$ can be compared to Fig. 3.10 in order to estimate the fraction of turbulence kinetic energy which is represented by particle motion. It can be seen that with the present seeding generator at least 90% of the turbulent energy should be contained in particle motion, a result which supports the excellent match of experiment and DNS in Fig. 3.28d.

4 Experimental Studies of Laminar and Turbulent Wall Flashback

Based on a detailed knowledge of the boundary layer flow structure, which has been provided in the previous chapter, results from flashback experiments will be presented with ascending degree of detail now. At the beginning, the experimental procedure is explained and the observed flashback patterns are described phenomenologically. Flashback limits of H_2-air and CH_4-air mixtures with different types of flame anchoring, varying adverse pressure gradients and preheated mixtures will be presented. At the end of the chapter, the detailed flame structure during wall flashback will be discussed.

4.1 Experimental Procedure for Flashback Measurements

All flashback experiments presented in this work followed a fixed start-up procedure:

- Ignition of the two pilot burners.
- Establishment of the air massflow, which is held constant during each experiment.
- Establishment of fuel flow (H_2 or CH_4) just above the lean ignition limit.
- Slow increase of fuel flow until the lower main flame remains stable without pilot burner operation.
- Shut-off of the lower pilot burner.

The experiments were carried out in the lean and stoichiometric regime only ($0 \leq \Phi \leq 1$).

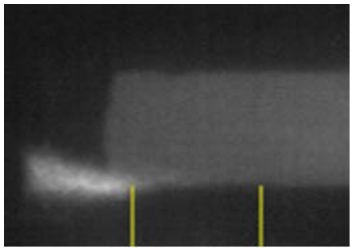

(a) Wake stabilization.

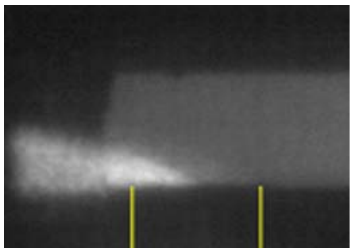

(b) Upstream creep on ceramic tile.

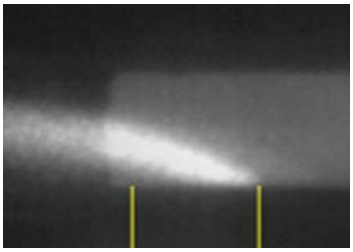

(c) Stabilization on ceramic tile.

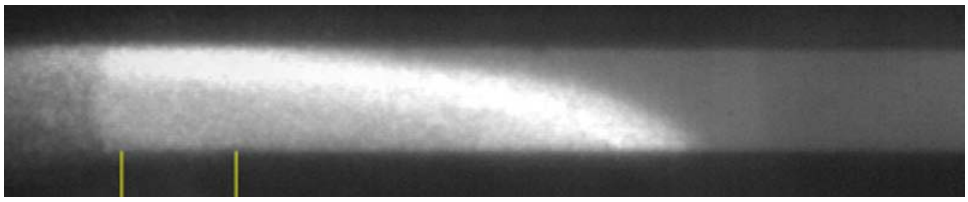

(d) Flame at flashback.

Figure 4.1: Side view of flame position before (a-c) and during (d) H_2-air flashback in the 0° channel.

4.1.1 Flashback Patterns in the Measurement Section

For the 0° channel, the equivalence ratio was increased in small steps until flashback occurred. The inverse of the equivalence ratio was used as control variable for the fuel massflow, which was adjusted in steps of 0.01 with a settling period of several seconds after each adjustment. Figures 4.1 illustrate the different flame configurations during flashback approach representative for H_2-air mixtures by instantaneous flame images. The ceramic tile of 20 mm thickness at the end of the measurement section (see Fig. 3.4) is attached flush with the lower channel wall in these figures and the flow direction is right to left. The images show overlays of the OH^* signal at an exposure time of 1 ms with an image of the measurement section at ambient light. The axial extent of the ceramic tile is marked by vertical yellow lines in each figure. In Fig. 4.1a, the flame is stabilized in the wake of the ceramic tile. The lower pilot burner was shut off at this point. On further increase of the fuel mass flow rate, the flame creeps upstream along the rough surface of the ceramic tile as shown in Fig. 4.1b. Some seconds before flashback, the flame stabilizes at the upstream end of the ceramic tile (Fig. 4.1c). Figure 4.1d shows the flame during

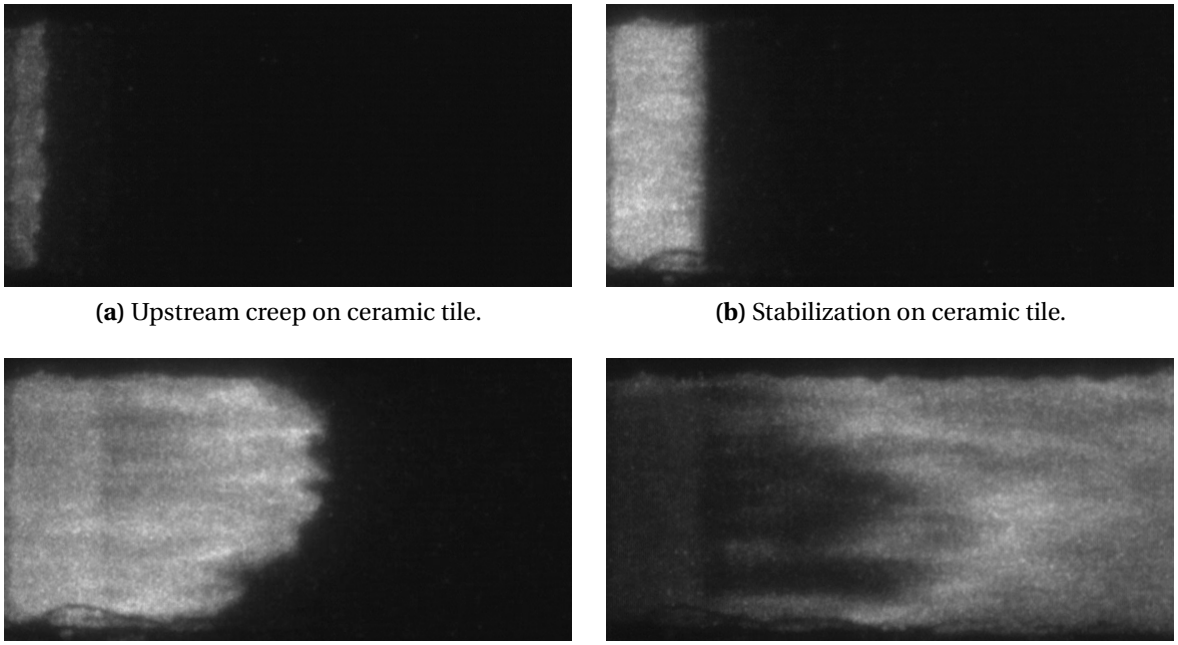

(a) Upstream creep on ceramic tile.

(b) Stabilization on ceramic tile.

(c) Leading part of the flame during flashback.

(d) Trailing part of the flame during flashback.

Figure 4.2: Top view of flame position before (a-b) and during (c-d) H_2-air flashback in the 0° channel.

flashback through the channel. The flame traveled upstream until it reached the thermocouple at the inlet of the measurement section which caused fuel shut-off. For very lean mixtures ($\Phi < 1/3$), the flame did not move upstream until shut-off in a sudden event, but entered the channel section only up to a certain upstream distance with strong oscillations in the axial position. In this case, the flashback point was defined conservatively as the point in time when the flame had entered the channel section such that it did not reattach to the ceramic tile during its axial oscillations. Figures 4.2 show essentially the same process during turbulent H_2-air flashback as Figs. 4.1, but from a top-view on the channel. The images show OH^* chemiluminescence with an exposure time of 1/30 s per image. After the upstream creep on the ceramic tile in Fig. 4.2a, the flame is stabilized uniformly on the tile surface as shown in Fig. 4.2b. Figure 4.2c shows the leading part of the flame during flashback. For the turbulent conditions shown here, the leading flame front has a jagged shape, as will be discussed in detail later. The trailing part of the flame is depicted in Fig. 4.2d, where the OH^* signal vanishes in the exhaust gas.

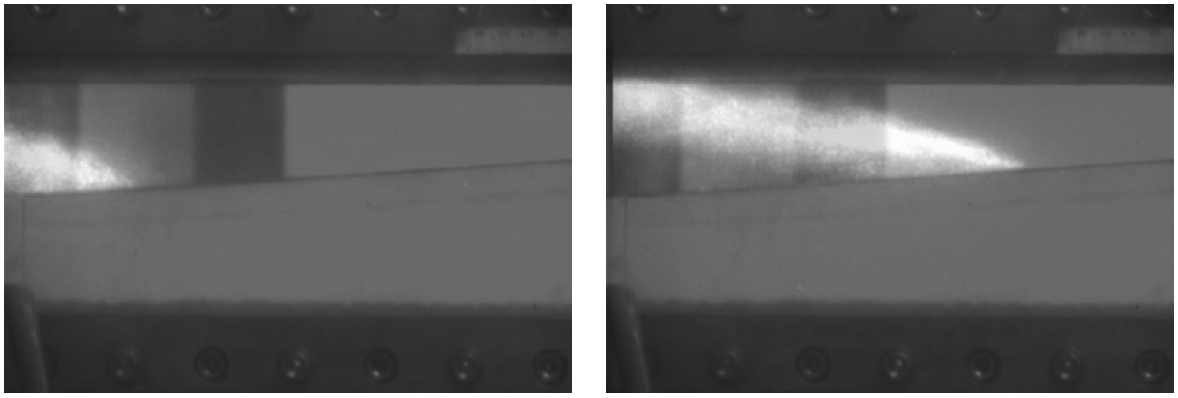

(a) Low equivalence ratio. **(b)** High equivalence ratio.

Figure 4.3: Instantaneous OH^* images of H_2-air flames during flashback in the 4° diffuser.

In the 2° and 4° diffuser configurations, sudden flashback through the whole measurement section is not observed. Due to the increasing wall shear in upstream direction, the flame propagates upstream only a finite distance until it reaches an equilibrium position with moderate axial fluctuations. The fluctuations have a frequency of a few Hertz. A correlation with a critical velocity gradient thus involves the determination of a mean axial position of the flame tip over a sufficiently long period of time. Although the term 'flashback' is not quite apt for the equilibrium flame stabilization inside the diffuser, it will be subsequently used for simplicity. Figures 4.3 illustrate the flame shape inside the 4° diffuser during flashback for two different equivalence ratios by OH^* images with an exposure time of 1 ms. As for Figs. 4.1, the geometry of the measurement section has been used as background to make the images more instructive. Figure 4.3a shows an instantaneous picture of the flame which is stabilized inside the boundary layer shortly upstream of the downstream end of the ramp. When the equivalence ratio is increased from this point, the flame moves upstream until it reaches a new equilibrium position, as shown in Fig. 4.3b. A top view on the flashback process in the diffuser geometries reveals a similar flame shape as in the 0° channel case.

4.1.2 Calculation of Wall Friction for Arbitrary Flashback Points

The wall shear stress was measured directly only for a limited number of flow velocities and pure air, as presented in Sec. 3.3. However, flashbacks were observed at a broad range of inlet massflows, mixture densities and viscosities. For this reason, wall shear distributions were calculated by means of semi-empirical correlations or numerical simulations for each experimental point, as will be described below. Mixture densities were calculated assuming ideal gas behavior, while the dynamic viscosity of a mixture was approximated by the method of Wilke (see [Whi05]). For both calculations, the temperature measured by the thermocouple at the inlet of the measurement section was considered as the mixture temperature.

Wall friction in the 0° channel has been calculated from a correlation for fully-developed channel flow between two parallel plates. A log-law approximation of the velocity profile across the entire channel can be integrated to give a relation between the bulk channel velocity $\overline{u}$ and the shear stress velocity [Whi05]:

$$\overline{u} = u_\tau \left(\frac{1}{\kappa} \ln \frac{h\, u_\tau}{\nu} + \mathrm{B} - \frac{1}{\kappa} \right) \tag{4.1}$$

From this relation, the velocity gradient g, which is contained in u_τ, can be iteratively calculated. A comparison of the wall friction determined from μ-PIV experiments in isothermal flow with the results of Eq. 4.1 is given in Fig. 4.4. On the x-axis, the distance from the downstream end of the ramp is shown. On the y-axis, the ratio between experimental and correlation wall shear is displayed. The graph shows entries for two air massflows, 30 g/s and 60 g/s, at the three measurement planes E1, E2 and E3. The measured shear stresses are converging towards the correlation value in downstream direction. Since the conditions at the downstream end of the channel are determining the flashback point, the wall shear approximation by Eq. 4.1 is an appropriate choice with a conservative error estimation of ±10%.

As already indicated, the derivation of critical velocity gradients for the diffuser geometries is a two-step process. First, the time-mean axial position of the flame tip has to be determined. Second, the wall shear along the lower wall of the diffuser is calculated by numerical simulation and the wall shear is

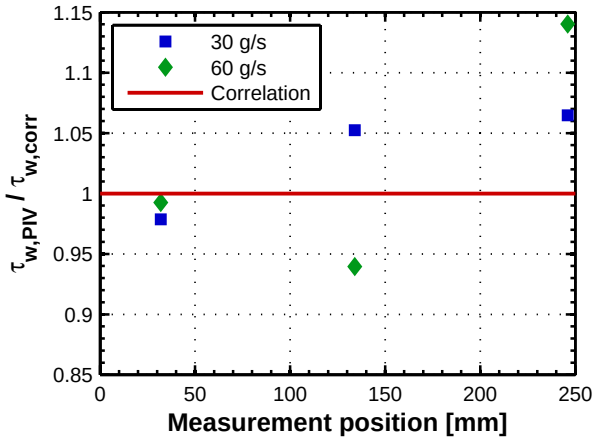

Figure 4.4: Comparison of wall shear stresses from PIV with a plane channel correlation.

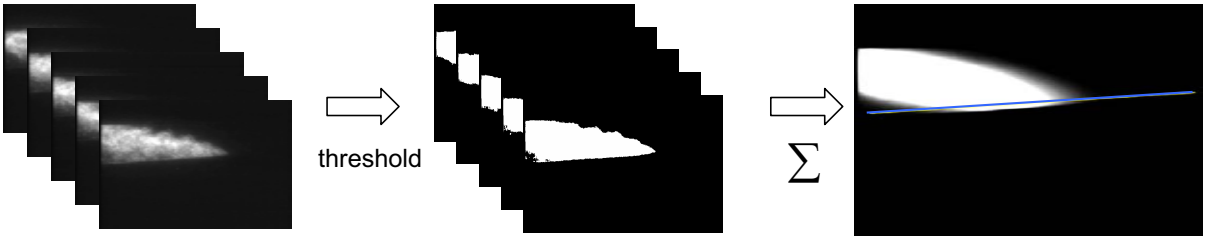

Figure 4.5: Derivation of mean flame position by image interpolation.

evaluated at the mean flame tip position. Figure 4.5 illustrates the averaging process used to determine the mean flame position. For each operation point, the flame was recorded at its equilibrium position for a fixed equivalence ratio using the Hamamatsu camera. Single images from a measurement series of 30 seconds duration were binarized with regard to the flame region by specifying a threshold. These images were summarized such that a time averaged image normalized between 0 and 1 was produced. Along a line parallel to the ramp surface, which intersected the mean flame tip region, and approaching this region from upstream, the point of 50% of the maximum intensity was taken as the mean flame tip position at wall flashback. The numerical simulation of the diffuser flow for wall shear determination was carried out in ANSYS CFX 12.0. A two-dimensional representation of the diffuser geometry with full resolution of the wall boundary layers was used in conjunction with the Shear Stress Transport (SST) RANS turbulence model with standard constants. At the inlet of the diffuser, a fully developed plane channel profile was specified.

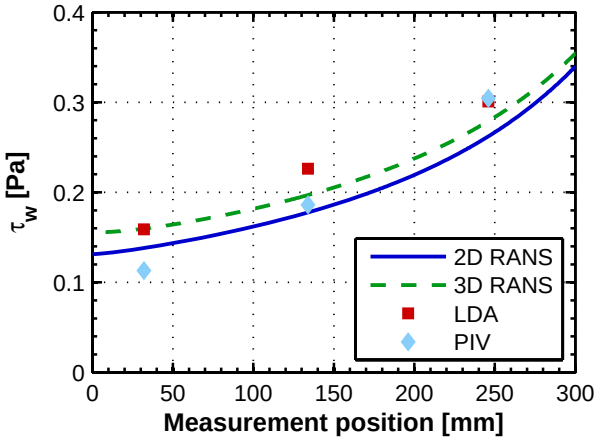

Figure 4.6: Comparison of wall shear stresses from numerical 2D RANS simulations and LDA measurements.

Further details of the numerical simulation can be found in [ES11a]. The validity of the RANS simulations for wall shear determination will be checked here by comparing simulations of 60 g/s pure air inlet massflow with velocity measurements inside the 4° diffuser. Figure 4.6 shows the numerical wall shear as a function of the measurement position for the two-dimensional grid used in [ES11a] and a three-dimensional grid with fully resolved boundary layers (5.6 million nodes) as well as mean LDA and PIV results at positions E1, E2 and E3. It is obvious that the simulation generally underpredicts the wall shear measured in the LDA experiment. The two-dimensional grid results deviate by -10% to -20% from the LDA values. Since the turbulence model is expected to perform reasonably well for the strong adverse pressure gradient flow investigated here [Wil93, Men94], these rather strong deviations are probably caused by a disagreement in boundary conditions. A more detailed modeling of the velocity profile at the inlet based on the CTA velocity profiles did not change the underprediction appreciably, but the deviations are approximately halved on the three-dimensional grid as shown in the figure, which indicates a certain influence of the boundary layer development on the side walls of the channel. Turning towards the PIV results, the gradient of wall shear along the diffuser ramp in the measurements is stronger than the simulation predicts. As it has already been discussed in Sec. 3.3.3, the mirror wake surely has an influence here.

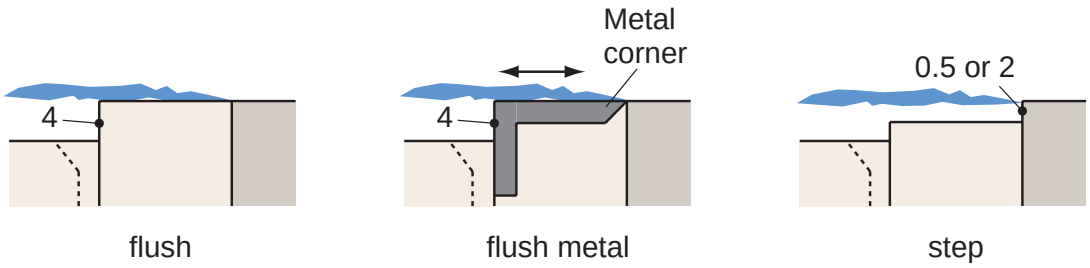

Figure 4.7: Different configurations for H_2-air flame stabilization in the 0° channel.

Conclusively, the qualitative match between LDA data and CFD results is superior compared to PIV data. A three-dimensional grid reduces deviations of wall shear towards 10% between RANS and LDA, however, this grid was not used for the data evulation due to its large computational cost. Since the qualitative shape of the two- and three-dimensional simulated wall shear agree well with each other, the flashback results of the 2° and 4° diffuser will be interpreted based on two-dimensional simulations with a quantitative uncertainty tending towards higher critical gradients.

4.2 Flashback Limits for Turbulent Boundary Layers

As the literature on turbulent wall flashback limits is limited to flows in tubes, results of the 0° channel are presented first to allow a direct comparison. Flashback limits for flows with adverse pressure gradients and preheated mixtures are presented afterwards.

4.2.1 Atmospheric Mixtures in the 0° Channel

The investigations of turbulent flashback in the 0° channel geometry were limited to H_2-air mixtures since only laminar flashback is observed for CH_4-air mixtures in that case. Different configurations for the stabilization of the lower main flame were examined in the 0° channel experiments as sketched in Fig. 4.7. In the 'flush' configuration, the ceramic tile is flush with the steel block. The ceramic block downstream of the ceramic tile has a vertical offset of 4 mm. The dotted lines represent the slit of the pilot burner. Configu-

ration 'flush metal' has the same dimensions, but a stainless steel corner has been mounted onto the ceramic tile. The corner is sharpened on its upstream end in order to minimize thermal contact between corner and steel block. In configuration 'step', the ceramic tile is offset by either 0.5 mm or 2 mm, which results in an offset between tile and ceramic block of 3.5 mm or 2 mm, respectively. The position of the flame prior to flashback is also illustrated in Fig. 4.7 for each configuration. In the flush case, the flame is situated right on the ceramic tile, as already shown in Fig. 4.1c. Due to the low thermal conductivity and high heat capacity of the ceramic material, a high surface temperature is achieved which acts as a stable flame holder. In contrast, the flame position on the metal corner is fluctuating since its thermal conductivity does not allow for thermal, but just aerodynamic stabilization of the flame due to surface inhomogeneities, such that the flame anchor is easily displaced by flow fluctuations. As a result, the experimental rig exhibited thermoacoustic instabilities for most of the operation points in the flush metal configuration, which is the reason for scarce flashback data for this case. In the third configuration, the flame is stabilized in the shear layer trailing behind the corner of the stainless ramp, which is assisted by a small product recirculation zone behind the backward facing step. The heat conduction to the ramp during flashback approach is maximum in this case. However, the impingement cooling inside the ramp was sufficient to keep the surface temperature of the ramp within bounds as during all experiments, the maximum measured wall temperatures lay below 40 °C, which has a negligible influence on the flashback process at atmospheric conditions [LE43].

Figure 4.8 shows the experimental results for turbulent wall flashback limits in terms of critical velocity gradients calculated from Eq. (4.1) for atmospheric H_2-air mixtures in the 0° channel. For the channel results, each symbol represents one flashback experiment. The data scatter of the flush series includes virtually all experimental error sources, such as day-to-day variations, re-manufacturing of ceramic components, different pilot burner configurations and reassembling of the whole measurement section. Additionally, the blowing air has been varied between 2% and 3% of the main air massflow at each operational point. It can be seen from the low scatter in the flush data that the resulting repeatability of flashback limits is very good. An offset of the

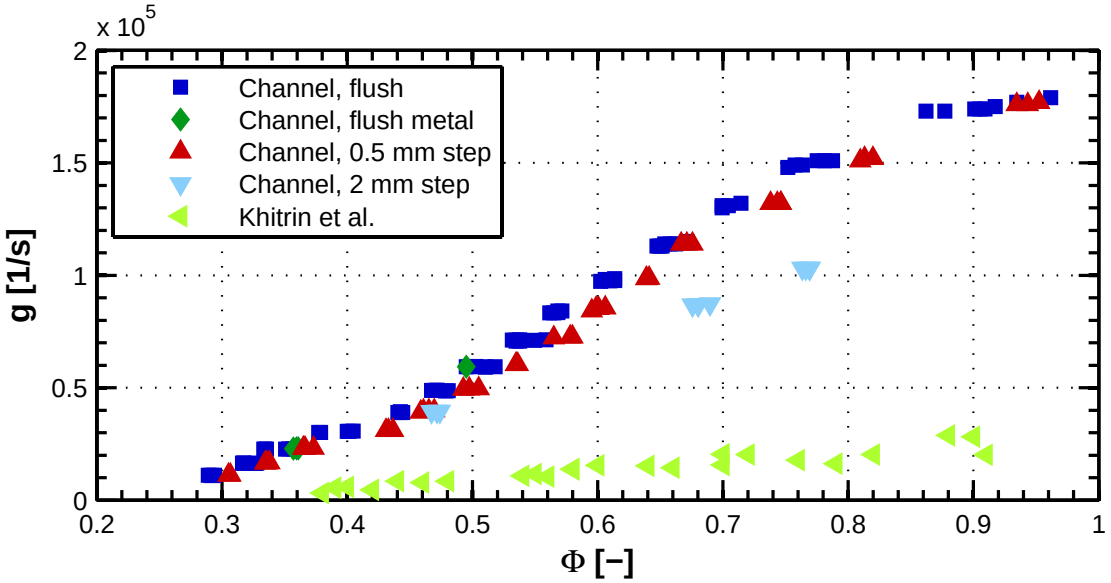

Figure 4.8: Turbulent wall flashback limits for atmospheric H_2-air mixtures in the 0° channel.

first three sets of points towards leaner conditions can be observed for both, flush and step configurations. This is explained by the gradual flashback behavior of the rig in this region as explained before. For higher Φ, flashback was a sudden event and thus more clearly defined.

For comparison, the turbulent flashback data from unconfined tube burners of [KMSS65] are included in Fig. 4.8. At a glance, it can be seen that the flashback limits in the channel geometry, where the flame is confined inside the channel already before flashback, differ by up to one order of magnitude from the tube burner limits. A trend regarding the influence of the backward-facing step used as flame holder can be determined by comparing the limits between the flush and the step configurations. The flashback limits for the 0.5 mm step lie consistently below the flush case for lean mixtures. Close to $\Phi = 1$, the difference vanishes. For the 2 mm step, the three different air massflows considered confirm the trend towards lower flashback susceptibility with increasing step height. The influence of the surface material of the 20 mm tile downstream of the stainless ramp, either ceramic or metal, is obviously negligible since the flush and flush metal cases have the same flashback limit for a given equivalence ratio. The large difference between flashback limits in unconfined tube burners, where the flame is anchored in free atmosphere, and the con-

fined 0° channel is an important finding because it demonstrates that existing literature results on turbulent flashback limits are not conservative for the design criteria of safety against a flame which accidentally has entered the premixing section.

If the difference between confined and unconfined flashback limits has universal character and is not caused by some peculiarity of the 0° channel experiment, elevated flashback limits should also be observed for a confined flame in a tubular geometry. An according experiment has been conducted by Baumgartner [EBS12]. He recorded flashback limits of premixed H_2-air flames in non-swirling, turbulent tube flow for both, unconfined and confined flame holding prior to flashback. The tube had an inner diameter of 40 mm. In the unconfined case, the flame was stabilized in free atmosphere above the cooled tube rim. For confined stabilization, a concentric ceramic block was attached downstream of the tube rim, which had a streamwise extension of 30 mm and an inner diameter of 44 mm. The ceramic provides a confined flame stabilization similar to the 2 mm 'step' configuration of the 0° channel. Therefore, the results of Baumgartner are a valuable validation set for the experiments presented here, since the flow and flame configuration as well as the rig structure are different, the only common ground being the flame stabilization inside the duct section.

Turbulent wall flashback limits for atmospheric H_2-air mixtures in the tube burner are summarized in Figs. 4.9 and 4.10. In Fig. 4.9, the flashback limits of the unconfined tube burner are compared to literature values from [KMSS65]. It can be clearly seen that the literature values for $d = 38$ mm could be reproduced accurately over a wide range of equivalence ratios. In Fig. 4.10, the flashback limits of the three different configurations of the channel setup are compared to confined tube burner limits. Furthermore, the unconfined tube burner limits of Baumgartner from Fig. 4.10 are included again. The flashback limits of the confined tube burner strictly follow the 0° channel values for very lean mixtures and also match the offset of the 2 mm step results from the channel for increasing Φ. These findings confirm that the increase in flashback propensity observed in the channel revealed a fundamental difference between confined and unconfined flame holding prior to flashback. A physi-

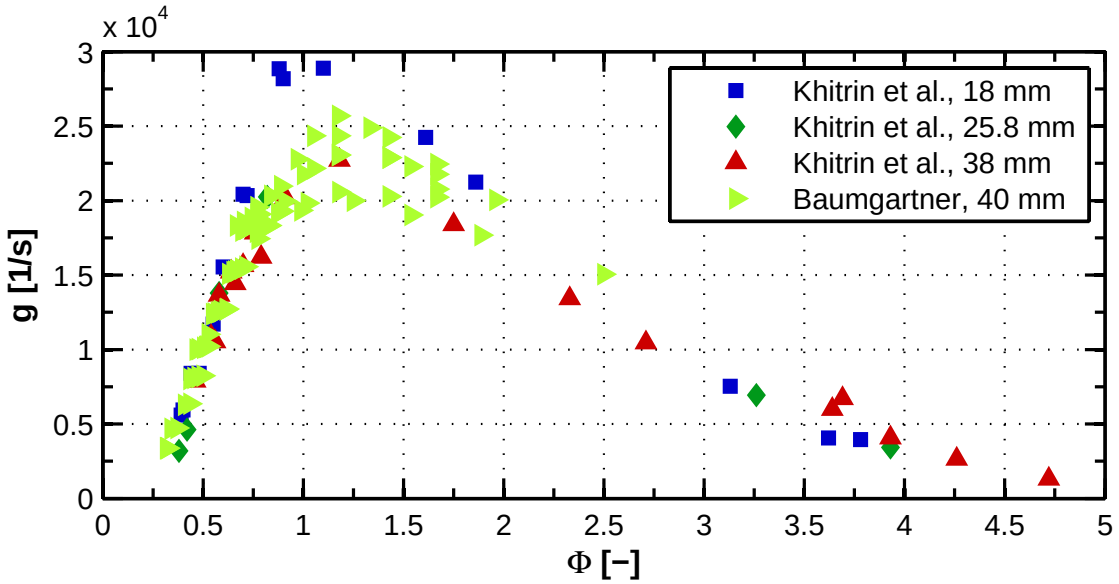

Figure 4.9: Turbulent wall flashback limits for atmospheric H_2-air mixtures in an unconfined tube burner [KMSS65, EBS12].

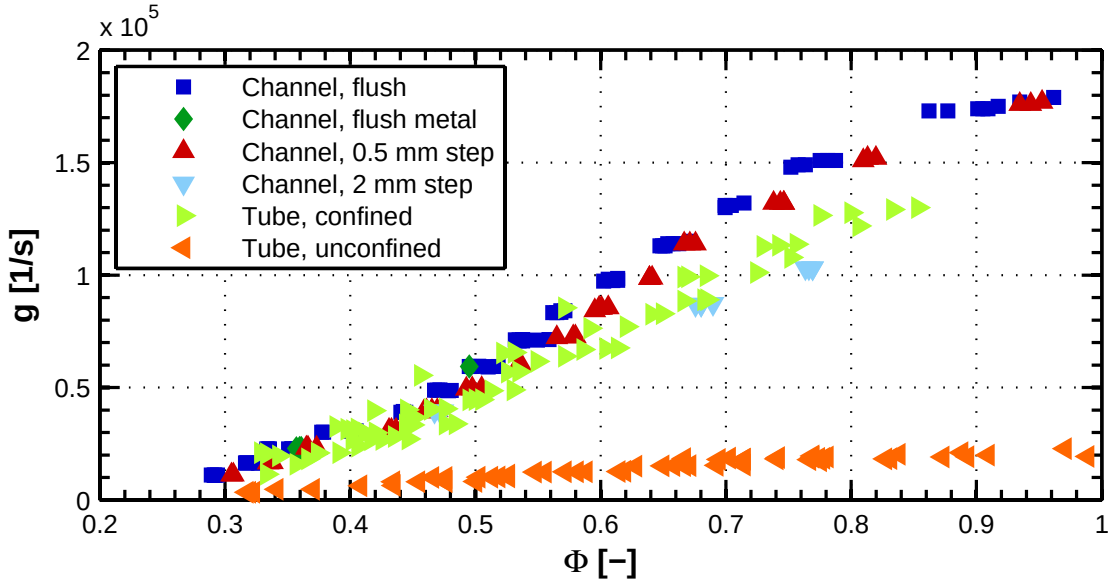

Figure 4.10: Turbulent wall flashback limits for atmospheric H_2-air mixtures in a confined tube burner [EBS12].

Table 4.1: Effect of wall heating for atmospheric turbulent wall flashback in the 4° diffuser.

Fuel	$\dot{m}_{air}$ [g/s]	Φ at flashback [-]	g_c [1/s]	$g_{c,t^*=0.5-1}$ [1/s]
CH_4	40	0.8	5329	5336
CH_4	50	0.8	6952	6952
H_2	50	0.25	8098	8067
H_2	60	0.25	10047	10121
H_2	100	0.29	31899	31798
H_2	120	0.29	42576	42786

cal explanation for the observed increase in flashback propensity for confined flames will be provided in Chap. 6. However, it can already be noted here that the difference between confined and unconfined wall flashback limits cannot be explained based on the critical gradient model since isothermal boundary layer development is not appreciably affected by the conditions at duct exit.

4.2.2 Atmospheric Mixtures in 2° and 4° Diffusers

According to the experimental procedure in the diffusers described before, the mean flame tip position was measured and mean critical gradients g_c were determined by numerical wall shear simulations for CH_4-air and H_2-air mixtures. Time averaged OH^* images for the determination of the mean flame tip position are exemplary shown for the 4° diffuser in Figs. 4.11. Main flow is going from right to left and the geometry of the measurement section has been used as background again. The images show very similar mean flame shapes, and it can be seen that there is a unique mean flame position when approaching the flame tip region from upstream. Before the results for mean critical gradients in the diffuser geometries are presented, the influence of wall heating during the recording of the flame at its equilibrium position on the ramp shall be discussed. During the measurement duration of 30 s, the temperature of the lower wall of the diffuser inevitably rises in spite of impingement cooling from below. In case of the 4° diffuser, the maximum wall temperature as

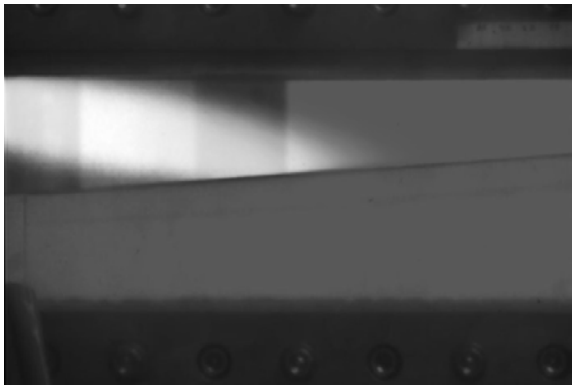

(a) CH_4-air, $\dot{m}_{air} = 40$ g/s, $\Phi = 0.8$.

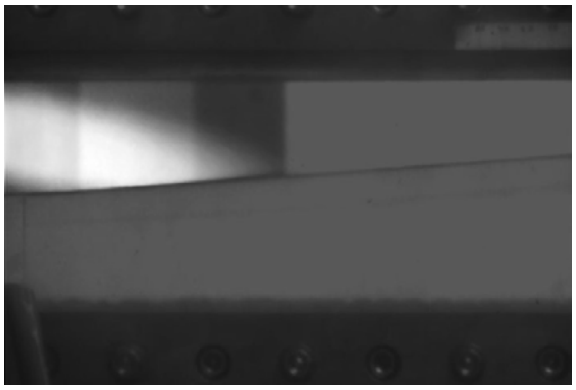

(b) CH_4-air, $\dot{m}_{air} = 50$ g/s, $\Phi = 0.8$.

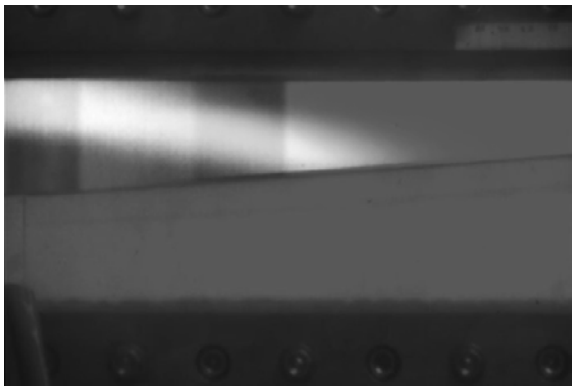

(c) H_2-air, $\dot{m}_{air} = 50$ g/s, $\Phi = 0.25$.

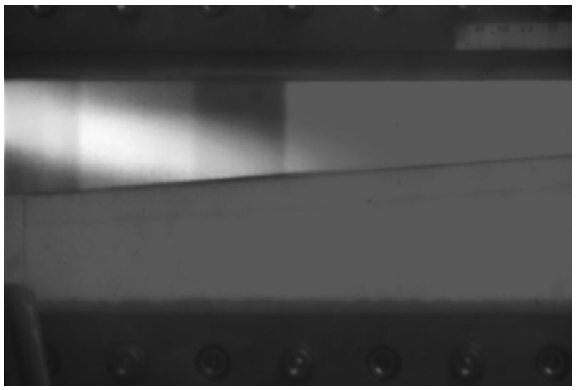

(d) H_2-air, $\dot{m}_{air} = 60$ g/s, $\Phi = 0.25$.

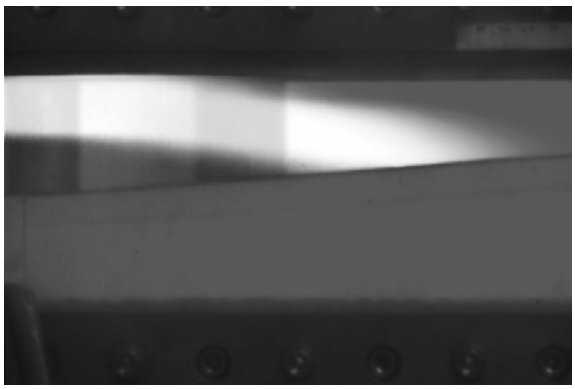

(e) H_2-air, $\dot{m}_{air} = 100$ g/s, $\Phi = 0.29$.

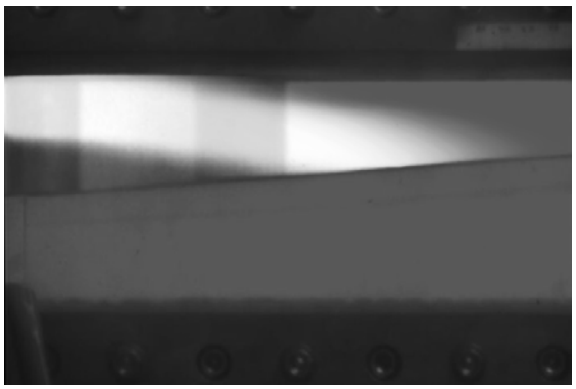

(f) H_2-air, $\dot{m}_{air} = 120$ g/s, $\Phi = 0.29$.

Figure 4.11: Time averaged flame images for the determination of mean flame tip position in the 4° diffuser for CH_4-air and H_2-air mixtures.

measured by the thermocouples was 80°C. Due to higher wall shear stresses and the resulting increased heat transfer, the maximum wall temperature in the 2° diffuser raised up to 160°C. Since the heating of the wall is a transient process, a proper way to examine the influence of wall heating on the equilibrium flame position is a comparison of mean flame positions determined from the first half and from the second half of an experimental record, each lasting 15 s. If the mean positions are close to each other, the heating of the wall has negligible influence on the mean flame position and thus on the critical gradients determined from it. Table 4.1 lists the effect of wall heating for the experiments in the 4° diffuser. In each line, the fuel as well as the air massflow rate are listed, followed by the equivalence ratio at which the position of the flame at flashback was recorded. The mean critical gradient g_c is given as extracted from the respective numerical wall friction simulation. The last column, $g_{c,t^*=0.5-1}$, is the mean critical gradient as calculated from the second half of each data set. By comparing g_c and $g_{c,t^*=0.5-1}$ in each line, it is concluded that the heating of the ramp during the experimental time had no significant effect on the determined mean flashback positions in the 4° diffuser. The same data for the 2° diffuser reveals differences of up to 8% in mean flame positions between first and second half of the experiments if the wall temperature had raised above 100°C at the end of the experiment, which is in accordance with the statement in [LE43]. In these cases, only the first half of each experiment was used for the determination of mean critical gradients.

The results for turbulent wall flashback limits of atmospheric H_2-air mixtures in the 2° and 4° diffusers are summarized in Fig. 4.12. For comparison, the 0° channel results for flush flame stabilization are also shown. Turbulent flashback of CH_4-air mixtures in the 2° diffuser was not achievable. The turbulent flashback limits for CH_4-air mixtures in the 4° diffuser are included in Table 4.1. By inspection of Fig. 4.12 it becomes clear that critical gradients of boundary layers with adverse pressure gradients tend to lie above straight channel limits for a given equivalence ratio. In the 2° diffuser, the limits are approximately the same for very lean mixtures and raise above the channel case starting from $\Phi \approx 0.35$. However, it must be kept in mind that the numerical simulation of diffuser flow tends to underpredict wall shear, as described by Fig. 4.6, such that the deviation may start earlier in reality. In the 4° diffuser, only

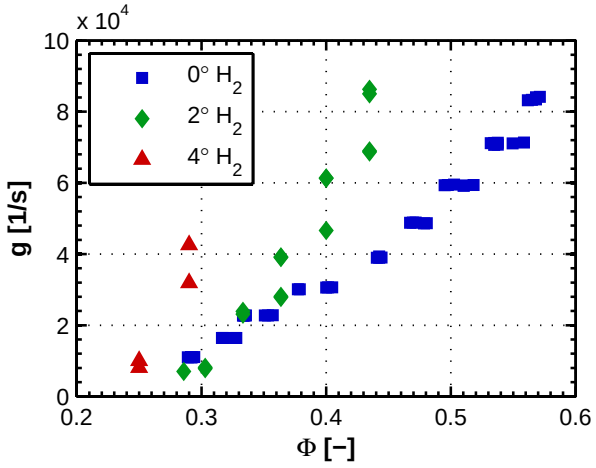

Figure 4.12: Turbulent wall flashback limits for atmospheric H_2-air mixtures with moderate to high adverse pressure gradients.

very lean mixtures could be investigated due to restrictions in the maximum massflow rates of air and fuel. The recorded values lie substantially above the 2° case, showing that an increase of the adverse pressure gradient increases the flashback propensity, too.

Another interesting observation can be made from Fig. 4.12. All experiments in the 4° diffuser (both fuels) as well as part of the 2° experiments (Φ = 0.364, 0.4 and 0.435) were carried out such that flashback at the same equivalence ratio was observed for two different air massflows. It turns out that the critical gradients for high $\dot{m}_{air}$ lie consistently above the data for lower $\dot{m}_{air}$, which can also be seen from Table 4.1. In other words, if the mean position at wall flashback lies more downstream from the diffuser inlet, as it is the case for higher $\dot{m}_{air}$ at a given Φ (see Fig. 4.11), then the boundary layer is obviously more susceptible to flashback as compared to positions closer to the inlet.

Conclusively, the results for the diffuser geometries challenge the critical gradient model once again. For a given velocity gradient, the velocity distribution in the near-wall region does not change appreciably between 0° channel flow and the diffuser flows with an adverse pressure gradient, at least for the 2° geometry (see discussion in Sec. 2.1.5). Therefore, a flashback model solely based on the wall velocity gradient should perform well if no further influ-

ential factors were present. Physical explanations for the observed deviations will be discussed in Sec. 4.3.3.

4.2.3 Preheated Mixtures in 0° Channel

Preheated experiments were limited to the 0° channel since flashback could only be observed in a broad range of equivalence ratios in this geometry due to its high wall shear. Only the flush configuration of the ceramic tile was considered. Care was taken to ensure that the lower wall of the diffuser is at approximately the same temperature as the mixture at the instant of flashback to allow a concise interpretation of the results. At the beginning of each preheated experiment, the rig was run at a higher massflow rate and at higher preheat temperature than the target values to heat up the wall of the ramp, which was additionally isolated with ceramic plates from below. In a transient procedure, the air massflow and electrical power of the preheater were reduced and equivalence ratio increased, such that the addition of cold H_2 to the hot air stream and the convective cooling of the ramp resulted in a close match between wall temperature and mixture temperature at flashback. The mixture temperature was measured with the centered thermocouple also used for flashback detection at the inlet of the measurement section. Two nominal mixture temperatures were aimed for, 200 °C and 400 °C. The deviations of the measured wall and mixture temperatures from the aimed value were within ±10 °C for 200 °C and ±15 °C for 400 °C, respectively.

The measured turbulent wall flashback limits for preheated H_2-air mixtures in the 0° channel are presented in Figs. 4.13. The wall shear has been determined from Eq. (4.1) again, which is justified since the correlation is based on the universal logarithmic law of the wall. In Fig. 4.13a, the measured flashback limits for 200 °C and 400 °C are compared to room temperature results for the flush configuration from Fig. 4.8. It is shown that critical gradients consistently increase with increasing preheat temperature of the mixture. Figure 4.13b compares the preheated flashback limits with the proportionality based on unconfined tube burner experiments proposed by Fine [Fin59] (Eq. (1.6)). The graphs make clear that the preheated confined flashback limits do not

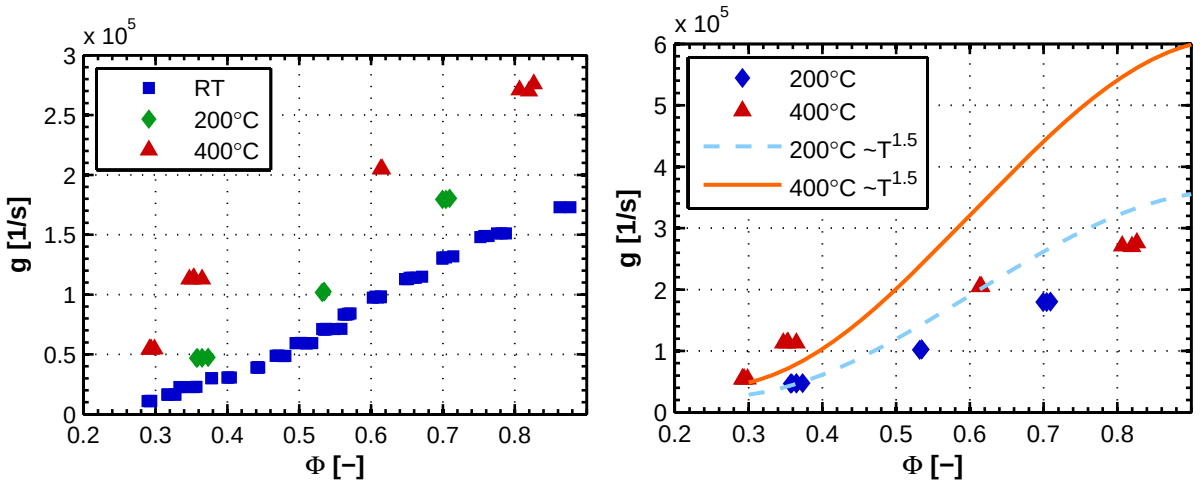

(a) Comparison to atmospheric channel results.

(b) Comparison to proportionality proposed by Fine [Fin59].

Figure 4.13: Turbulent wall flashback limits for preheated H_2-air mixtures in the 0° channel.

follow the temperature power law derived from unconfined tube burner experiments. Thus in Chap. 6, a new correlation model for wall flashback will be proposed which also includes temperature dependencies.

4.2.4 Turbulent Combustion Regimes

For scaling purposes, it is useful to classify the turbulent combustion regimes according to Fig. 2.11 in which wall flashbacks have been observed in the present work. In order to compare flame length and time scales with turbulent quantities during wall flashback, a meaningful definition of integral turbulent quantities l_t and $u_t^{'}$ at the position of the flame anchor inside the boundary layer has to be found.

As will be shown later, the flame tip is located inside the buffer layer and the beginning of the logarithmic region of the turbulent boundary layer during wall flashback. The dominant turbulent structures in this region are quasi-streamwise vortices. Thus for kinematic reasons, the diameter of these vortices, which is approximately $d^+ \approx 30$ as already mentioned (see Sec. 2.1.4), will be used as the integral turbulent length scale l_t. Concerning turbulent fluctuation velocities, it has been shown that axial fluctuations $u^{'}$ contain

most of the turbulent kinetic energy (see Figs. 2.3). Furthermore, the peak value of u_{rms}^2/u_τ^2 at $y^+ \approx 15$ is mainly a function of the adverse pressure gradient. Thus for a conservative estimation of the impact of turbulent fluctuations on the flame, the integral velocity fluctuations u_t' will be calculated from the friction velocity u_τ times a constant factor which depends on the ramp angle as follows: For 0°, 2° and 4°, the factors are the square roots of 7 (Figs. 3.28), 8.5 (Figs. 3.26) and 10 (Figs. 3.24), respectively. To estimate the flame thickness δ_f, Eq. (2.23) has been used.

Figure 4.14 shows the resulting turbulent combustion regime diagram according to Fig. 2.11 with a representation of the whole span of flashback conditions measured in the present work. The diagram makes clear that the ob-

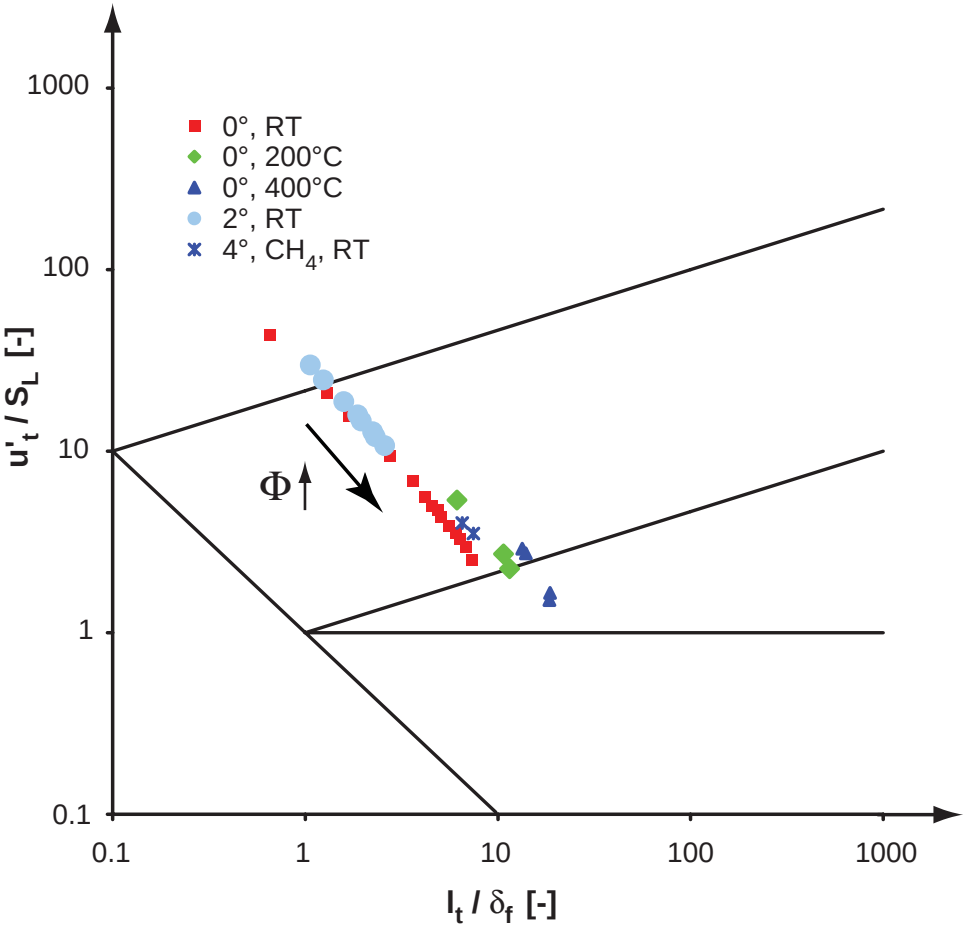

Figure 4.14: Turbulent combustion regimes of wall flashbacks observed in the present work.

served flashback points mainly lie within the regime of thin reaction zones. At

the lean end of the atmospheric 0° and 2° samples, the plotted data is doubtful as the prediction of laminar burning velocities by the Cantera simulations tend to zero, thus the points close to and inside the broken reaction zone regime should not be over-interpreted here. The highest equivalence ratios of the preheated experiments stretch towards the corrugated flamelet regime. Indeed, flames at wall flashback in preheated mixtures showed a change in macroscopic structure towards higher smoothness of the flame surface. Finally, it has to be noted that the flame thickness assumed for the discussion above provides scaling for one-dimensional, unstretched and adiabatic flames. Close to the wall, however, these assumptions are not valid and Fig. 4.14 only can have approximate character.

4.3 Details of Flame Propagation in the Near-Wall Region

The detailed flame structure during wall flashback will be presented in this section. The experiments cover the channel and both diffuser geometries, laminar and turbulent flow regimes as well as H_2-air and CH_4-air mixtures at room temperature.

4.3.1 Macroscopic Flame Structure

Figures 4.15 illustrate the fundamental difference between laminar and turbulent wall flashback observed in the measurement section. The pictures show a top view on the flame at wall flashback without the mirror holder inside the flow path. On the left, flames in the 0° channel are depicted. The laminar CH_4-air flame shown in Fig. 4.15a propagates with a homogeneous, unwrinkled reaction surface. The leading flame zone has only one local maximum with low curvature in the center region of the channel. Left and right of the leading flame zone, the normal of the flame front departs from the axial direction, which indicates flow velocities exceeding the flame velocity in that region. In contrast, the reaction surface of the turbulent H_2-air flame in Fig. 4.15c is highly irregular, showing macroscale wrinkling and flame cusps in its leading zones. On the right, wall flashbacks in the 4° channel are shown. Here,

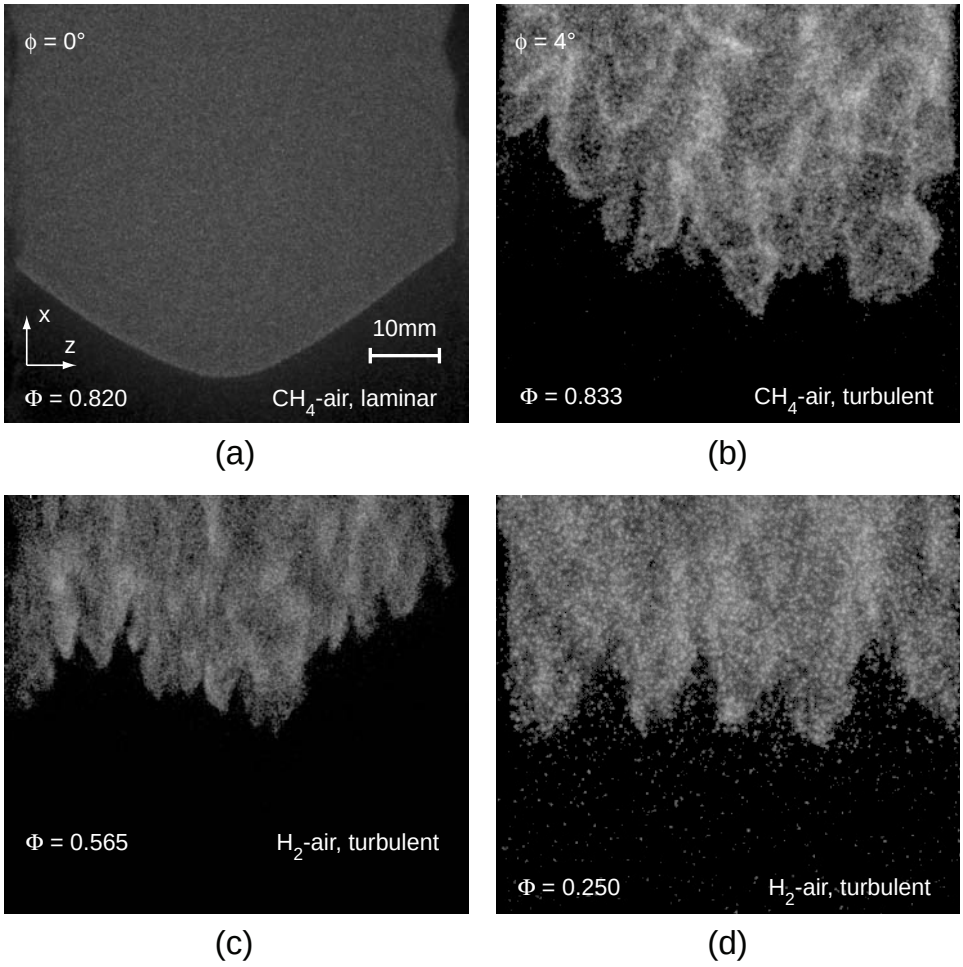

Figure 4.15: Top view on macroscopic flame structure during laminar and turbulent wall flashback.

turbulent flashback can be observed for both fuels, CH_4 and H_2. The leading flame zones have a similar cusp structure as in the turbulent 0° channel case. This is remarkable since the fuel-air mixtures in the right part of the figure have very different Lewis numbers and equivalence ratios.

The detailed structure of the cusps, however, is not the same for different ramp angles and fuels. In general, the cusps follow a well-defined pattern of formation and break-up for H_2-air flashback in the 0° and 2° geometries, which is shown in Fig. 4.16 exemplarily for the 0° channel. The images show a time series of OH^* shots from top view. Three cusp groups have been marked by circles to facilitate tracking. After formation, a cusp either travels upstream,

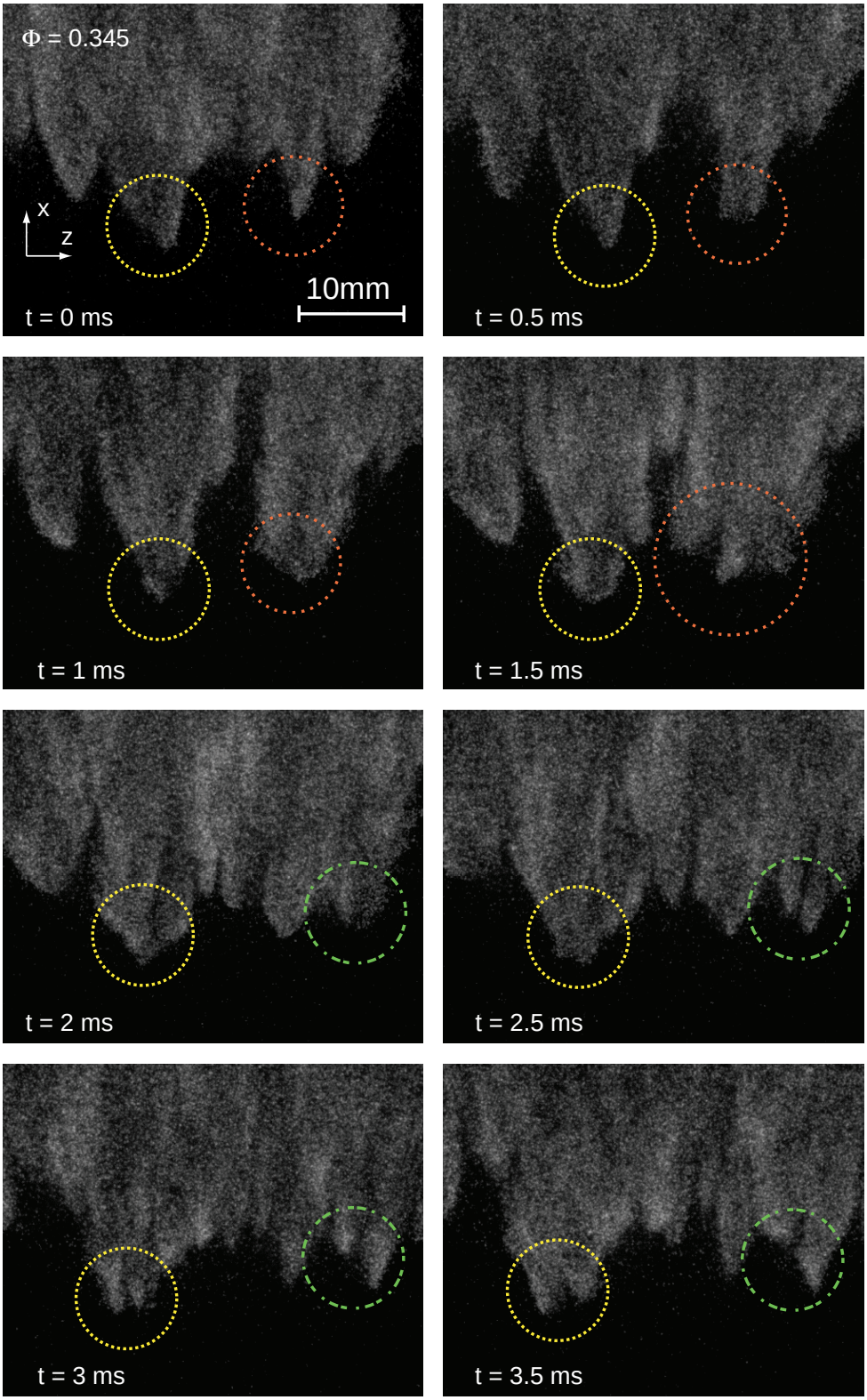

Figure 4.16: Formation and break-up of discrete flame cusps during turbulent H_2-air wall flashback in the 0° channel.

Table 4.2: Statistics of cusp formation and propagation.

Fuel	ϕ [°]	Φ [-]	No. of insp. cusps	Mean upstream velocity [m/s]	Cusp separation [%]
H_2	0°	0.360	69	1.37	40.6
H_2	2°	0.351	225	1.59	43.6
CH_4	4°	0.833	374	1.27	19.8

stays at the same axial position or is washed downstream. The cusp shape changes abruptly after a few milliseconds as the tip widens laterally. Subsequently, the blunt cusp separates into new cusps, which is the beginning of a new cycle. The global motion of the turbulent flame thus represents a stochastic process which results in flashback since a sufficiently high fraction of the evolving flame cusps moves upstream.

For a closer evaluation, the cusp patterns of turbulent H_2-air flames in the 0° and 2° geometries as well as turbulent CH_4-air flames in the 4° diffuser have been analyzed. At other operation points either the flame luminosity was to low to allow detailed observations (e.g., Fig. 4.15d) or the repetition rate of the APX I^2 camera was too low for a sufficient tracking of the cusps. From time series recorded at repetition frequencies of 1 kHz (CH_4-air) or 2 kHz (H_2-air), those cusps were analyzed which propagated in axial direction against the flow or stayed at about the same axial position. Due to the complexity of the flame shape, this was a manual procedure. Table 4.2 summarizes the statistics from the cusp analysis. For the H_2-air flames just described, separation into new cusps could be clearly observed for about 40% of the analyzed events. In contrast, only about 20% of the cusps of the CH_4-air flame in the 4° diffuser separate into new cusps, while the majority is washed downstream after lateral widening of the tip and vanishes in the main flame body. Furthermore, a widening of the cusp tip during upstream propagation has been observed. This indicates a slightly different propagation pattern of the CH_4-air flame in the 4° diffuser, which probably stems from a combination of differences in fuel characteristics and the strong adverse pressure gradient in the 4° diffuser.

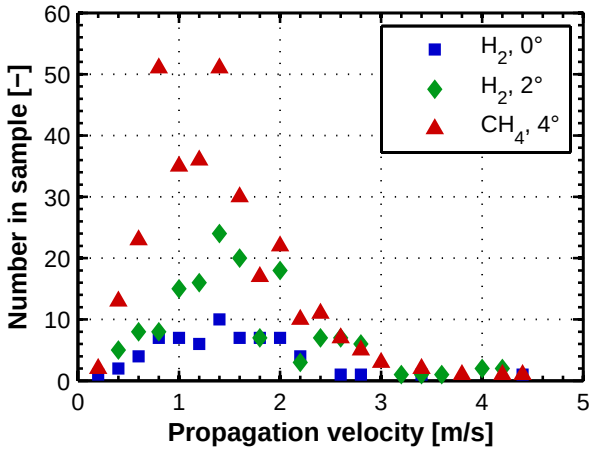

Figure 4.17: Frequency distribution of mean upstream propagation velocities of flame cusps.

Table 4.2 also lists upstream propagation velocities in an absolute frame of reference of those cusps in the analyzed samples which were not stagnating in axial direction. The velocities were calculated from the net axial propagation distance and the time between first observation of a spike until its disappearance, thus the values represent a mean over the whole propagation cycle of a cusp. It is interesting to see that mean propagation velocities are very close to each other for the analyzed samples. Figure 4.17 plots the frequency distribution of upstream propagation velocities in bins of 0.2 m/s width. The curves show a similar skewed distribution with maximum velocities up to 4.5 m/s. A correlation between upstream propagation velocity and lifetime of a cusp could not be observed clearly in the data. However, due to the manual character of the data sampling, such a correlation should not be excluded at this point.

The lifetime of the cusps can be compared to the quenching time of a head-on quenching configuration as calculated in Eq. (2.47) in order to estimate whether unsteady heat release due to radical combination at the wall influences H_2-air wall flashback. For wall flashback in the 0° channel at $\dot{m}_{air}$ = 60 g/s (Fig. 4.15c), Δt_f = 0.13 ms. The time scale of unsteady quenching according to Eq. (2.47) is Δt_q = 1.82 ms. The mean cusp lifetime is around 0.5 ms or less in that case, which indicates that unsteady quenching of flamelets that are pushed to the wall by turbulent fluctuations could play a role for turbulent H_2-air wall flashback at certain operating points.

4.3.2 Microscopic Flame Structure

The detailed propagation mechanism of the flame close to the wall is the central issue for understanding and modeling wall flashback. The μ-PIV system with simultaneous flame chemiluminescence recordings, as introduced in Sec. 3.2.5, allows a simultaneous measurement of the approximate position of the reaction zone and the two-dimensional velocity field upstream of the flame. The system was used to observe flames at wall flashback in a wide range of equivalence ratios, two different fuels, the 0° channel, the 2° and 4° diffusers as well as for laminar and turbulent flow conditions. The experiments were always conducted in the same fashion. Combustion was initiated identically as in the flashback limit experiments (see Sec. 4.1). The cameras were operated in endless First-In First-Out (FIFO) mode at a frequency of 2 kHz. A common stop trigger provided the timewise correlation between both sequences.

In the following, contours of instantaneous wall-parallel velocities calculated from single PIV image pairs will be presented (e.g., Fig. 4.18). The contours are superimposed on Mie-scattering images and scaled such that they cover the area of all vectors used for the plot. It is obvious that the extent of the wall reflections does not bias the velocity contours for all contours presented. Corresponding OH^* flame images from a top view are included in the first row of each figure, which have been recorded with a shutter time of 0.5 ms and which are synchronous to the first shot of a PIV pair. The PIV measurement volume is represented by a bright line in each top view image. The thickness of the line corresponds to the measurement depth (see Appendix B, Eq. (B.3)), while its axial length is close to 5 mm, as mentioned before. To provide an estimation of the flame position in the PIV measurement volume, one Mie-scattering image of each PIV contour plot is included where appropriate.

Figure 4.18 shows the propagation sequence of a flame cusp during turbulent H_2-air wall flashback in the 0° channel at $\Phi = 0.345$, which includes upstream motion, lateral widening and division into two new cusps. In the first image, the flame is situated just next to the PIV volume, which is not clearly reflected in the contour plot. In the second image, the flame cusp is located symmetrically in the PIV volume during upstream propagation. A pronounced backflow

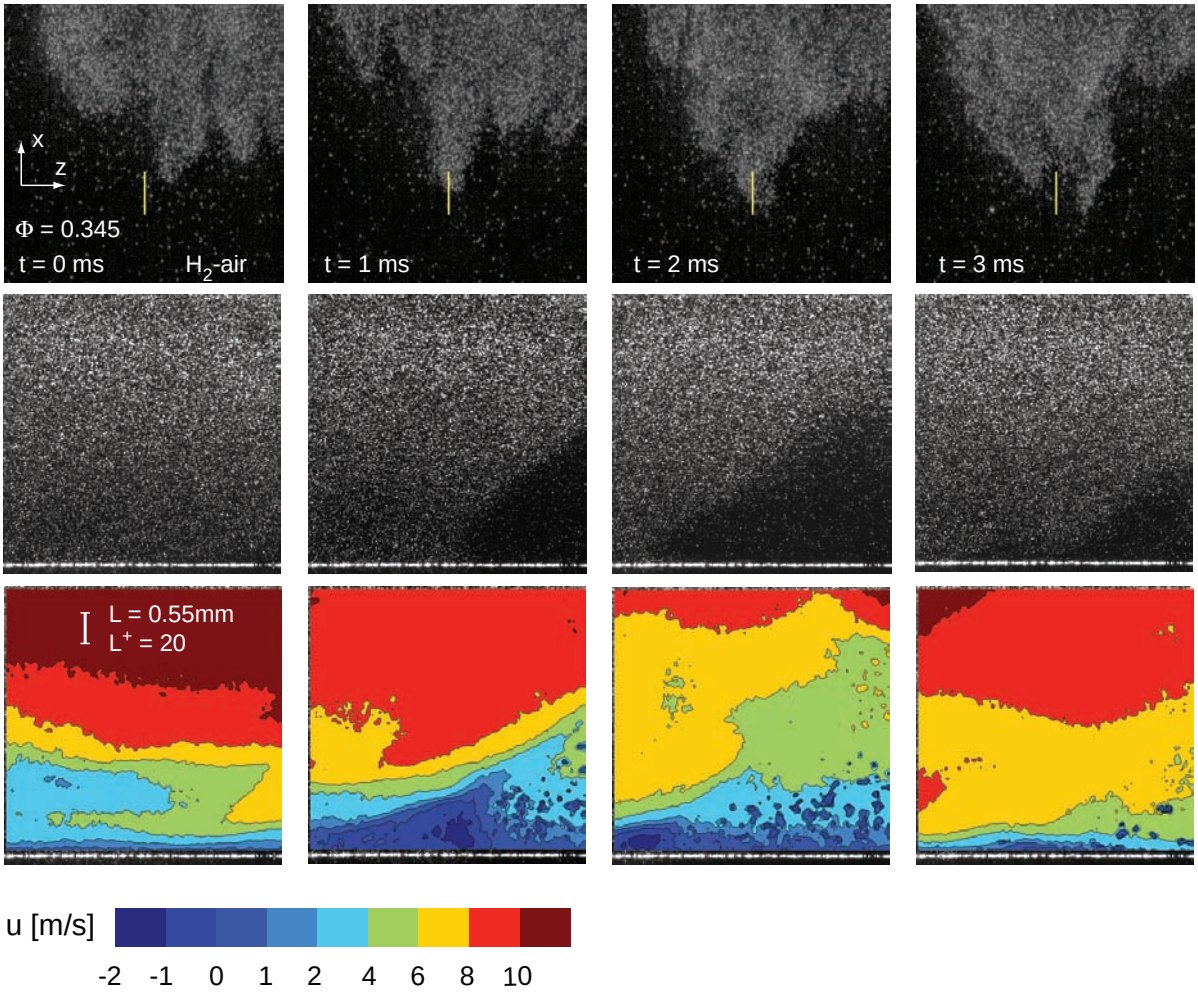

Figure 4.18: Axial velocity contours during turbulent H_2-air wall flashback in the 0° channel at $\Phi = 0.345$.

region is located in front of the propagating flame. The backflow region is attached to the wall and its maximum of negative axial velocities is located close to the flame tip. The Mie-scattering image suggests that the reaction zone of the flame cusp is not appreciably wrinkled in the x-y plane. During widening of the flame tip shown in the third image, the recirculation diminishes while the upper part of the flame seems to be pushed in downstream direction. In the last image, only a small portion of low-density fluid remains in the Mie-scattering image, while the recirculation has virtually disappeared. Other PIV shots which captured the widening and separation of flame cusps sometimes showed an uplifting of the flame away from the wall. In general, backflows of

similar size upstream of the flame tip have been observed in *every* case when a flame cusp was propagating upstream and was captured close to its symmetry axis by the PIV measurement volume. This situation could be observed for 10 cusps at $\Phi = 0.345$.

Figure 4.19 shows a similar process for $\Phi = 0.543$ in the same geometry. Please

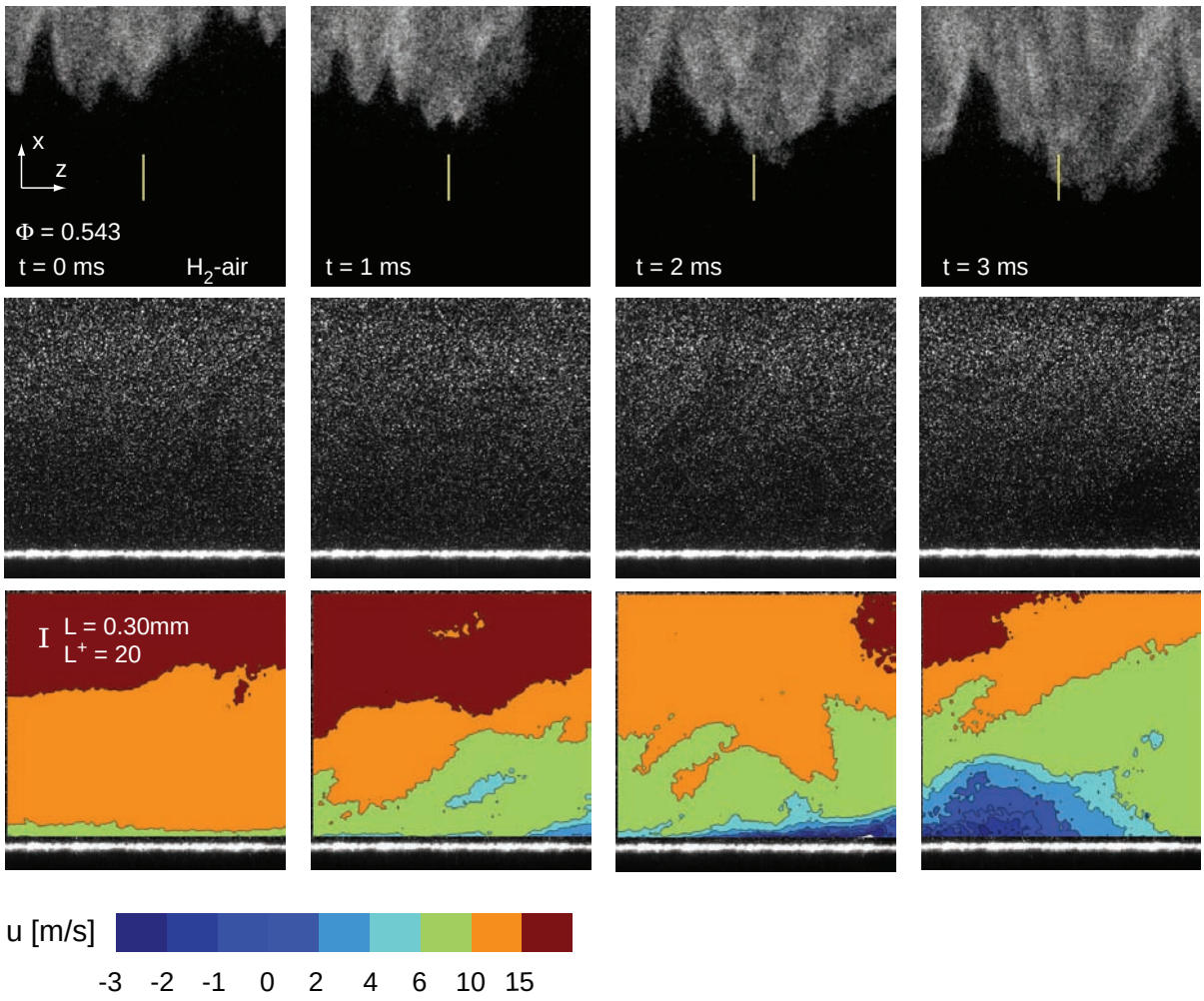

Figure 4.19: Axial velocity contours during turbulent H_2-air wall flashback in the 0° channel at $\Phi = 0.543$.

note the different contour scaling compared to Fig. 4.18. Again, the upstream propagating flame cusp is headed by a recirculation zone, as can be seen from the third and fourth contours, which has a similar development of the velocity field as observed for the leaner case. With one exception, backflows of similar

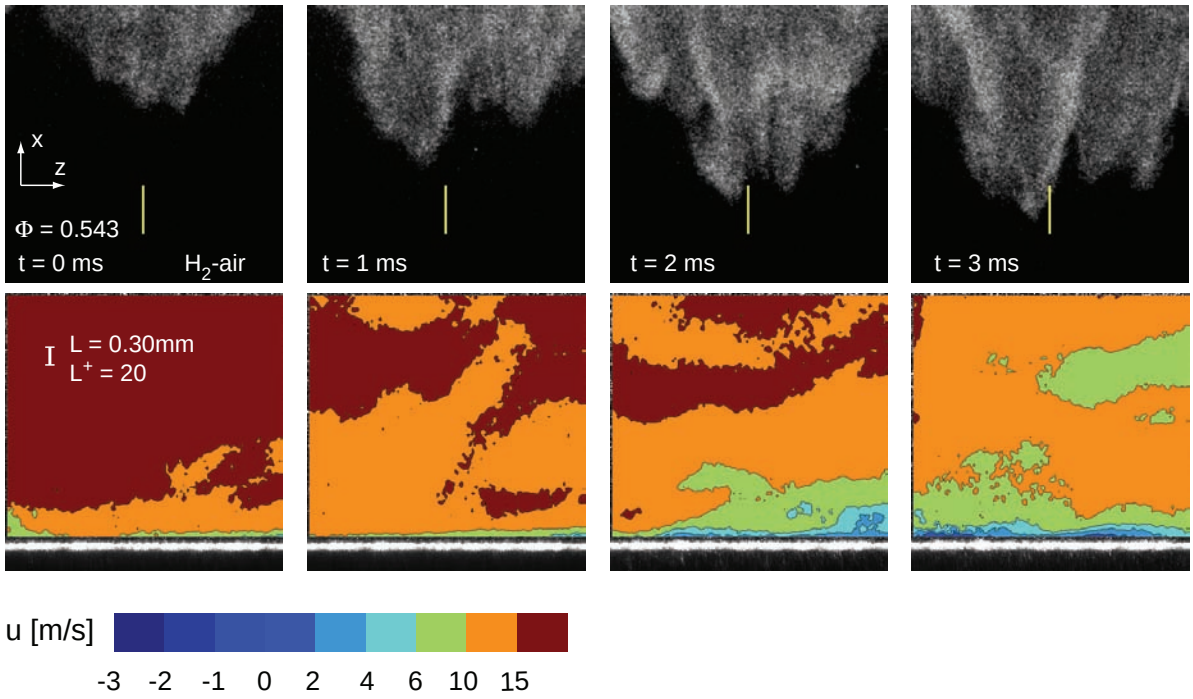

Figure 4.20: Axial velocity contours of flame approach and sidecut of a cusp for turbulent H_2-air wall flashback in the 0° channel at $\Phi = 0.543$.

size have again been observed in every case when a flame cusp was propagating upstream and was captured close to its symmetry axis by PIV, which was observed for 9 cusps at $\Phi = 0.543$.

A close examination of the turbulent μ-PIV data in the 0° channel has shown that the recirculation regions just described are limited to the close proximity of the flame tip. This is exemplary verified by Fig. 4.20. As the flame approaches the measurement volume, negative axial velocities are not observed if the flame tip is a few millimeters downstream of the measurement volume (first and second images) or if the angled side part of a flame cusp is captured by the measurement volume (third and fourth image).

The effect of the macroscopic lateral distribution and axial motion of the flame body on time-resolved boundary layer velocities during flashback is analyzed in Fig. 4.21. The sequence of a wall flashback event in the 0° channel at $\Phi = 0.543$ is shown in the figure. The graphs plot axial averages of instantaneous PIV velocity fields at four different wall distances as a function of time as

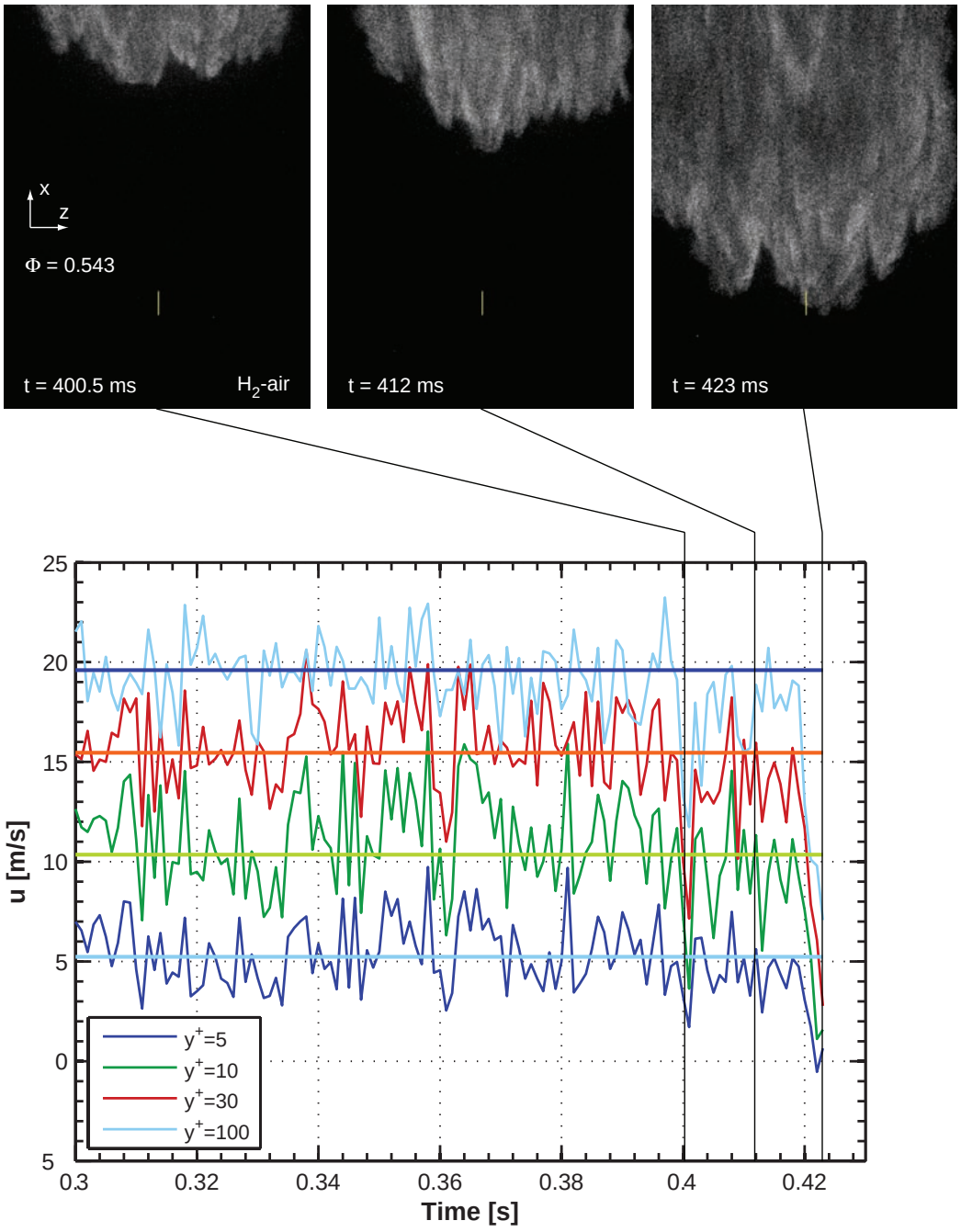

Figure 4.21: Influence of approaching flame body on instantaneous boundary layer velocities in the 0° channel.

the flame is approaching the PIV measurement volume. The mean axial velocities for an isothermal channel flow of the unburnt mixture according to the Spalding profile are shown as bold lines for each height. At the beginning of the time record ($t = 0.3$), the flame was still stabilized on the ceramic tile. The mean of the axial velocities inside the PIV volume are well represented by the isothermal mean value in this first period. Shortly after $t = 0.36\,\mathrm{s}$, a sudden decay in the near wall region can be observed. This instant probably corresponds to the detachment of the flame from the tile and the beginning of flashback, which is confirmed by assuming a constant flashback velocity of the flame and calculating the beginning of flashback from the axial distance the flame has traveled until it enters the image area of the top view camera. The velocities recover quickly to their original values, though, as the flame moves upstream. Only after $t = 0.4\,\mathrm{s}$, the influence of the flame backpressure is becoming noticeable in the boundary layer velocities by a slight decay at each height considered in the plot. The position of the flame relative to the PIV volume at three points in time is shown above the graph. The last image corresponds to the last image of Fig. 4.19. It can be determined from the graphs that the strong decay towards negative velocities in the near wall region is a sudden process, which underlines the local character of the flow field modification which occurs during wall flashback.

Figures 4.22 and 4.23 show velocity contours of flashback sequences along the $\tilde{x}$ direction in the 2° and 4° diffusers for turbulent H_2-air mixtures. For the calculation of L^+ for each figure, the wall frictions of isothermal air flow as measured by PIV (see Sec. 3.3.3 and 3.3.4) at the respective air massflow have been used. Backflow regions upstream of the propagating flame cusps are observed for both adverse pressure gradients. The extent of the backflow for the 2° diffuser is comparable to the 0° channel results. In contrast, the size of the backflow region in the 4° diffuser is much larger in axial and wall-normal extent. Figure 4.24 shows a similar sequence as Fig. 4.23, but for a CH_4-air mixture at stoichiometric conditions. It can be seen from the contour plots that flashback is accompanied by strong separation which spans more than half of measurement volume height.

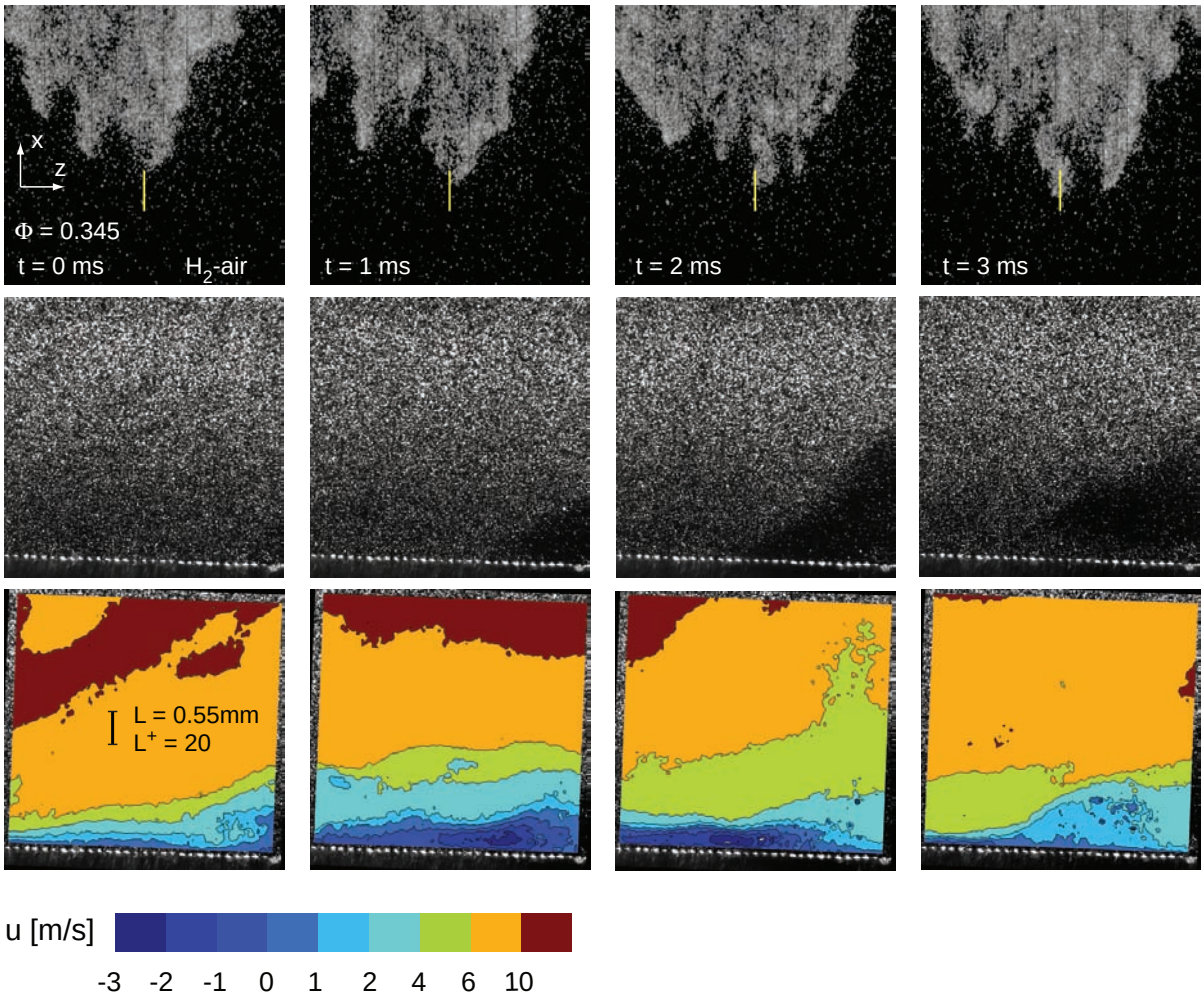

Figure 4.22: Axial velocity contours during turbulent H_2-air wall flashback in the 2° diffuser at $\Phi = 0.345$.

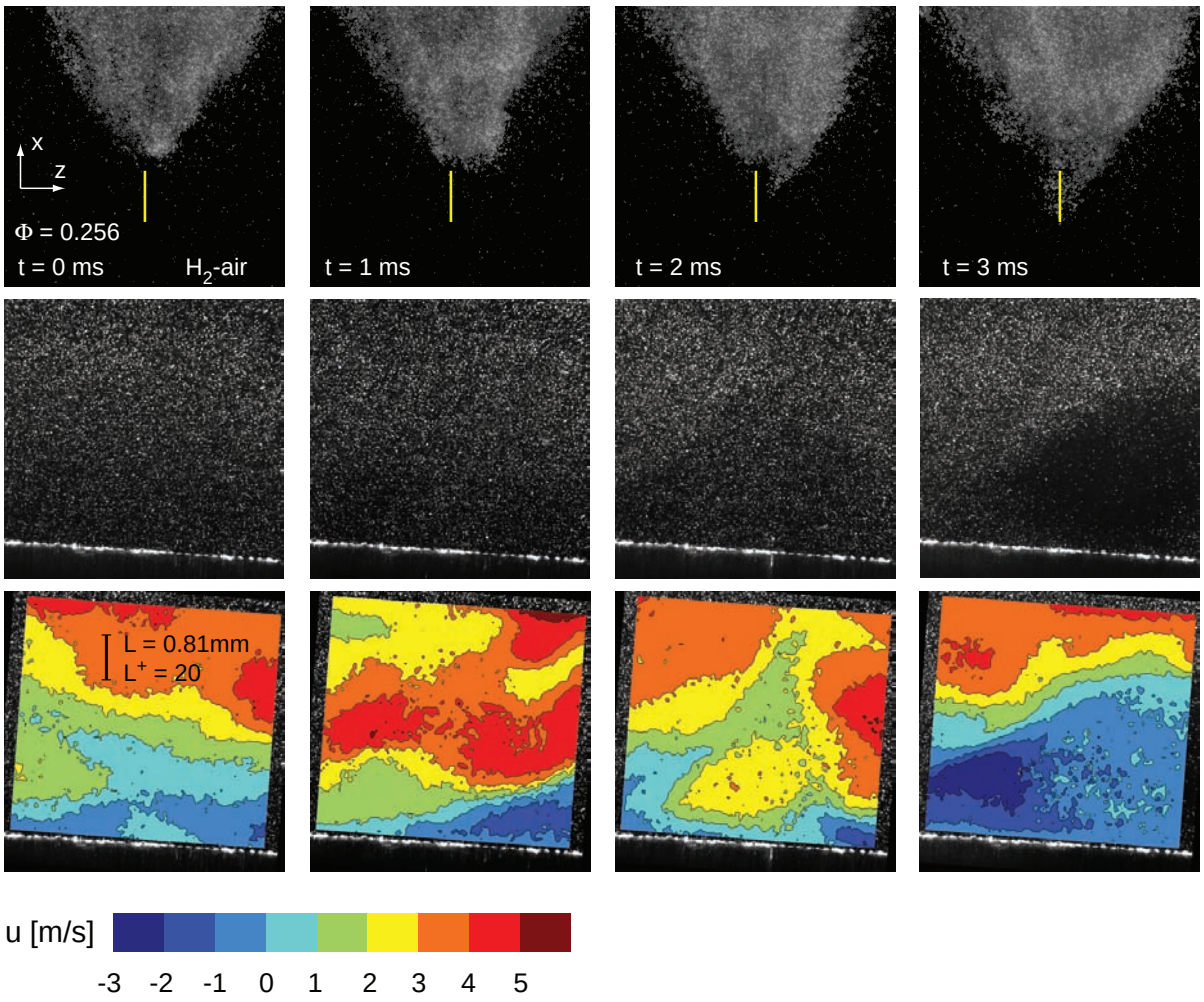

Figure 4.23: Axial velocity contours during turbulent H_2-air wall flashback in the 4° diffuser at $\Phi = 0.256$.

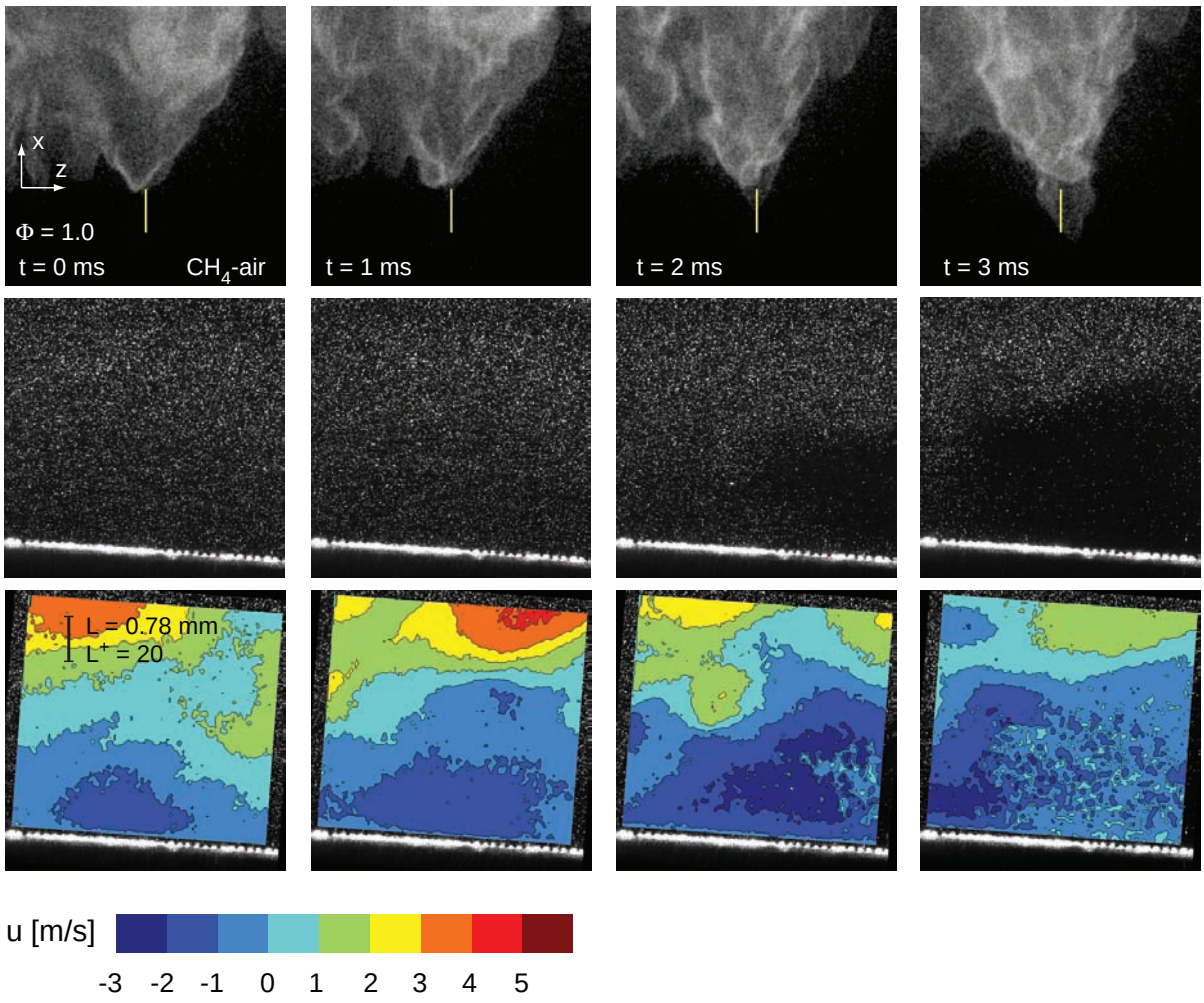

Figure 4.24: Axial velocity contours during turbulent CH_4-air wall flashback in the 4° diffuser at $\Phi = 1.0$.

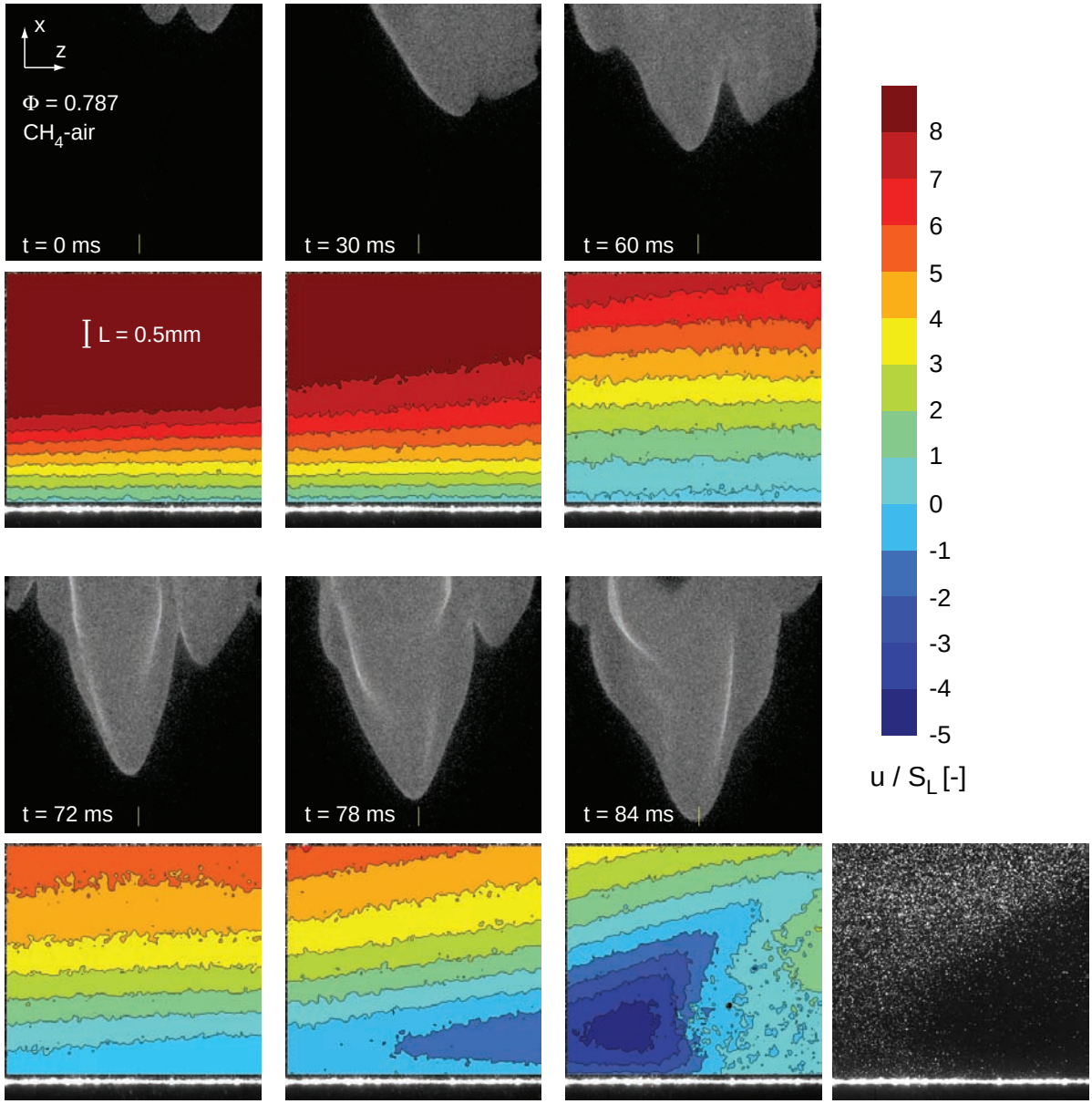

Figure 4.25: Axial velocity contours during laminar CH_4-air wall flashback in the 0° channel at $\Phi = 0.787$.

So far, only results of turbulent wall flashbacks have been presented. Of course, the question arises whether the observed flow detachment upstream of the flame is specific for turbulent conditions. For clarification, Fig. 4.25 shows PIV results of laminar CH_4-air wall flashback in the 0° channel at $\Phi = 0.787$. The contour plots are normalized by the laminar burning velocity $S_L = 0.248\,\mathrm{m/s}$ for the given CH_4-mixture as predicted by Cantera using

the GRI3.0 mechanism. Laminar flashback sequences occurred in a regular and slow fashion compared to turbulent flows, which allows a more detailed description of the process with the available temporal resolution. By comparing Figs. 4.25 and 4.15a, the influence of the mirror holder on the shape of the laminar flame at flashback can be seen. On the one hand, the wake introduces fluctuations in the freestream, which result in large-scale, low frequency perturbations of the flame body. On the other hand, the blockage of the mirror holder and the resulting low-velocity wake reduce the wall shear on the lower wall, such that the side parts of the flames are stronger inclined than in Fig. 4.15. Please note that the effect of the mirror holder on turbulent wall flashback in the same geometry was not clearly visible, most probably because turbulent momentum transport caused a faster decay of the disturbances. After all, as the velocity profiles in Figs. 3.27 have shown, the mean flow profile in the wake has a laminar character. Furthermore, well-ordered backflow regions have been observed in each of four experiments in which the PIV measurement volume was close to the flame tip of the laminar flame, which indicates that non-deterministic fluctuations did not change the observed phenomenon appreciably. A frequency analysis of velocity fluctuations upstream of the propagating flame supports this statement [ES11b]. Conclusively, the observations made in the following are not invalidated by the wake disturbances.

As the flame approaches the PIV measurement volume in Fig. 4.25, the flow velocities close to the wall reduce continuously, until a backflow region starts to develop about 14 mm upstream of the flame. The backflow reaches its highest distance from the wall just upstream of the flame tip, amounting to 3.3 mm. Repetition experiments with similar positions of the PIV measurement volume relative to the flame lead to values of 11.6 mm and 20.6 mm for the axial extent and 2.4 mm and 3.6 mm for the maximum wall distance of the recirculation. Further experiments have shown that the axial extent as well as the maximum height of the recirculation decreases with increasing lateral distance from the flame tip, which indicates a crescent-shaped recirculation zone in front of the leading flame zone.

4.3.3 Discussion of Flame Propagation Measurements

The simultaneous measurements of flame position and two-dimensional velocity field around the flame during wall flashback suggest a completely different physical picture compared to the well-established critical gradient model of Lewis and von Elbe. Whereas the Lewis and von Elbe model assumes an uncoupled flame propagation against the local flow direction during flashback, which leads to a simple balance between flame speed and local isothermal flow speed to describe flashback limits, the present results reveal an unidirectional motion of flame and flow in the flame tip region. The pressure field upstream of the flame obviously interacts strongly with the boundary layer flow and leads to local flow separation. This basic mechanism of upstream propagation is similar for laminar and turbulent flow conditions, different fuels and varying adverse pressure gradients, which points towards the universality of a recirculation-assisted flame motion during wall flashback.

In particular, the interpretation that the backflow region is formed by local boundary layer separation is supported by two observations:

- For laminar wall flashback, the sequence in Fig. 4.25 is an almost perfect representation of theoretical laminar boundary layer separation due to an adverse pressure gradient as illustrated in Fig. 2.5.

- For turbulent wall flashback, the observation of local, short-lived backflows in narrow regions of the near-wall flow corresponds well to observations of turbulent separation due to adverse pressure gradients as described in Sec. 2.1.6.

According to this analysis, the difference between laminar and turbulent flashback limits based on critical velocity gradients of the *mean* isothermal profile is most probably caused by the fact that the flame propagates in low-velocity structures in the turbulent case, which only propagate at a fraction of the local mean velocity (see Figs. 4.26a and 4.26b).

Details of Turbulent Wall Flashback

The similarity between turbulent wall flashback and turbulent separation in the 0° channel, i.e. in a zero pressure gradient flow, is further manifested by the following points:

- The strong similarity of cusp formation and break-up processes, which are distributed along the whole lateral width of the observed channel region, suggest a propagation in near-wall turbulent structures which are known to show strong similarity among themselves (see Sec. 2.1.4).
- The maximum dimensionless height of the backflow region in Figs. 4.18 and 4.19 is roughly $y^+ = 25$, which corresponds well to the view that turbulent separation is initiated inside low-speed streaks (see Sec. 2.1.6) that are known to show a well-defined structure up to $y^+ = 30$ to 40 [SM83].
- The widening and/or uplifting of flame cusps at the end of upstream propagation (e.g., Fig. 4.18) corresponds well to the observation of shear layers between high-speed upstream and low-speed downstream fluid by Robinson [Rob91a] (see Sec. 2.1.4).

As already mentioned, low-speed streaks have a mean nondimensional lateral distance of $z^+ \approx 100$ (see Sec. 2.1.4). However, spatial auto-correlation of flame fronts in the 0° channel which are formed by cusps, such as shown in Fig. 4.15c, did not result in a characteristic lateral distance of flame cusps. This could be explained by the fact that not every low-speed streak is actually burning, but only those which are most affected by the adverse pressure gradient produced by the flame.

Details of Turbulent Wall Flashback with Adverse Pressure Gradients

The finding that wall flashback is driven by boundary layer separation allows interpretation of the deviating observations for wall flashback limits with adverse pressure gradients, which were

- In general, higher g_c for a given equivalence ratio.

- In detail, higher flashback propensity towards the downstream end of the diffuser for a given equivalence ratio.

Looking at the first statement, the adverse pressure gradient apparently increases the separation susceptibility of the boundary layer in the near wall region during wall flashback for a given value of g. Hence, either the mean or time-resolved shape of the boundary layer is different or the effective flame backpressure acting on the boundary layer is different - or all at the same time.

Looking at the first option, mean boundary layer profiles in adverse pressure gradient flow have a different outer region as indicated by Eq. (2.11). However, since increasing adverse pressure gradients tend to produce a faster wake region in nondimensional coordinates (e.g., [NTH98,Whi05], see also Figs. 4.27), this fact should not increase separation propensity if boundary layer profiles with the same velocity gradient at the wall are compared.

Concerning the time-resolved shape of the boundary layer, it is instructive to evaluate the distribution of turbulent fluctuations close to the wall by calculating Cumulative Distribution Functions (CDF). A CDF of a stochastic process lists the frequencies of observations in discrete bins of the process results, which simply represents the integration of the Probability Density Function (PDF) of the stochastic process. Figures 4.26a and 4.26b compare CDFs of instantaneous scaled axial velocities $u(x,t)/\langle u(x)\rangle$ from PIV measurements at E2 in isothermal 0° channel and 4° diffuser flow for two wall heights, $y^+ = 5$ and 15. Please note that in this region, rms fluctuations of PIV and LDA measurements were in excellent agreement in Figs. 3.25b, 3.25d and 3.25f. Interrogation areas of 8x8 pixel have been used for the underlying velocity fields of Figs. 4.26 to increase spatial resolution. The two figures reveal that strong low-speed fluctuations close to the wall in the 4° diffuser are much more frequent than in the 0° channel. Since turbulent flashback is occurring in backflowing low-velocity structures close to the wall, this observation indicates increased flashback propensity.

Concerning the effective strength of the flame backpressure, it will be shown later that relatively low wake velocities tend to increase the effective pressure gradient in the boundary layer. Since the wake region is faster in adverse pres-

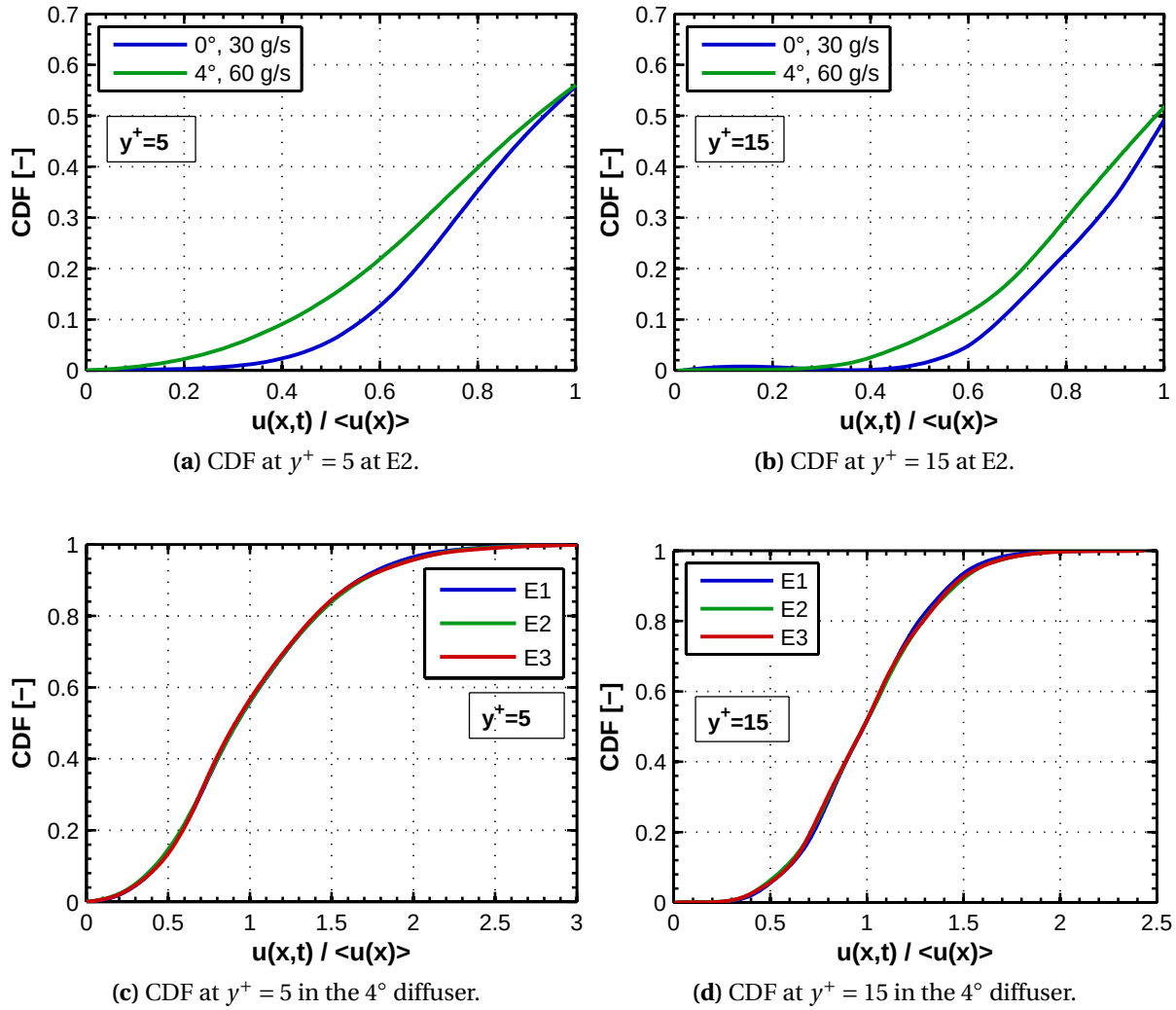

(a) CDF at $y^+ = 5$ at E2.

(b) CDF at $y^+ = 15$ at E2.

(c) CDF at $y^+ = 5$ in the 4° diffuser.

(d) CDF at $y^+ = 15$ in the 4° diffuser.

Figure 4.26: Cumulative distribution functions of wall-parallel velocities on the centerline of the 0° channel and the 4° diffuser: PIV measurements.

sure gradient flows, as mentioned before, this effect cannot explain increased flashback propensity.

Conclusively, only the higher frequency of strong negative axial fluctuations in the diffuser indicates higher separation tendency of low-speed structures in the near-wall region which promotes wall flashback. If this mechanism causes the generally higher flashback propensity of the diffuser flow or if, for example, hysteresis effects play an additional role here needs to be further investigated, though.

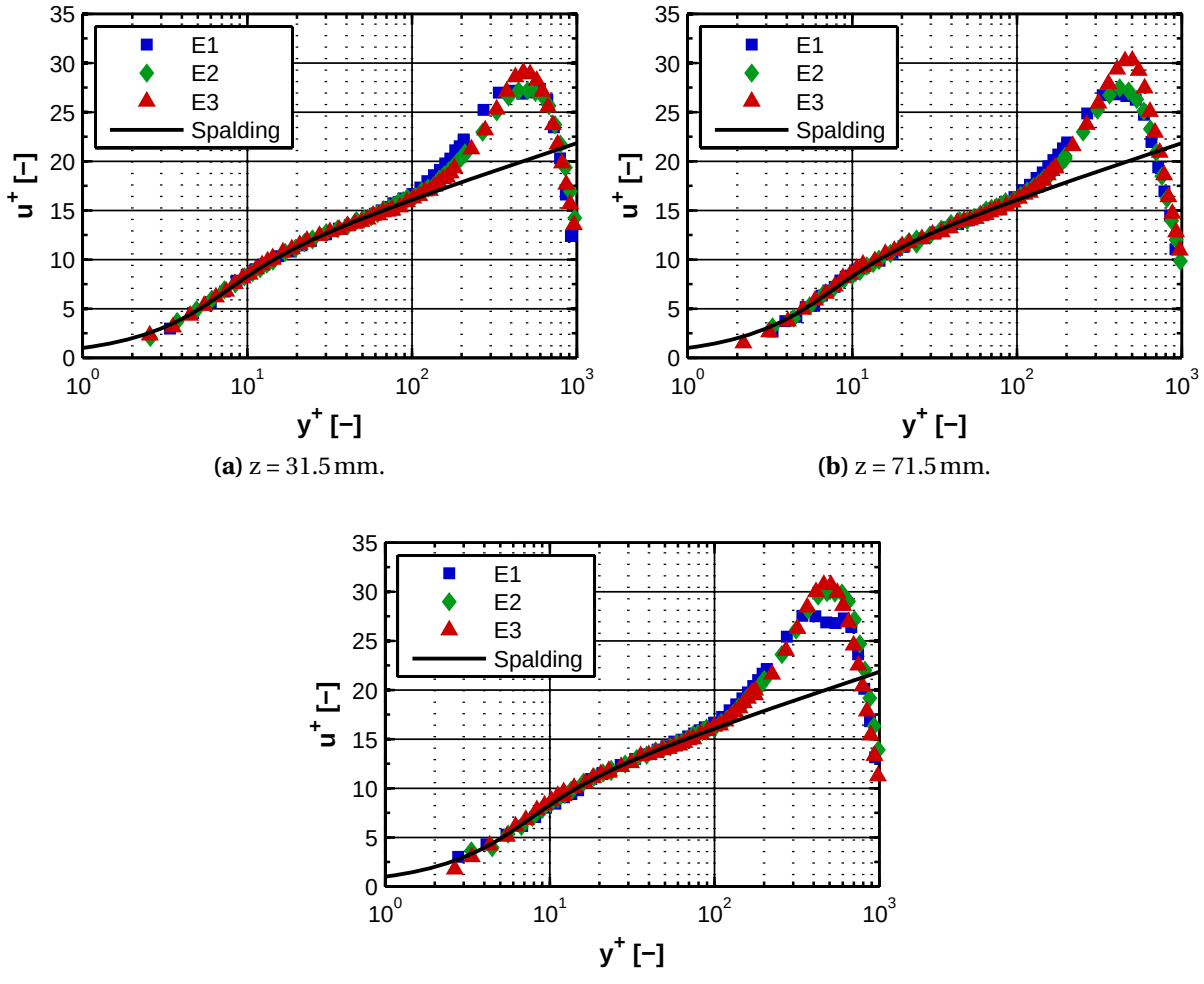

(a) z = 31.5 mm.

(b) z = 71.5 mm.

(c) z = 111.5 mm.

Figure 4.27: Boundary layer development in the 4° diffuser at $\dot{m} = 60\,\mathrm{g/s}$: LDA measurements.

Finally, the second statement, i.e. why the flow towards the downstream end of the diffuser is more susceptible to flashback, shall be discussed. Again, mean and time-resolved boundary layer profiles and the effective flame backpressure will be considered. Concerning mean flow, the strength of the adverse pressure gradient itself cannot be the reason for higher flashback propensity downstream since its value decreases in axial direction as already shown in Figs. 3.21. Regarding the wake development of the boundary layer, Figs. 4.27 show the axial development of the boundary layer in the 4° diffuser in nondimensional coordinates separately for three lateral points as measured by LDA. It can be seen that the wake of the boundary layer is very similar for E2 and E3

at each axial position. Since the evaluation of equilibrium flashback positions for Fig. 4.12 mainly took place close to E2 and E3, deviations in the mean velocity profile along the axial coordinate probably play a minor role for higher flashback propensity at the downstream end of the diffuser.

Regarding the time-resolved structure of the boundary layer, the axial development of the CDF in the 4° diffuser is shown in Figs. 4.26c and 4.26d. Very interestingly, the distribution of low- and high-speed fluctuations stays nearly constant along the axial direction. A change in fluctuation distribution can hence be excluded to be the reason for increasing flashback propensity in downstream direction.

Regarding the effective flame backpressure, it will be shown later that higher duct heights tend to increase the backpressure. Accordingly, this may be the reason for increased flashback propensity in direction of the duct expansion. However, a firm validation of this hypothesis needs further investigation.

5 Numerical Simulation of Laminar Wall Flashback

The experimental results strongly point towards a universal wall flashback mechanism involving a backflow region upstream of the flame. However, the temporal origin of the backflow region cannot be determined with certainty solely based on the experimental data, which only provided information on a flame at flashback, but not during the approach towards it. In principle, two different situations are possible. On the one hand, the initiation of flashback could be independent of the existence of the recirculation, which only forms later during the upstream propagation of the flame and increases the velocity of a yet existing flashback. In that case, the critical gradient model could still be feasible for the prediction of flashback limits. On the other hand, the recirculation zone could be formed prior to flashback, such that recirculation becomes decisive for the onset of flashback. Before a new model concept can be developed, this question has to be answered. Numerical simulations will be used in the following to provide the missing insight.

5.1 Numerical Setup and Combustion Model

The vicinity of the flame holder used in the H_2-air experiments, a hot tile on the lower channel wall, has been simulated numerically for atmospheric conditions using ANSYS CFX 12.0. An H_2-air flame in a laminar two-dimensional boundary layer is considered, which can be well resolved at moderate computational costs with considerably less physical modeling involved compared to a turbulent unsteady Reynolds-averaged Navier-Stokes (URANS) simulation, for example.

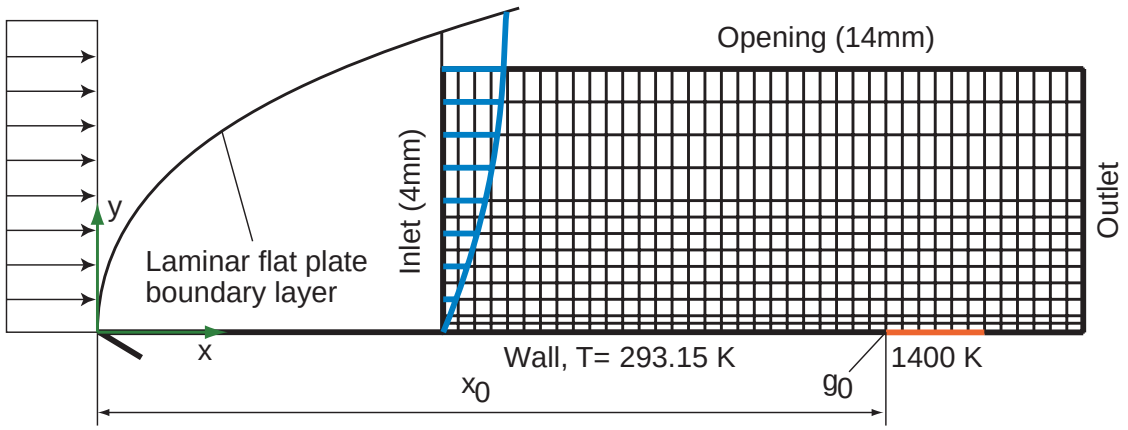

Figure 5.1: Computational domain for laminar wall flashback simulations.

In order to achieve high velocity gradients at the wall in a laminar and well-defined flow situation, the configuration displayed in Fig. 5.1 has been chosen here. The computational domain comprises an area of 4 mm height and 14 mm length of a laminar flat plate boundary layer. The flame is stabilized inside the domain by a hot wall segment of 1400 K and 2 mm length, the end of which is located 2 mm upstream of the outlet. The remaining part of the wall is isothermal at 293.15 K, which is equal to the inlet temperature of the mixture. The velocity profile at the constant velocity inlet of the domain is calculated from the Blasius solution of the laminar flat plate boundary layer (see Eq. (2.5)) tabulated in [Whi05] such that the Reynolds number at the upstream edge of the hot wall segment is $\mathrm{Re}_{x_0} = 50000$ (laminar regime) with a wall velocity gradient of $g_0 = 30000\,\mathrm{s}^{-1}$ at the same position. The resulting distance x_0 between the virtual leading edge of the flat plate and the hot wall segment is about $x_0 \approx 50\,\mathrm{mm}$. In order to eliminate artificial pressure fluctuations inside the domain, the inlet is modeled acoustically non-reflective based on an implementation of the Navier-Stokes Characteristic Boundary Conditions (NSCBC) [PL92] described in [WNA06]. At the outlet and at the top of the domain, constant pressure openings are specified. The domain has a hexahedral mesh with cell sizes $\Delta x = 0.035\,\mathrm{mm}$, $\Delta y = 0.035\,\mathrm{mm}$ for $0.05\,\mathrm{mm} \leq y \leq 2\,\mathrm{mm}$ and $\Delta y = 0.07\,\mathrm{mm}$ for $2\,\mathrm{mm} \leq y \leq 4\,\mathrm{mm}$. For $y < 0.05\,\mathrm{mm}$, the cells are refined towards $\Delta y = 1\,\mu\mathrm{m}$ at the wall. Symmetry planes are placed in the x-y plane on both sides of the domain. The transient time step is constant for all conservation equations at $\Delta t = 0.1\,\mu\mathrm{s}$.

In order to keep the numerical effort tolerable, premixed laminar combustion is modeled by a five-species, three-step H_2-O_2 mechanism which has been derived from a detailed mechanism by systematic reduction based on steady state assumptions for O, OH and H_2O_2 [BJSW11]:

$$3H_2 + O_2 \rightleftharpoons 2H_2O + 2H \tag{5.1a}$$

$$H + H + M \rightleftharpoons H_2 + M \tag{5.1b}$$

$$H_2 + O_2 \rightleftharpoons HO_2 + H\,. \tag{5.1c}$$

For the implementation of the three-step mechanism in ANSYS CFX, forward and backward reaction rates of each reaction had to be specified explicitly. The net reaction rate ω of one elementary reaction is given in terms of forward and backward reaction rates ω_f and ω_b according to

$$\omega = \underbrace{k_f \prod_{i=1}^{N} c_i^{\nu_i'}}_{\omega_f} - \underbrace{k_b \prod_{i=1}^{N} c_i^{\nu_i''}}_{\omega_b}\,, \tag{5.2}$$

where ν_i' and ν_i'' are the stoichiometric factors of a species i on the educt and product side, respectively, and N is the number of species in the reaction. The ratio of k_f over k_b can be expressed by the equilibrium constant at constant pressure $K_p(T)$:

$$\frac{k_f}{k_b} = \frac{K_p(T)}{(\mathscr{R}T)^{\sum_{i=1}^{N}\left(\nu_i''-\nu_i'\right)}}\,. \tag{5.3}$$

Please note that $K_p(T)$ is only a function of temperature for an ideal gas. In the present approach, $K_p(T)$ was specified as a polynomial function for each of the three reactions in Eqs. (5.1). The required tables of $K_p(T)$ in turn were calculated from equilibrium constants for formation $K_{p,i}^0(T)$ of each species i according to [Law06]

$$K_p(T) = \prod_{i=1}^{N}\left[K_{p,i}^0(T)\right]^{\left(\nu_i''-\nu_i'\right)}\,. \tag{5.4}$$

Since ω is provided by the H_2-O_2 mechanism, either k_f or k_b can be calculated by combining Eq. (5.2), (5.3) and (5.4), and the second factor simply results

from Eq. (5.3). The dynamic viscosity, thermal conductivity and Fickian binary diffusion coefficients for each species are specified as 4th-degree polynomials of temperature, while specific heat capacity is specified by NASA polynomials. The diffusion coefficient of each species into the local mixture is approximated by a mixture formula also used in CHEMKIN II ([KDLW+86]). Soret diffusion is neglected. Mixture values for dynamic viscosity, thermal conductivity and heat capacity are calculated from a local mass-average, which introduces some approximation for the first two quantities. The density of the mixture is calculated from the ideal gas law. The modeling of the reacting mixture accounts for non-equidiffusion effects, which is important for a correct prediction of flame propagation since the considered educts have Le < 1. Conductive heat loss to the wall is accounted for, while radiative heat transfer is not modeled.

The code has been validated by calculating laminar flame speeds in a quasi-one-dimensional domain for a timestep of $\Delta t = 0.1\,\mu$s and two different mesh resolutions at an equivalence ratio of $\Phi = 0.625$. The results are summarized in Table 5.1. By comparing S_L for the two grid resolutions, it is verified that

Table 5.1: Laminar flame velocities of the 3-step H_2-O_2 mechanism at $\Phi = 0.625$ and two different grid resolutions.

Software	S_L [m/s]
CFX, $\Delta x = 35\,\mu$m	1.10
CFX, $\Delta x = 20\,\mu$m	1.07
Cantera, Li et al.	0.97

$\Delta x = 35\,\mu$m is sufficient to capture the laminar flame propagation. Furthermore both values compare well to a prediction of Cantera using the Li et al. mechanism instead of the San Diego mechanism used for the derivation in [BJSW11], which may add to the observed difference.

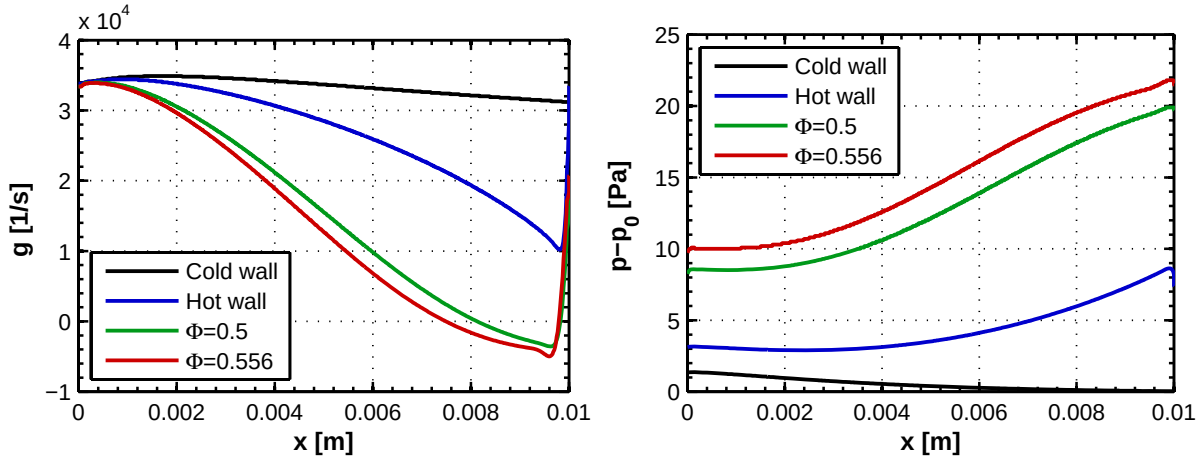

(a) Velocity gradient at the wall.

(b) Static pressure at the wall.

Figure 5.2: Numerical flow development at the wall during flashback approach.

5.2 Results for Laminar H_2-Air Wall Flashback

Figures 5.2 show the development of the wall velocity gradient g and relative static pressure $p - p_0$ ($p_0 = 1\,\text{atm}$) at the wall from the inlet up to the leading edge of the hot wall segment. In each figure, four curves are plotted which represent the gradual approach to flashback conditions:

- Flow with an isothermal wall without reaction.
- Flow with the wall including the hot wall segment without reaction.
- Reacting flow at two different equivalence ratios with still stable flames starting close to the upstream edge of the hot wall segment.

From Fig. 5.2a it can be determined that the thermal expansion above the hot wall segment without reaction already leads to a strong reduction in wall friction upstream. This result is not surprising in light of the work of Higuera [Hig97]. For reacting flow and yet stable flames, the wall shear steeply declines in axial direction until a separation point $g = 0$ is reached well upstream of the flame stabilization. It is thus demonstrated that a recirculation zone yet exists in the stable regime before flashback occurs. The axial extent of the separation region increases with equivalence ratio during flashback approach. The

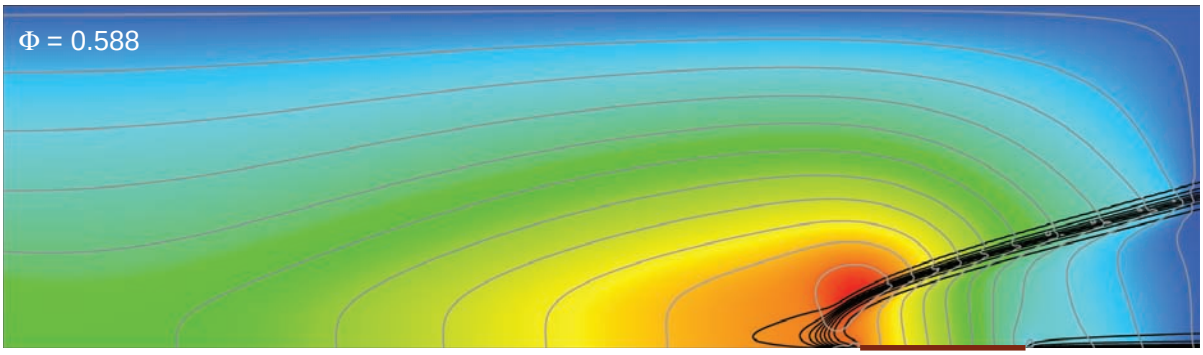

Figure 5.3: Isolines and contour of relative static pressure and isolines of density for a stable laminar flame.

existence of a recirculation region has not been observed in prior numerical investigations of laminar flashback [LT82, MDG98, KFTT+07], potentially due to insufficient axial length of the domains in combination with a fixed velocity inlet. The relative static pressure development in Fig. 5.2b allows estimation of the pressure rise caused by the different physical mechanisms involved. The contribution of wall friction is negligible as can be seen from the very small pressure decrease for isothermal conditions. The hot wall segment causes a rise of about 5.5 Pa in the domain, whereas it is about 12 Pa in the reacting case. It is interesting to compare this value to the theoretical one-dimensional flame backpressure according to Eq. (2.35). For an H_2-air flame at $\Phi = 0.556$, the pressure loss p_f is only 2.4 Pa. This result underlines the two-dimensional nature of the pressure rise upstream of the flame, which apparently cannot be predicted based on simple one-dimensional considerations.

To provide more details on the pressure distribution inside the domain, relative static pressure contours and isolines (grey) as well as density isolines (black) are shown in Fig. 5.3 for a yet stable flame at $\Phi = 0.588$. The pressure gradient close to the wall is aligned with the axial flow direction upstream of the flame. A maximum of relative static pressure is located close to the tip of the flame, which is caused by a local maximum of axial deceleration and vertical acceleration of fluid by the flame, i.e. an upward deflection of streamlines. Furthermore, the fresh gases in the backflow region are preheated by heat transfer from the flame tip, as can be seen from the increasing separation of density isolines.

Figure 5.4 illustrates the development of flame thickness and axial velocity field during flashback approach. The axial velocity contours are scaled by the respective laminar flame speed S_L obtained from Cantera simulations. Black isolines of H_2 molar fraction, equally distributed across the respective span for each equivalence ratio, are included to mark the extent of the reaction zone. The first three contours represent a stable flame with increasing Φ. The location of the hot wall segment is marked by a dark line in the lower right corner of the first three contours. As Φ increases, the axial extent as well as the maximum height of the recirculation increases. The stretching of isolines of H_2 molar fraction close to the wall reveals that radicals are transported upstream by the backflow. However, heat loss to the wall as well as to external streamlines slows down the reaction such that the gases inside the backflow do not ignite. The last plot in Fig. 5.4 shows the flame at flashback after it has already traveled upstream a short distance. The flame is burning at the downstream end of the backflow with a more compact reaction zone close to the wall. Please note the qualitative agreement of the simulated velocities at flashback with laminar μ-PIV contours in Fig. 4.25. Table 5.2 lists the simulated velocities of the flame and the separation point, as seen by an external observer, as well as the highest negative axial velocity in the backflow at $\Phi = 0.625$. Each row

Table 5.2: Simulated velocities of flame, separation point and backflow for a laminar H_2-air flame at $\Phi = 0.625$.

Relative time [ms]	Flame [m/s]	Separation point [m/s]	Maximum backflow [m/s]
0	1.21	1.18	-0.92
0.1	1.24	1.14	-0.94
0.2	1.29	1.29	-0.96
0.3	1.32	1.05	-0.97

of Table 5.2 represents average velocities over a time span of 0.1 ms. It can be seen by comparing columns 2 and 3 that as the flame moves along the wall, the backflow is dynamically dislocated upstream by the pressure rise in front of the flame. By adding columns 2 and 4, the relative speed of the flame with respect to the backflow, i.e. the local burning velocity, can be calculated. The

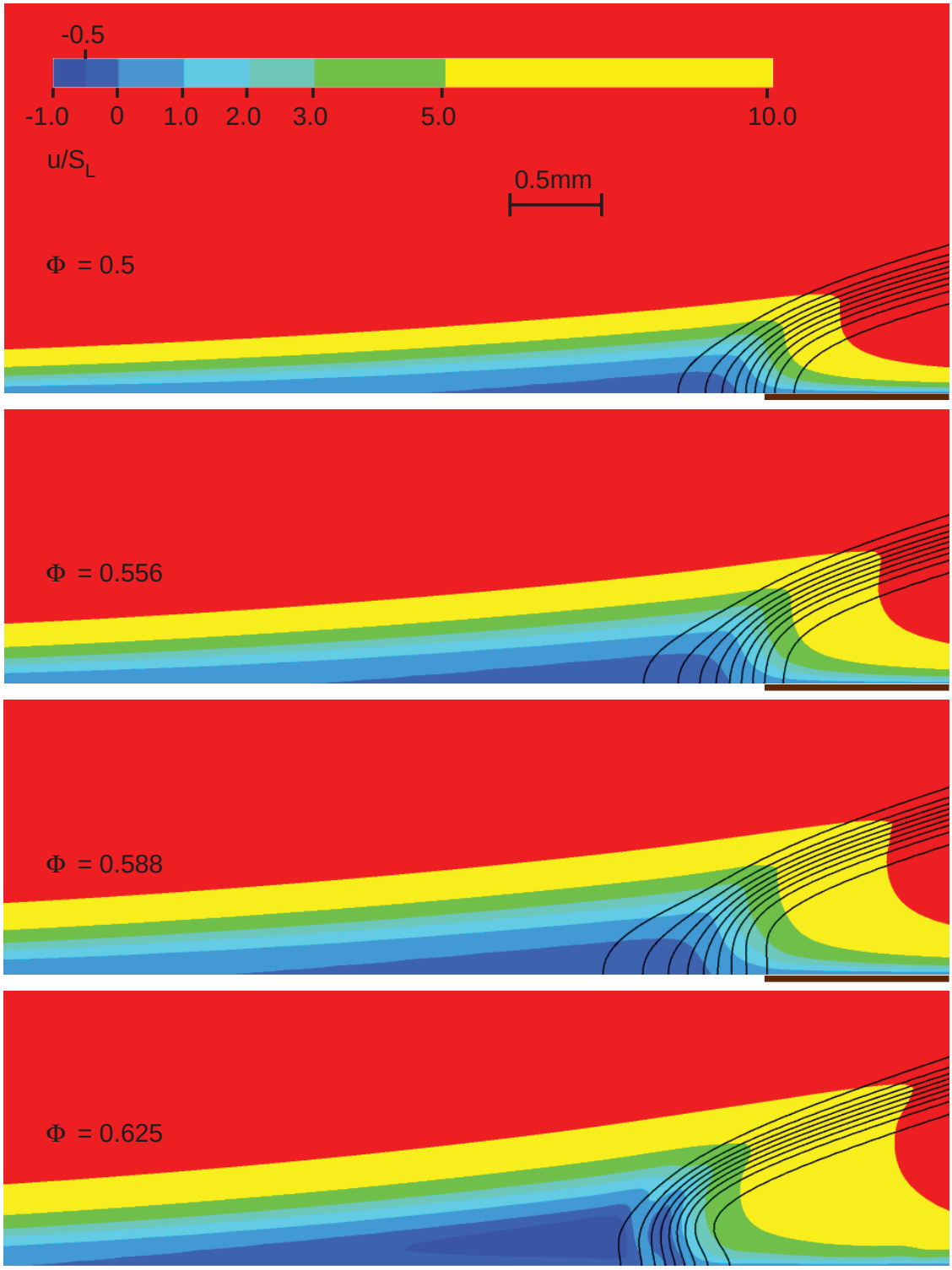

Figure 5.4: Axial velocity contours of laminar flashback simulations

result of $S_f \approx 0.3\,\mathrm{m/s}$ is lower than the one-dimensional adiabatic laminar burning velocity, which is $S_L = 0.97\,\mathrm{m/s}$. This deficiency is probably a combination of heat loss to the wall, which lowers the reaction speed, and the fact that the maximum backflow velocity may not be representative for the velocity of fluid in which the flame actually propagates. The sequence shown in Fig. 5.4 suggests thermal quenching as the limiting factor for the flashback of premixed flames in wall boundary layers. The backflow region already exists before flashback conditions are reached, but its extent above the wall is too small to allow reaction. The flashback point is determined by the equivalence ratio at which the backpressure of the flame causes the backflow region to raise above a certain height at which reaction can be established.

To support this interpretation, Figs. 5.5 show contours of the radicals HO_2 and H close to the flashback limit ($\Phi = 0.588$) and during flashback ($\Phi = 0.625$). Temperature isolines at 400, 600, 900, 1200 and 1500 K are shown in black in each figure to mark the exten of the reaction zone. Furthermore, white isolines of zero axial velocity are included to mark the border of the backflow region. In Fig. 5.5a, which shows a stable, stationary case as already mentioned, HO_2 is convected upstream from the reaction zone and accumulated in the slightly preheated backflow region. Although HO_2 is a precursor of the *H* radical in a flame without heat losses (see Fig. 2.7), the H radicals are quickly quenched by the forward reaction of (5.1b) due to heat losses to the wall, as can be seen in Fig. 5.5b. Therefore, the backward reaction of (5.1c) is slowed down due to vanishing H concentration such that HO_2 is not consumed anymore in the backflow region. The same mechanism of HO_2 accumulation can be observed during flashback in Fig. 5.5a. However, due to the dynamical upstream displacement of the backflow region, the axial extent of the accumulation zone is reduced. By comparing the relative height of the backflow region and the H molar fraction contours in Figs. 5.5b and 5.5d, it is confirmed that the flame propagates upstream once that the main reaction zone is included in the backflow.

Finally, Fig. 5.6 depicts the flow field during flashback at $\Phi = 0.625$ by streamlines, axial velocity profiles and temperature contours to mark the extent of the flame. The figure is taken at the same instant as the last image in Fig.

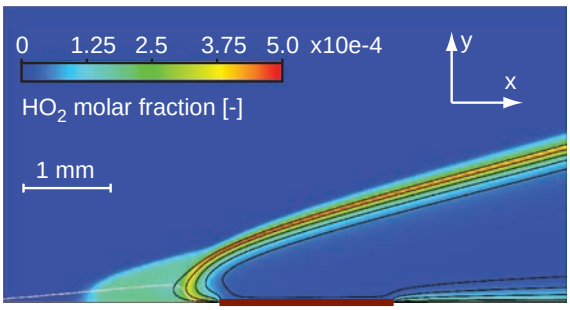

(a) Stable, $\Phi = 0.588$.

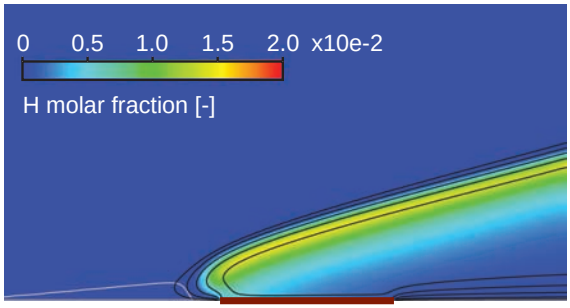

(b) Stable, $\Phi = 0.588$.

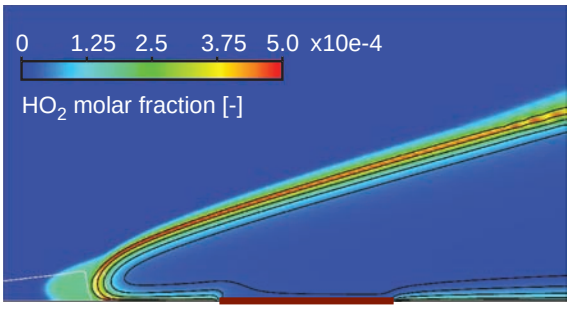

(c) Flashback, $\Phi = 0.625$

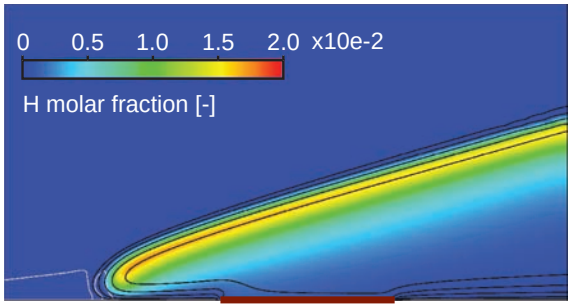

(d) Flashback, $\Phi = 0.625$

Figure 5.5: Numerical flow and flame development at the wall during flashback approach

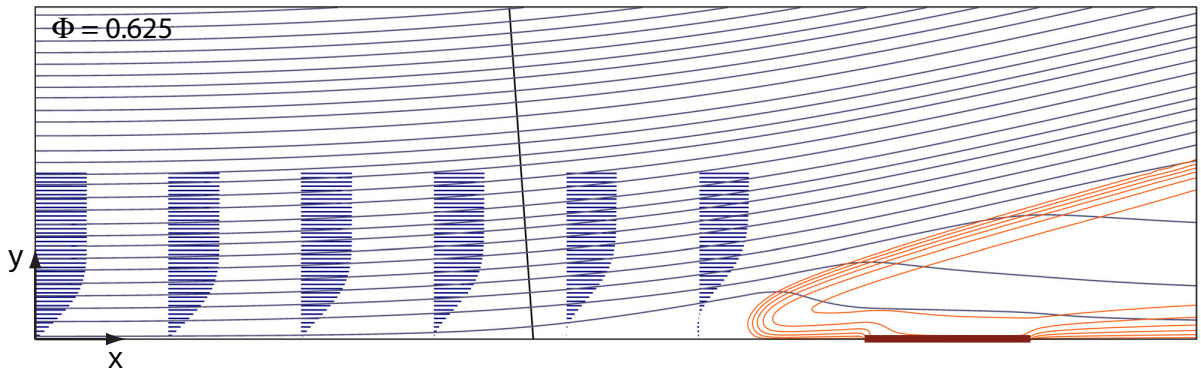

Figure 5.6: Streamlines, axial velocity profiles and temperature contours of a laminar H_2-air flame during flashback.

5.4. The development of the axial velocity profiles towards the backflow region represents typical boundary layer separation due to an adverse pressure gradient as shown in Fig. 2.5. The presence of the flame causes a strong upward deflection of the freestream which, according to inviscid flow theory, must be accompanied by a pressure gradient pointing outwards from the center of cur-

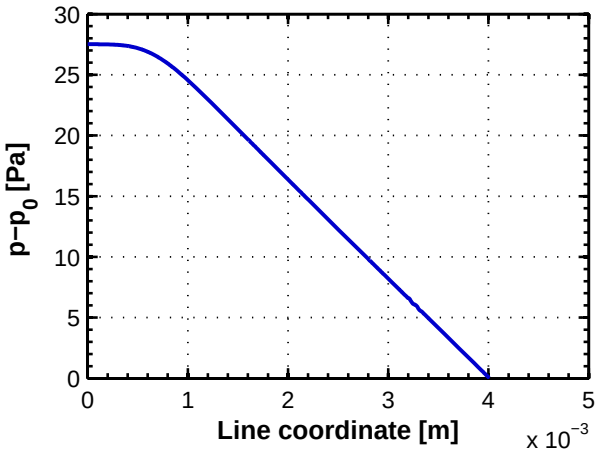

Figure 5.7: Pressure distribution normal to streamlines during wall flashback.

vature. As will be shown now, it is this macroscopic flow displacement which effects the strong static pressure rise upstream of the flame, as already shown in Figs. 5.2b and 5.3, that could not be explained by one-dimensional flame backpressure. The equation for equilibrium between centrifugal forces and pressure forces normal to a curved streamline is [GTG04]

$$\rho \frac{u^2}{R_c} = \frac{\partial p}{\partial r}\,, \tag{5.5}$$

where R_c is the local radius of curvature of the streamline and r is the radial coordinate with respect to the center of curvature. From Fig. 5.6, the radius of curvature has been estimated as $R_c \approx 65\,\mathrm{mm}$. Using the respective density of $\rho = 0.967$ and freestream velocity of $u = u_\infty = 19.64\,\mathrm{m/s}$, the radial pressure gradient according to Eq. (5.5) is $\partial p/\partial r = 5738\,\mathrm{Pa/m}$. For comparison, the relative static pressure of the flashback simulation from bottom to top of the angled black line shown in Fig. 5.6 is depicted in Fig. 5.7. The pressure distribution approaches an essentially constant pressure gradient in the freestream, which corresponds to about $\partial p/\partial r = 8200\,\mathrm{Pa/m}$. This compares well to the inviscid value priorly calculated in light of its approximate character. This result has an important consequence for the correlation of wall flashback. The distribution of streamline curvature is mainly determined by the following three factors:

- Boundary layer velocity profile far upstream of the flame.

- Development of the burning velocity towards the freestream.
- Development of the flame backpressure towards the freestream.
- Boundary conditions opposite to the wall at which flashback occurs.

The burning velocity of the flame and its backpressure as a function of wall distance are considered to be important at the same time: On the one hand, the pressure field upstream of the flame influences the direction of the incoming flow, which in turn changes the angle at which streamlines intersect the flame region. On the other hand, the velocity component of the fresh gases which is perpendicular to the flame zone must match the local burning velocity at steady conditions. Therefore, the stable position of the flame will be adjusted such that both requirements, momentum conservation of the streamlines and the kinematic balance of the premixed flame are fulfilled. The local backpressure and burning velocity of the flame are influenced by flame stretch effects and by heat loss to the wall, such that asymptotic values will only be reached in freestream regions with low velocity gradients. Additionally, the presence of a wall below the angled flame reduces the flow volume of the exhaust gases, such that higher velocities and hence increased backpressures compared to the 1D prediction in Eq. (2.35) are the result.

The influence of the fourth factor of the list above can be understood by placing a wall on top of the simulated domain instead of an opening. Since streamlines must finally be parallel to this wall, less streamline curvature is produced for given inflow conditions such that the adverse pressure gradient and hence the formation of a backflow is weakened. Indeed, such an additionally made simulation showed flashback only for substantially lower inflow velocities for a given equivalence ratio.

6 A New Physical Model for Wall Flashback

The experiments on laminar and turbulent wall flashback and the subsequent detailed simulations of the laminar case have revealed a consistent mode of interaction between the flow field and the flame during the approach and the final phase of wall flashback. These findings will be summarized into a new physical model for wall flashback, which is based on direct observation of the involved physical processes.

Figure 6.1 summarizes the main aspects of the configuration of flame and flow during wall flashback in a model scheme. On the left-hand side of the figure, the development of the boundary layer profile is sketched as it approaches the flame. The position of the flame on the right-hand side of the figure represents the distribution of a flame quantity which is sensitive to thermal quenching, such as the molar concentration of the H radical (see Fig. 5.5). The essentials of the model can be summarized as follows:

- The boundary layer profile on the left-hand side of the figure separates due to an adverse pressure gradient as it approaches the flame. A back-flow with $u < 0$ is formed close to the wall.

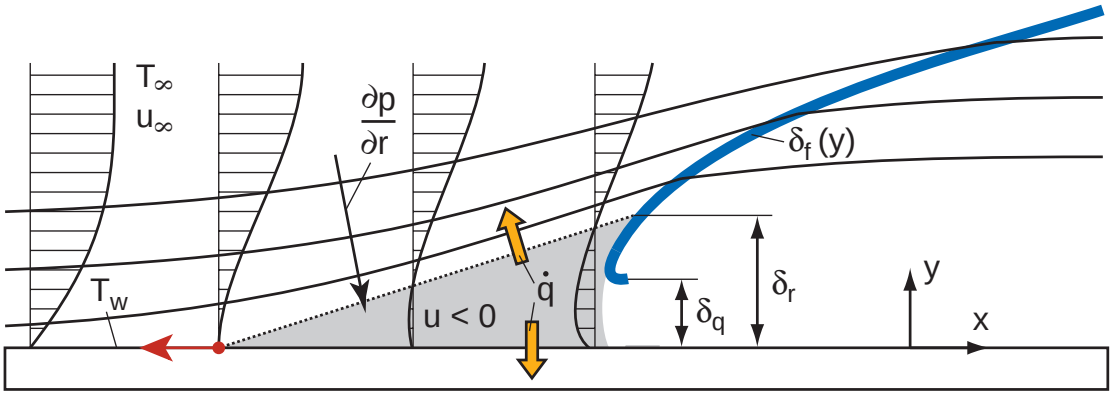

Figure 6.1: Physical model for laminar and turbulent wall flashback.

- The adverse pressure gradient is mainly formed by flow displacement due to the two-dimensional distribution of the reaction zone towards the freestream, which effects streamline curvature upstream of the flame and an according positive pressure gradient towards the wall. The presence of a wall below the flame tail amplifies flow displacement and thus the pressure gradient due to higher expansion velocities of the exhaust gases.

- The flame is only able to propagate upstream if it is anchored inside the backflow. Since quenching by heat losses $\dot{q}$ to the wall and to external streamlines takes place in the backflow region, the maximum backflow height δ_r must exceed the local quenching distance δ_q, which is a measure of the distance at which the reaction is barely sustained inside the backflow region. Backflow thus can exist prior to flashback if the flame is anchored in the boundary layer region by other means.

- The separation point is dislocated upstream by flame propagation inside the backflow, which continuously provides fresh mixture to the flame. Once flashback conditions are reached, the flame propagates upstream at a finite velocity in an absolute frame of reference since the flow velocity in the backflow is < 0.

The prediction of the flashback point thus requires three considerations:

1. **Streamline curvature and the induced pressure rise upstream of the flame due to the presence of the two-dimensional flame shape in the flow**: Since the tail of the flame extends into the main flow, streamlines in the outer regions of the boundary layer and eventually in the freestream are deflected upwards by the local flame backpressure. The effective pressure rise in front of the flame results from the integration of the radial pressure gradient which is induced by streamline curvature in the region of the flame tip. In other words, the pressure rise upstream of the flame is indirectly caused by the backpressure of a considerably larger portion of the flame than just the tip region which is located close to the backflow. If the amount of displaced fluid above the flame tip is large, such as in a flat-plate situation without an opposite wall, the effective flame back-

pressure can probably be predicted well without consideration of the detailed flame shape in the quenching region close to the wall.

2. **Height of the backflow region**: Once that the pressure rise upstream of the flame is known, the height of the backflow region δ_r must be estimated, e.g. based on boundary layer separation theory.

3. **Quenching distance of the flame at backflow conditions**: The quenching distance δ_q is probably most difficult to predict due to the complex flow situation at the flame tip and the presence of the wall. A Peclet number approach based on flame thickness (see Eq. (2.45)) may be feasible for scaling of experimental values.

The model is considered to describe the underlying physics for both, laminar and turbulent flow conditions. As can be seen from experiments and numerics, the physical picture in Fig. 6.1 is representative for the temporal evolution of laminar wall flashback. In the turbulent case, the model describes the local conditions in the discrete flame cusps which were observed in experiments.

Based on this model, the true distance of the flame tip from the wall during turbulent wall flashback can be estimated, which could not be inferred directly from the Mie-scattering images. For the turbulent flashbacks with zero pressure gradient observed in Figs. 4.18 and 4.19 and flashbacks with moderate adverse pressure gradient in Fig. 4.22, the flame is not stabilized inside the laminar sublayer as the critical gradient model predicts, but is rather anchored inside the upper region of the backflow, which is located in the buffer layer ($y^+ \approx 25$ to 35). For a statistical analysis of these heights, the data base is not sufficient, though. For strong adverse pressure gradients, the backflow extends into the logarithmic region, a fact which is not fully understood at the moment. The existence of substantial low-momentum regions in the logarithmic layer of adverse pressure gradient flows could play a role here (see Sec. 2.1.5).

Table 6.1 lists approximate maximum heights of the backflow region in front of the flame as obtained from Figs. 4.18, 4.19, 4.22, 4.23 and 4.24. It has to be emphasized that these numbers are based on single flashback events and thus do not represent statistical information, but provide an estimate of the order

Table 6.1: Approximate wall distances of turbulent flames during wall flashback.

Fuel	ϕ [°]	Φ [-]	δ_r^+ [-]	δ_r [mm]	$\mathrm{Pe_q}$ [-]
H_2	0°	0.345	35	0.96	1.5
H_2	0°	0.543	36	0.53	1.4
H_2	2°	0.345	23	0.63	1.0
H_2	4°	0.256	53	2.13	-
CH_4	4°	1.0	63	2.44	20

of magnitude. The last column of Table 6.1 shows quenching Peclet numbers $\mathrm{Pe_q} = \delta_r/\delta_f$, where Eq. (2.22) has been used to evaluate δ_f. For H_2-air flashback in the 4° diffuser, the mixture was too lean to evaluate δ_f by Cantera simulations. The quenching Peclet numbers for the 0° channel case are of the same order as the value of Enomoto [Eno02] for laminar H_2-air sidewall quenching listed in Table 2.1.

6.1 Difference between Confined and Unconfined Flame Holding prior to Flashback

It has been experimentally observed that wall flashback propensity in geometries with confined flame holding can exceed unconfined limits by an order of magnitude. After the development of the physical model shown in Fig. 6.1, this behavior can be explained in detail. The configuration between flame and flow prior to flashback for unconfined flame holding is illustrated in Fig. 6.2. The main flow direction is from left to right. On the lower left of the figure, part of the burner rim is shown. Streamlines of the fresh mixture are sketched above the rim which subsequently interact with the boundary region of the flame. Compared to a confined geometry, the adverse pressure gradient acting on the boundary layer at burner exit is reduced for two reasons:

1. The burner rim quenches the reaction next to it by heat losses $\dot{q}$. Since $p_1 > p_\infty$, the resulting gap forms a relaxation passage for the pressure

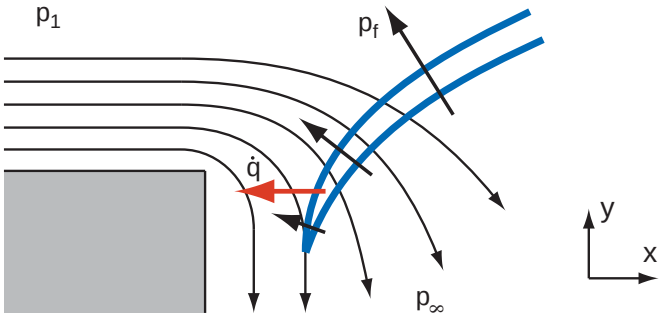

Figure 6.2: Unconfined flame holding prior to flashback.

field and hence a reduction in $\partial p/\partial x$ seen by the approaching boundary layer. As an effect, the fresh mixture at the inner burner wall is accelerated towards the quenching gap, which leads to the well known overhang of the reaction zone in that region [Fra77, LE87, SY05]. As secondary effects, the flame backpressure p_f is reduced by thermal quenching and flame stretch on the one hand, which adds to the decrease in axial pressure gradient. On the other hand, the flame is deterred from entering the boundary layer region due to the outward fluid motion.

2. The expansion of the exhaust gases is not obstructed by a wall, such that the backpressure of the freestream part of the flame, the resulting streamline curvature and the induced adverse pressure gradient at the flame base are diminished.

For a confined flame stabilized at a small backward-facing step, such as the 'step' configuration of the 0° channel shown in Fig. 4.7 or the confined tube burner setup in [EBS12], the physical picture is slightly different. The quenching of the chemical reaction causes a gap downstream of the step edge with an associated pressure drop in the same way as for the unconfined case. However, the flow of fresh mixture through this gap is obstructed by the offset channel wall. Thus, with decreasing step height, the fluid motion perpendicular to the main flow direction diminishes and the flame anchor moves closer to the boundary layer region of the fresh mixture. Moreover, the quenching distance is decreasing since a decrease of the gap leakage flow reduces the convective heat loss from the preheat zone of the flame. These two effects in combination with the backpressure increase by the presence of the wall below the flame tail

result in an increased flashback propensity with decreasing step height, which has been observed experimentally (see Fig. 4.8).

A confined flame which is stabilized flush with the duct wall represents the most critical configuration in terms of flashback propensity. On the one hand, the flame is always present inside the boundary layer. Also in this case, streamlines close to the wall are deflected towards the quenching gap below the flame, but this motion does not displace the flame tip appreciably. Furthermore, the quenching distance of this sidewall configuration is known to be smaller than the axial distance between burner rim and an unconfined flame stabilized above it [Woh53]. On the other hand, the compression effect of the wall is maximized if no step exists downstream of the flame holding location.

6.2 Correlation of Turbulent Flashback Limits

For the purpose of flashback-safe burner design, the correlation of experimental flashback limits by a function of parameter groups Π_i which include the influence of temperature, pressure and fuel-oxidizer mixture is desirable. To derive such a function, a physical model is needed which connects variables in such a way that the resulting equation structure remains the same for arbitrary values of Π_i. For the proposed model of wall flashback, this fundamental equation which is assumed to be invariant is the balance between the height of the backflow and a measure of the minimum flame distance from the wall, as it has already been described for the physical model in Fig. 6.1:

$$\delta_r = K\,\delta_q\,. \tag{6.1}$$

In Eq. (6.1), K is a proportionality factor which is yet to be described. In order to form parameter groups which express the variables in Eq. (6.1) by accessible properties of the flow and the flame, the influential variables on δ_r, K and δ_q have to be determined. In the following, only turbulent flow will be considered. However, a respective procedure for laminar flow would be feasible as well since Eq. (6.1) is assumed to be valid for both flow regimes.

6.2.1 Determination of Influential Variables for Turbulent Flow

In the previous chapter, the main factors which determine the height of the backflow region δ_r have already been discussed. The boundary layer velocity profile far upstream of the flame, flame backpressure and burning velocity as well as the geometrical confinement of the flame were mentioned. The large number of influential variables on the quenching distance δ_q has already been indicated by Eq. (2.44). Finally, the proportionality factor K may itself be a complicated function. Therefore, simplifications will be made at this point in order to to develop a useful correlation model.

For the determination of the backflow height δ_r, the following simplifications are introduced:

- The influence of turbulent fluctuations on the backflow formation in the near-wall region is only included implicitly by scaling with inner wall units (see Eq. (2.6)). Consequently, the correlation results will be specific for canonical boundary layers at comparable conditions. Please note that large changes in Reynolds number shift the scaling of the mean turbulent quantities by inner wall units (see Figs. 2.3). Furthermore, it has been shown in this work that adverse pressure gradients cause crucial changes in the intermittency and strength of low-speed events close to the wall, such that different diverging or converging geometries will lead to different correlation maps as compared to channel flow.
- The influence of changes in freestream turbulence, which increases the local burning velocity and hence the flame backpressure, is not accounted for.
- The influence of non-equidiffusion effects is not included. If this omission can be considered as a second-order effect cannot be stated with certainty at this point.
- The duct height, which has been shown to influence the degree of streamline curvature and thus the pressure increase upstream of the flame, is not introduced as a variable. Hence, correlations are specific for similar duct geometries.

- The mean velocity distribution in the outer boundary layer region and the freestream, which plays a decisive role for the determination of the pressure rise due to streamline curvature, is assumed to scale with inner wall units as well. This is justified for a given internal flow situation (Eqs. (1.9) and (4.1)) if the weak dependence on duct height or diameter is neglected and if adverse pressure gradients are similar. Thus in addition to the sensitivity to adverse pressure gradients, which was already mentioned in the first item, strong geometrical scaling of experimental models thus can lead to deviating correlation maps.

In summary, the height of the backflow is assumed to be dependent on the following variables:

$$\delta_r = f(g, \mu_1, \rho_1, S_L, T_2/T_1)\,, \tag{6.2}$$

The first three variables on the right-hand side of Eq. (6.2) define u_τ and L_+, which provide inner scaling of the canonical turbulent boundary layer. The last three variables define the flame backpressure according to Eq. (2.35) as well as the burning velocity within the simplifications stated above. It should be emphasized here that the influence of swirl on the development of the boundary layer and the freestream velocity distribution has not been taken into account for the derivation of Eq. (6.2).

For the determination of the quenching distance δ_q, the following simplifications are made:

- Although δ_q surely is a complicated function of properties of the flow, the flame and the wall, a Peclet number scaling of the form

  $$\mathrm{Pe_q} = \text{const.} \tag{6.3}$$

  will be adopted, which means that

  $$\delta_q = f(\delta_f) = f(S_L, a_1)\,. \tag{6.4}$$

  Equation (2.22) has been used for the right-hand side of Eq. (6.4).

- As it has already been discussed in Sec. 2.4, the quenching Peclet number is influenced by the type of fuel and oxidizer for a given quenching configuration. For sure, the ratio of T_1/T_w also plays a decisive role

(usually, $T_1 = T_w$ is assumed for quenching studies). Mixture preheating is likely to lower $\mathrm{Pe_q}$ compared to atmospheric values if $T_1 = T_w$ is assumed, since T_2/T_1 decreases with preheating. As probably secondary effects, the equivalence ratio and mixture pressure have an influence on $\mathrm{Pe_q}$. In sum, the correlation model should be considered to be sensitive at least to strong changes in fuel-oxidizer type as well as to wall cooling and mixture preheating.

Finally, it will be assumed for the correlation model that the proportionality factor K in Eq. (6.1) is only depending on the variables which are included in Eqs. (6.2) and (6.4).

A correlation map which is based on the approximations introduced above should remain valid if the geometry, the inflow turbulence level, fuel and oxidizer type and stoichiometry regime (fuel-lean or fuel-rich) as well as the wall cooling conditions are similar and if boundary layers are fully turbulent in the region of interest. Furthermore, mixture preheating should be included in the experimental database which is used to form correlation maps in order to capture the effect of the temperature difference $T_2 - T_w$ on the quenching process. Hence, the correlation model will be particularly useful to extrapolate wall flashback limits of non-swirling, preheated duct flows at atmospheric pressure to higher pressures for a given burner geometry.

6.2.2 Dimensional Analysis

On the whole, there are 5 dimensional variables and 1 nondimensional variable in Eqs. (6.2) and (6.4) which define the flashback condition of Eq. (6.1). Since flashback conditions can be approached very slowly, the time has not been introduced as a further variable. Using a dimensional system of length, mass and time to reduce the dimensional variables according to the Pi theorem [Spu92], three nondimensional groups

$$\Pi_1 = \frac{T_2}{T_1} \tag{6.5a}$$

$$\Pi_2 = \frac{S_L^2}{a_1\, g} = \mathrm{Da} \tag{6.5b}$$

$$\Pi_3 = \frac{\nu_1}{a_1} = \mathrm{Pr} \tag{6.5c}$$

can be formed. The variable Π_1 is the temperature ratio across the flame which is important for the momentum balance between unburnt and burnt gases. The variable Π_2 is a Damköhler number which corresponds to Eq. (1.14). In the context of turbulent wall flashback, Π_2 compares the characteristic timescale of the turbulent boundary layer flow $t_+ = 1/g$ (see Eq. (2.7)) with the timescale of the laminar flame. Finally, Π_3 is the Prandtl number, which compares the diffusivity of momentum in the boundary layer flow to the thermal diffusivity which is important in the preheat zone of the flame and for the quenching process.

The function $\Pi_1 = f(\Pi_2, \Pi_3)$ is not known a priori. However, it can be obtained by an interpolation fit of measurement values in the three-dimensional space of Eqs. (6.5) based on wall flashback experiments for a specific setup with regard to geometry, mixture type and flow conditions as explained in the previous section. However, such an interpolation may not be necessary for an extrapolation of experimental wall flashback limits to higher pressures if preheated experiments at atmospheric pressure have been conducted at the same equivalence ratio and using the same fuel as intended for the high pressure case, as will be shown in the following.

6.2.3 Correlation Map for Turbulent H_2-Air Wall Flashback in the 0° Channel

The turbulent wall flashback limits obtained from the flush 0° channel configuration for atmospheric and preheated H_2-air mixtures have been converted to the coordinates Π_1, Π_2, and Π_3. Figure 6.3 shows two projections of the re-

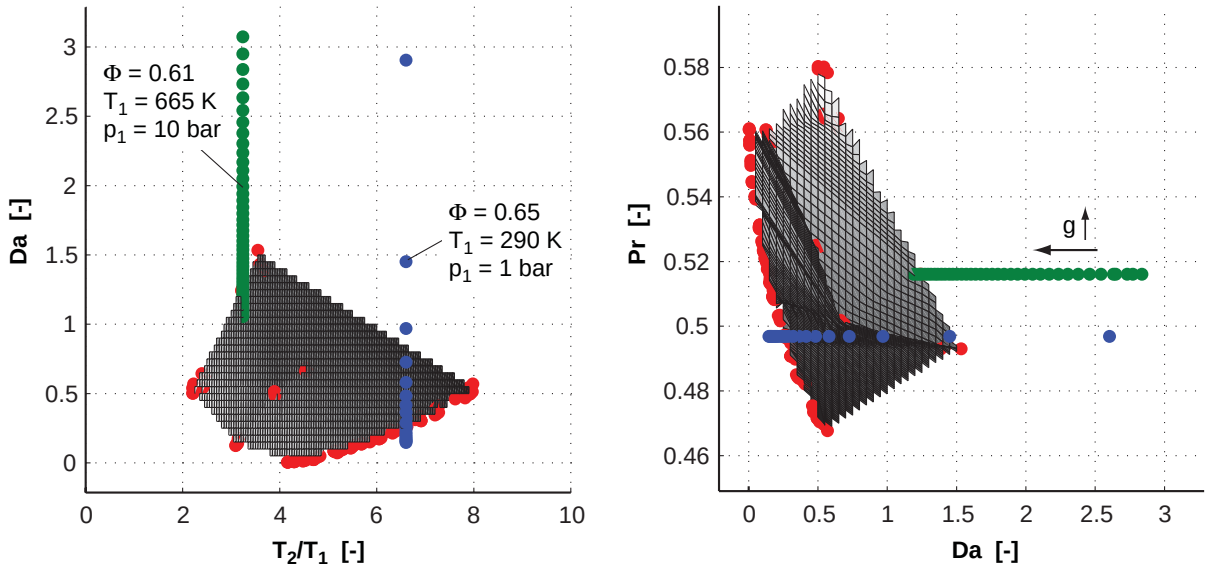

Figure 6.3: Interpolation of correlation function f based on atmospheric and preheated turbulent wall flashback limits of H_2-air mixtures for flush flame holding in the 0° channel.

spective three-dimensional coordinate system, where the experimental flashback points are plotted as red circles. An interpolation plane fitted to the experimental data is also included in the plot. Due to little measurement data for preheated mixtures (see also Fig. 4.13a), the shape of the interpolation plane is not very smooth, but the trend is visible.

Two examples of a search for flashback limits in terms of g are included in Fig. 6.3 as green and blue circles. It becomes clear that for a given operation point in terms of Φ, T_1 and p_1, the Prandtl number and the temperature ratio T_2/T_1 are fixed only by chemistry and mixture properties, such that the flashback limit is approached on a straight line which is parallel to the Da-axis by varying g. The critical gradient is determined by the intersection with the interpolation plane. The blue circles represent an atmospheric case, while the green circles represent an operation point of a gas turbine at $T_1 = 665\,\mathrm{K}$ and $p_1 = 10\,\mathrm{bar}$. The distance between the symbols for each approach correspond to a step of $\Delta g = 10000\,1/\mathrm{s}$.

Two important conclusions can be made from a comparison between the atmospheric and the high pressure and temperature examples. The first point

regards the sensitivity of the Damköhler number to small changes in the velocity gradient at the wall, which to first order is proportional to

$$\frac{\partial \Pi_2}{\partial g} = -\frac{1}{g^2}\frac{S_L^2}{a_1}\,. \tag{6.6}$$

From Eq. (6.6) it becomes clear that the sensitivity rapidly declines with increasing g. Hence for large critical gradients, the flashback limit in terms of g_c becomes hard to determine exactly, especially if S_L^2/a_1 is small at the same time. This effect can be seen from the distance between the symbols close to the flashback plane, which is much larger for the atmospheric case where $g_c = 113000\,1/\mathrm{s}$ when compared to the high pressure and temperature case, where $g_c \approx 600000\,1/\mathrm{s}$ as determined from the intersection with the plane.

The second conclusion regards the actual influence of pressure on the three coordinates in Fig. 6.3. For an ideal gas,

$$\nu \sim \frac{1}{p}\,, \qquad a \sim \frac{1}{p} \qquad \Rightarrow \qquad \mathrm{Pr} \neq f(p)\,. \tag{6.7}$$

Furthermore, the temperature ratio of T_2/T_1 is only a weak function of pressure for lean H_2-air mixtures. This means that for the high pressure case which is shown by green symbols in Fig. 6.3, the pressure influence is well represented only by the Damköhler number. Therefore, if the flashback limit $g_{c,0}$ of a preheated case at atmospheric pressure is compared to the flashback limit g_c at a higher pressure at the same temperature, the Damköhler number at the flashback limit stays constant. This leads to

$$g_c = g_{c,0}\,\frac{S_L^2}{S_{L,0}^2}\,\frac{a_{1,0}}{a_1} = g_{c,0}\,\frac{S_L^2}{S_{L,0}^2}\,\frac{p}{p_0}\,. \tag{6.8}$$

For the right term in Eq. (6.8), ideal gas behavior according to Eq. (6.7) has been used. Equation (6.8) reveals the pressure influence on the wall flashback process if the change in T_2/T_1 with pressure can be neglected. Although the laminar flame speed decreases with increasing pressure, the strong decrease in thermal diffusivity, which is inversely proportional to pressure, effectively reduces the chemical time scale a_1/S_L^2 and thus increases flashback propensity. For the example in Fig. 6.3, an experiment at atmospheric pressure, but

at the same Φ and T_1 gave $g_{c,0} = 205000\,1/\mathrm{s}$. The scaling factor to 10 bar is 2.93 according to Eq. (6.8), which leads to the intersection value at the flashback plane of about $g_c \approx 600000\,1/\mathrm{s}$ in Fig. 6.3 as mentioned before. The correlation proposed by Fine [Fin58] (see Eq. (1.8)) predicts a substantially higher increase of g_c with pressure for flashback limits of unconfined tube burners. This deviation may be explained by a different dependence of the flame base position and the height of the backflow on pressure in an unconfined setup, however, this point clearly needs further investigation.

7 Summary and Conclusions

The physical processes governing wall flashback, a failure scenario critical for the safety and reliability of premixed H_2-rich fuel burners, have been investigated. Literature analysis has revealed a general lack of understanding regarding wall flashback in turbulent flows as well as the influence of geometrical boundary conditions on that process.

Experiments on wall flashback limits in fully-premixed atmospheric and preheated turbulent flow and various geometries have shown a strong influence of the degree of flame confinement during flashback approach. The most critical case has been identified as a flush stabilization of the flame inside the duct prior to flashback. For this type of flame holding, it has been shown that adverse pressure gradients further move the flashback limit to higher flow velocities for a given mixture, which is a first indication of the inadequacy of the critical gradient model. Mixture preheating shifts the flashback limit to higher critical gradients, though the increase is not as strong as predicted for unconfined flames. According to a prediction based on canonical boundary layer turbulence, the observed wall flashbacks lay in the thin reaction zone regime of turbulent combustion for atmospheric mixtures. For preheated mixtures, a regime change to corrugated flamelets has been predicted which is supported by experimental observations.

Detailed experiments using μ-PIV and simultaneous OH^* chemiluminescence with high temporal resolution to observe the flame motion during wall flashback in laminar and turbulent flows of two different fuels inside various geometries have elucidated the wall flashback process and critical parameters for flashback propensity. The well-established critical gradient model of Lewis and von Elbe has been shown to be physically inadequate to describe the detailed propagation of the flame close to the wall. While the critical gradient model predicts a counterflow propagation of the leading flame tip close

to the wall, experiments as well as numerical simulations have revealed that the flame actually propagates in the same direction as the fresh gases inside a backflow region. This process is similar to flashback due to CIVB, for which the flame is only able to propagate against high flow velocities inside the trailing part of a backflow region in much the same way. The observed wall distances of the flame tip during turbulent H_2-air wall flashback in channel flow lay in the height of the buffer layer between laminar sublayer and logarithmic region of the isothermal boundary layer profile.

During wall flashback, the backflow is caused by boundary layer separation due to a static pressure rise upstream of the flame. The separation point is continuously dislocated upstream due to the propagation of the flame relative to the backflow, such that fresh gases are continuously decelerated and subsequently consumed by the flame. For laminar flashback, the backflow region is stable as it moves upstream. During turbulent flashback, backflow regions dynamically form and disappear in intermittent low-velocity regions in the near-wall region of the turbulent boundary layer. This observation is similar to isothermal incipient turbulent separation by adverse pressure gradients, which shows a comparable backflow behavior. Moreover, the difference in laminar and turbulent flashback limits in terms of critical velocity gradients can be explained by flashback in low-velocity regions in the turbulent case.

The observed aggravating influence of global adverse pressure gradients, which was generated by a diffuser, on the separation process during turbulent wall flashback is probably due to an increased frequency of low axial velocity events in the time-resolved flow structure close to the wall. However, this point needs further clarification.

Numerical simulations of laminar H_2-air wall flashback with a reduced chemistry model in a flat plate boundary layer have shown that the backflow region already exists prior to flashback for a flame stabilized flush with the wall. However, the reaction is quenched by thermal losses if the height of the backflow region is yet small. The flashback limit is determined by the point when the height of the backflow reaches a certain value such that reaction can be sustained inside the backflow.

A new physical model for wall flashback has been proposed based on the results described above. Using dimensional analysis, three nondimensional numbers have been identified as model parameters for correlation of flashback limits. Based on the limited wall flashback data obtained here, a prediction of wall flashback at elevated temperatures and pressures led to significantly higher flashback limits than for atmospheric pressures, while the position in the turbulent combustion regime was not appreciably affected.

The results of this work indicate necessity for further research on wall flashback:

- The numerical prediction of backflow existence prior to flashback should be assessed experimentally.
- The transition from atmospheric to preheated wall flashback probably induces a regime change of turbulent combustion which should be investigated in depth.
- The proposed correlation model should be validated by wall flashback experiments under elevated pressures.
- The existence of a hysteresis between wall flashback limit and wash-out of a yet ongoing wall flashback should be checked by laser ignition inside the duct geometry, for example.
- The influence of swirling flow on wall flashback is of importance for the design of gas turbine burners and thus should be investigated.

A Details of the LDA Setup

3-Axis Automatic Traverse System

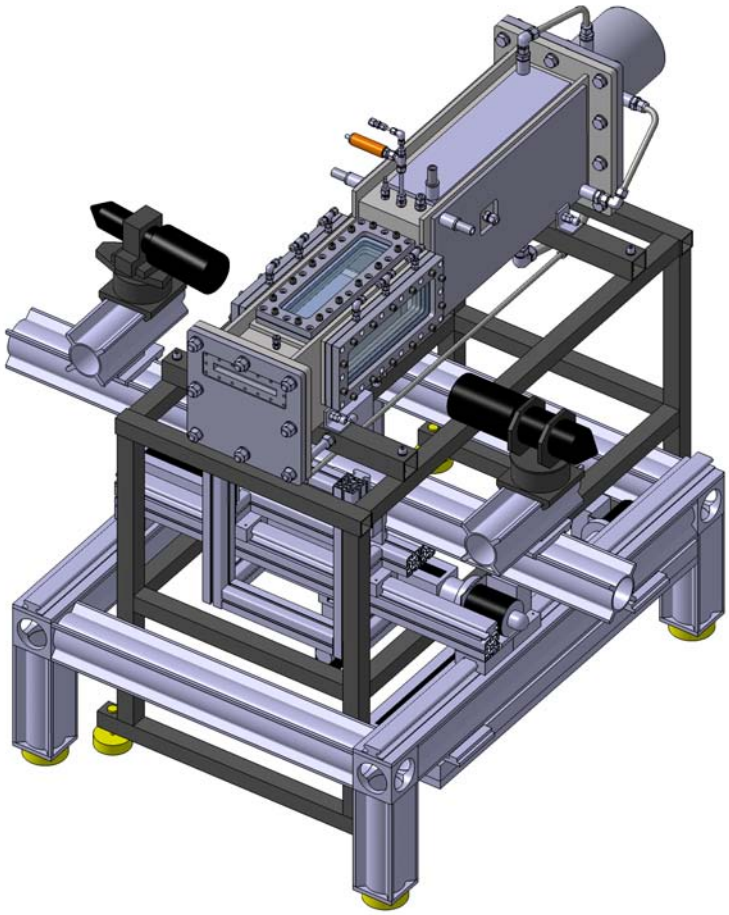

Figure A.1: 3D traverse system for LDA measurements.

Figure A.1 shows the 3D traverse system which has been designed and implemented for precise and efficient LDA measurements. The system is based on three Isel linear guides with 0.02 mm positioning repeat accuracy which are operated by an Isel C142-4 controller.

Geometrical Parameters and BSA Settings

Context	Parameter	Value	Unit
LDA Optics Parameters	Wavelength	514.5	nm
	Focal length	310	mm
	Beam diameter	2.2	mm
	Expander ratio	1.98	-
	Beam spacing [1]	27.415	mm
	Number of fringes	15	-
	Fringe spacing	2.95	μm
	Full beam angle	5.004	deg
	Measurement volume: dx, dy	0.047	mm
	Measurement volume: dz	0.535	mm
BSA Range/Gain	Velocity Units	m/s	m/s
	Range - Center	variable	m/s
	Range - Span	variable	m/s
	Record Length	32	-
	High Voltage On/Off	On	-
	High Voltage	1000	V
	Signal Gain	30	dB
	Calibration	2.95	m/s/MHz
BSA Timing/Triggering	Clock Source	Private	-
	Coincidence Mode	Private	-
	Arrival Time Clock	Internal	-
BSA Data Collection/Buffering	Data Collection Mode	Burst	-
	Output Buffer Mode	FIFO	-
	Number of Bursts	10000	-
	Meas. interval	10	s
	Validation	Yes/On	-
	Validation Level	0	-
	Dead Time	0	ms
	Duty Cycle	0	%
BSA Advanced Options	Frequency Shift	Yes/On	-
	Manual shift	0	Hz
	Quality Factor	80	%
	Oversize Reject Level	1	-
	Anode Current Limit	1.6	mA
	Burst detection mode	Both	-
	Pedestal Attenuation	0	-

Table A.1: Geometrical Parameters and BSA Settings for LDA experiments.

[1] Prior to beam expansion

B Measurement Accuracy of the μ-PIV System

The following discussion will be concerned with an estimation of main error sources during μ-PIV measurements with the used setup. The error sources considered can be divided into four categories:

- Flow-particle and particle-flow interaction.
- Optical distortions between object and image plane.
- Evaluation of the PIV images by cross-correlation.
- Random errors in the whole experimental setup.

These different error sources will be discussed below.

Influence of High Seeding Density on Turbulent Fluctuations

It has already been discussed in Sec. 3.2.3 that the seeding particles should be sufficiently small to follow turbulent fluctuations with negligible slip. It was also shown that the TiO_2 particles used here are expected to follow turbulent fluctuations without appreciable slip, such that this error source can be excluded. However, the derivation of the BBO equation mentioned in Sec. 3.2.3, which was used to approximate the particle tracking, assumes that there is no feedback of the particles to the flow, such that energy transfer only occurs unidirectionally from the flow to the particles. It is obvious though that this assumption is not feasible anymore for flows with high particle volume fraction Φ_p, defined as

$$\Phi_p = \frac{N_p V_p}{V} \tag{B.1}$$

In Eq. (B.1), N_p is the number of particles in the volume V and V_p is the volume of the particle. There exists a broad literature on particle-turbulence interaction in particle-laden flows due to their importance for the process industry. A recent overview on the topic has been given by Poelma and Ooms [PO06]. They mention the work of Elghobashi on the influence of particles on the spatial turbulence spectrum of a fluid, who tabulated different ways of particle-turbulence interaction in dependence on three nondimensional groups in a chart [Elg94]. The three groups were Φ_p (see Eq. (B.1)) and the ratio of the particle response time (assuming Stokes flow) to two different turbulent timescales. The limit of one-way coupling, i.e. negligible influence of the particles on turbulence, was specified as $\Phi_p \leq 10^{-6}$. The particle density in the

Table B.1: Particle volume load in seeded flow.

Mean particle diameter [μm]	Φ_p at 50 μm mean particle spacing
0.3	$1.1 \cdot 10^{-7}$
0.5	$5.2 \cdot 10^{-7}$
1.0	$4.2 \cdot 10^{-6}$
3.0	$1.1 \cdot 10^{-4}$
5.0	$5.2 \cdot 10^{-4}$

μ-PIV experiments presented here has been determined very roughly by estimating the mean particle spacing of the smallest particles (1-2 pixel diameter) on raw PIV images. Since the particle size is much smaller than the pixel size of the image sensor, the particles considered lie in the focus plane or a small distance outside, such that their unfocused image still does not exceed the pixel size of the image sensor. This results in a rough, conservative estimate of 10 pixels or 50 μm mean particle separation. Table B.1 lists the according particle volume fractions Φ_p for different mean particle diameters and the assumption of an isotropic particle density distribution. The result is putting emphasis on the sensible choice of seeding density for PIV experiments, as the table shows that the chosen volume load for the TiO_2 seeding used ($d_p = 0.3...1\,\mu$m) is at the upper limit for a feasible assumption of one-way interaction.

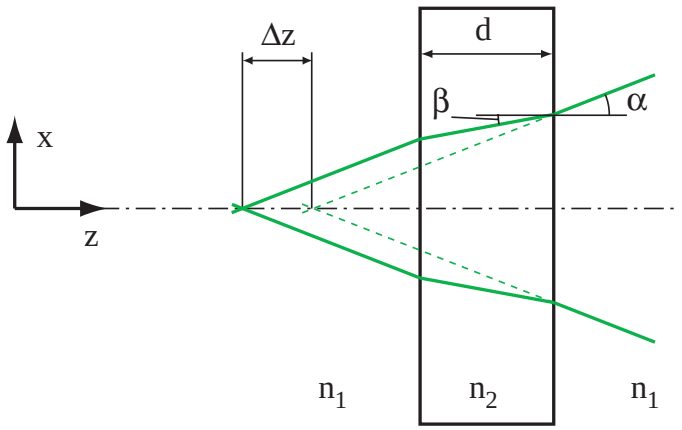

Figure B.1: Refraction of focused light beams passing through a window.

Effect of a Window Between Measurement Volume and Microscope Lens

The unique feature of the present study in comparison with other long-distance μ-PIV investigations is the investigation of highly-reactive flows with the possibility of fast deflagrations and even detonations in the worst case. For security reasons and owing to the demand of flush walls inside the channel, the measurement section is equipped with strong windows of 41 mm thickness. On the one hand, windows absorb some of the scattered light energy, which was not a problem for the chosen dimensions though. On the other hand, light rays are refracted due to the difference of the refractive index of air ($n_1 \approx 1$) and quartz glass ($n_2 \approx 1.47$). In contrast to macroscopic PIV, where object distances are high and numerical apertures are small, refraction effects cannot be neglected for μ-PIV setups. Two effects can be identified for a plane window in the framework of geometrical optics [GS27] (diffraction is not included). To explain the first effect, Fig. B.1 shows the geometrical configuration of a pair of focused light beams passing through a window of thickness d. The refraction at both sides of the window causes an increase of the focal distance by Δz, which is equal to

$$\Delta z = d\left(1 - \frac{\cos(\alpha)}{\sqrt{(n_2/n_1)^2 - \sin^2(\alpha)}}\right) \tag{B.2}$$

Equation (B.2) shows that the distance Δz is dependent on the incident angle α. Only for small values of α, Δz is approximately constant. If a particle in the

focal plane is considered, only light beams with small α will contribute to a sharp image, while other beams still captured by the aperture will produce a defocused image.

The second aberration is observed if the particle position does not coincidence with the optical axis in the focal plane. This effect is known as *astigmatism*, but it occurs in a slightly different form for a plane window as compared to classical astigmatism of lens systems. For lenses, a separation of meridional and sagittal focus planes is observed since the incident beam is refracted asymmetrically [GS27]. In contrast to a lens, the refraction through a window is always isogonic. However, the displacement between two parallel beams on each side of the window is depending on the incident angle, as already described by Fig. B.1. Now if the main axis of the light beam emitted by the particle hits the window surface at a finite angle, the sectional line of the beam and the window plane is an ellipse. Hence the distribution of incident angles is not rotationally symmetric anymore with respect to the main axis of the incident beam. The cross-section of the beam will be deformed to an ellipse after passing the window, which is then focused by the microscope lens. This astigmatism is additive to the defocusing effect explained in Fig. B.1.

The final question whether the presence of the window causes a systematic velocity bias in the PIV results is not straightforward to answer. The first effect described above blurs the particle image, which possibly leads to reduced correlation signals. The second effects distorts the shape of the particle image. However, a velocity bias is only expected if the shape of the particle image changes appreciably during the particle displacement by Δx. Since particle displacements are small with respect to the image plane, this bias is considered to be negligible.

Optical Aberrations and Distortions of the Microscope Lens

The imaging characteristics of the microscope lens used here have been carefully analyzed by Kähler et al. [KMS05, KSO06] for monochromatic laser light. They came to the conclusion that the device is well apt for μ-PIV investigations with respect to the quality of particle images and the magnitude of op-

tical aberrations. The authors used a camera with a large CCD chip (36.6 mm x 24.5 mm), which the microscope is not designed for. Indeed, they observed image distortions in the boarder region of the image which had to be corrected during postprocessing. The camera used for the present experiments has an image sensor of 20.5 mm x 20.5 mm, and appreciable distortions could not be determined in the calibration image. This observation will be validated towards the end of this discussion by comparing average velocities of an undisturbed boundary layer at constant height y, where no systematic bias should be observable in x-direction.

True Measurement Volume due to Out-of-focus Particles

As mentioned in the text, the depth of field in μ-PIV investigations is usually much smaller than the thickness of the illuminated flow volume. To get an estimate of the relation for the present setup, the thickness of the focused lightsheet at the measurement position has been determined by measuring the thickness of its image on a metal block which was inclined by a small angle to the lightsheet axis. The measured lightsheet thickness at focus was $\delta_L \approx 0.2\,\mathrm{mm}$, which is an order of magnitude larger than δ_F. Consequently, the thickness of the measurement volume is not well-defined by δ_F because out-of-focus particles are likely to contribute to the image, too. The derivation of a more representative concept was conducted by Meinhart et al. [MWS00]. They define the *measurement depth* as twice the distance from the center of the object plane from which the image intensity of a particle is a certain fraction of the maximum in-focus intensity. The authors recommend an intensity fraction of 0.1 as a sensible choice. For the case that the pixel size of the image sensor is much larger than the particle diameter and measurements in air, as it is the case for the present setup, the according measurement depth δ_m can be calculated by

$$\delta_m = \frac{3\lambda}{NA^2} + \frac{3.568\,\frac{e}{M} - d_p}{\frac{NA}{\sqrt{1-NA^2}}} \tag{B.3}$$

In Eq. (B.3), NA is the numerical aperture of the lens, λ is the laser wavelength, M is the total magnification of the system and e is the spacing between pix-

els on the image sensor. Table B.2 lists the results from Eq. (B.3) for different

Table B.2: Measurement depth for the present μ-PIV optics.

Mean particle diameter [μm]	δ_F [μm]
0.3	182
0.5	181
1.0	178
3.0	165
5.0	152

particle diameters. It can be concluded that the depth-of-field is a factor of 9 smaller than the measurement depth for the current setup, which means that also defocused particles will contribute to the correlation. On the one hand, this will broad the correlation peaks and eventually may lead to a lower number of valid vectors. On the other hand, it is important to know the true depth δ_F of the measurement volume to specify the spatial resolution of the system as well as the influence of velocity gradients $\partial u/\partial z$ and $\partial v/\partial z$.

A concept similar to the measurement depth defined in Eq. (B.3), which is known as *depth of correlation* analysis (e.g., [OA00]), investigates the influence of defocused particles on the correlation function (see Eq. (3.11)). However, as Raffel et al. [RWWK07] point out, the correlation function is approximately proportional to δ_m^2, such that Eq. (B.3) is a proper representation of that concept, too. It follows that the chosen intensity fraction of 0.1 for Eq. (B.3) corresponds to a cut-off influence of about 1% for the correlation function. Recently, Olsen [Ols09] showed that the depth of correlation is also dependend on fluid shear in the object plane. The effect is limited to high numerical aperture lens and the results indicate that the long-distance microscope with $NA = 0.152$ used here is not susceptible to this issue.

Velocity Bias and RMS Errors from Cross-correlation Analysis

In addition to optical distortions, the quality of the velocity field resulting from cross-correlation analysis is depending on several factors [FMPS04, RWWK07] (recommended values in brackets):

- Cross-correlation algorithm
- Particle image diameter (2-3 pixels)
- Particle image shift (small as possible)
- Particle image density (5-10 particles per interrogation area)
- Fraction of optical active sensor area (high as possible)
- Background noise
- Out-of-plane velocity component
- Velocity gradients

Each of these factors contributes to systematic velocity bias as well as RMS errors. The cross-correlation algorithm used by VidPIV 4.6 uses an adaptive window-deformation technique (see [RWWK07] for principles) with subpixel shifting using B-spline interpolation and Whittaker peak fitting. This advanced algorithm largely reduces errors from velocity gradients and large particle image shifts. Regarding particle image diameter, the recommended value of 2-3 pixel is matched closely for most particles. The recommended value for the particle density is typically reached for interrogation areas of 16x16 pixel in the present study. The fraction of the optically active area of the image sensor, also called *CCD fill*, has no influence on the velocity errors for current particle image diameters of 2-3 pixels, as shown in [FMPS04]. The background noise has been estimated from the pixel intensities of dark regions between particles, which results to about 10%. According to [RWWK07], this amount of noise has virtually no influence on the derived velocity field. The influence for out-of-plane motion is restricted to turbulent fluctuations in the z-direction

for the boundary layer measurements presented here. The magnitude of these fluctuations can be approximated by $w' \approx 1.5u_\tau$ [FMPS04]. The mean out-of-plane displacement during two pulses, $w'\Delta t_{PIV}$, should be lower than about 20% of the effective lightsheet thickness for negligible influences on errors. For the present measurements, out-of-plane displacements only amount to about 10% of the depth-of-field of the microscope (which is an order of magnitude lower than the effective measurement depth, as already explained), thus appreciable errors due to out-of-plane motion can clearly be excluded here.

In sum, the μ-PIV measurements with the current setup and evaluation software are close to the optimum to ensure a cross-correlation with low bias and noise as along as wall reflections are not deteriorating the particle images. To get an estimation of the remaining errors, results of [FMPS04] for an optimized setup and a bicubic subpixel interpolation for the window-shift technique are considered, which result in a mean bias of ±0.02 pixel and an equal RMS uncertainty of ±0.02 pixel. Thus for instantaneous velocity plots, the overall uncertainty is ±0.04 pixel. For time-averaged values, the RMS error vanishes for large sample sizes and only bias errors with ±0.02 pixel are expected.

Experimental μ-PIV Measurement Accuracy

The discussion of random and bias errors will be completed by analyzing own isothermal boundary layer measurement results.

The influence of small interrogation areas compared to particle size and density will be discussed first. Figs. B.2 compares cross-correlations of identical data sets with interrogation areas of size 16x16 and 8x8 pixels. Figure B.2a shows dimensionless mean axial flow profiles. The experimental data sets were non-dimensionalized by the same wall shear determined from the 8x8 correlation results. It can be seen that apart from the first point above the wall, which is underestimating the velocity gradient, the results of 16x16 correlation windows follow exactly the 8x8 values. The fluctuating velocities shown in Fig. B.2b reveal slight deviations of about 3% (axial) and 8% (wall-normal) in the logarithmic region, were gradients are comparably small. Small interrogation

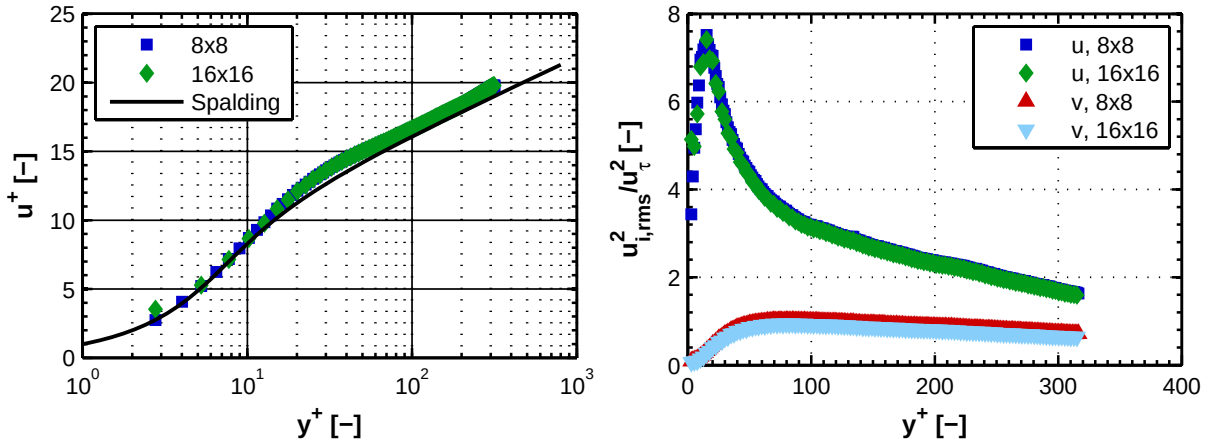

(a) $\dot{m} = 60\,\mathrm{g/s}$: Mean velocities.

(b) $\dot{m} = 60\,\mathrm{g/s}$: RMS velocities.

Figure B.2: PIV: Comparison of 8x8 and 16x16 interrogation areas.

windows thus seem to introduce only noise in the current setup, which is cancelled out in the mean, but shifts rms velocities to slightly higher values.

Potential bias due to aberrations of the window and microscope optics is evaluated from mean PIV velocities by calculating the standard deviation of axial velocities along the x-direction at a fixed height above the wall. The aberrations explained in Sec. 3.2.4 become stronger with increasing distance from the optical axis, such that their influence on the cross-correlation increases towards the borders of the image at a fixed y-position, an effect that should appear in the velocity values. Figure B.3 shows the standard deviations of average velocities, σ_x, related to the mean velocity at a given height y, which has been normalized by the y-height of the PIV measurement area h_{PIV}, in percent for the laminar data sets at E1, E2 and E3 already shown in Fig. 3.27. Please note that the position of the microscope and the orientation of the laser sheet has been re-adjusted for each measurement position, hence inaccuracies from this manual procedure are included. On the x-axis, the distance from the wall related to the height of the PIV measurement plane is shown. The standard deviations have their maximum close to the wall due to the low velocities and spurious wall reflections. Within the remaining part of the flow field, the deviations are exceptionally low. It is concluded that the μ-PIV arrangement does not introduce any appreciable bias due to optical distortions.

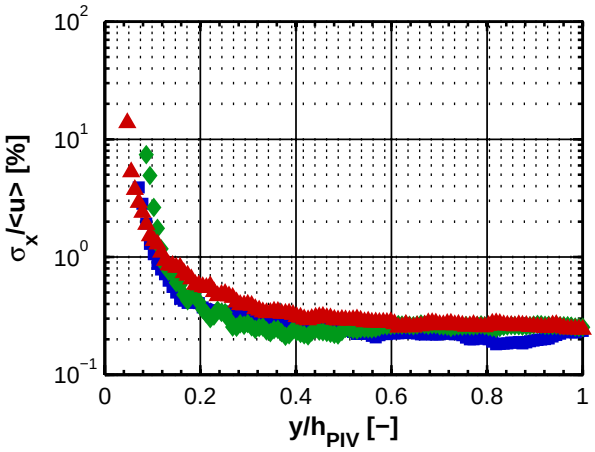

Figure B.3: PIV: Horizontal standard deviation of average velocities for laminar flow.

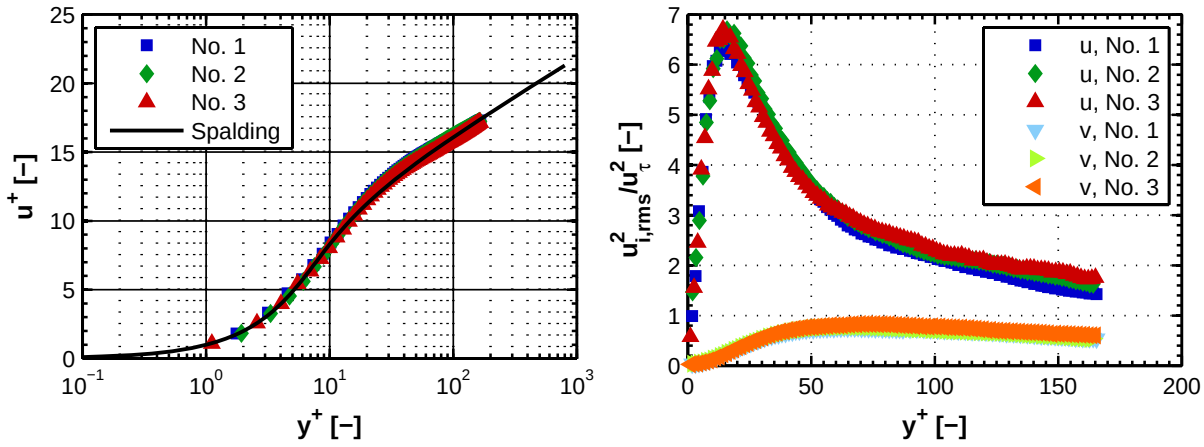

(a) $\dot{m} = 30\,\mathrm{g/s}$: Mean velocities.

(b) $\dot{m} = 30\,\mathrm{g/s}$: RMS velocities.

Figure B.4: PIV: Repeat accuracy and timestep dependence.

Each PIV set presented in the main part of this work represents the average of one single measurement due to the large amount of data and time-consuming evaluation. Therefore, it is important to estimate the reproducibility of the measurements. Figures B.4 show the profiles of three measurements at the same nominal operation point of 30 g/s at position E2. Measurements No. 1 and 2 were taken successively without touching the PIV setup. Measurement No. 3 is taken after a re-adjustment of the system at a different day. Furthermore, the temporal separation Δt between PIV pulses is about twice as high as for No. 1 and 2. Figure B.4a shows dimensionless axial velocities of the three

sets, which have been related to the mean of the three shear stress values. The individual shear stresses have a spread of ±4% from the mean. The mean axial velocities show very good agreement, deviations from the mean are within ±1%. The corresponding rms velocities are shown in Fig. B.4b. The reproducibility for fluctuating velocities is satisfying, deviations from the mean are within ±10%.

Bibliography

[AB00] ANDRAE, J. C. G. ; BJÖRNBOM, P. H.: Wall Effects of Laminar Hydrogen Flames over Platinum and Inert Surfaces. In: *AIChE Journal* 46 (2000), S. 1454–1460

[ABDT03] ALBRECHT, H.-E. ; BORYS, M. ; DAMASCHKE, N. ; TROPEA, C.: *Laser Doppler and Phase Doppler Measurement Techniques*. Springer-Verlag, 2003

[AE05] AUBERTINE, C. D. ; EATON, J. K.: Turbulence Development in a Non-equilibrium Turbulent Boundary Layer with Mild Adverse Pressure Gradient. In: *J. Fluid Mech.* 532 (2005), S. 345–364

[AH81] ALY, S. L. ; HERMANCE, C. E.: A Two-Dimensional Theory of Laminar Flame Quenching. In: *Combust. & Flame* 40 (1981), S. 173–185

[AR02] ALSHAALAN, T. ; RUTLAND, C. J.: Wall Heat Flux in Turbulent Premixed Reacting Flow. In: *Combust. Sci. and Tech.* 174 (2002), S. 135–165

[BAPF96] BRUNEAUX, G. ; AKSELVOLL, K. ; POINSOT, T. ; FERZIGER, J. H.: Flame-wall Interaction Simulation in a Turbulent Channel Flow. In: *Combust. & Flame* 107 (1996), S. 27–44

[BBZ+93] BELOKON, A. A. ; BRAININ, B. I. ; ZHUK, V. A. ; MASLOV, V. P. ; MINEYEV, B. I. ; SECUNDOV, A. N.: Experimental Investigation of the Premixed Combustion under Flashback. In: *SPIE Optical Monitoring of the Environment* 2107 (1993), S. 529–540

[BE56] BOLLINGER, L. E. ; EDSE, R.: Effect of Burner-tip Temperature on Flash Back of Turbulent Hydrogen-Oxygen Flames. In: *Ind. Eng. Chem.* 48 (1956), S. 802–807

[BJSW11] BOIVIN, P. ; JIMÉNEZ, C. ; SÁNCHEZ, A.L. ; WILLIAMS, F.A.: An Explicit Reduced Mechanism for H_2–air Combustion. In: *Proc. Combust. Inst.* 33 (2011), S. 517–523

[BKLS03] BELLENOUE, M. ; KAGEYAMA, T. ; LABUDA, S. A. ; SOTTON, J.: Direct Measurement of Laminar Flame Quenching Distance in a Closed Vessel. In: *Exp. Therm. Fluid Sci.* 27 (2003), S. 323–331

[BL77] BALLAL, D. R. ; LEFEBVRE, A. H.: Ignition and Flame Quenching in Flowing Gaseous Mixtures. In: *Proc. R. Soc. Lond. A.* 357 (1977), S. 163–181

[Bla08] BLASIUS, H.: Grenzschichten in Flüssigkeiten mit kleiner Reibung. In: *Z. Angew. Math. Phys.* 56 (1908), S. 1–37

[Bol52] BOLLINGER, L. E.: Studies on Burner Flames of Hydrogen-Oxygen Mixtures at High Pressures / Wright Air Development Center. 1952 (WADC Tech. Rep. 52-59)

[Bol58] BOLLINGER, L. E.: Evaluation of Flame Stability at High Reynolds Numbers. In: *Jet Propulsion* 28 (1958), S. 334–335

[BP57] BERLAD, A.L. ; POTTER, A.E.: Relation of Boundary Velocity Gradient for Flash-back to Burning Velocity and Quenching Distance. In: *Combust. & Flame* 1 (1957), S. 127 – 128

[Bri74] BRIGHAM, E. O.: *The Fast Fourier Transform.* Prentice-Hall, Inc., 1974

[Bru95] BRUUN, H. H.: *Hot-Wire Anemometry - Principles and Signal Analysis.* Oxford University Press, 1995

[BSLB07] BOUST, B. ; SOTTON, J. ; LABUDA, S. A. ; BELLENOUE, M.: A Thermal Formulation for Single-wall Quenching of Transient Laminar Flames. In: *Combust. & Flame* 149 (2007), S. 286–294

[Bui97] BUICE, C.U.: *Experimental Investigation of Flow Trough an Asymmetric Plane Diffuser*, Stanford University, Diss., 1997

[Bur08] BURMBERGER, S.: *Investigation of the Flame Stabilization in Swirl Burners for the Premixed Combustion of Alternative Fuels at Ambient and Elevated Pressure*, Technische Universität München, Diss., 2008

[CD08] CICCARELLI, G. ; DOROFEEV, S.: Flame Acceleration and Transition to Detonation in Ducts. In: *Prog. Energy Combust. Sci.* 34 (2008), S. 499–550

[Cla54] CLAUSER, F. H.: Turbulent Boundary Layers in Adverse Pressure Gradients. In: *J. Aeronaut. Sci.* 21 (1954), S. 91–108

[CN85] CHENG, R. K. ; NG, T. T.: Conditional Reynolds Stress in a Strongly Heated Turbulent Boundary Layer with Premixed Combustion. In: *Phys. Fluids* 28 (1985), S. 473–488

[Coa80] COATS, C. M.: Comment on "Review of Flashback Reported in Prevaporizing/Premixing Combustors". In: *Combust. & Flame* 37 (1980), S. 331–333

[CS83] CATTOLICA, R. J. ; SCHEFER, R. W.: Laser Fluorescence Measurements of the OH Concentration in a Combustion Boundary Layer. In: *Combust. Sci. and Tech.* 30 (1983), S. 205–212

[DCVP03] DABIREAU, F. ; CUENOT, B. ; VERMOREL, O. ; POINSOT, T.: Interaction of Flames of H_2 + O_2 with Inert Walls. In: *Combust. & Flame* 135 (2003), S. 123–133

[DE00] DEGRAAFF, D. B. ; EATON, J. K.: Reynolds-number Scaling of the Flat-plate Turbulent Boundary Layer. In: *J. Fluid Mech.* 422 (2000), S. 319–346

[DFC05] DAVU, D. ; FRANKO, R. ; CHOUDHURI, A.: Investigation on Flashback Propensity of Syngas Premixed Flames. In: *41st AIAA/ASME/SAE/ASEE Joint Propulsion Conference & Exhibit, Paper No. AIAA 2005-3585*, 2005

[DM02] DAOU, J. ; MATALON, M.: Influence of Conductive Heat-Losses on the Propagation of Premixed Flames in Channels. In: *Combust. & Flame* 128 (2002), S. 321–339

[Dug55] DUGGER, G. L.: Flame Stability of Preheated Propane-air Mixtures. In: *Ind. Eng. Chem.* 47 (1955), S. 109–114

[EBS12] EICHLER, C. ; BAUMGARTNER, G. ; SATTELMAYER, T.: Experimental Investigation of Turbulent Boundary Layer Flashback Limits for Premixed Hydrogen-air Flames Confined in Ducts. In: *J. Eng. Gas Turbines Power* 134 (2012), S. 011502

[Elg94] ELGHOBASHI, S.: On Predicting Particle-laden Turbulent Flows. In: *Appl. Sci. Res.* 52 (1994), S. 309–329. – ISSN 0003–6994

[EM45] ELBE, G. von ; MENTSER, M.: Further Studies of the Structure and Stability of Burner Flames. In: *J. Chem. Phys.* 13 (1945), S. 89–100

[Eno01] ENOMOTO, M.: Head-on Quenching of a Premixed Flame on the Single Wall Surface. In: *JSME Int. J. B - Fluid. T.* 44 (2001), S. 624–633

[Eno02] ENOMOTO, M.: Sidewall Quenching of Laminar Premixed Flames Propagating along the Single Wall Surface. In: *Proc. Combust. Inst.* 29 (2002), S. 781–787

[ES11a] EICHLER, C. ; SATTELMAYER, T.: Experiments on Flame Flashback in a Quasi-2D Turbulent Wall Boundary Layer for Premixed Methane-Hydrogen-Air Mixtures. In: *J. Eng. Gas Turbines Power* 133 (2011), S. 011503

[ES11b] EICHLER, C. ; SATTELMAYER, T.: Premixed flame flashback in wall boundary layers studied by long-distance micro-PIV. In: *Exp. Fluids* Online First (2011). `http://dx.doi.org/10.1007/s00348-011-1226-8`. – DOI 10.1007/s00348–011–1226–8

[FB84] FOX, J. S. ; BHARGAVA, A.: Flame Speed and Flashback Gradient for Simulated Biomass Gasification Products. In: *Intersociety Energy Conversion Engineering Conference, Honolulu, Hawaii*, 1984

[Fin58] FINE, B.: The Flashback of Laminar and Turbulent Burner Flames at Reduced Pressure. In: *Combust. & Flame* 2 (1958), S. 253 – 266

[Fin59] FINE, B.: Effect of Initial Temperature on Flash Back of Laminar and Turbulent Burner Flames. In: *Ind. Eng. Chem.* 51 (1959), S. 564–566

[FKS01] FRITZ, J. ; KRÖNER, M. ; SATTELMAYER, T.: Flashback in a Swirl Burner with Cylindrical Premixing Zone. In: *ASME Turbo Expo, Paper No. 2001-GT-0054*, 2001

[FMPS04] FOUCAUT, J. M. ; MILIAT, B. ; PERENNE, N. ; STANISLAS, M.: Characterization of Different PIV Algorithms Using the EUROPIV Synthetic Image Generator and Real Images from a Turbulent Boundary Layer. In: STANISLAS, M. (Hrsg.) ; WESTERWEEL, J. (Hrsg.) ; KOMPENHANS, J. (Hrsg.): *Particle Image Velocimetry: Recent Improvements (Proceedings of the EUROPIV 2 Workshop, Zaragoza, Spain, 2003)*, Springer-Verlag, 2004

[Fra77] FRANCE, D. H.: Flashback of Laminar Monoport Burner Flames. In: *J. I. Fuel* 50 (1977), S. 147–152

[Fri03] FRITZ, J.: *Flammenrückschlag durch verbrennungsinduziertes Wirbelaufplatzen*, Technische Universität München, Diss., 2003

[Gay74] GAYDON, A. G.: *The Spectroscopy of Flames*. Chapman and Hall, London, 1974

[Geo75] GEORGE, W. K.: Limitations to Measuring Accuracy Inherent in the Laser Doppler Signal. In: *Proceedings of the LDA-Symposium, Copenhagen, Denmark*, 1975

[Goo07] GOODWIN, D. G.: *Cantera 1.7*. 2007

[GPW+05] GHONIEM, A. F. ; PARK, S. ; WACHSMAN, A. ; ANNASWAMY, A. ; WEE, D. ; ALTAY, H. M.: Mechanism of Combustion Dynamics in a Backward-facing Step Stabilized Premixed Flame. In: *Proc. Combust. Inst.* 30 (2005), S. 1783–1790

[Gro55] GROSS, R. A.: Boundary Layer Flame Stabilization. In: *Jet Propulsion* 25 (1955), S. 288–290 + 293

[Gru58] GRUMER, J.: Flashback and Blowoff Limits of Unpiloted Turbulent Flames. In: *Jet Propulsion* 28 (1958), S. 756–759

[Gru06] GRUBER, A.: *Direct Numerical Simulation of Turbulent Combustion Near Solid Surfaces*, NTNU, Diss., 2006

[Gru10] GRUBER, A.: *DNS of Premixed H_2-air Wall Flashback in a Turbulent Channel with Detailed Chemistry*. October 2010. – Private Communication

[GS27] GEIGER, H. (Hrsg.) ; SCHEEL, K. (Hrsg.): *Handbuch der Physik, Band 18; Geometrische Optik, Optische Konstante, Optische Instrumente*. Berlin : Springer, 1927

[GSHC10] GRUBER, A. ; SANKARAN, R. ; HAWKES, E. R. ; CHEN, J. H.: Turbulent Flame-wall Interaction: A Direct Numerical Simulation Study. In: *J. Fluid Mech.* 658 (2010), S. 5–32

[GTG04] GREITZER, E. M. ; TAN, C. S. ; GRAF, M. B.: *Internal Flow*. Cambridge University Press, 2004

[HGT+10] HEEGER, C. ; GORDON, R. ; TUMMERS, M. ; SATTELMAYER, T. ; DREIZLER, A.: Experimental Analysis of Flashback in Lean Premixed Swirling Flames: Upstream Flame Propagation. In: *Exp. Fluids* 49 (2010), S. 853–863

[Hig97] HIGUERA, F. J.: Boundary Layer Separation due to Gas Thermal Expansion. In: *Phys. Fluids* 9 (1997), S. 2841–2850

[HM07] HUTCHINS, N. ; MARUSIC, I.: Evidence of Very Long Meandering Features in the Logarithmic Region of Turbulent Boundary Layers. In: *J. Fluid Mech.* 579 (2007), S. 1–28

[Ind05] INDINGER, T.: *Einfluss eines positiven Druckgradienten auf turbulente Grenzschichten an glatten und gerillten Oberflächen*, Technische Universität München, Diss., 2005

[JHSK97] JEONG, J. ; HUSSAIN, F. ; SCHOPPA, W. ; KIM, J.: Coherent Structures near the Wall in a Turbulent Channel Flow. In: *J. Fluid Mech.* 332 (1997), S. 185–214

[KÖ4a] KÄHLER, C.J.: Investigation of the Spatio-temporal Flow Structure in the Buffer Region of a Turbulent Boundary Layer by Means of Multiplane Stereo PIV. In: *Exp. Fluids* 36 (2004), S. 114–130

[KÖ4b] KÄHLER, C.J.: *The Significance of Coherent Flow Structures for the Turbulent Mixing in Wall-bounded Flows*, Georg-August-Universität zu Göttingen, Diss., 2004

[KBS83] KLINE, S. J. ; BARDINA, J. G. ; STRAWN, R. C.: Correlation of the Detachment of Two-Dimensional Turbulent Boundary Layers. In: *AIAA Journal* 21 (1983), S. 68–73

[KDLW+86] KEE, R. J. ; DIXON-LEWIS, G. ; WARNATZ, J. ; COLTRIN, M. E. ; MILLER, J. A.: A Fortran Computer Code Package for the Evaluation of Gas-phase, Multicomponent Transport Properties / SANDIA. 1986 (Report No. SAND86-8246)

[KFB+10] KATHROTIA, T. ; FIKRI, M. ; BOZKURT, M. ; HARTMANN, M. ; RIEDEL, U. ; SCHULZ, C.: Study of the H + O + M Reaction Forming OH*: Kinetics of OH* Chemiluminescence in Hydrogen Combustion Systems. In: *Combust. & Flame* 157 (2010), S. 1261–1273

[KFL00] KURDYUMOV, V. N. ; FERNÁNDEZ, E. ; LIÑÁN, A.: Flame Flashback and Propagation of Premixed Flames near a Wall. In: *Proc. Combust. Inst.* 28 (2000), S. 1883–1889

[KFTT+07] KURDYUMOV, V. ; FERNÁNDEZ-TARRAZO, E. ; TRUFFAUT, J.-M. ; QUINARD, J. ; WANGHER, A. ; SEARBY, G.: Experimental and Numerical Study of Premixed Flame Flashback. In: *Proc. Combust. Inst.* 31 (2007), S. 1275–1282

[KKS07] KIESEWETTER, F. ; KONLE, M. ; SATTELMAYER, T.: Analysis of Combustion Induced Vortex Breakdown Driven Flame Flashback in a Premix Burner With Cylindrical Mixing Zone. In: *J. Eng. Gas Turbines Power* 129 (2007), Nr. 4, S. 929–936

[KKW85] KARIM, G. A. ; KIBRYA, G. ; WIERZBA, I.: Flashback and Flame Propagation Limits through Streams of Premixed Fuel and Air. In: *Proc. 7th Int. Symp. on Air Breathing Engines (ISABE)*, 1985, S. 783–786

[KL88] KARIM, G. A. ; LAPUCHA, R.: Flame Flashback for Low Reynolds Number Flows. In: *Progr. Astronaut. Aero.* 113 (1988), S. 367–383

[KMM87] KIM, J. ; MOIN, P. ; MOSER, R.: Turbulence Statistics in Fully Developed Channel Flow at Low Reynolds Number. In: *J. Fluid Mech.* 177 (1987), S. 133–166

[KMS05] KÄHLER, C. J. ; MCKENNA, R. ; SCHOLZ, U.: Wall-shear-stress Measurements at Moderate Re-numbers with Single Pixel Resolution using Long Distance μ-PIV - An Accuracy Assessment. In: *6th International Symposium on Particle Image Velocimetry Pasadena, California, USA*, 2005

[KMSS65] KHITRIN, L.N. ; MOIN, P.B. ; SMIRNOV, D.B. ; SHEVCHUK, V.U.: Pecularities of Laminar- and Turbulent-Flame Flashbacks. In: *10th Symposium (International) on Combustion*, 1965, S. 1285 – 1291

[Kon05] KONLE, M.: *Simultane PIV-LIF-Messungen zur Bestimmung der Flammenstreckungsrate*, Lehrstuhl für Thermodynamik, Technische Universität München, Diplomarbeit, 2005

[KRSR67] KLINE, S. J. ; REYNOLDS, W. C. ; SCHRAUB, F. A. ; RUNSTADLERS, P. W.: The Structure of Turbulent Boundary Layers. In: *J. Fluid Mech.* 30 (1967), S. 741–773

[KS09] KONLE, M. ; SATTELMAYER, T.: Interaction of Heat Release and Vortex Breakdown during Flame Flashback Driven by Combustion Induced Vortex Breakdown. In: *Exp. Fluids* 47 (2009), S. 627–635

[KSO06] KÄHLER, C. J. ; SCHOLZ, U. ; ORTMANNS, J.: Wall-shear-stress and Near-wall Turbulence Measurements up to Single Pixel Resolution by Means of Long-distance Micro-PIV. In: *Exp. Fluids* 41 (2006), S. 327–341

[KVK+81] KELLER, J.O. ; VANEVELD, L. ; KORSCHELT, D. ; GHONIUM, A.F. ; DAILY, J.W. ; OPPENHEIM, A.K.: Mechanisms of Instabilities in Turbulent Combustion Leading to Flashback. In: *AIAA 19th Aerospace Sciences Meeting*, 1981

[Law06] LAW, C. K.: *Combustion Physics*. Cambridge University Press, 2006

[LE43] LEWIS, B. ; ELBE, G. von: Stability and Structure of Burner Flames. In: *J. Chem. Phys.* 11 (1943), S. 75–97

[LE87] LEWIS, B. ; ELBE, G. von: *Combustion, Flames and Explosion of Gases*. Academic Press, Inc., 1987

[LMSS08] LIEUWEN, T. ; MCDONELL, V. ; SANTAVICCA, D. ; SATTELMAYER, T.: Burner Development and Operability Issues Associated with Steady Flowing Syngas Fired Combustors. In: *Combust. Sci. and Tech.* 180 (2008), Nr. 6, S. 1169–1192

[LS00] LAW, C. K. ; SUNG, C. J.: Structure, Aerodynamics, and Geometry of Premixed Flamelets. In: *Prog. Energy Combust. Sci.* 26 (2000), S. 459–505

[LS09] LEE, J.-H. ; SUNG, H. J.: Structures in Turbulent Boundary Layers Subjected to Adverse Pressure Gradients. In: *J. Fluid Mech.* 639 (2009), S. 101–131

[LT82] LEE, S. T. ; T'IEN, J. S.: A Numerical Analysis of Flame Flashback in a Premixed Laminar System. In: *Combust. & Flame* 48 (1982), S. 273 – 285

[LZKD04] LI, J. ; ZHAO, Z. ; KAZAKOV, A. ; DRYER, F.L.: An Updated Comprehensive Kinetic Model of Hydrogen Combustion. In: *Int. J. Chem. Kin.* 36 (2004), S. 566–575

[MB79] MEHTA, R.D. ; BRADSHAW, P.: Design Rules for Small Low Speed Wind Tunnels. In: *Aeronaut. J.* 73 (1979), S. 443–449

[MDG98] MALLENS, R. M. M. ; DE GOEY, L. P. H.: Flash-back of Laminar Premixed Methane/Air Flames on Slit and Tube Burners. In: *Combust. Sci. and Tech.* 136 (1998), S. 41–54

[Meh85] MEHTA, R.D.: Turbulent Boundary Layer Perturbed by a Screen. In: *AIAA Journal* 23 (1985), S. 1335–1342

[Mel97] MELLING, A.: Tracer Particles and Seeding for Particle Image Velocimetry. In: *Meas. Sci. Technol.* 8 (1997), S. 1406–1416

[Men94] MENTER, F. R.: Two-Equation Eddy-Viscosity Turbulence Models for Engineering Applications. In: *AIAA Journal* 32 (1994), S. 1598–1605

[MHN+09] MONTY, J.P. ; HUTCHINS, N. ; NG, H.C. ; MARUSIC, I. ; CHONG, M.S.: A Comparison of Turbulent Pipe, Channel and Boundary Layer Flows. In: *J. Fluid Mech.* 632 (2009), S. 431–442

[Mis07] MISHRA, D. P.: Experimental Studies of Flame Stability Limits of CNG-air Premixed Flame. In: *Energ. Convers. Manage.* 48 (2007), S. 1208–1211

[MKM99] MOSER, R. D. ; KIM, J. ; MANSOUR, N. N.: Direct Numerical Simulation of Turbulent Channel Flow up to Re_τ= 590. In: *Phys. Fluids* 11 (1999), 943-945. `http://turbulence.ices.utexas.edu/MKM_1999.html`

[MP91] MENEVEAU, C. ; POINSOT, T.: Stretching and Quenching of Flamelets in Premixed Turbulent Combustion. In: *Combust. & Flame* 86 (1991), S. 311–332

[MS68] MOIN, F. B. ; SHEVCHUK, V.U.: Flame "Blow-back" in the Combustion of Premixed Gases in Flow-through Systems. In: *Combustion, Explosion, and Shock Waves* 4 (1968), S. 121–123

[MSS+11] MAYER, C. ; SANGL, J. ; SATTELMAYER, T. ; LACHAUX, T. ; BERNERO, S.: Study on the Operational Window of a Swirl Stabilized Syngas Burner under Atmospheric and High Pressure Conditions. In: *ASME Turbo Expo, Paper No. GT2011-45125*, 2011

[Mus79] MUSKER, A. J.: Explicit Expression for the Smooth Wall Velocity Distribution in a Turbulent Boundary Layer. In: *AIAA Journal* 17 (1979), S. 655–657

[MWS00] MEINHART, C.D. ; WERELEY, S.T. ; SANTIAGO, J.G.: A PIV Algorithm for Estimating Time-Averaged Velocity Fields. In: *J. Fluid Eng.* 122 (2000), S. 285–289

[NPMW98] NAJM, H. N. ; PAUL, P. H. ; MUELLER, C. J. ; WYCKOFF, P. S.: On the Adequacy of Certain Experimental Observables as Measurements of Flame Burning Rate. In: *Combust. & Flame* 113 (1998), S. 312–332

[NTH98] NAGANO, Y. ; TSUJI, T. ; HOURA, T.: Structure of Turbulent Boundary Layer Subjected to Adverse Pressure Gradient. In: *Int. J. of Heat and Fluid Flow* 19 (1998), S. 563–572

[NTT93] NAGANO, Y. ; TAGAWA, M. ; TSUJI, T.: *Effects of Adverse Pressure Gradients on Mean Flows and Turbulence Statistics in a Boundary Layer*. S. 7-21, In: Durst, F., Friedrich, R., Launder, B.E., Schmidt, F.W., Schumann, U., Whitelaw, J.H. (Eds.), Turbulent Shear Flows, Vol. 8, Springer-Verlag, 1993

[OA00] OLSEN, M. G. ; ADRIAN, R. J.: Out-of-focus Effects on Particle Image Visibility and Correlation in Microscopic Particle Image Velocimetry. In: *Exp. Fluids* 29 (2000), S. 166–174

[OJ94] ORLANDI, P. ; JIMÉNEZ, J.: On the Generation of Turbulent Wall Friction. In: *Phys. Fluids* 6 (1994), S. 634–641

[Ols09] OLSEN, Michael G.: Directional Dependence of Depth of Correlation due to In-plane Fluid Shear in Microscopic Particle Image Velocimetry. In: *Meas. Sci. Technol.* 20 (2009), S. 015402

[PB97] POPP, P. ; BAUM, M.: Analysis of Wall Heat Fluxes, Reaction Mechanisms, and Unburnt Hydrocarbons during the Head-on Quenching of a Laminar Methane Flame. In: *Combust. & Flame* 108 (1997), S. 327–348

[Pet99] PETERS, N.: The Turbulent Burning Velocity for Large-scale and Small-scale Turbulence. In: *J. Fluid Mech.* 384 (1999), S. 107–132

[Pet00] PETERS, N.: *Turbulent Combustion.* Cambridge University Press, 2000

[PJ49] PUTNAM, A. A. ; JENSEN, R. A.: Application of Dimensionless Numbers to Flash-back and Other Combustion Phenomena. In: *Third Symposium on Combustion, Flame and Explosion Phenomena* The Combustion Institute, 1949, S. 89–98

[PL92] POINSOT, T. J. ; LELE, S. K.: Boundary Conditions for Direct Simulations of Compressible Viscous Flows. In: *J. Comp. Physics* 101 (1992), S. 104 – 129. – ISSN 0021–9991

[PM78] PLEE, S. L. ; MELLOR, A. M.: Review of Flashback Reported in Prevaporizing/Premixing Combustors. In: *Combust. & Flame* 32 (1978), S. 193 – 203

[PMSJ07] PAYRHUBER, K. ; MOLIÈRE, M. ; SCHOLZ, M. ; JONES, R. M.: Future Energy Challenges in a Carbon Constrained Environment - Fuel Flexibility as a Growing Need. In: *VGB PowerTech* 10 (2007), S. 23–29

[PO06] POELMA, C. ; OOMS, G.: Particle-Turbulence Interaction in a Homogeneous, Isotropic Turbulent Suspension. In: *Appl. Mech. Rev.* 59 (2006), S. 78–90

[Pra04] PRANDTL, L.: Über Flüssigkeitsbewegung bei sehr kleiner Reibung. In: *Verhandlg. III. Intern. Math. Kongr., Heidelberg,* 1904, S. 484–491

[REC08] BUNDESMINISTERIUM FÜR UMWELT, NATURSCHUTZ UND REAKTORSICHERHEIT, GERMANY: RECCS - Strukturell-ökonomisch-ökologischer Vergleich regenerativer Energietechnologien (RE) mit Carbon Capture and Storage (CCS). 2008

[Rob91a] ROBINSON, S. K.: Coherent Motions in the Turbulent Boundary Layer. In: *Annu. Rev. Fluid Mech.* 23 (1991), S. 601–639

[Rob91b] ROBINSON, S. K.: The Kinematics of Turbulent Boundary Layer Structure / National Aeronautics and Space Administration (NASA). 1991 (Technical Memorandum 103859)

[RWWK07] RAFFEL, M. ; WILLERT, C. ; WERELY, S. ; KOMPENHANS, J.: *Particle Image Velocimetry*. 2nd edition. Springer-Verlag Berlin, 2007

[Sch82] SCHLICHTING, H.: *Grenzschicht-Theorie*. Verlag G. Braun, 1982

[Sim96] SIMPSON, R. L.: Aspects of Turbulent Boundary-Layer Separation. In: *Prog. Aerospace Sci.* 32 (1996), S. 457–521

[SKW01] SCHÄFER, O. ; KOCH, R. ; WITTIG, S.: Flashback in Lean Prevaporized Premixed Combustion: Non-swirling Turbulent Pipe Flow Study. In: *ASME Turbo Expo, Paper No. 2001-GT-0053*, 2001

[SM83] SMITH, C. R. ; METZLER, S. P.: The Characteristics of Low-speed Streaks in the Near-wall Region of a Turbulent Boundary Layer. In: *J. Fluid Mech.* 129 (1983), S. 27–54

[SMK09] SHENG, J. ; MALKIEL, E. ; KATZ, J.: Buffer Layer Structures Associated with Extreme Wall Stress Events in a Smooth Wall Turbulent Boundary Layer. In: *J. Fluid Mech.* 633 (2009), S. 17–60

[Spa61] SPALDING, D.B.: A Single Formula for the "Law of the Wall". In: *J. Appl. Mech* 28 (1961), S. 455–458

[Spa88] SPALART, P. R.: Direct Simulation of a Turbulent Boundary Layer up to $Re_\theta = 1410$. In: *J. Fluid Mech.* 187 (1988), S. 61–98

[Spu92] SPURK, J. H.: *Dimensionsanalyse in der Strömungslehre*. Springer, 1992

[STK06] SMALLBONE, A. ; TSUNEYOSHI, K. ; KITAGAWA, T.: Turbulent and Stable/Unstable Laminar Burning Velocity Measurements from Outwardly Propagating Spherical Hydrogen-Air Flames at Elevated Pressures. In: *J. Therm. Sci. Tech. - Jpn* 1 (2006), S. 31–41

[SWM+98] SANTIAGO, J. G. ; WERELEY, S. T. ; MEINHART, C. D. ; BEEBE, D. J. ; ADRIAN, R. J.: A Particle Image Velocimetry System for Microfluidics. In: *Exp. Fluids* 25 (1998), S. 316–319

[SY05] SOGO, S. ; YUASA, S.: Flame Stretch Rate of Laminar Flame Base just before Flashback at Different Burner Temperatures. In: *20th International Colloquium on the Dynamics of Explosions and Reactive Systems*, 2005

[TA03] TOMKINS, C. D. ; ADRIAN, R. J.: Spanwise Structure and Scale Growth in Turbulent Boundary Layers. In: *J. Fluid Mech.* 490 (2003), S. 37–74

[TC98] THIBAUT, D. ; CANDEL, S.: Numerical Study of Unsteady Turbulent Premixed Combustion: Application to Flashback Simulation. In: *Combust. & Flame* 113 (1998), S. 53 – 65

[TnSP90] TREVIÑO, C. ; STÜTTGEN, W. ; PETERS, N.: Pressure Gradients due to Gas Expansion in the Boundary Layer Combustion of a Condensed Fuel. In: *Wärme- und Stoffübertragung* 25 (1990), S. 309–319

[Tur58] TURCOTTE, D. L.: *An Experimental Investigation of Flame Stabilization in a Heated Turbulent Boundary Layer,* California Institute of Technology, Diss., 1958

[Tur00] TURNS, S. R.: *An Introduction to Combustion.* McGraw-Hill, 2000

[VT04] VOLCHKOV, É. P. ; TEREKHOV, V. I.: Flow Structure and Heat and Mass Transfer in Boundary Layers with Injection of Chemically Reacting Substances (Review). In: *Combustion, Explosion, and Shock Waves* 40 (2004), S. 1–16

[WEB72] WALLACE, J. M. ; ECKELMANN, H. ; BRODKEY, R. S.: The Wall Region in Turbulent Shear Flow. In: *J. Fluid Mech.* 54 (1972), S. 39–48

[Whi05] WHITE, F. M.: *Viscous Fluid Flow.* McGraw-Hill, 2005

[Wil77] WILLIAMS, J. C.: Incompressible Boundary-Layer Separation. In: *Annu. Rev. Fluid Mech.* 9 (1977), S. 113–144

[Wil93] WILCOX, D.C.: Comparison of Two-Equation Turbulence Models for Boundary Layers with Pressure Gradient. In: *AIAA Journal* 31 (1993), S. 1414–1421

[Wil07] WILLIAM, K. G.: Is There a Universal Log Law for Turbulent Wall-bounded Flows? In: *Phil. Trans. R. Soc. A* 365 (2007), S. 789–806

[WK92] WIERZBA, I. ; KAR, K.: Flame Flashback within Turbulent Streams of Lean Homogeneous Fuel Mixtures and Air. In: *J. Energ. Resour.* 114 (1992), S. 142–145

[WNA06] WIDENHORN, A. ; NOLL, B. ; AIGNER, M.: Accurate Boundary Conditions for the Numerical Simulation of Thermoacoustic Phenomena in Gas-turbine Combustion Chambers. In: *ASME Turbo Expo, Paper No. GT2006-90441*, 2006

[Woh53] WOHL, K.: Quenching, Flash-Back, Blow-Off - Theory and Experiment. In: *4th Symp (Int.) on Combustion* (1953), S. 68 – 89

[WOK93] WIERZBA, I. ; OLADIPO, A. B. ; KARIM, G. A.: The Limits for Flame Flashback Within Streams of Lean Homogeneous Fuel-Diluent-Air Mixtures Involving Hydrogen. In: *Int. J. Hydrogen. Energ.* 18 (1993), S. 223–226

[WPW10] WILLIAMS, S. ; PARK, C. ; WERELEY, S.: Advances and Applications on Microfluidic Velocimetry Techniques. In: *Microfluid. Nanofluid.* 8 (2010), S. 709–726

[Wäs07] WÄSLE, J. G.: *Vorhersage der Lärmemission turbulenter Vormischflammen*, Technische Universität München, Diss., 2007

[WZS08] WEISS, M. ; ZARZALIS, N. ; SUNTZ, R.: Experimental Study of Markstein Number Effects on Laminar Flamelet Velocity in Turbulent Premixed Flames. In: *Combust. & Flame* 154 (2008), S. 671–691

[ZDN03] ZANOUN, E.-S. ; DURST, F. ; NAGIB, H.: Evaluating the Law of the Wall in Two-dimensional Fully Developed Turbulent Channel Flows. In: *Phys. Fluids* 15 (2003), S. 3079–3089

[ZS98] ZAGAROLA, M.V. ; SMITS, A.J.: A New Mean Velocity Scaling for Turbulent Boundary Layers. In: *Proceedings of FEDSM'98 ASME Fluids Engineering Division Summer Meeting*, 1998